

Microseismic Response of Rock Masses for Assessment of Caprock Integrity

by

Cyrus Khazaei

A thesis submitted in partial fulfillment of the requirements for the degree of

Doctor of Philosophy

Geotechnical Engineering

Department of Civil and Environmental Engineering  
University of Alberta

© Cyrus Khazaei, 2016

## ABSTRACT

Two major applications of microseismic (MS) monitoring in petroleum engineering are hydraulic fracturing operations and caprock integrity assurance. With respect to caprock integrity, this research has investigated the observation of the absence of detectable magnitudes of microseismic events as a postulate for no damage occurring within the caprock. The research explored the mechanisms of microseismic response of rock masses for the assessment and quantification of the extent of caprock damage occurring during geological storage of CO<sub>2</sub> using continuum and discontinuum modeling approaches.

In the first part of the thesis, microseismic response of rock masses is studied in two sections: intact rocks and weak planes. In order to study the microseismic response of intact rocks, a dataset of 73 uniaxial compression tests conducted by CANMET is analyzed. Acoustic emissions have also been recorded during the tests. Using the laboratory data, the relation between the total consumed energy and the released seismic energy for each type of rock is investigated. Using PFC3D, similar tests have also been conducted numerically. A modification of Gutenberg-Richter formula is proposed to get more realistic crack-induced magnitudes from PFC3D models. In order to quantify damage based on microseismic observations, a damage parameter is defined as the observed crack surface area during the test divided by the total possible crack surface area based on size of particles. The damage parameter is correlated with the cumulative released microseismic energy for each rock type at failure.

In order to study the MS response of weak planes, a biaxial shear test on a specimen of Sierra granite with a single fault diagonally installed in it is numerically modeled using PFC3D. The details of experiment including microseismic data are extracted from literature. In order to get slip-induced microseismic data from PFC3D, a new algorithm is developed. The PFC3D results have

been compared with real data. A parametric study is also conducted to investigate the effect of various parameters on stick-slip induced MS events.

In the second part of the thesis, in order to explore the applicability of numerical modeling for assessment of caprock integrity using microseismic data, Weyburn CCS project has been studied as a case history. Therefore, a field-scale geomechanical model has been developed to study the likelihood of tensile and shear failure in the caprock of Weyburn. A one-way coupling has been conducted between the reservoir simulator (GEM) and the geomechanical simulator (FLAC3D). The results showed that in general, the likelihood of shear failure along preexisting weak planes has been about 27% greater than that of tensile failure. A discussion is also presented on the relevance of this study for interpretation of microseismic data recorded in caprock.

Finally, in order to investigate the magnitudes of crack-induced and slip-induced MS emissions, a cubic representative elementary volume (REV) model with a weak plane at its center is made using PFC3D for the caprock of Weyburn reservoir. The REV is loaded to the conditions similar to those in the caprock of Weyburn. A parametric study has also been conducted to investigate the effect of varying factors on MS magnitudes. The results show that for the conditions studied in this research, slip-induced magnitudes range from  $\sim -1$  to  $-6$  while crack-induced magnitudes range from  $\sim -7$  to  $-11$ . Therefore, considering the capability of geophones, crack-induced emissions may have been too small to be recordable in the caprock. Finally, a model is proposed to link the slip-induced microseismic energies to the state of stress in the surrounding of its parent weak plane.

Considering the results of the coupled reservoir-geomechanical model as well as the magnitudes obtained from the REV model, it is concluded that microseismic monitoring in caprock is capable of recording slip-induced events greater than a certain magnitude. However,

the lack of microseismic emissions recorded by geophones, does not rule out the possibility of crack development within intact parts as well as slow-slip deformations along weak planes. Also, microseismic monitoring does not seem to be capable of recording hydrofracture initiation in the caprock.

## Preface

This thesis is an original work by Cyrus Khazaei based on four journal papers as following:

A version of Chapter 3 is published in:

Khazaei, C., Hazzard, J., & Chalaturnyk, R. (2015). Damage quantification of intact rocks using acoustic emission energies recorded during uniaxial compression test and discrete element modeling. *Computers and Geotechnics*, 67, 94-102. DOI: 10.1016/j.compgeo.2015.02.012

The laboratory experiments used in this chapter are conducted by CANMET. I was responsible for the concept formation, data analysis, numerical modeling as well as manuscript composition. Dr. Hazzard assisted in the technical details of paper as well as the numerical routines for recording crack-induced microseismicity. Dr. Chalaturnyk was the supervisory author and involved with the concept formation.

A version of Chapter 4 is published in:

Khazaei, C., Hazzard, J., & Chalaturnyk, R. (2016). Discrete Element Modeling of Stick-Slip Instability and Induced Microseismicity. *Pure and Applied Geophysics*, 173(3), 775-794. DOI: 10.1007/s00024-015-1036-7

I was responsible for concept formation, developing the numerical routines for recording slip-induced microseismicity, all the numerical analyses as well as the manuscript composition. Dr. Hazzard assisted with the concept formation and development of numerical routines. Dr. Chalaturnyk was the supervisory author.

A version of Chapter 5 is submitted for peer-review:

Khazaei, C., & Chalaturnyk, R. (2016). A large scale one way coupled reservoir geomechanical model to study the likelihood of tensile and shear failure in the caprock of Weyburn reservoir for CO<sub>2</sub>-EOR period.

I was responsible for concept formation, numerical modeling as well as manuscript composition. Dr. Chalaturnyk was the supervisory author and involved with the concept formation.

A version of Chapter 6 is published in:

Khazaei, C., Hazzard, J., & Chalaturnyk, R. (2016). A discrete element model to link the microseismic energies recorded in caprock to geomechanics. *Acta Geotechnica*, DOI: 10.1007/s11440-016-0489-x.

I was responsible for the concept formation, numerical modeling as well as manuscript composition. Dr. Hazzard assisted with the technical details of paper. Dr. Chalaturnyk was the supervisory author.

*To my parents...*

## **Acknowledgements**

My sincere gratitude goes to my supervisor Dr. Rick Chalaturnyk for his continuous support, nice personality and more importantly, for his understanding and believing in me through the hard times at the start of this journey. I am grateful to our other members of RG<sup>2</sup> specially Hope Walls and Nathan Deisman who were always helpful and supportive.

I would like to thank the Itasca Consulting Group Inc. for accepting me in the IEP program, the internship opportunity in the summer of 2013 in Toronto and providing me with a PFC5.0 license untill the end of my PhD. I really appreciate the support by Dr. Sacha Emam with PFC5.0 and Dr. Joe Cheng with FLAC3D. I am especially grateful to Dr. Jim Hazzard whose extensive knowledge of microseismicity and numerical modeling was a great help throughout my entire research even long before and after the internship.

Finally, I am indebted to the everlasting support and encouragement from my family in all these years. I could've not come this far without having faith that you were always there for me. Thank you.

# Table of Contents

Chapter 1 Introduction .....	1
1.1 Introduction .....	1
1.2 Statement of the Problem.....	4
1.3 Research Objectives .....	5
1.4 Methodology and Structure of Thesis.....	5
Chapter 2 Microseismic Monitoring and Numerical Modeling.....	8
2.1 Introduction .....	8
2.2 Recording Microseismic Data .....	8
2.3 Interpretation of Microseismic Data .....	10
2.3.1 Source Location .....	11
2.3.2 Source Mechanism (Moment Tensors) .....	12
2.3.3 Limitations of SMTI .....	17
2.3.4 Magnitudes.....	18
2.3.5 Frequency-Magnitude Relationship .....	20
2.4 Numerical Modeling.....	21
2.4.1 Continuum Modeling .....	21
2.4.2 Discontinuum Modeling.....	23
2.4.3 Coupled Continuum-Discontinuum Modeling.....	24
2.4.4 Particle Flow Code (PFC3D) .....	25
2.5 Conclusions .....	29
Chapter 3 Microseismicity within Intact Rocks.....	30
3.1 Abstract.....	30
3.2 Introduction .....	30
3.3 Theory.....	32
3.4 Description of the Material and Experiment.....	33
3.4.1 Analysis of the Experimental Data.....	36
3.5 Numerical Model.....	39
3.5.1 Algorithm for Recording AE Events.....	40

3.5.2 Results.....	41
3.6 A Comparison between Granite and Shale .....	47
3.7 Discussion.....	49
3.8 Conclusion.....	52
Chapter 4 Microseismicity along Weak Planes .....	54
4.1 Abstract.....	54
4.2 Introduction .....	55
4.3 Theory of Slip.....	56
4.4 Description of the Experiment.....	58
4.5 Algorithm for Recording the Slip-Induced Microseismicity .....	59
4.6 Results .....	62
4.7 Parametric Study.....	69
4.7.1 Studying the Effect of Space Window’s Size .....	70
4.7.2 Studying the Effect of Normal Stress Threshold for Seismic Events.....	71
4.7.3 Studying the Effect of Discretization (Size of Particles).....	72
4.7.4 Studying the Effect of Fault’s Coefficient of Friction (sj_fric).....	72
4.7.5 Studying the Effect of Particles Elasticity (ba_Ec) .....	72
4.7.6 Studying the Effect of Fault’s Normal Stiffness (sj_kn) .....	75
4.7.7 Studying the Effect of Fault’s Shear Stiffness (sj_ks).....	76
4.7.8 Studying the Effect of Fault’s Elasticity (sj_kn & sj_ks).....	77
4.7.9 Studying the Effect of Normal Stress.....	78
4.8 Discussion.....	79
4.9 Conclusion.....	80
Chapter 5 Weyburn CCS Project: Part 1 .....	83
5.1 Abstract.....	83
5.2 Introduction .....	83
5.3 Geology of Weyburn Field .....	88
5.4 Stress Regime in Weyburn .....	91
5.5 Microseismic Monitoring in Weyburn .....	94
5.6 Numerical Modeling.....	98

5.6.1 Caprock-Reservoir Stress Transfer in a CO <sub>2</sub> Injection Scenario .....	98
5.6.2 Reservoir Model (GEM).....	99
5.6.3 Geomechanical Model (FLAC3D) .....	102
5.6.4 One-way Reservoir Geomechanical Coupling.....	106
5.6.5 Results .....	111
5.7 Discussion.....	113
5.8 Conclusion.....	119
Chapter 6 Weyburn CCS Project: Part 2 .....	121
6.1 Abstract.....	121
6.2 Introduction .....	122
6.3 A Representative Elementary Volume (REV) Model for the Caprock of Weyburn.....	123
6.4 Calibration of Microseismic Recording Algorithms for Weyburn .....	126
6.5 Parametric Study.....	129
6.5.1 Studying the effect of weak plane's orientation .....	129
6.5.2 Studying the effect of coefficient of friction .....	133
6.5.3 Studying the effect of weak plane's elasticity .....	134
6.6 Post-observation analysis of microseismic events .....	137
6.7 A general model for estimating the state of stress from MS energies recorded in the caprock .....	142
6.8 Conclusions .....	146
Chapter 7 Summary and Conclusions.....	148
References .....	152

## List of Figures

Figure 1.1: Frequency spectrum in different type of released acoustic energy in typical supposed environments (modified by (Cai et al., 2007) after (Hardy, 1981)) .....	3
Figure 2.1: A schematic illustration of waveform and related parameters (Lozev, 1997) .....	8
Figure 2.2: A schematic view of geophone (Barzilai, 2014) .....	10
Figure 2.3: Theoretical 2D source location. Sensors are shown with S1, S2 and S3. The source location is shown with the blue mark (Nivesrangsan et al., 2007) .....	11
Figure 2.4: A schematic representation of p and s wave arrivals. The noise is bound between red lines. This wave has a good signal-to-noise ratio ( $SNR=A/B$ ) (modified after (Forouhideh, 2011)) .....	13
Figure 2.5: Nine generalized components of the moment tensor (Li et al., 2015) .....	14
Figure 2.6: (Top) A schematic decomposition of moment tensor. (Bottom) Particle motions .....	16
Figure 2.7: Calculation logic of PFC models (Itasca, 1999) .....	25
Figure 2.8: Schematic formulation for BPM model. Top right shows increments of elastic force and moment. I and J are moment of inertia and polar moment of inertia of parallel bond cross section and A is the area of the cross section. Right bottom shows the maximum tensile and shear stresses that a bond can tolerate. If any of these strengths exceed then the bond and its forces and moments are removed from the model. Left bottom: the maximum shear strength (Potyondy & Cundall, 2004) .....	27
Figure 2.9: a) standard contact model with relative normal and tangential forces with regard to their orientation b) displacement of the particles bonded by standard contact model assuming the bottom ball is fixed c) normal and tangential forces on the particles whose contact is located along the smooth joint regarding their orientation with respect to the joint c) displacement of particles bonded by smooth joint model (Mas Ivars, 2008) .....	28
Figure 3.1: Schematic load-deformation curve for an intact rock. OAE and OAD curves are response curves for a brittle and ductile rock, respectively. Shaded area is the excess energy released as acoustic emission (modified after (Fairhurst, 2013)) .....	33
Figure 3.2: ISRM classification of rocks based on uniaxial compressive strength .....	34
Figure 3.3: Young's modulus versus unconfined compressive strength for the specimens tested by CANMET (data is color coded according to the ISRM classification) .....	35
Figure 3.4: Variations of b-values obtained for DGR-1, DGR-2 and DGR-3 tests conducted by CANMET versus unconfined compressive strength .....	37
Figure 3.5: The maximum energy release versus the UCS .....	37
Figure 3.6: Variations of the total recorded acoustic energy versus the total consumed energy by the specimen .....	38

Figure 3.7: A sample test with particles (blue), measurement spheres (green) and bond breakages (black) as well as stress-strain curves for each measurement sphere shown next to it. Calibration would be based on UCS and Young’s modulus from an average value obtained from the three measurement spheres with functions already available in PFC3D routines library .....	43
Figure 3.8: Variations of the Released Acoustic Energy versus the Total Consumed energy .....	44
Figure 3.9: Variations of damage parameter versus the consumed energy per unit volume of PFC3D models .....	46
Figure 3.10: Variations of damage parameter versus the released AE energy per volume of rock .....	47
Figure 3.11: Variations of total crack surface area possible versus average diameter of particles in a REV with $0.5 \times 0.5 \times 0.5$ m dimensions .....	48
Figure 3.12: A comparison between the MS response of brittle and ductile rocks. (a) Lac Du Bonnet granite modified after [Martin, 1993]. (b) Kannagawa powerhouse granite (Cai et al., 2008). (c) Hong Kong granite (point A was believed to be due cracking within grains) (Liu et al., 2000). (d) Opalinus clay (AE events are shown by circles. The red line shows the cumulative AE events) (Amann et al., 2011) (e) Soft tuff rock called “Tage tuff” (Mori et al., 2007). (f) Soft sedimentary rocks obtained from Horonobe URL (Mito et al., 2007).....	50
Figure 4.1: a) Solid red line is variations of the resistive frictional force. The simplified change in friction is shown in dotted blue. The dashed green line shows variations of the driving force once the block starts to move until it stops. b) Horizontal section of a more realistic model for the fault. The masses, stiffness of springs and normal stress on each block are not necessarily equal due to heterogeneity. Three arbitrary patches are shown with dotted red, solid purple and dashed green. The red and green patches can slide simultaneously. ....	56
Figure 4.2: (Left) McLaskey’s experimental setup. (Right) Slip sensors and piezoelectric sensors. Piezoelectric sensors are mounted on top and bottom of the sample. Flatjacks are marked with FJ1 to FJ4. Strain gages are shown by S1 to S15. (McLaskey & Kilgore, 2013) .....	59
Figure 4.3: A section of the fault illustrating the clustering process for three contacts, A, B and C. It’s assumed no other contacts within the space window slipped from 0.10 to 0.20 s. Size of the elliptic event is determined based on the closest and farthest contacts to the center of the event (i.e. B and A, respectively).....	62
Figure 4.4: The PFC3D model. The fault extends from the top right to the bottom left.....	63
Figure 4.5: Stress measurements during the test. Dotted blue curve starting at 5 MPa is the direct measurement of normal stress from the particles along the fault. The solid green curve at 5 MPa is the normal stress along the fault determined from the wall-based stresses by the transformation matrix. The solid black curve starting at 0 MPa is shear stress along the fault directly measured from the smooth joint contacts. The two dashed symmetrical red and purple curves are the wall-based stresses along the x and y directions, respectively. ....	65

Figure 4.6: The average shear stress along the fault versus time. Shear force is a vector with 3 components. Average shear stress of all the contacts with smooth joint model along the x and y directions are calculated by summing up their respective forces divided by their areas. Then, the average shear stress along the 45° fault has been calculated by the stress transformation matrix.....	66
Figure 4.7: The top figure shows the location of events reported by (McLaskey et al., 2014). Foreshocks and aftershocks are shown by circles and diamonds, respectively. They have not reported the events near the fault ends. The two figures at the bottom with blue background are the location of slips in the PFC3D model at both sides of the faults. The figure between these two is a side view of the fault with the location of events around it. No clustering is shown in this figure. ....	67
Figure 4.8: The clustered events in PFC3D model. A bigger radius shows a larger patch. Concentric circles represent consecutive slips on the same contact. ....	68
Figure 4.9: Variations of stick-slip behavior in different contacts along the fault. Normal and shear forces are shown with blue and red, respectively. ....	69
Figure 4.10: b-value plots as well as frequency of the number of events recorded during the tests for three different sizes of space windows.....	70
Figure 4.11: b-value plots as well as frequency of the number of events recorded during the simulations illustrating the model’s behavior for different normal stress thresholds for the slips to be considered seismic .....	71
Figure 4.12: Variations of model’s behavior for different resolutions .....	73
Figure 4.13: Variations of model’s behavior for different coefficients of friction .....	74
Figure 4.14: Variations of model’s behavior for different Young’s modulus of the particles. Distribution of magnitudes for the softest model are plotted based on the events recorded until 2 mm and 9.6 mm displacements .....	75
Figure 4.15: Variations of model’s behavior for different normal stiffness values of the fault. The shear stiffness of the fault is kept the same in all the models ( $sj\_ks=2.1e10$ ) .....	76
Figure 4.16: Variations of model’s behavior for different shear stiffness values of the fault. The normal stiffness of the fault is kept the same in all the models ( $sj\_kn=2.1e10$ ).....	77
Figure 4.17: Variations of model’s behavior for different elastic properties of the fault. Distribution of magnitudes for the model with softest fault properties are plotted based on the events recorded until 2 mm and 3.8 mm displacements.....	78
Figure 4.18: Variations of model’s behavior for different normal stresses. Distribution of magnitudes for the model with 7 MPa normal stress are plotted based on the events recorded until 2 mm and 2.8 mm displacements .....	79

Figure 5.1: Location of the Weyburn field and Phases as well as stress orientations (modified after (Bell & Babcock, 1986; Bell et al., 1994; Soltanzadeh, 2009; Whittaker, 2010a). The Phase map is courtesy of Cenovus Energy. The dots in the map represent wells. ....	87
Figure 5.2: Average reservoir pressure after history matching (modified after (Jafari et al., 2011)). The red line shows the maximum recommend pressure, 29.5 MPa (Wilson & Monea, 2004) .....	88
Figure 5.3: Geological units of the Mississippian strata (Baharvand Ahmadi et al., 2011).....	89
Figure 5.4: Schematic generalized SW-NE cross-section of the Weyburn reservoir. Subdivisions of Vuggy are shown with V1, V2 etc. and subdivisions of Marly are shown with M1 and M3 (modified after (Burrowes & Gilboy, 2000; Steve Whittaker, 2010b)) .....	90
Figure 5.5: (Left) In situ stresses at Weyburn (Jimenez, 2007) and (Right) schematic illustration of the principal stresses with regard to the borehole breakout (red) and direction of fracture propagation (green) (modified after (Gomez, 2006b)).....	93
Figure 5.6: Summary of the maximum horizontal stress in Western Canadian Sedimentary Basin (data plotted by (Gomez, 2006b) after (Bell et al., 1994)).....	93
Figure 5.7: (Left) Location map of phases IA and IB. The location of the monitoring well for microseismic study is the red dot in the east pattern of Phase IB – (Right) map of wells in vicinity of the microseismic monitoring well in the Eastern pattern of Phase IB. The microseismic array was installed in August 2003 (Wilson and Monea, 2004). ....	95
Figure 5.8: The injection rates in well 121/06-08. Periods of not recording MS events are shown with green (Verdon, 2012). The black bars show the number of reliably locate microseismic events (“ESG Weyburn Microseismic Progress Report,” 2011).....	95
Figure 5.9: Microseismic events located in Weyburn during 7 years of monitoring. The color coding is based on the time of occurrence (data plotted after (“ESG Weyburn Microseismic Progress Report,” 2011)). Two events on February 27 <sup>th</sup> of 2004 and one event in September 24 <sup>th</sup> of 2007 are not shown since they were far away from this area. ....	97
Figure 5.10: Schematic representation of stress transfer in a caprock-reservoir system. The regions of decreased minimum stress are shown with light blue (modified from (Kaldi et al., 2011) after (Marsden, 2007)) .....	99
Figure 5.11: Phases IA and IB as well as the area modeled by GEM ( $\Delta ABCD$ ). The area modeled by FLAC3D includes the reservoir section similar to the GEM model plus 20 km sideburden at each side. The boundaries of the FLAC3D model are not to scale in this figure. ....	100
Figure 5.12: Location of the wells for which the in-situ pressure has been measured (the microseismic observation well is marked by red). The color coding is based on the “Grid Top” elevation below mean sea level (Jafari et al., 2011) .....	101
Figure 5.13: Comparison between the measured (red dot) and simulated pressures (blue line) for the well 194090600613W2 (Jafari et al., 2011).....	102

Figure 5.14: A 2D vertical cross section of the GEM model (CD side in Figure 5.11) as well as elevations of the layers added to the FLAC3D model. The reservoir and primary seal layers are color coded based on their thickness in meters (figure is not to scale). .....	103
Figure 5.15: A schematic illustration of how refining the zones contributes to better replication of stratigraphy. Three reservoir layers (purple, green and yellow) separated by three horizons ( $H_{n-1}$ , $H_n$ , and $H_{n+1}$ ) are shown. The zones with centers bound between two horizons are assigned the same “group name”. However, in figure 8(a), the layer bound between $H_{n-1}$ and $H_n$ cannot be identified due to low resolution. ....	104
Figure 5.16: Zoomed reservoir section in FLAC3D. ....	104
Figure 5.17: The entire FLAC3D model as well as the orientation and in-situ stress gradients as reported by (Gomez, 2006a). ....	105
Figure 5.18: Reservoir pressures of the M1 layer (Top) and M3 layer (Bottom) in July 1 <sup>st</sup> , 2003 imported from GEM (Left) to FLAC3D (Right). This cross section corresponds to ( $\Delta ABCD$ ) in Figure 5.11. The GEM and FLAC3D pore pressures in the legend are in kPa and Pa, respectively. ....	108
Figure 5.19: Reservoir pressures of the V1 layer (Top) and V2 layer (Bottom) in July 1 <sup>st</sup> , 2003 imported from GEM (Left) to FLAC3D (Right). This cross section corresponds to ( $\Delta ABCD$ ) in Figure 5.11. The blank zones in the GEM layers are due to stratigraphy and pinch-outs. The GEM and FLAC3D pore pressures in the legend are in kPa and Pa, respectively. ....	109
Figure 5.20: Reservoir pressures of the V3 layer (Top) and V6 layer (Bottom) in July 1 <sup>st</sup> , 2003 imported from GEM (Left) to FLAC3D (Right). This cross section corresponds to ( $\Delta ABCD$ ) in Figure 5.11. The blank zones in the GEM layers are due to stratigraphy and pinch-outs. The GEM and FLAC3D pore pressures in the legend are in kPa and Pa, respectively. ....	110
Figure 5.21: An example of pressure distribution along the height of the reservoir layers at corner C shown in Figure 5.16. The layers 1, 2, 3, 4, 5 and 6 represent M1, M3, V1, V2, V3 and V6, respectively. ....	111
Figure 5.22: Contours of fracture margin ratio, $P_{fmr}$ , and shear margin ratio, $P_{smr}$ , for the M03F layer at nine timesteps. The MS area is shown with grid. The areas with values greater than one are prone to failure. ....	117
Figure 5.23: Maximum failure margin ratios (tensile and shear) observed in the entire M03F layer for the timesteps modeled in present study. ....	118
Figure 5.24: Maximum failure margin ratios (tensile and shear) observed only in the MS area within the M03F layer for the timesteps modeled in present study along with the number of microseismic events located above -1430 m. Periods of not recording are shown with green. ....	118

Figure 5.25: b-value plots at four periods in Weyburn. Each plot belongs to the events only recorded in that period above -1430 m. Data plotted after (“ESG Weyburn Microseismic Progress Report,” 2011)..... 119

Figure 6.1: (Top) The PFC3D model (REV) in the caprock above the reservoir. A weak plane with  $1\text{m}^2$  area is implemented at the center of it and the load is applied along the y direction by moving the bottom platen upwards to resemble the loading scheme applied to the caprock as a result of stress transfer due to increase in reservoir pressures. The measurement sphere is shown with green. (Bottom) A reservoir model along with the chart shows history matched average reservoir pressures (Jafari et al., 2011). Red line is the maximum allowed pressure, 29.5 MPa (Wilson & Monea, 2004). This figure is schematic to illustrate the logic behind the model and is not to scale. .... 125

Figure 6.2: b-value plots for real data and numerical models with two different sizes of space window (Real data plotted after (Verdon, 2010)) ..... 129

Figure 6.3: The top two plots show nine orientations of weak plane considered in parametric study. The bottom plot is the overall stress-strain curve obtained from measurement sphere shown in Figure 6.1 ..... 131

Figure 6.4: b-value plots for the nine orientations of weak plane shown in Figure 6.3. Real b-value plots are obtained using data after (Verdon, 2010) ..... 132

Figure 6.5: Location of slip-induced events along the faults. Although the events are spread at both sides of each fault, only one side is shown in this figure. The area of each slip patch for calculation of scalar seismic moment is calculated as an ellipse (Khazaei et al., 2015b). However, due to plotting difficulties, the events are shown with circles. The faults in this figure have been rotated, if necessary, to increase the visibility of the events ..... 133

Figure 6.6: b-value plots for models with different coefficients of friction of the fault ..... 134

Figure 6.7: Effect of stiffness properties of weak plane on MS energies ..... 137

Figure 6.8: Events recorded in Weyburn between Sep and Oct of 2010. The events above -1400 m are marked with yellow and have been used for analyses. The orange events are located below -1400 m. The single event circled with red is excluded from the analyses. The axes x and z are along the maximum and minimum horizontal stresses, respectively. The plane makes the angle  $\alpha$  with x direction and passes through  $(x_0, z_0)$  that is an arbitrary point on the plane taken as (591800, 5479600). The distance of each event with this plane is  $d$ . ..... 140

Figure 6.9: The REV with  $5\text{ m} \times 5\text{ m} \times 5\text{ m}$  dimensions made for studying the events in the caprock of Weyburn from September to November of 2010. The weak plane makes an angle of  $45^\circ$  with x and z directions. .... 141

Figure 6.10: a) The b-value plot for events located above -1400 m in September of 2010 (red) and the b-value plot for all the events above -1400 m recorded from September to November of 2010

in Weyburn (black) (Real data plotted after (“ESG Weyburn Microseismic Progress Report,” 2011)). The b-value plots obtained from PFC3D are also shown for two states of loading. b) b-value plot for crack-induced events recorded by PFC3D for the REV loaded to failure. No crack-induced events were observed for the REV loaded to 9.4 MPa deviator stress c,d) The Stress-strain and volumetric strain-axial strain curves for the REV loaded to 9.4 M (green) and loaded to failure (blue) ..... 142

Figure 6.11: Schematic illustration of how evolution of b-value plots for microseismic events can be related to the state of stress in the surrounding rock. Each b-value plot corresponds to a state of stress within the REV ..... 143

Figure 6.12: (a) The b-value plots for slip-induced events obtained from PFC3D at five states of loading. (b) b-value plot for crack-induced events recorded by PFC3D for the REV at five states of loading. No crack-induced events were observed for the REV loaded to 9.4 MPa deviator stress..... 145

Figure 6.13: Consumed energy per volume of REV,  $W_{\text{cons./vol}}$ , versus total released seismic energy due to stick-slips,  $E_T$  ..... 146

## List of Tables

Table 2.1: Categorization of AE level based on spill alert device used for monitoring by (Koerner & Lord, 1984) .....	11
Table 3.1: Rock types identified by CANMET (Gorski et al., 2009a) .....	34
Table 3.2: Calibration parameters of PFC3D specimens. The average radius for all the models has been 2 mm (14043 particles). The coefficient of friction (ba_fric) for all the specimens has been equal to 3.5 and the Young's modulus for all the balls has been set equal to the Young's modulus of parallel bonds (ba_Ec=pb_Ec). .....	42
Table 4.1: Micro-parameters used in PFC3D model of Sierra granite.....	64
Table 5.1: Lithological properties of the Weyburn reservoir (Burrowes & Gilboy, 2000).....	90
Table 5.2: Properties used in the geomechanical model (Gomez, 2006b; Verdon, 2010).....	105
Table 5.3: Sideburden properties in the geomechanical model. The properties are chosen equal to the zones with the same elevation in the reservoir section.....	105
Table 5.4: GEM and FLAC3D timesteps. Each timestep in FLAC3D includes cycling the model to equilibrium after pressures of two consecutive GEM timesteps are applied to the model. The average pore pressures (PP) are calculated based on pore pressures of all the 33316 reservoir zones in the GEM model.....	107
Table 6.1: Calibration parameters for parallel bond properties in REV .....	125
Table 6.2: Micro-parameters used in PFC3D model for calibration of slip-induced microseismic recording routines.....	128

## List of Abbreviations

<b>Abbrev.</b>	<b>Definition</b>	<b>First Use</b>
AE	Acoustic Emission .....	2
AECL	Atomic Energy of Canada Limited .....	24
CCS	Carbon Capture and Sequestration .....	1
CLDV	Compensated Linear Vector Dipole.....	14
CSS	Cyclic Steam Stimulation .....	1
DC	Double Couple .....	14
DEM	Distinct Element Method .....	25
DGR	Deep Geologic Repository .....	33
EOR	Enhanced Oil Recovery .....	1
FLAC3D	Fast Lagrangian Analysis of Continua.....	6
FTC	First Threshold Crossing .....	35
GEM	Generalized Equation of State Model Reservoir Simulator .....	6
HDT	Hit Definition Time .....	9
IEA	International Energy Agency .....	84
ISO	Isotropic.....	14
MS	Microseismic .....	2
OPG	Ontario Power Generation .....	33
PDT	Peak Definition Time .....	35
PFC	Particle Flow Code.....	5
PTRC	Petroleum Technology Research Center.....	84
RESCUE	REServoir Characterization Using Epicentre.....	106
REV	Representative Elementary Volume .....	7
RMS	Root Mean Squared .....	12
SAGD	Steam Assisted Gravity Drainage.....	1
SMTI	Seismic Moment Tensor Inversion.....	13
SNR	Signal to Noise Ratio .....	12
UCS	Uniaxial Compression Strength .....	36
URL	Underground Research Laboratory .....	24

# Chapter 1

## Introduction

### 1.1 Introduction

Proven oil reserves in Canada were estimated to be 173.6 billion barrels as of the beginning of 2012 which makes Canada third place in the world after Saudi Arabia and Venezuela (U.S. (EIA), 2014). Almost 98% of Canada's oil reserves are oil sands that are considered unconventional (U.S. (EIA), 2014). Due to high oil viscosity in unconventional reservoirs, it is not possible to extract it by direct methods. Therefore, enhanced oil recovery (EOR) techniques such as gas injection, hot water injection, steam assisted gravity drainage (SAGD) and cyclic steam simulation (CSS) have been developed to reduce the oil viscosity and assist the extraction process. Also, another commonly used EOR technique is injection of CO<sub>2</sub> in the form of gas or liquid into the reservoir. Liquefied CO<sub>2</sub> reduces the oil viscosity and improves its displacement. In Canada, CO<sub>2</sub>-EOR started in the Weyburn field (Phase IA) in Saskatchewan since 2000 with the purpose of boosting oil production.

Although injection of CO<sub>2</sub> in the ground has been practiced in the oil industry for a long time, carbon capture and sequestration (CCS) is relatively a modern driver for injection of CO<sub>2</sub> in deep geological formations. Fossil fuel based power plants and other industries produce a large amount of CO<sub>2</sub> that contribute to climate change. Therefore, from a cost-benefit perspective, the sequestration of CO<sub>2</sub> is being considered as a value-added element of CO<sub>2</sub>-EOR projects, including depleted oil and gas reservoirs. Application of CCS in a conventional power plant is estimated to reduce the amount of CO<sub>2</sub> emission in the atmosphere to about 80-90% compared to a plant without CCS (Metz et al., 2005).

However, the feasibility and efficiency of all these underground operations are sometimes questioned regarding concerns about possible damage to the surrounding environment, in particular the caprocks overlying the injection horizons. Such damage may provide leakage paths for CO<sub>2</sub> and other fluids (i.e. brine, hydrocarbons) to reach the surface. Leakage of contaminants must be prevented first because its presence in the biosphere and the human environment can be deleterious and secondly because hydrocarbons are a valuable resource and poses challenges with resource conservation.

In any type of underground injection scenario there is always a trade-off between the economics of the project that encourages high-pressure injection in high volumes on the one hand and the safety of the project that requires low pressures to ensure everything is under control, on the other hand. Once steam/liquid is injected into the reservoir, it induces stress changes and potentially, fluid pore pressures in the caprock that can cause new fractures within intact parts or trigger shear along weak planes facilitating a pathway for the escape of contaminant and jeopardizing its confinement within the reservoir. As a result, caprock integrity has become a major focus in both oil sand and CCS technologies in Western Canada and around the world. Therefore, once the injection begins, reliable monitoring methods such as remote sensing, active seismic monitoring and passive seismic monitoring etc. are employed to ensure both optimization and safety requirements are met.

Among monitoring techniques, passive seismic monitoring refers to recording of elastic waves, known as acoustic emission or microseismic, generated as a result of the material undergoing deformations. The elastic waves can be captured by sensors and transferred to a computer station for processing. Analyzing the waveforms reveals information such as the location and mechanism of damage. The results can be reported to operators for modifying the operations.

The two terms, acoustic emission and microseismic, are sometimes used interchangeably but technically, they refer to the waves with different frequency ranges. A general categorization of released acoustic energy with typical observed frequencies in different environments is shown in Figure 1.1. In this text, the terms “microseismic (MS)” and “acoustic emission (AE)” will be used interchangeably.

The main advantage of using MS monitoring is locating and evaluating the damage almost continuously. Therefore, it helps understanding how the ground responds to the new forms of stress where direct observation is not possible. It can also serve as a surveillance program.

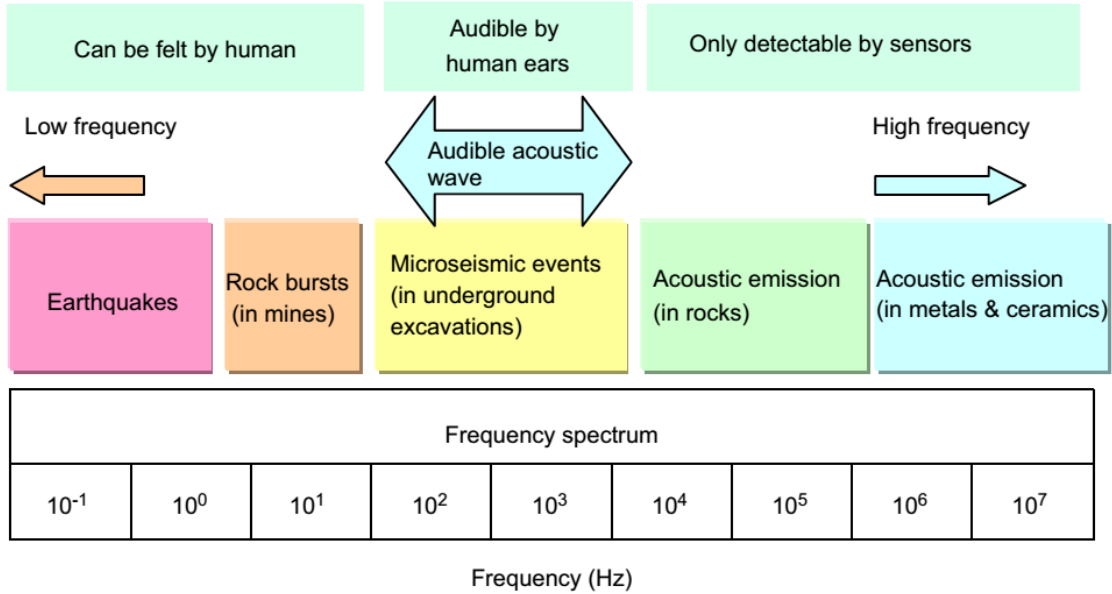


Figure 1.1: Frequency spectrum in different type of released acoustic energy in typical supposed environments (modified by (Cai et al., 2007) after (Hardy, 1981))

However, there are practical considerations behind the recording techniques as well as conceptual differences between the physical meanings of a certain amount of released acoustic energy in different types of rocks at different scales depending on their constitutive behavior. Therefore, in order for microseismic monitoring to be efficient, a cause and effect link has to be established between the recorded events and physical damage. If so, using microseismic data, a real time picture can be inferred with regard to the integrity of caprock.

For this purpose, laboratory experiments are a great tool for studying the microseismic behavior and observing the damage progress simultaneously. Using high pressure and temperature laboratory setups, it is possible to expose retrieved cores from the caprock to similar conditions that they encounter in the reservoir and observe how this material reacts to it in a small scale. However, these lab tests will never reflect the complexity of the behavior that exists in the large-scale rock mass covering the reservoir. Also, due to economical and practical limitations, it is not always possible to extract a good number of core samples and test them under all the likely scenarios.

Therefore, decisions have to be made based on limited data in hand and thus numerical modeling seems to be an inevitable tool that provides a better insight on situations where direct prototype testing is not possible. For the particular problem of microseismic monitoring in the large-scale

caprock, numerical modeling assists in understanding how this type of material behaves and how its seismic response is in real-life conditions.

## **1.2 Statement of the Problem**

Two major applications of MS monitoring in petroleum engineering are a) in hydrofracture operations and b) as a caprock monitoring tool. In hydrofracture operations, the injection pressure is deliberately high enough to induce fractures in the rock. Therefore, microseismic events are usually first detected close to the injection well propagating outwards. Having this picture in mind makes understanding the physical interpretation of the recorded events easier. Also, the number of events correlates to the increase in permeability and increase in production. However, in caprock monitoring for CCS or SAGD projects the injection pressure is deliberately kept low enough (lower than the fracture gradient) to prevent any damage to the caprock. Therefore, emergence of MS events in the caprock raises the concern about the mechanism behind them and how much damage they do represent. Such events are wide spread throughout the caprock and their number is significantly lower compared to other instances of MS monitoring in hard rocks such as tunneling projects.

In this regard, two hypotheses are proposed and will be investigated in this research:

1- The number of events in the caprock as recorded and analyzed is reasonable. However, regarding the shear mechanism along weak planes compared to the rupture mechanism of intact rocks, the extent and type of damage in caprock problems is not the same as what it would be for the same number of events in smaller scale hard rock problems. With the Weyburn dataset, the hypothesis is that the very fact that a few detectable magnitudes of microseismic events have been recorded implies that the actual extent of shear damage is extensively large and that is the only way that the emitted waves could have reached the geophones.

2- The real number of events is much greater than what can be recorded and the reason for this difference is capability of geophones to record and process the waveforms. Therefore, the statement of “early warning detection system” may no longer be valid for the large scale MS monitoring of caprock.

### **1.3 Research Objectives**

This research seeks to explore the mechanism of microseismic response of rock masses for the assessment and quantification of the extent of caprock damage occurring during geological storage of CO<sub>2</sub>.

Therefore, the fundamental mechanism of microseismic response in intact rocks as well as weak planes will be studied and its implication as a monitoring tool for caprock integrity in geological storage of CO<sub>2</sub> will be explored.

### **1.4 Methodology and Structure of Thesis**

The objectives of this research will be pursued according to the following methodology as separated in steps for different chapters of the final thesis:

An introduction to the role and importance of microseismic monitoring in petroleum projects, statement of the problem, objectives and organization of thesis is presented in Chapter 1.

Chapter 2 is divided in two parts. In the first part, the basics required for understanding how microseismic data is recorded and processed (how different type of sensors work and how the location and mechanism of damage are determined) will be presented. In the second part, a review of previous works on numerical modeling of microseismicity using both continuum and discontinuum methods is presented. Also, since Particle Flow Code (PFC3D) is the main numerical tool for studying microseismicity in this research, it is introduced in this chapter.

Chapter 3 contributes to the fundamental understanding of microseismic response of intact rocks. A version of this chapter is published in (Khazaei et al., 2015a). The idea is that the microseismic response of rock mass can be regarded as the weak planes response (governed by shear along weak planes) and the intact rock response (governed by crack development). Therefore, crack-induced events and shear-induced events are separately investigated. This goal is achieved by using the Particle Flow Code (PFC3D) as introduced in Chapter 2. In order to study the crack-induced acoustic emissions, first the theory of the release of energy due to cracking is introduced. Then, a wide range of laboratory tests reported by CANMET conducted as a part of

deep geologic repository design for the Ontario Power Generation is analyzed. The uniaxial compressive strength of the specimens tested by them ranges from 1 MPa to 150 MPa and thus it seems to be an appropriate data set for this study. Also, because of the small scale of laboratory specimens and lack of weak planes in them, it is assumed that the majority of the events reported by CANMET have a crack-based origin. In an attempt to find a relation between the released acoustic energy and strength properties of the rock, various items such as b-value, absorbed energy by the specimen and cumulative released energy are investigated. Also, in order to better understand the crack-induced events, using the routines for recording crack-induced events, specimens with the same size, strength and stiffness properties as those of CANMET are modeled by PFC3D and the results are compared with CANMET data.

Chapter 4 is dedicated to the fundamental understanding of MS response through weak planes. A version of this chapter is published in (Khazaei et al., 2015b). In order to study the shear-induced events along preexisting weak planes, the physics of slip theory are introduced. Then, the experiment reported by (McLaskey & Kilgore, 2013) on a large specimen of Sierra granite with a single pre-existing diagonal fault is numerically modeled. The advantage of their experiment is that there were AE sensors installed along the fault so that once the specimen was biaxially loaded; the shear induced release of acoustic energy (stick-slips) could be recorded. Unlike previous PFC3D models that were only able to identify crack-induced bond breakages (events), new routines have been developed that allow studying the slip-induced acoustic emissions. Details of these routines as well as a comparison between the numerical and experimental data are included in this chapter. This comparison provides confidence on validity of the numerical model. Also, conducting a parametric study, the effect of various factors on stick-slip events is explored.

The Weyburn CO<sub>2</sub>-EOR project is introduced in Chapter 5. That includes the geology, the reservoir and its seal layers, history of production, and history of microseismic recording in Weyburn. Then, a description of the reservoir model built in GEM (Generalized Equation of State Model Reservoir Simulator) and details of constructing the field scale geomechanical model in FLAC3D (Fast Lagrangian Analysis of Continua) including the generation of stratigraphy and how the pressures can be imported to the FLAC3D are discussed. Eventually, using the coupled model, the effect of evolution in reservoir pore pressures on variations of in situ stresses and its

implication on tensile and shear failure in the caprock is investigated. A version of this chapter is submitted to (Khazaei & Chalaturnyk, 2016).

In Chapter 6, using PFC3D, a representative elementary volume (REV) model is made for the caprock of Weyburn reservoir. The REV is loaded with the conditions similar to those in the caprock of Weyburn. Two algorithms for recording crack-induced and slip-induced MS emissions as introduced in Chapter 3 and Chapter 4, respectively, have been used simultaneously during the tests. This allows studying both crack-induced and slip-induced MS emissions at the same time. Also, a parametric study is conducted to investigate the effect of varying factors on release of MS energies. Finally, a simple model is presented to correlate the seismic energy released due to stick-slips along a weak plane to the total energy consumed by the REV. A version of this chapter is accepted for publication in (Khazaei et al., 2016).

Summary and conclusions of the research are presented in Chapter 7.

# Chapter 2

## Microseismic Monitoring and Numerical Modeling

### 2.1 Introduction

The first part of this chapter is devoted to some basic geophysical information on microseismic monitoring. This includes recording devices, source location and analysis of waveforms. In the second part, previous studies on numerical modeling (continuum and discontinuum) of microseismicity are reviewed. Finally, Particle Flow Code (PFC3D), which is the main software for studying microseismicity in this thesis, is introduced.

### 2.2 Recording Microseismic Data

AE/MS is referred to the elastic waves emitted as a result of a disturbance within the material (e.g. cracks, slippage, strain etc.). A schematic AE signal (waveform) is shown in Figure 2.1. As can be observed in this figure, several properties such as peak amplitude, duration and rise time could be obtained from a waveform. A threshold is also used to filter out the background noise and eliminate weak signals.

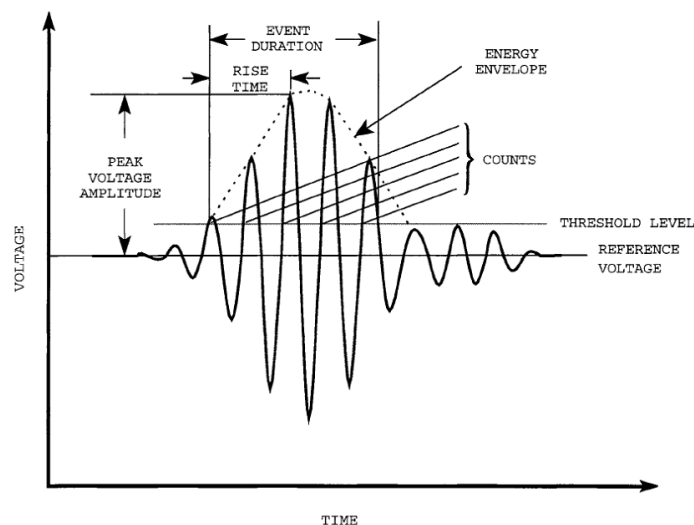


Figure 2.1: A schematic illustration of waveform and related parameters (Lozev, 1997)

In order to record these waves, a mechanism is required to convert displacements into electric signals. For the purpose of microseismic monitoring, two of the most common tools are piezoelectric sensors, mostly used in laboratory recordings and geophones, mostly used in large-scale reservoirs.

### **Piezoelectric Sensors**

A piezoelectric sensor has a piezoelectric material that is capable of converting displacements into voltage. This property is called “Transduction” and can be found in materials such as quartz, lead (Pb) zirconate (Zr) titanate (Ti) (also known as PZT) or synthetic ceramics. The sensor is coupled to the body of interest in which acoustic waves propagate. In order to get a good response from any sensor, there should be a proper connection/coupling between the sensor and the surface of the material in which AE waves propagate. As the wave gets to the sensor, the motion of the particles is received by the sensor and is converted into voltage. The particle motion can have three components. Therefore, the AE sensor can be designed to respond to some or all of these components. As the sensor receives the wave, it passes through a preamplifier, which boosts the voltage. The “gain” of the amplifier is defined as input voltage divided by output voltage and is mentioned in decibels (dB). The gain usually used for concretes and rocks ranges from 60 dB to 100 dB. Filters are then used to eliminate the background noise. The pre-amplification and filtering processes are sometimes referred to as “conditioning”. After conditioning, the signal is sent to a detection circuit where it is compared to a threshold defined by the operator.

Whenever the amplified signal exceeds the threshold, a digital pulse is generated. The first pulse shows the start of a “hit”. As the hit is initiated, for a period called “hit definition time (HDT)”, the system monitors for any new pulses that might be generated due to the voltage exceeding the threshold. If nothing is received during the HDT, the hit is deemed terminated, the measurement circuit is reset and the results are sent to a computer for processing.

### **Geophones**

Geophones are another type of recording device mostly used in field applications. Although there has been some research to develop “piezoelectric geophones”, traditionally they are velocity-sensing devices based on a spring-mounted magnetic mass that can move within a wire coil and thus convert deformations into voltage. Figure 2.2 shows a schematic view of geophones. As the

ground motion gets to the geophone, the coil starts to move by the springs in the electric field of the magnet and thus an output signal is generated. Similar to piezoelectric sensors, pre-amplification and filtering techniques may be applied to the recorded waveforms before sending them to a computer station for processing.

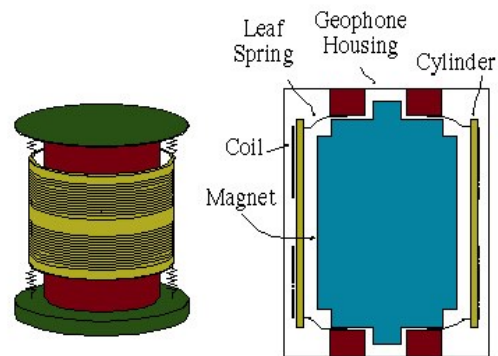


Figure 2.2: A schematic view of geophone (Barzilai, 2014)

## 2.3 Interpretation of Microseismic Data

As can be observed in Figure 2.1, one of the outputs of the waveform analysis is the number of hits/counts (i.e. the number of times that the wave has been strong enough to exceed the threshold). Due to its simplicity, many studies in geotechnical engineering have relied only on the number of counts recorded during the operation. Therefore, one of the elementary methods of quantification has been to propose a criterion merely based on the number of counts. For instance, (Koerner & Lord, 1984) proposed a spill alert device for earth dam failure warning using the acoustic emission monitoring. Table 2.1 shows their suggested criteria for the specific problem and material they were dealing with in the spillway system.

However, in order to find a more accurate estimation of damage in modern usage of MS monitoring, two other pieces of information may also be obtained from analysis of waveforms:

- Source Location
- Source Mechanism

Table 2.1: Categorization of AE level based on spill alert device used for monitoring by (Koerner & Lord, 1984)

Acoustic emission level (counts/min.)	Soil deformation	Relative safety	Recommendation
Negligible (0 to 10)	None	Good	Visit periodically
Low (10 to 100)	Slight	Marginal	Continue to monitor
High (100 to 1,000)	Large	Poor	Remedial measures required
Very high (greater than 1,000)	Very large	None	Evacuate downstream

### 2.3.1 Source Location

Theoretically, the 2D problem of locations can be solved by a technique called triangulation. Knowing the location of three sensors, recording the time of arrival at each sensor and assuming a constant wave velocity, two hyperbolas are formed and the source location is determined (Figure 2.3).

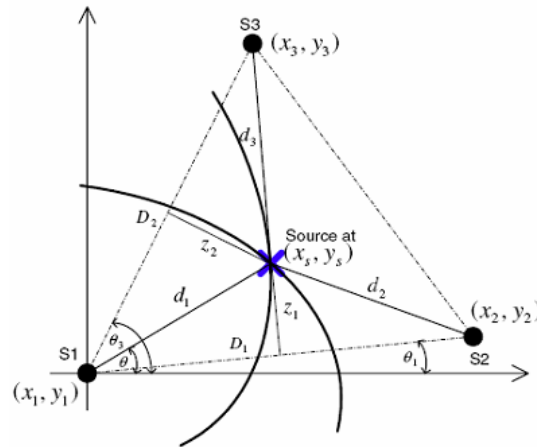


Figure 2.3: Theoretical 2D source location. Sensors are shown with S1, S2 and S3. The source location is shown with the blue mark (Nivesrangsan et al., 2007)

However, owing to the advances in computer technology, this problem can also be solved by numerical methods. Various location algorithms are available in the literature. The simplest one would be to consider the velocity defined as the distance between the source and sensor divided by the wave's travel time, which is  $(t-t_0)$ , where  $t$  is the time of arrival recorded by sensors and  $t_0$  is the time of occurrence that is unknown. Therefore, in a 3D problem, four unknowns exist; the

location of an event with three components (x, y and z) as well as  $t_0$  and thus at least four recordings (sensors) are required to solve the problem of locations in a 3D space.

### 2.3.2 Source Mechanism (Moment Tensors)

In order to relate the recorded seismic waves to the source, a model is required. For this purpose, “equivalent forces” are defined as forces that can produce equivalent displacements at the receiver as those generated by real forces at the source. Assuming the seismic source can be represented with nine equivalent force couples in a matrix called “moment tensor”, following model can be used:

$$\begin{pmatrix} u_1 \\ \vdots \\ u_n \end{pmatrix} = \begin{pmatrix} G_{11} & G_{12} & G_{13} & G_{14} & G_{15} & G_{16} \\ \vdots & \vdots & \vdots & \vdots & \vdots & \vdots \\ G_{n1} & G_{n2} & G_{n3} & G_{n4} & G_{n5} & G_{n6} \end{pmatrix} \begin{pmatrix} m_{11} \\ m_{12} \\ m_{13} \\ m_{22} \\ m_{23} \\ m_{33} \end{pmatrix} \quad (2.1)$$

Conceptually,  $u$ ,  $M$  and  $G$  represent displacements, forces and properties of the medium through which the waves propagate, respectively.

In more detail,  $u$  is a column vector containing  $n$  amplitudes of P and S wave arrivals recorded by sensors. These amplitudes may be corrected for different errors such as geometrical spreading, attenuation, free surface effects and receiver coupling. A schematic wave with P and S wave arrivals is shown in Figure 2.4. In order for the P and S wave amplitudes to be extractable, the signal-to-noise ratio (SNR) of a waveform has to be high enough. In practice, either the maximum absolute value of P and S wave arrivals or statistical measures such as root-mean-squared (RMS) amplitudes of P and S wave arrivals may be used in analyses (Forouhideh, 2011). Also, depending on the angle of arrival, the potential for P-S converted waves may need to be taken into account.

$G$  is a  $n \times 6$  matrix containing derivatives of Green’s function. Green’s function is defined as the displacement field in time and space at the receiver as a result of applying a unit impulse at the source (Aki & Richards, 2002).  $G$  could be obtained from the equation of radiation patterns of P

and S waves. It represents the properties of the medium between source and receiver. A simple form of  $G$  would be to assume a homogeneous, isotropic continuum medium. However, more sophisticated forms have also been suggested (Baker & Young, 1997).

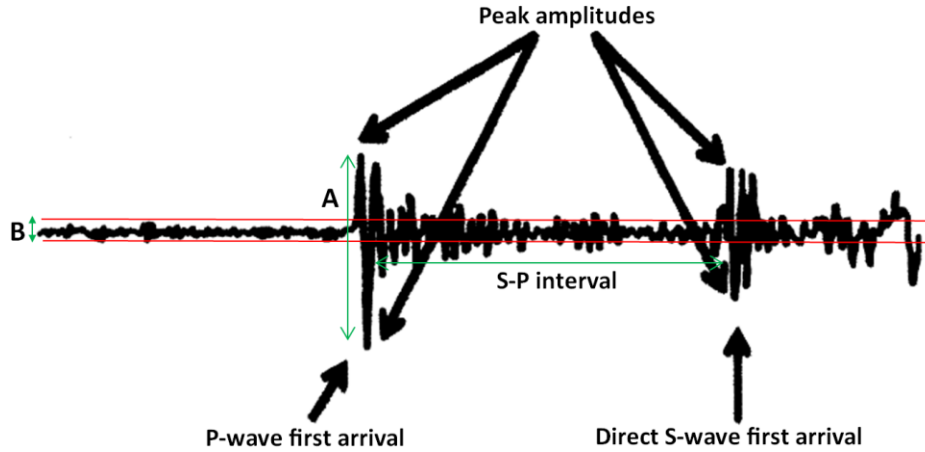


Figure 2.4: A schematic representation of p and s wave arrivals. The noise is bound between red lines. This wave has a good signal-to-noise ratio ( $SNR=A/B$ ) (modified after (Forouhideh, 2011))

$M$  is a  $6 \times 1$  vector containing the independent elements of the moment tensor matrix that defines the source. A moment tensor matrix has nine components but due to conservation of angular momentum, it is symmetric and thus it has only six independent components.  $M$  is the only unknown of Equation (2.1) and can be obtained mathematically in a process called “seismic moment tensor inversion (SMTI)”. Since  $G$  is not square, it is not invertible and thus Equation (2.1) is solved as:

$$M = (G^T G)^{-1} G^T u \quad (2.2)$$

The superscripts  $T$  and  $-1$  represent the transpose and inverse of the matrix, respectively. Each component of matrix  $M$  represents a force couple (two equal opposite forces) as shown in Figure 2.5. The reason it is called “moment tensor” is because the numerical value of each component would be the product of the magnitude of one force times distance between them.

Having the moment tensor matrix, three eigenvalues and eigenvectors (representing direction of principal axes) can be determined. The direction of pressure and tension at the source would be along the direction of largest and smallest eigenvectors, respectively. Considering the definition

of equivalent forces, these directions also represent the directions of far-field maximum and minimum stresses at the source.

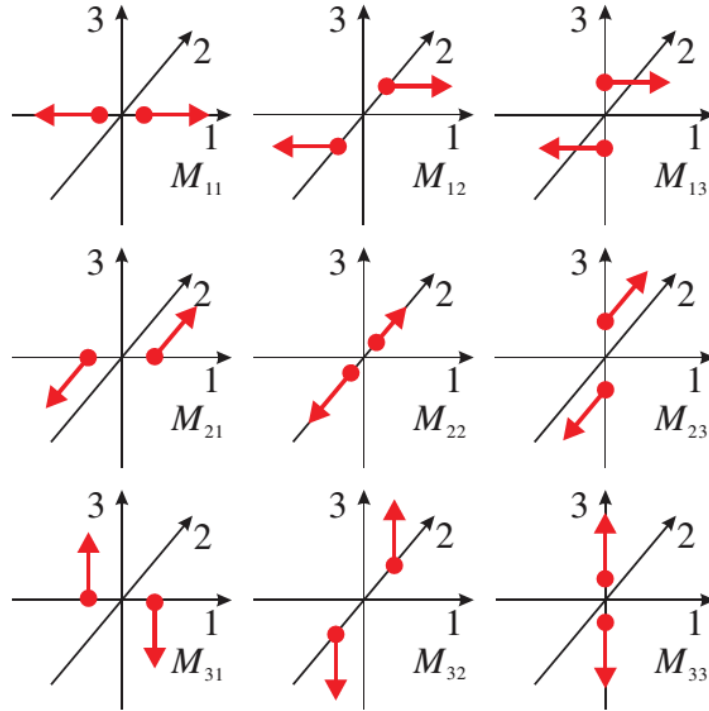


Figure 2.5: Nine generalized components of the moment tensor (Li et al., 2015)

Studying the components of the moment tensor reveals information about the mechanism involved in forming the event. In order to make physical interpretations about the source, the moment tensor could be decomposed into double couple (DC), isotropic (ISO) and compensated linear vector dipole (CLVD) components as (Jost & Herrmann, 1989):

$$M = \underbrace{\frac{1}{3} \text{tr}(M) \begin{pmatrix} 1 & 0 & 0 \\ 0 & 1 & 0 \\ 0 & 0 & 1 \end{pmatrix}}_{M_{ISO}} + \underbrace{|\varepsilon| M_{\max}^* \begin{pmatrix} -1 & 0 & 0 \\ 0 & -1 & 0 \\ 0 & 0 & 2 \end{pmatrix}}_{M_{CLVD}} + \underbrace{(1-2|\varepsilon|) M_{\max}^* \begin{pmatrix} -1 & 0 & 0 \\ 0 & 0 & 0 \\ 0 & 0 & 1 \end{pmatrix}}_{M_{DC}} \quad (2.3)$$

where  $\text{tr}(M)$  is the sum of three eigenvalues of the tensor. The sum of ISO and CLVD components is called non-DC and the sum of CLVD and DC components is called deviatoric moment tensor,  $M^*$ . In Equation (2.3),  $\varepsilon$  is a measure of the size of CLVD relative to DC component defined as:

$$\varepsilon = -\frac{M_{|\min|}^*}{|M_{|\max|}^*|} \quad (2.4)$$

where  $M_{|\max|}^*$  and  $M_{|\min|}^*$  are the absolute values of maximum and minimum eigenvalues of  $M^*$ , respectively. Therefore,  $\varepsilon = 0$  and  $\varepsilon = \pm 0.5$  represent a pure DC source and pure CLVD source, respectively. The percentages of each component in forming the source could be calculated using following equations:

$$\%ISO = \frac{100tr(M)}{|tr(M)| + \sum_{i=1}^3 |m_i^*|} \quad (2.5)$$

$$\%DC = \frac{m_3^*(1-2F)}{|m_3^*(1-2F)| + |2m_3^*F|} (100 - \%ISO) \quad (2.6)$$

$$\%CLVD = \frac{2m_3^*F}{|m_3^*(1-2F)| + |2m_3^*F|} (100 - \%ISO) \quad (2.7)$$

where  $F = -m_1^* / m_3$ . By looking at the contribution of each component (i.e. percentages), a physical interpretation about the source maybe obtained.

Figure 2.6 illustrates a decomposed moment tensor by equivalent force vectors, and a schematic demonstration of particle motions as well as matrix forms. As can be observed in this figure, the trace of the isotropic component (ISO) is non-zero and therefore it represents volumetric changes that can be either implosive or explosive (Jost & Herrmann, 1989). Isotropic sources only generate P waves.

The double-couple component (DC) represents pure shear with no volume change (trace=0). It is the known mechanism of typical earthquakes. For a DC source, both P and S waves are generated.

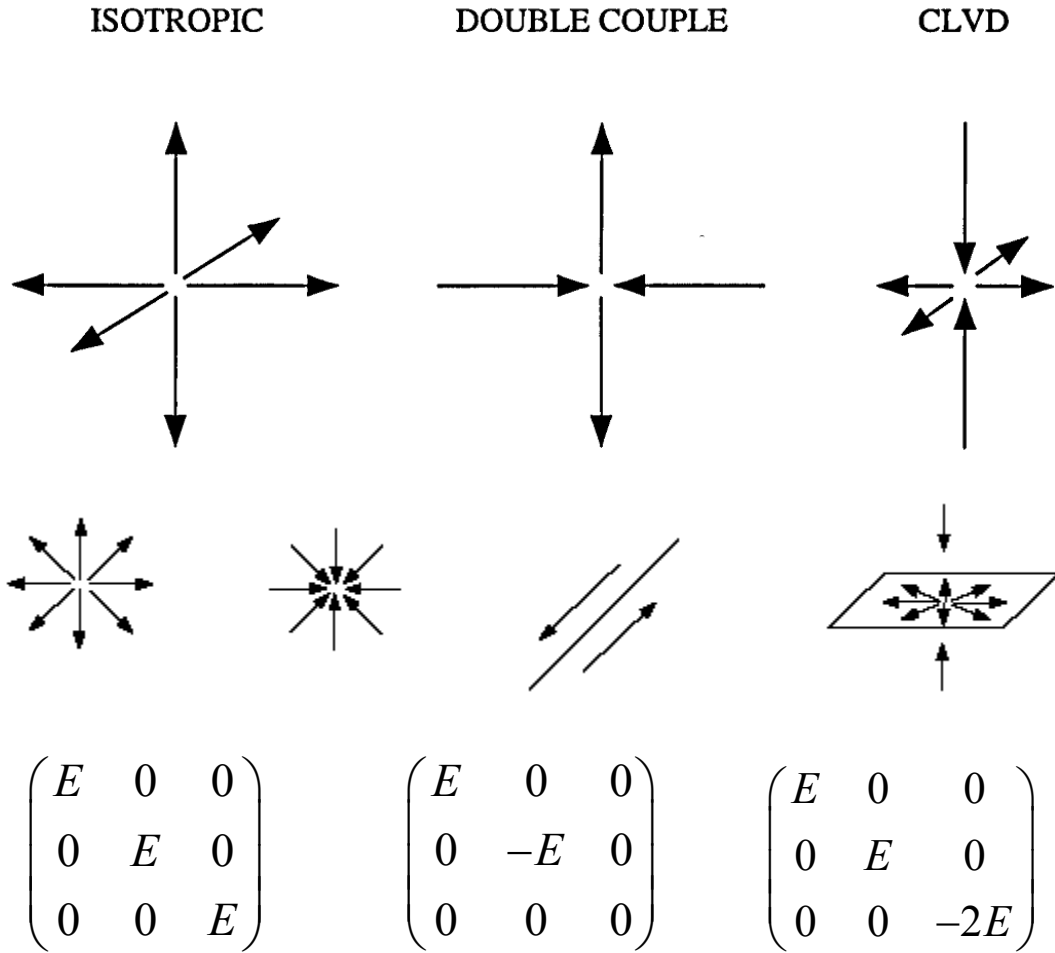


Figure 2.6: (Top) A schematic decomposition of moment tensor. (Bottom) Particle motions

A compensated linear vector dipole (CLDV) source generates both P and S waves. The volume change is compensated and thus the trace is zero. A physical example of CLDV sources would be crack opening under tension such as magma dyke inflating in a volcanic event (Stein & Wysession, 2009) as well as compressive induced tension. Another example is volume change in mining processes (Vavryčuk, 2001). For instance, the MT for crack opening under tension could be expressed as the sum of an isotropic and a CLVD component as:

$$\underbrace{\begin{pmatrix} \lambda & 0 & 0 \\ 0 & \lambda & 0 \\ 0 & 0 & \lambda+2\mu \end{pmatrix}}_M = \underbrace{\begin{pmatrix} K & 0 & 0 \\ 0 & K & 0 \\ 0 & 0 & K \end{pmatrix}}_{M_{ISO}} + \underbrace{\begin{pmatrix} -\frac{2}{3}\mu & 0 & 0 \\ 0 & -\frac{2}{3}\mu & 0 \\ 0 & 0 & \frac{4}{3}\mu \end{pmatrix}}_{M_{CLVD}} \quad (2.8)$$

where  $\mu$  and  $\lambda$  are 1<sup>st</sup> and 2<sup>nd</sup> Lamé's constants.  $K$  is the bulk modulus equal to  $\lambda + 2/3\mu$ . Another example of a CLVD source would be near simultaneous earthquakes along close faults with different geometries. This is shown in Equation (2.9) as a CLVD matrix is decomposed into the sum of two pure shear (DC) components:

$$\underbrace{\begin{pmatrix} M_0 & 0 & 0 \\ 0 & M_0 & 0 \\ 0 & 0 & -2M_0 \end{pmatrix}}_{CLVD} = \underbrace{\begin{pmatrix} M_0 & 0 & 0 \\ 0 & 0 & 0 \\ 0 & 0 & -M_0 \end{pmatrix}}_{DC} + \underbrace{\begin{pmatrix} 0 & 0 & 0 \\ 0 & -2M_0 & 0 \\ 0 & 0 & 2M_0 \end{pmatrix}}_{DC} \quad (2.9)$$

Many earthquakes in volcanic or geothermal fields are observed to have strong non-DC sources (Julian et al., 1998). A review of many possible scenarios resulting in non-DC components is presented by (Julian et al., 1998).

### 2.3.3 Limitations of SMTI

The limitations could be summarized as below:

- a) As can be observed, moment tensor decomposition is not unique and therefore a judgment has to be made based on stress regime, geological constraints and previous case histories in that area (Forouhideh, 2011).
- b) Due to low quality of waveforms in downhole environment such as low signal-to-noise ratio, the P and S wave amplitudes may not be easily recognizable. Therefore, a minimum SNR of 5 was suggested by (Forouhideh, 2011). A SNR of 10 was recommended.

c) In practice for many projects, microseismic data is recorded by a single vertical array of geophones. The problem with using only a single vertical array is that all the nine components of MT cannot be resolved (Forouhideh, 2011). Therefore, (Eaton & Forouhideh, 2011) suggested that the arrays and the source should make a solid angle. This means that they should not be on the same plane. Hence, at least two vertical arrays making a solid angle with the source or one vertical array and one surface array would be required to resolve all the nine components. It was shown by (Rodriguez et al., 2011) that a single deviated well can also result in resolution of all the nine components.

### 2.3.4 Magnitudes

Assuming a double-couple source, and having the moment tensor matrix, a measure of earthquake strength called scalar seismic moment,  $M_0$ , can be calculated as:

$$M_0 = \frac{1}{2}(|m_1| + |m_2|) \quad (2.10)$$

where  $m_1$  and  $m_2$  are the two largest eigenvalues in an absolute sense. Equivalently, Equation (2.11) can also be used (Silver & Jordan, 1982):

$$M_0 = \left( \frac{\sum m_i^2}{2} \right)^{1/2} \quad (2.11)$$

where  $m_i$  are the eigenvalues of the moment tensor matrix. There is also a more physical definition of  $M_0$  as shown in Equation (2.12):

$$M_0 = \mu DA \quad (2.12)$$

where  $\mu$  is the shear modulus,  $A$  is the fault area and  $D$  is the average fault displacement. In practice, the displacement,  $D$ , is estimated from surface displacements or from reconstructing the displacements on the fault plane using instrumental or geodetic modeling (McCalpin, 2009). Also, by looking at surface rupture, aftershock patterns, or geodetic data, an estimate of the area of rupture,  $A$ , is obtained. An assumption in this model is that the rupture area is rectangular. The shear

modulus of typical crustal rocks is assumed  $\sim 30\text{-}35$  GPa (Aki, 1966; Slemmons, 1990).  $M_0$  is associated with the total non-elastic “work” in the source volume rather than dealing with actual time history of faulting (Bormann & Di Giacomo, 2011). Since measuring  $\mu$ ,  $D$  and  $A$  is not straightforward, an indirect method such as Equation (2.11) is more common. Also, scalar seismic moment is proportional to the amplitude of the displacement in the far field and thus,  $M_0$  can be estimated from analyzing the amplitude spectra (Bonnin et al., 1988).

There are different types for magnitude of earthquakes based on a specific seismic wave in a certain frequency range with a certain instrument (McCalpin, 2009). A few of them are introduced as following.

### **Local (Richter) Magnitude, $M_L$**

Richter magnitude (Local Magnitude,  $M_L$ ) is the most famous one. The Richter magnitude 0 earthquake is defined as the earthquake which produces a maximum amplitude of 0.001 mm at a distance of 100 km. A 10 time increase or decrease in amplitude causes one time increase or decrease in magnitude, respectively. For instance, 1 mm amplitude equals  $M_L 3.0$ . Richter magnitude underestimates the earthquakes larger than  $M_L 6.5$  (McCalpin, 2009). This problem is referred to as “saturation” of  $M_L$  in large magnitudes.

### **Moment Magnitude ( $M_w$ or $M$ )**

Moment magnitude,  $M_w$ , can be calculated using Equation (2.13) (Hanks & Kanamori, 1979):

$$M_w = \frac{2}{3} \log M_0 - 6.0 \quad (2.13)$$

where  $M_0$  is the scalar seismic moment. Moment magnitude is a measure of the size of an earthquake.  $M_w$  is dimensionless and  $w$  stands for mechanical work. Unlike some other definitions of magnitude such as  $M_L$ ,  $M_w$  more represents the seismic energy released due to rupture at the source rather than relying on the effect of that energy on recording devices far away.

### **Energy Magnitude, $M_E$**

Another type of magnitude is “energy magnitude” based on strain energy (Choy & Boatwright, 1995):

$$M_e = \frac{2}{3} \log E_s - 3.2 \quad (2.14)$$

where  $E_s$  is the seismic energy in N.m (Joules).  $M_e$  is dimensionless.

### **$M_w$ versus $M_E$**

$M_w$  is a function of  $M_0$  that in turn is a measure of total released energy (work) and estimates the size of earthquake according to its definition. Therefore,  $M_w$  and  $M_0$  do not provide any information on the small elastic wave energy,  $E_s$ . However,  $M_e$  is a measure of radiated seismic energy and thus it represents the strength of an earthquake (i.e. the potential hazard of damage due to earthquake). Therefore, it was suggested by Bormann and Di Giacomo (2011) that if possible, both these magnitudes be determined and jointly considered. The relation between scalar seismic moment and radiated seismic energy can be estimated as:

$$E_s \approx (1.6 \times 10^{-5}) M_0 \quad (2.15)$$

The two magnitudes,  $M_E$  and  $M_w$ , are related according to Equation (2.16) as suggested by (Bormann & Di Giacomo, 2011):

$$M_e = M_w + (\Theta + 4.7) / 1.5 \quad (2.16)$$

where  $\Theta = \log(E_s / M_0)$ .

### **2.3.5 Frequency-Magnitude Relationship**

Another very common parameter used in microseismic literature is the seismic b-value that gives an indication of the magnitude distribution of the events. The b-value is defined by Gutenberg-Richter formula that relates the frequency of earthquake occurrence to its magnitudes using Equation (2.17) (Gutenberg & Richter, 1954):

$$\log N = a - bM \quad (2.17)$$

where  $N$  is the number of events greater than magnitude  $M$  and  $a$  and  $b$  are constants. Therefore, it can be concluded that a greater b-value indicates a larger portion of small earthquakes and vice

versa. The b-value is known as an indication of self-similarity of earthquake properties at all magnitudes (Pacheco et al., 1992). It has been observed that this relation also applies to aftershocks (Utsu, 1958, 1961). The b-value would depend on tectonics, structural heterogeneity and stress distribution (Ohnaka & Mogi, 1982; Scholz, 1968).

## **2.4 Numerical Modeling**

Regardless of its limitations, recording the waveforms and seismic moment tensor inversion is a technique that provides valuable information about the source of seismicity. However, the question of how microseismic data could inform caprock integrity analyses remains a challenge. In other words, using the models such as Equation (2.1), the recorded waveforms are related to the source by geophysics. As a result, information such as source location, magnitude and hopefully mechanism of the source are provided. Then, using this information, the challenge for geomechanics is to quantify the source/damage. In order to study microseismicity and find a link between microseismic data and geomechanics, a review of previous numerical modeling approaches (continuum/discontinuum) is presented here.

### **2.4.1 Continuum Modeling**

Continuum modeling is one of the oldest modeling techniques where the material is represented as a continuum meshed to smaller zones. A zone cannot displace independently. In other words, in continuum models the deformation field is also continuous. Therefore, a constitutive model is required to relate stresses and deformations together. Many researchers have used continuum models to simulate microseismicity.

(Guest & Settari, 2010) used a finite difference continuum approach to model hydraulic fracturing in massive homogeneous shale as well as a heterogeneous turbidite depositional reservoir. The degree of heterogeneity was implemented into their model by a random distribution function for material properties such as Young's modulus and compressive and tensile strengths. They assumed that the damage initiates once the Mohr-Coulomb or tensile failure criteria are satisfied locally. In order to simulate hydrofracture injections, fluid pressures were increased in the model with time. As a result, in situ pressures would change and cracks

would develop throughout the model. Once damage occurred at any element, depending on whether or not it was due to compression or tension, the damaged Young's modulus was recalculated and updated using a damage variable. Each point of failure in the continuum model was considered as one AE event. In order to study the rupture mechanisms, they applied the same decomposition technique that is used for MTs to the effective stress field immediately after cracks were formed. They observed that for massive shale, microseismic events formed a narrow belt whereas for the turbidite fan the microseismic events were more spread.

Using a two-layer upscaled reservoir model, (Verdon et al., 2013) adapted the concept of "fracture potential" which represents the distance between the current state of stress and the Mohr-Coulomb line in the finite element model to study the injection-induced microseismicity in the caprock of reservoir. The fracture potential was defined as:

$$f^p = \frac{q}{q_{crit}} = \frac{\sigma'_1 - \sigma'_3}{2(c \cos \phi_f + p \sin \phi_f)} \quad (2.18)$$

where  $p$  is the mean principal effective stress defined as  $p = (\sigma'_1 + \sigma'_2 + \sigma'_3)/3$ ,  $c$  is cohesion,  $\phi_f$  is the angle of friction. Verdon et al., (2013) postulate that since in nature, MS events usually occur along preexisting weak planes at small scales, it was not possible to make any conclusions with regard to temporal or spatial distribution of MS events. However, by identifying the zones with higher fracture potential, it would be possible to identify the zones that are more likely to show MS events. Using the known reservoir parameters, they did not observe any significant change in fracture potential above production wells where many events had been recorded on site. Then by using a softer reservoir model they observed higher evolution of  $f^p$  above production wells and thus concluded that a softer reservoir may have been the case in Weyburn.

The advantage of using continuum modeling is that it is fast and it allows a more detailed simulation of the real conditions compared to the time-consuming discontinuum modeling. Also, the parameters have mostly physical meanings. The problem with the continuum approach is that, for instance, although a failed zone in the model would represent a failure in the real caprock and this would be accompanied by an acoustic emission, this emission may have not been strong enough to be recorded by geophones at all and even if it was recorded, the magnitudes may not be easily reproducible by the model. In other words, since it is not possible

to directly model the microseismicity by the continuum model, it is difficult to directly link the degree of damage and the amount of released acoustic energy.

This is important because as will be shown in Chapter 6, weak planes can be emissive even long before the failure of the surrounding rock is reached and therefore simply assuming a failed zone as a microseismic event is not accurate.

## **2.4.2 Discontinuum Modeling**

The discrete element modeling approach is capable of directly modeling the rupture process and therefore provides a better approximation or simulation of source mechanisms. The material is modeled as a group of particles bonded together. No continuum constitutive models are required and the displacement field does not have to be continuous.

(Hazzard & Young, 2004) used PFC3D to model the compressive behavior of Lac Du Bonnet granite in laboratory tests. Each bond breakage (crack) was recorded and clustered together in time and space to form realistic events. Moment tensor and magnitudes were calculated by integrating the forces around each event.

(Zhao & Young, 2011) studied injection induced seismicity in a naturally fractured reservoir by 2D discrete element models. In their study, tensile cracks were considered as AE events.

Hazzard & Pettitt (2013) proposed a simple approach for modeling the stick-slip phenomenon in a 3DEC model. In their model, the stick slip at one point at the middle of the fault was monitored and it was assumed that the entire fault moved together. Pirayeshgar & Dusseault (2015) used UDEC with fluid coupling to study MS events along a fault. They used average displacements of the fault to get the magnitudes.

The problem with current discontinuum models is that:

- a) in all previous studies of microseismicity using PFC, only the crack-induced events have been assumed as the source of microseismicity while it is known that the MS events along weak planes is governed by a stick-slip process and
- b) in two recent studies of that stick-slips were modeled using UDEC/3DEC (Hazzard & Pettitt, 2013 and Pirayeshgar & Dusseault, 2015), the fault was assumed to displace all at once and thus the average displacements of the fault were used to calculate magnitudes.

The problem with these approaches is that due to heterogeneity, stick-slips occur almost independently at various positions along the fault releasing small amounts of energy (small MS magnitudes). The average-taking approach will miss recording such events and may not be as accurate.

### **2.4.3 Coupled Continuum-Discontinuum Modeling**

As mentioned before, continuum modeling is fast and is capable of modeling more geometrical details of a problem. On the other hand, discontinuum modeling allows direct observation of the damage process. Therefore, some researchers tried to couple continuum with discontinuum modeling to take the advantage of both.

(Hazzard & Young, 2002) introduced the technique for getting moment tensors and moment magnitudes for the seismic events captured by PFC. The approach was tested by modeling the mine-by tunnel excavated in highly stressed massive Lac du Bonnet granite in Manitoba, Canada. It was part of the Atomic Energy of Canada Limited's (AECL) Underground Research Laboratory (URL) to evaluate the feasibility of nuclear waste disposal in that site. The notch region of the tunnel was modeled by PFC inclusion and was then coupled with FLAC. (Young et al., 2001) used this approach for the URL project. They were not able to make a direct comparison between the actual and simulated moment tensors due to the 2D nature of the model. Also, the magnitudes were overestimated in their model.

(Mercerat et al., 2005) used a coupled FLAC-PFC model to study the microseismicity above a salt mine due to excavations. They considered each crack in the PFC inclusion as an event and studied the "number of events" only. No magnitudes or mechanism were investigated.

(Cai et al., 2007) used a 2D coupled FLAC/PFC model to study the acoustic emission evolution at the Kannagawa underground powerhouse cavern in Japan. In their model, a small section around the excavation was modeled using PFC inclusion. The excavation was then performed in stages. The number of bond breakages in the PFC model at any stage was normalized to the total number of observed bond breakages during the whole excavation. These normalized numbers of bond breakages were compared with the same number obtained from real data. Their agreement was used to conclude the validity of the geotechnical model. No magnitudes or mechanism were studied.

## 2.4.4 Particle Flow Code (PFC3D)

In this research, Particle Flow Code (PFC3D) v.5.0 is used as the main tool to study microseismicity. PFC3D is an explicit implementation of the Distinct Element Method (DEM) developed by Itasca. A PFC model is basically a group of particles bonded together by models such as parallel bond model or smooth joint model. The model is usually generated within the boundaries of some walls that could be deleted later if necessary. Size distribution of particles allows modeling the geometrical heterogeneity, which is an advantage, compared to continuum models. Unlike continuum models, PFC does not require mesh generation. In this code, it is assumed that the particles are rigid (non-deformable) so they cannot break. However, deformation or overlap can occur at contacts. The calculation cycle is explained in Figure 2.7.

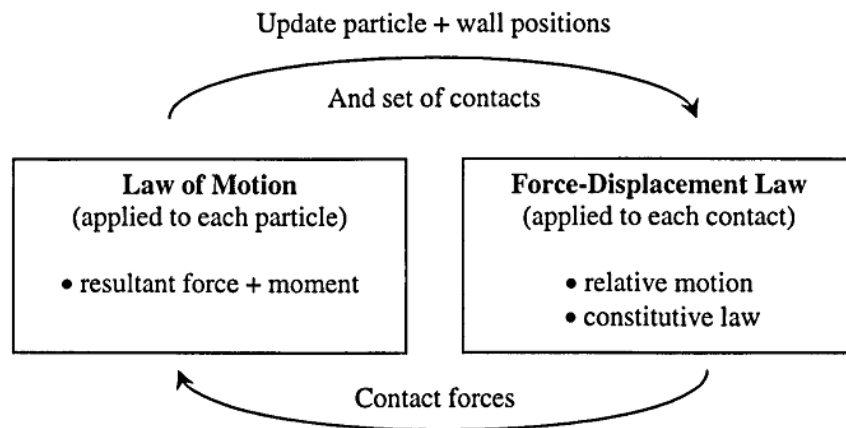


Figure 2.7: Calculation logic of PFC models (Itasca, 1999)

A load could be applied to the model by accelerating the walls or assigning velocities to particles. In PFC3D, it is assumed that due to small time steps, a disturbance cannot propagate farther than neighbor particles and therefore velocities and accelerations can be considered constant during each cycle. Once a load is applied to the model, integrating the Newton's second law of motion ( $\text{Force} = \text{Mass} \times \text{Acceleration}$ ) using the time step, the displacements are calculated and the position of particles is updated. Then using the force-displacement law ( $\text{Force} = \text{Stiffness} \times \text{Displacement}$ ), new forces are calculated and so on. This process of cycling is continued until a pre-defined criterion is met.

The stress and strain can be measured using walls, gauge balls or measurement spheres that are representative volumes within the specimen (Itasca, 2015). A complete formulation of how calculations are performed within a measurement sphere could be found in the PFC3D manual (Itasca, 1999).

The micro parameters of a PFC model are calibrated in a trial and error process by changing them until a desired macro response is observed. A known problem of PFC is that it is almost impossible to calibrate the model for both compressive and tensile strengths. As a result, once calibrated for the compressive strength (which is a common practice), the tensile strength is overestimated. In order to solve this problem, (Cho et al., 2007) used clumps, a group of spherical/circular particles bonded together, to form more realistic shapes of grain. A more recent solution is Flat Jointed contact bond (Potyondy, 2012). Unlike parallel bonds that break at a “point”, Flat jointed bonds break gradually over an area of contact (Potyondy, 2015).

#### **2.4.4.1 Linear Parallel Bond Model**

Parallel bonds represent the mechanical behavior of cementation between grains. While grains can only transmit forces, parallel bonds connecting the grains can transmit both forces and moments. A parallel bond can be envisioned as a short length beam or a “set” of elastic springs uniformly distributed over a circular cross section at the contact point (Potyondy & Cundall, 2004). The general strength and deformability relations of grains and parallel bonds are illustrated in Figure 2.8.

Once the load is applied to the model, there will be some displacements (overlap) of entities (could be particles or walls) in contact (i.e.  $U^n > 0$ ). If there is a gap between two grains, then  $U^n \leq 0$  and normal and shear forces are equal to zero. When two particles overlap ( $U^n > 0$ ), a contact is formed and shear force is set to zero. Having  $U^n$ , normal stiffness of the balls and coefficient of friction, the maximum shear force is calculated. Each increment in  $U^s$  causes an increase in shear force. If maximum shear force is reached, then slip occurs and force is set equal to its maximum. Therefore, existence of parallel bonds does not prevent slipping.

At the same time, having the increments of  $U^n$ , normal and shear stiffness values of contacts and contact areas, current values of compressive and shear stresses at each contact are updated and compared with compressive and shear strengths of contacts. If the strength is reached, the force

drops to zero and the contact breaks either in compression or tension. Therefore, at any time a contact is either bonded or slipping. A bond breakage is called “crack”. The name “Parallel bond” refers to the fact that they act “in parallel” with the grain portion of force-displacement law.

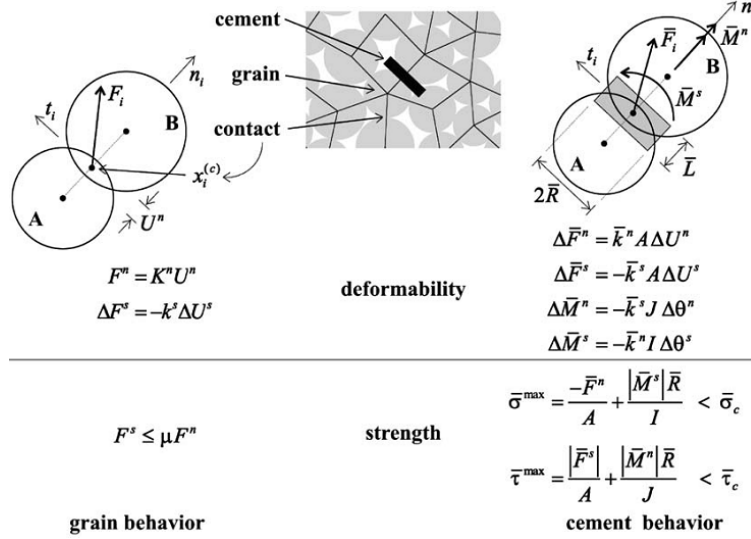


Figure 2.8: Schematic formulation for BPM model. Top right shows increments of elastic force and moment. I and J are moment of inertia and polar moment of inertia of parallel bond cross section and A is the area of the cross section. Right bottom shows the maximum tensile and shear stresses that a bond can tolerate. If any of these strengths exceed then the bond and its forces and moments are removed from the model. Left bottom: the maximum shear strength (Potyondy & Cundall, 2004)

The strain energy of contacts is stored in the linear springs representing parallel bonds as:

$$\bar{E}_k = \frac{1}{2} \left( \frac{(\bar{F}_n)^2}{k_n} + \frac{\|\bar{F}_s\|^2}{k_s} \right) \quad (2.19)$$

#### 2.4.4.2 Smooth Joint Model

Smooth joint model is used to simulate interfaces. The traditional way to model an interface is to change the properties such as strength of the bonds along the interface to those representing the real interface. The problem with this approach is bumpiness of the boundaries that can affect the behavior of the system. The effect of these bumpy boundaries could become more important, when it comes to modeling joints or weak planes. A possible solution is to use smaller size particles along the interface, which is not practical in large models. In order to solve this problem, another type of bond that simulates an “interface” regardless of the orientation of the

particles along it, is the “Smooth Joint Contact Model” (Mas Ivars et al., 2008). This model could be assigned to all the contacts between particles that lie on or along the opposite sides of the interface. This model overcomes the drawback of the boundaries that are bumpy. The reason for calling it “smooth” is because of the constitutive behavior that allows particles bonded by this contact model to overlap and to “slide” on each other instead of moving around one another. Once a smooth joint model is created, the already existing contact or parallel bond models are deleted automatically for the contacts along the interface. Figure 2.9 shows the behavior of smooth joint model compared to the usual parallel bond model.

The smooth joint contacts can only slip once their shear strength is reached. The force increments are updated similar to parallel bonds. The shear strength is calculated as coefficient of friction times the normal force. The shear force is increased linearly until the shear strength is reached at which point the contact slips.

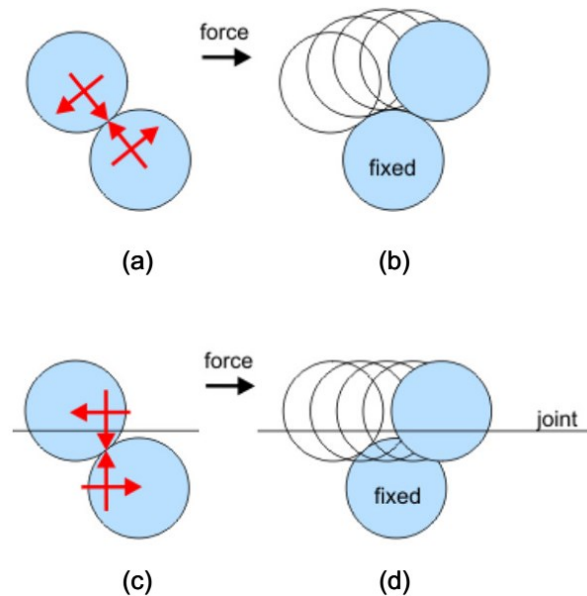


Figure 2.9: a) standard contact model with relative normal and tangential forces with regard to their orientation b) displacement of the particles bonded by standard contact model assuming the bottom ball is fixed c) normal and tangential forces on the particles whose contact is located along the smooth joint regarding their orientation with respect to the joint c) displacement of particles bonded by smooth joint model (Mas Ivars, 2008)

## 2.5 Conclusions

Microseismic recording is a technique to monitor the possible damage occurring in the caprock as a result of petroleum operation. For this purpose, geophones are used to record elastic waves emitted from the source of damage. The waveforms are analyzed by geophysics to provide information about the location and mechanism of the source. Therefore, source locations, event magnitudes and hopefully source mechanisms are reported to the operators. Beyond this point, the question is how this data could be informative with regard to integrity of caprock and modifying the operations. Therefore, it is still required to link microseismic data to Geomechanics.

For this purpose numerical modeling (continuum and discontinuum) has been used by previous researchers. The advantage of continuum modeling is that it is fast, many details can be taken into account and also the numerical parameters usually have well known physical meanings. The problem is that the damage mechanism cannot be easily simulated.

On the other hand, discontinuum models are capable of directly modeling the damage process. Some level of geometrical heterogeneity is taken into account due to size distribution of particles. However, they are computationally slow and thus there will be limitations in terms of the scale of the models. Also, micro parameters of the discrete model may not necessarily have a well-known physical meaning.

Therefore, in this research discontinuum modeling is used to study the microseismic response of intact rocks as well as weak planes. Then, a combination of both continuum and discontinuum modeling is used to analyze the caprock integrity using microseismic data.

# Chapter 3

## Microseismicity within Intact Rocks<sup>1</sup>

### 3.1 Abstract

In this chapter, acoustic emission (AE) energies recorded during 73 uniaxial compression tests on weak to very strong rock specimens have been analyzed by studying the variations in b-values, total recorded acoustic energy and the maximum recorded energy for each test.

Using PFC3D, uniaxial compression tests have been conducted on discrete element models of rocks with various strength and stiffness properties. An algorithm has also been used to record the AE data in PFC3D models based on the change in strain energy upon each bond breakage. The relation between the total released acoustic energy and total consumed energy by the specimens has been studied both for the real data and numerical models and as a result, a linear correlation is suggested between the released AE energy per volume and consumed energy per volume of the intact rocks.

Comparing the recorded acoustic energies in numerical models with real data, suggestions are made for extracting realistic AE magnitudes due to bond breakages (cracks) from PFC3D models by proposing a modification on Gutenberg-Richter formula that has been originally proposed for large scale shear induced earthquakes along faults.

Also, using the numerical model, an attempt has been made to quantify the damage to the intact rock by proposing a damage parameter defined as the total crack surface observed during the tests divided by the total crack surface possible based on size of particles.

### 3.2 Introduction

It is known that the damage process of intact rocks starts with tensile cracks growing parallel to the maximum principal stress until a “critical crack density” is reached and a “process zone” is formed (Reches & Lockner, 1994; Scholz, 1968). This manifests with reduction in cohesion during development and coalescence of cracks until a dominantly frictional rupture occurs along

---

<sup>1</sup> A version of this chapter is published in Computers and Geotechnics Journal. <http://dx.doi.org/10.1016/j.compgeo.2015.02.012>

the formed shear band and the specimen fails (Lockner et al., 1991; Martin & Chandler, 1994). A technique to observe the damage process of rocks is acoustic emission (AE) monitoring. Acoustic emission is defined as an elastic wave propagated due to a rapid release of energy within the material (Lockner, 1993). Analyzing the waveforms and using techniques such as Seismic Moment Tensor Inversion (SMTI), source locations as well as the mechanism of events can be identified (Kishi et al., 2000).

There have been many attempts to correlate the observed AE activity with the stress level or different stages of rupture in geo-materials. It is known that there is an overall correlation between the evolution of stress strain curve in rocks and the AE rate (Eberhardt et al., 1999; Scholz, 1968a). Therefore, the simplest technique would be to correlate the number of events with the observed mechanical behavior (Koerner & Lord, 1984; Ohnaka & Mogi, 1982; Seto et al., 2002). However, it has been suggested that instead of cumulative number of events, the cumulative AE energy would be physically more meaningful (Ganne et al., 2007; Přikryl et al., 2003; Yukalov et al., 2004).

Although there have been several studies on the AE behavior of granular soils (Hill et al., 1998; Koerner et al., 1977, 1981), clays (Koerner et al., 1977; Lavrov et al., 2002; Thoeny et al., 2010), soft rocks such as Tuff and Shale (Amann et al., 2011; Fujii et al., 2009; Hall et al., 2006; Mito et al., 2007; Mori et al., 2007; Niandou et al., 1997; Valès et al., 2004) and hard rocks mostly granite (Cox & Meredith, 1993; Sellers et al., 2003; Sondergeld & Estey, 1981; Zang et al., 2000), the literature review reveals that there is an absence of reports on the variations of released energies specially for weak rocks. The main reason is probably the high attenuation of such material and the fact that many events are too small to trigger the sensors. Also, the majority of AE studies in rock materials are devoted to hard rocks while new applications of AE monitoring especially in petroleum engineering require understanding of the release of AE energy in weaker classes of rocks.

Therefore, in this chapter a wide range of rocks with different strength and stiffness properties have been studied with the purpose of understanding the relation between the amounts of released acoustic energy with the total consumed energy. Also, using discrete element modeling, an attempt has been made to quantify the amount of damage in terms of crack surface for the materials studied.

### 3.3 Theory

Any extra energy put into a system such as intact rock, which is already in a state of equilibrium, has to somehow dissipate so that the system regains its stable equilibrium by reaching its minimum potential energy. This decrease in potential energy to reach the equilibrium state is achieved by continuous lengthening of cracks passing the rock from an unbroken to broken condition (Griffith et al., 1997; Griffith, 1921). The dissipation of energy can be in various forms such as propagation of cracks or acoustic waves.

Figure 3.1 shows the stress-deformation curve for an arbitrary rock. The area under the loading curve (solid line),  $A(\Delta OAB)$ , is the extra energy put into the system. Two possible response curves of the rock are shown with dotted lines. The area under these two curves,  $A(\Delta OAE)$  and  $A(\Delta OAD)$ , would be the energy required to extend the cracks.

If  $A(\Delta OAB) < A(\Delta OAD)$  which is the case for a ductile rock with smaller Young's modulus, the crack will not propagate but it is possible that it undergoes some form of time-dependent weakening due to various phenomena such as flow of fluid to the crack that in turn result in reduction of the energy required to extend the crack (shifting the curve AD towards AB). In this case, although there is no excess energy yet to produce seismicity, the crack can still propagate (aseismic deformation) (Fairhurst, 2013). If  $A(\Delta OAB) > A(\Delta OAE)$  which is the case for a brittle rock with higher Young's modulus, the excess energy shown as the shaded area contributes to acceleration of cracks and release of seismic energy.

Figure 3.1 is a simplified demonstration of how ductility contributes to the extent of AE energy with the rock being loaded elastically until point A and seismic energy released during the unloading after point A. In practice, AE events have been observed as early as the crack initiation strength (~40%-60% of the peak strength) is reached (Cai, Morioka, et al., 2007; Cai, 2010).

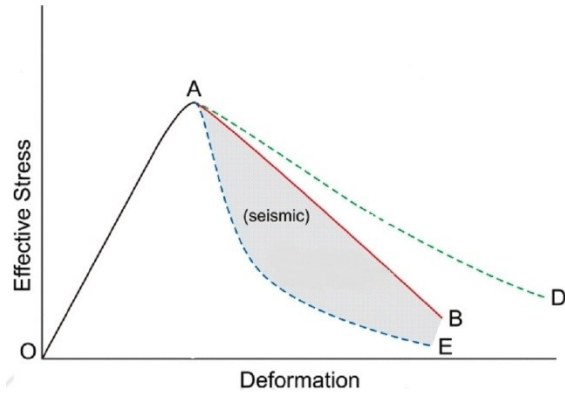


Figure 3.1: Schematic load-deformation curve for an intact rock. OAE and OAD curves are response curves for a brittle and ductile rock, respectively. Shaded area is the excess energy released as acoustic emission (modified after (Fairhurst, 2013))

### 3.4 Description of the Material and Experiment

“Intact rock” in engineering terms is referred to the rocks with no significant fractures (Harrison & Hudson, 2000). In order to understand how the intact rocks responds acoustically, a large database of laboratory tests reported by CANMET conducted as a part of low and intermediate level radioactive waste Deep Geologic Repository (DGR) design for the Ontario Power Generation (OPG) is analyzed in this chapter. The repository is located within the sedimentary bedrock beneath the Bruce site near Kincardine, Ontario at about 660 m depth (Gorski et al., 2009a). The Precambrian Granite basement of the site at 860 m is overlain by flat lying Palaeozoic age dolostone, shale and limestone sedimentary rocks. A review of the geomechanical properties of the rocks in DGR excavations is presented by (Lam et al., 2007).

A total number of 73 uniaxial tests were conducted on specimens of shale, limestone and dolostone rocks with acoustic emissions being monitored during the tests. Although an abrupt shift in stress-strain curves has been observed for some specimens indicating the existence of planes of weakness that caused failure (Gorski et al., 2009a) and questioning the “intact” nature of them, due to the small size of laboratory specimens, it is assumed that the majority of specimens have been intact and therefore the observed AE response would belong to the intact rock. According to the results, several rock units were identified based on ASTM D5878 (ASTM, 2005). The rocks have also been classified according to ISRM classification (Brown, 1981) (Figure 3.2). The classifications are summarized in Table 1.

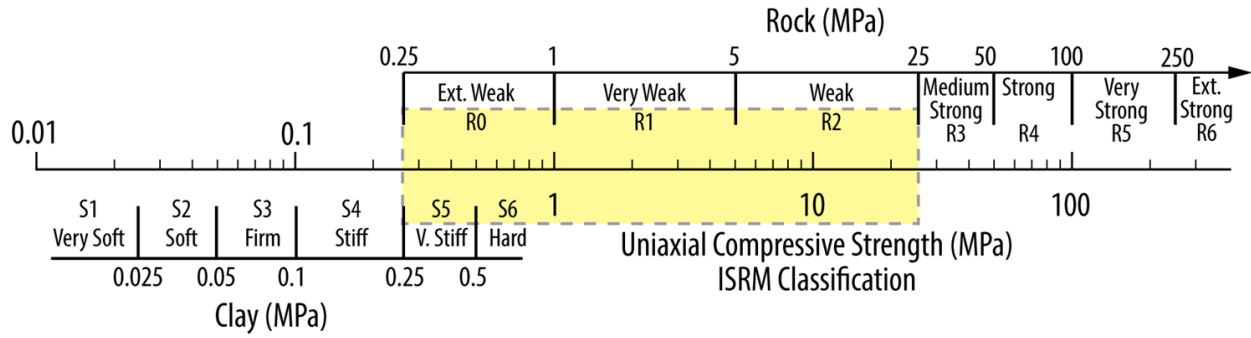


Figure 3.2: ISRM classification of rocks based on uniaxial compressive strength

Table 3.1: Rock types identified by CANMET (Gorski et al., 2009a)

Rock Type	Description	ISRM Class	UCS (MPa)
brecciated dolostone	weak	R1-R2	5-25
dolomitic shale	medium strong	R3	25-50
shale	medium strong	R3	25-50
shale with limestone layers	medium strong	R3	25-50
limestone with shale layers	medium strong	R3	25-50
dolostone	strong	R4	50-100
argillaceous limestone	very strong	R5	100-250
crystalline dolostone	very strong	R5	100-250

The specimens showed a wide range of compressive strengths from 1 to 200 MPa and Young's moduli from 0.5 to 60 GPa as shown in Figure 3.3.

The specimens had an average length and diameter of 176 mm and 74 mm, respectively. The loading in uniaxial compression tests was conducted in stress controlled manner to imminent failure at the rate of 0.75 MPa/s based on ASTM D7012 (ASTM, 2007). The AE recording system consisted of 12 transducer channels, 16 bit, 10 MHz, 40 dB preamplification, 60 dB gain, high and low pass filters and source location software. Two arrays of 3 piezoelectric sensors were mounted on the outer surface at the top and bottom halves of each specimen. The sensors on each array were 120° apart.

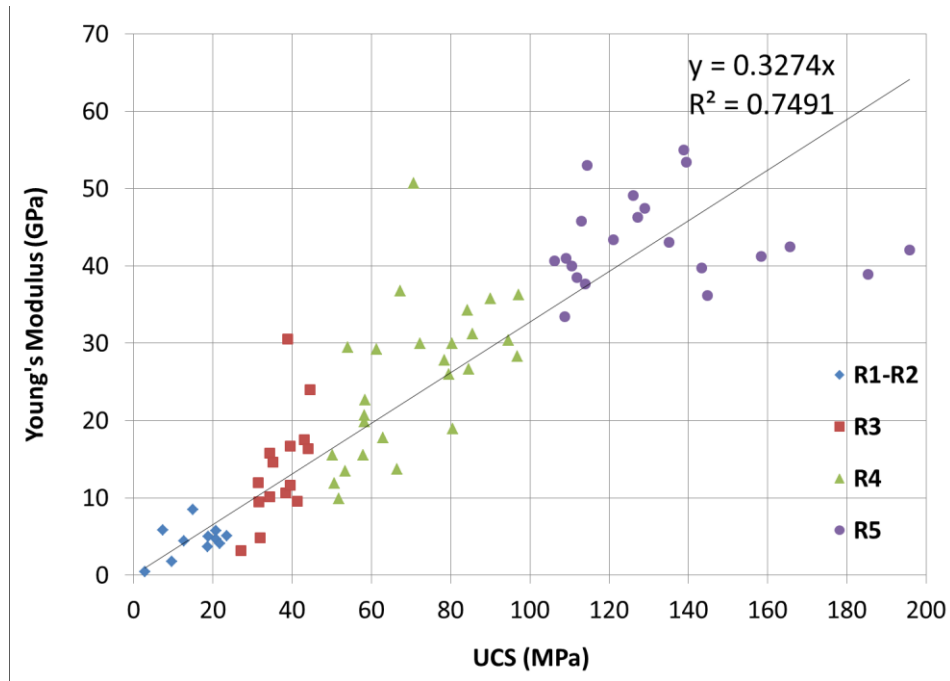


Figure 3.3: Young's modulus versus unconfined compressive strength for the specimens tested by CANMET (data is color coded according to the ISRM classification)

AEWin software was used to record the AE data in the lab. Since the outputs of this software will be used for analyses in the next sections, it is necessary to describe what the recorded energies by AEWIn signify. The reported energies by CANMET are “Absolute Energy”. This energy is based on the sum of squared voltage readings divided by a token resistance  $R$ , as explained by Pollock (Pollock, 2013) and shown in Equation (3.1)<sup>2</sup>:

$$U = \frac{1}{R} \sum_{FTC}^{PDT} V_i^2 \cdot \Delta t \quad (3.1)$$

where  $R$  is equal to  $10 \text{ K}\Omega$  representing the input impedance of the preamplifier, FTC stands for “First Threshold Crossing” and PDT stands for “Peak Definition Time”. The energies were reported in attojoules ( $\text{aJ} = 10^{-18}$  Joules). This “Absolute Energy” is a good feature to deal with larger signals resulting from burst type emissions (Pollock, 2013). Also, absolute energy is a measure for true energy of an AE hit.

<sup>2</sup> Energy is equal to voltage times current. Current is equal to voltage divided by impedance ( $R$ ). Impedance is a measure of circuit's resistance when a voltage is applied.

Although since the events have a very high frequency and it is likely that there has been spreading/attenuation even on the small scale of tested specimens, due to lack of source location data, in this chapter it is assumed that the energy is non-dispersive and therefore, the energies recorded at the sensors are equal to the released energies at the source. Thus, without any further corrections to consider signal loss due to attenuation, having the released energy, magnitude of an AE event can be calculated by the empirical Equation (3.2) (Scholz, 2002):

$$M_e = \frac{2}{3} \log E - 3.2 \quad (3.2)$$

where E is the energy in Joules.

### 3.4.1 Analysis of the Experimental Data

In order to study the variations of AE behavior in different rocks, various items such as b-value, maximum released energy during the test, total released AE energy and total consumed energy by the specimen have been investigated in this section.

A parameter often used in seismic studies is b-value defined by the Gutenberg-Richter relationship as shown in Equation (3.3) (Gutenberg & Richter, 1954):

$$\log N = a - bM \quad (3.3)$$

where  $N$  is the number of AE events greater than the magnitude  $M$ . The b-value represents a statistical distribution of magnitudes (Manthei et al., 2000). A large b-value indicates larger proportion of small events. Variations of b-values with uniaxial compression strength (UCS) are shown in Figure 3.4.

As expected, a slight reduction in b-values is observed for stronger rocks indicating dominance of larger magnitude events in them. In other words, larger b-values in weaker rocks indicate the abundance of smaller scale events. However, b-values do not provide any info on the range of energy release in each class of rocks. Therefore, in order to investigate the greatest amount of energy release (the largest magnitude) expected from a certain type of rock, variations of the maximum-recorded energy in each test versus UCS are also plotted in Figure 3.5.

According to Figure 3.5 and using Equation (3.2), the largest magnitudes recorded for all the specimens in uniaxial compression tests are almost in the range of -9 to -10.

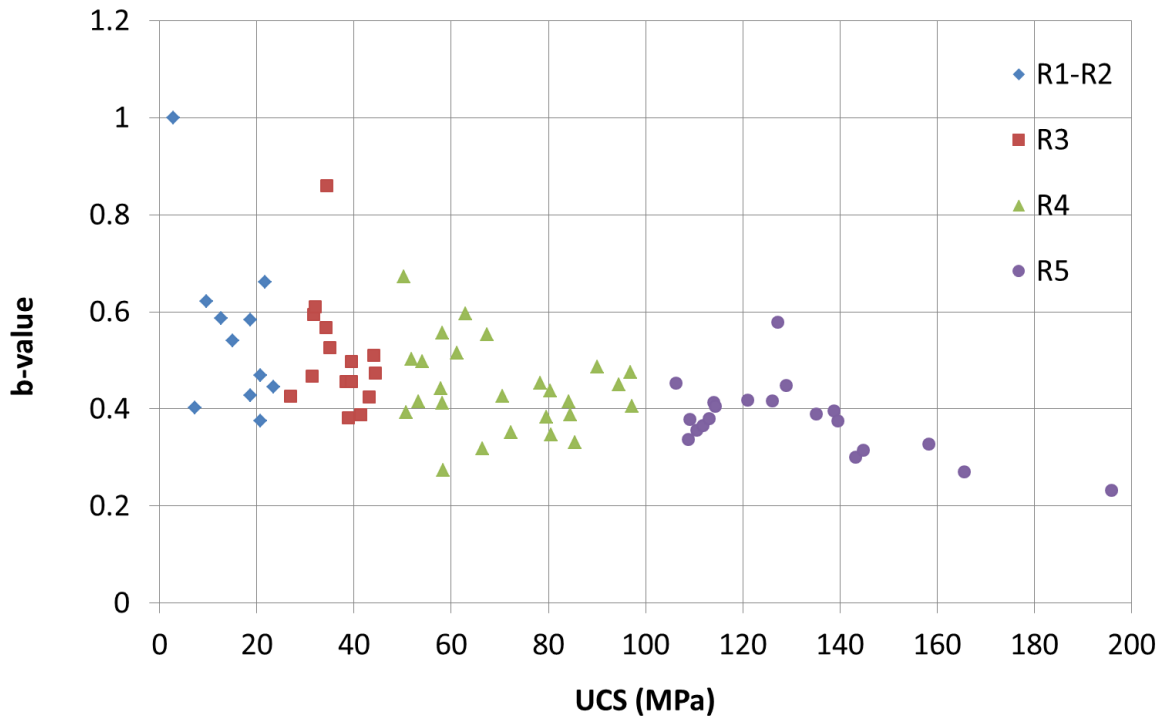
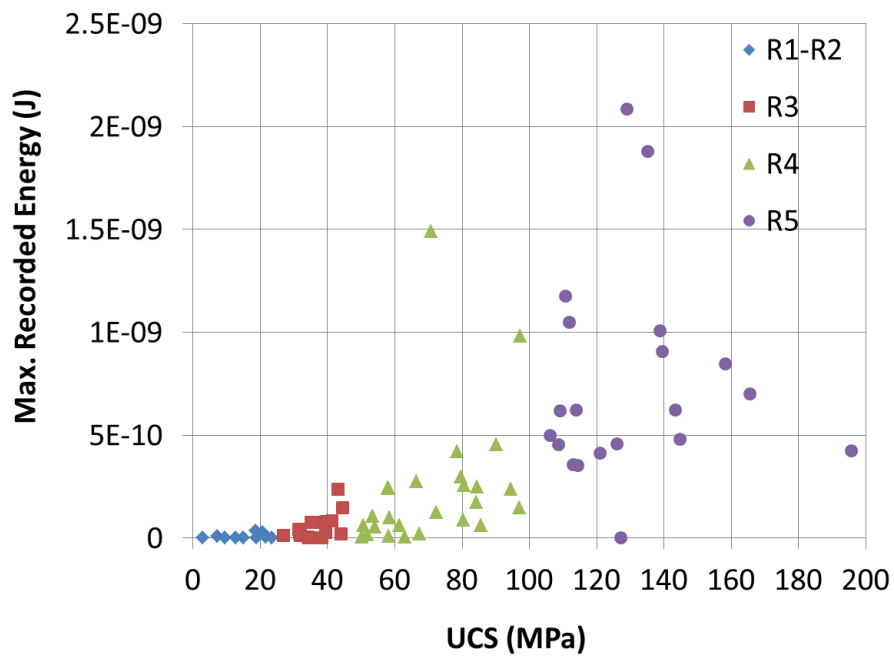


Figure 3.4: Variations of b-values obtained for DGR-1, DGR-2 and DGR-3 tests conducted by CANMET versus unconfined compressive strength



On the other hand, the damage process usually involves the emission of hundreds of events and thus, the relation between the total consumed energy by the specimen and total released acoustic energy is also studied. The stress-strain plots reported by CANMET show that most of the tests have been stopped almost right after the peak strength was reached (Gorski et al., 2009a, 2009b). Also, it is known that the stress-strain curve of rocks shows a non-linear response upon initial loading due to closure of cracks and a non-linear response prior to the peak stress. However, for this research, the consumed energy by each specimen is estimated considering a linear curve from the start up to the peak stress and therefore, using the peak compressive strength (UCS) and its corresponding strain, the total energy consumed by the specimen per unit volume is estimated by Equation (3.4) and plotted versus the total recorded acoustic energy divided by the volume of each specimen in Figure 3.6.

$$W_{cons.} = \sum(\sigma \times \Delta\varepsilon) \approx \left[ \frac{\sigma_p \times \varepsilon_p}{2} \right] \quad (3.4)$$

where  $W_{cons.}$  has units of  $\frac{N \cdot m}{m^3}$  (also Joules/m<sup>3</sup>),  $\Delta\varepsilon$  is the strain increment,  $\sigma_p$  is the unconfined compressive strength of the specimen in Pa and  $\varepsilon_p$  is the strain corresponding to  $\sigma_p$ .

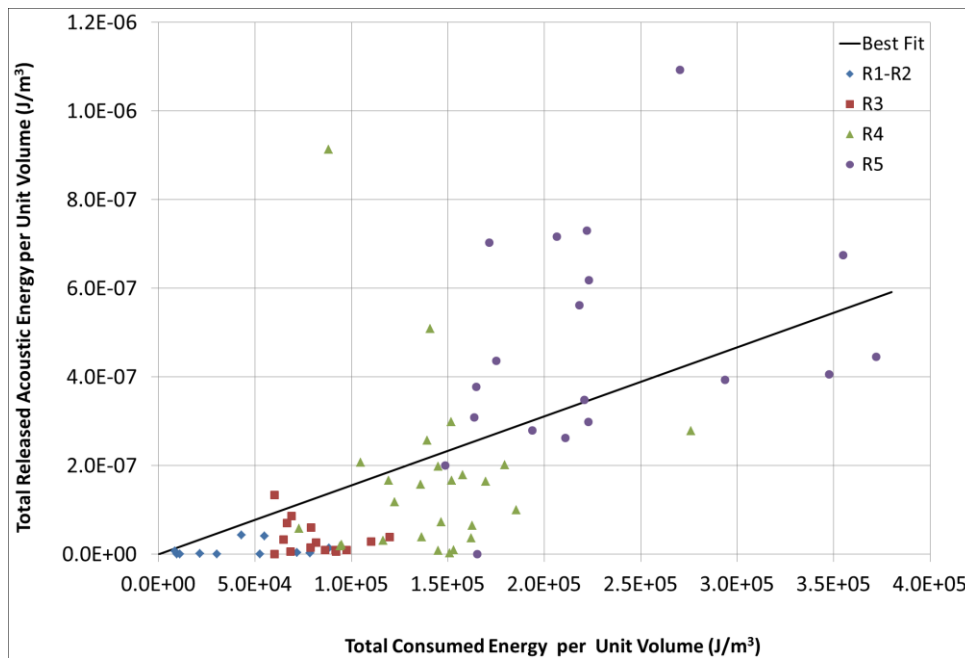


Figure 3.6: Variations of the total recorded acoustic energy versus the total consumed energy by the specimen

As illustrated in Figure 3.6, there is a large discrepancy amongst the data and although there seems to be a power law correlation between the x and y values, a linear fit would result in a higher  $R^2$  and also for the sake of simplicity, a linear fit has been applied to the data as shown in Equation 3.5 (adjusted  $R^2=0.62$ ):

$$E_{UCT} = (1.56 \times 10^{-12}) W_{UCT} \quad (3.5)$$

where  $E_{UCT}$  is the sum of all recorded AE energies during the test divided by the volume of each specimen and  $W_{UCT}$  is the total energy consumed per volume of the specimen calculated using Equation (3.4).

### 3.5 Numerical Model

Discrete element modeling allows detailed observation of the changes in energy as damage occurs within the rock specimen. In this chapter PFC3D v5.0 (Itasca Consulting Group, 2014), has been used to model uniaxial compression tests on specimens with the same size as those tested by CANMET. More details on PFC were presented in section 2.4.4.

The micro parameters of parallel bonds are calibrated in a trial and error process where the micro-parameters are changed until the desired macro-response is observed. In this chapter, the models have been calibrated for a range of uniaxial compressive strengths and Young's moduli based on the data presented in Figure 3.3.

Once the geometry of the model is generated and appropriate measurement spheres are installed, the load is applied to the model and then integrating twice the Newton's second law of motion, velocities and positions of all the particles are updated resulting in calculation of new contact forces with a force-displacement law. This cycle of calculating displacements and forces continues until a certain criterion is met (Itasca, 1999). This process results in breakage of some bonds (cracks) that can be considered as AE events.

### 3.5.1 Algorithm for Recording AE Events

A common method to record seismic magnitudes in PFC is by monitoring changes in forces around each new bond breakage within a certain distance and time and then calculating the moment tensors, scalar moment and moment magnitudes based on that (Hazzard & Young, 2000, 2002, 2004). However, some studies suggest this approach may overestimate the magnitudes (Young et al., 2005).

Another approach proposed by (Hazzard & Damjanac, 2013) is to record the release of strain energy within a small volume around the newly formed cracks for a short period of time and then calculating the magnitudes using Equation (3.2). The change in energy would increase as the monitored volume increased and the appropriate volume would depend on the nature of cracking (e.g. tensile cracks in a compression regime or in a tensile regime) as well as location of events relative to the edge of the specimen (Damjanac, 2010).

A review of all techniques on how AE data can be obtained from PFC models is presented by (Hazzard & Damjanac, 2013). According to that study, the latter algorithm based on energy changes is believed to provide more accurate magnitudes and is used in the present chapter.

In this algorithm, a “space window (small volume)” is monitored around each crack once it’s formed for a “time window” during which the crack is considered “active”. If each bond breakage is considered single AE events, all the magnitudes will be close to each other which is not realistic and thus a common practice is to cluster the events in PFC models. In order to cluster the events, if a new crack is formed within the space window of a crack while the strain energy is still being monitored, the two cracks are considered part of one event, the time window is reset and the space window is expanded with regard to the new centroid of the event (that is now consisted of two particles). Otherwise, the crack is assumed part of a new event. The time and space windows of 40 steps and 2 average particle diameter, respectively, were suggested by (Hazzard & Damjanac, 2013) to provide realistic distribution of magnitudes and are used in this chapter too.

### 3.5.2 Results

Fifteen uniaxial compression tests have been conducted on cylindrical specimens generated by PFC3Dv5.0, the calibration of which is summarized in Table 3.2. Since the purpose of this research is to study the overall AE activity with regard to the strength properties, the calibrations do not represent any specific real specimens and instead, the UCS values are chosen only so that they cover the range of rocks similar to the real data. The Young's moduli are chosen based on Figure 3.3. The lengths and diameters of all the numerical specimens were equal to 176 mm and 37 mm, respectively.

The microseismic recording algorithm has been initiated once the loading started for each test. Three measurement spheres have been installed along the height of each specimen and stress strain response has been monitored for each measurement sphere throughout the test. The tests have been stopped once the average stress was dropped to 20% of the peak stress. This threshold was chosen to capture the post peak behavior as well although the lab tests by CANMET were stopped almost right after the peak. The total consumed energy by the specimen was estimated as the sum of the area under these 3 stress-strain curves. As an example, one specimen is shown in Figure 3.7 along with the measurement spheres and recorded stress-strain curves.

As seen in Figure 3.7, there is a correspondence between the absorbed energy by each section and the bond breakages as well as the AE released energy. Variations of the total released acoustic energy versus total consumed energy by each specimen are plotted in Figure 3.8.

Based on the results shown in Figure 3.8, the following correlation exists between the AE energies recorded by PFC3D and total consumed energy by each specimen (adjusted  $R^2=0.67$ ):

$$E_{PFC3D} = (1.21 \times 10^{-2}) W_{PFC3D} \quad (3.6)$$

Assuming the consumed energies by numerical models and real specimens are equal,  $W_{UCT} = W_{PFC3D}$  and substituting  $W_{PFC3D}$  from Equation into Equation (3.5), a correlation between real AE energies and numerical AE energies is obtained as following:

$$E_{UCT} = (1.29 \times 10^{-10}) E_{PFC3D} \quad (3.7)$$

Table 3.2: Calibration parameters of PFC3D specimens. The average radius for all the models has been 2 mm (14043 particles). The coefficient of friction (ba\_fric) for all the specimens has been equal to 3.5 and the Young's modulus for all the balls has been set equal to the Young's modulus of parallel bonds (ba\_Ec=pb\_Ec).

Rock	Macro Parameters		Micro Parameters (Parallel Bond Properties)		
	UCS (MPa)	Young's Modulus (GPa)	Young's Modulus pb_Ec (GPa)	Mean Normal Strength pb_sn_mean (MPa)	Standard Deviation of the Strength pb_sn_dev (MPa)
<b>S1</b>	21	5.9	5.4	14	3.8
<b>S2</b>	40	12.9	11.7	27	7.3
<b>S3</b>	41.7	13.7	12.5	28.6	7.8
<b>S4</b>	53.4	17.3	15.6	35.7	9.8
<b>S5</b>	61.5	21.3	19.5	44.6	12.3
<b>S6</b>	80.9	24.5	22.5	55	15
<b>S7</b>	84.3	27.8	25.7	58.7	16.2
<b>S8</b>	85	26.7	24.4	55.8	15.4
<b>S9</b>	95.4	32.2	30	66	18.2
<b>S10</b>	99.6	33.3	30.5	69.7	19.2
<b>S11</b>	108.6	35.3	32.5	74.2	20.4
<b>S12</b>	112.2	40.2	36.5	83.4	23
<b>S13</b>	123.9	41.6	38.1	87.2	24
<b>S14</b>	143.5	46.4	42.9	98.1	27
<b>S15</b>	158	52.5	47.7	109	30

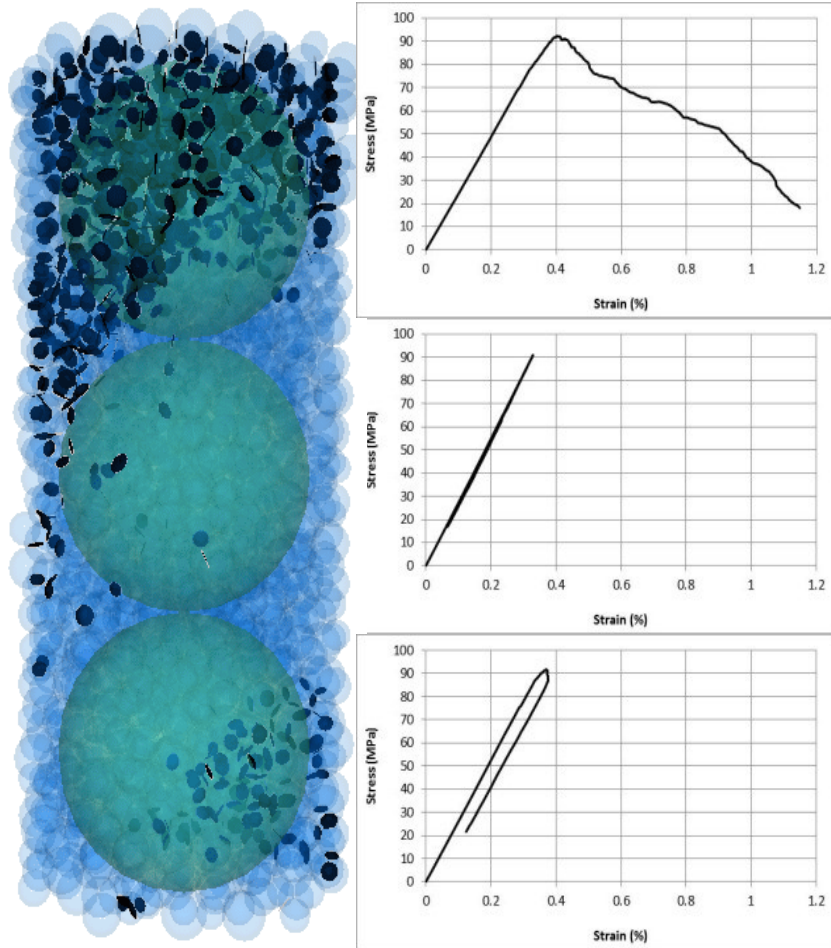
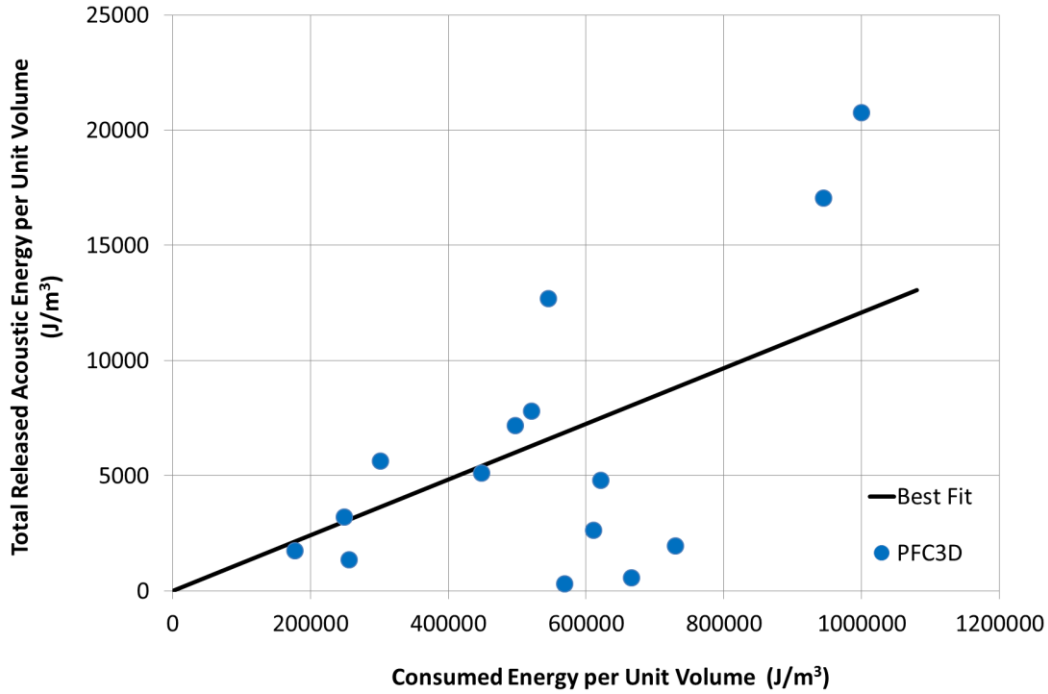


Figure 3.7: A sample test with particles (blue), measurement spheres (green) and bond breakages (black) as well as stress-strain curves for each measurement sphere shown next to it. Calibration would be based on UCS and Young's modulus from an average value obtained from the three measurement spheres with functions already available in PFC3D routines library



**Figure 3.8: Variations of the Released Acoustic Energy versus the Total Consumed energy**

This is actually reasonable since all the events are not recorded in the lab due to various practical limitations but in a PFC model, all the events are recorded and therefore the energy would never balance. Substituting the real energy,  $E_{UCT}$ , from Equation (3.7) into Equation (3.2), a modified form of Gutenberg-Richter equation is obtained that would work for the AE events in PFC3D models:

$$M_e = \frac{2}{3} \log E_{PFC3D} - 9.8 \quad (3.8)$$

In order to have a real estimate of the extent of cracking at each level and its correspondence with the AE data and consumed energy, it would be required to: a) use techniques such as X-ray tomography on samples of failed specimens to have an estimate of the crack length/surface (Elaqra et al., 2007; Suzuki et al., 2010; Watanabe et al., 2004) b) have the location and energy of AE events and c) use local stress-strain measurements along the height of specimens to have an estimate of the consumed energy at each level. Unfortunately, there has been no X-ray tomography and local stress-strain measurements for the data analyzed in this research and except the recorded energies; the quality of the source location data is not good enough for further analyses. However, it was hoped that the numerical model could provide an alternative.

In the PFC3D models, the length of each crack (bond breakage) is estimated to be the average of the diameters of the two particles forming that crack. Assuming a circular surface for all the cracks, the area of each crack can be calculated having its diameter. A damage parameter based on the crack surface area is defined in this study as following:

$$Damage(\%) = \frac{\text{total observed crack surface}}{\text{total possible crack surface}} \times 100 \approx \frac{\text{total observed crack surface}}{(\text{No. of contacts}) \times \frac{\pi D_{ave.}^2}{4}} \times 100 \quad (3.9)$$

The total possible crack surface has been calculated using a simple algorithm by going through all the contacts and summing up the contact area having average diameter of their forming particles. However, it could also be estimated having the average diameter of particles in each specimen,  $D_{ave}$ .

In order to provide a platform for comparison between the amounts of damage in each type of rock, the resolution (or in other words, the number of contacts in each specimen) was kept constant for all the specimens whose properties are listed in Table 3.2. Therefore, the total possible crack surface area has been equal to 426 mm for all the PFC3D specimens. It is worth mentioning that since the damage parameter is defined based on the crack “surface area”, it is not dependent on the size of particles and thus it was not necessary to repeat the tests with different size of particles as it would be if the “crack length” was used instead of the crack surface area.

As was discussed previously, the PFC3D magnitudes are overestimated even for the algorithm used in the present research that works based on changes in strain energy. Therefore, instead of correlating the damage parameter to PFC3D acoustic emission energies, it would be more reasonable to first correlate it to the consumed energies by PFC3D specimens and then assuming  $W_{PFC3D} = W_{UCT}$ , find the correlation between the damage parameter and real energies. For this purpose, variations of the damage parameter versus total consumed energy by PFC3D specimens are plotted in Figure 3.9.

The best fitted line in this Figure can be represented by Equation (3.10) (adjusted  $R^2=0.12$ ):

$$D(\%) = 56.31 \times W_{PFC3D}^{-0.16} \quad (3.10)$$

Assuming  $W_{PFC3D} = W_{UCT}$  and therefore substituting  $W_{UCT}$  from Equation (3.7) with  $W_{PFC3D}$  in Equation (3.10), a correlation between the real released AE energy per volume and damage parameter is obtained as:

$$D(\%) = 0.73 \times E_{UCT}^{-0.16} \quad (3.11)$$

For simplicity, Figure 3.10 illustrates the variations of damage parameter based on Equation (3.11).

As can be observed in this figure, the greater amounts of released AE energy that obviously correspond to greater amounts of consumed energy belonging to stronger rocks would result in less amount of damage meaning a more localized damage.

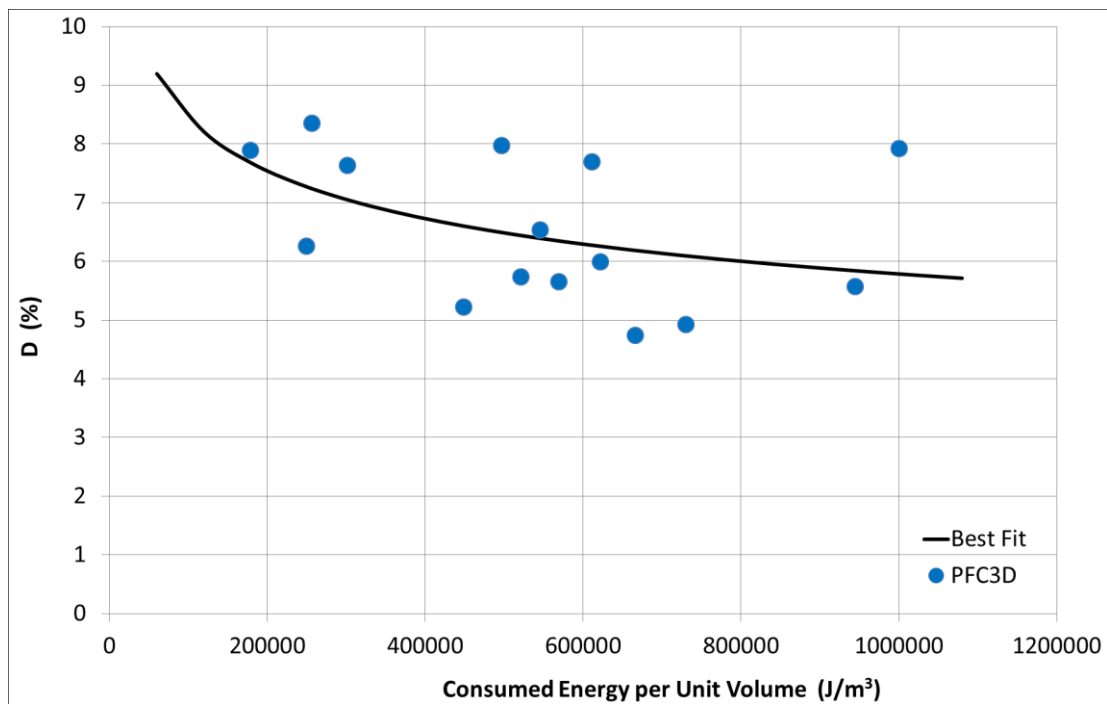


Figure 3.9: Variations of damage parameter versus the consumed energy per unit volume of PFC3D models

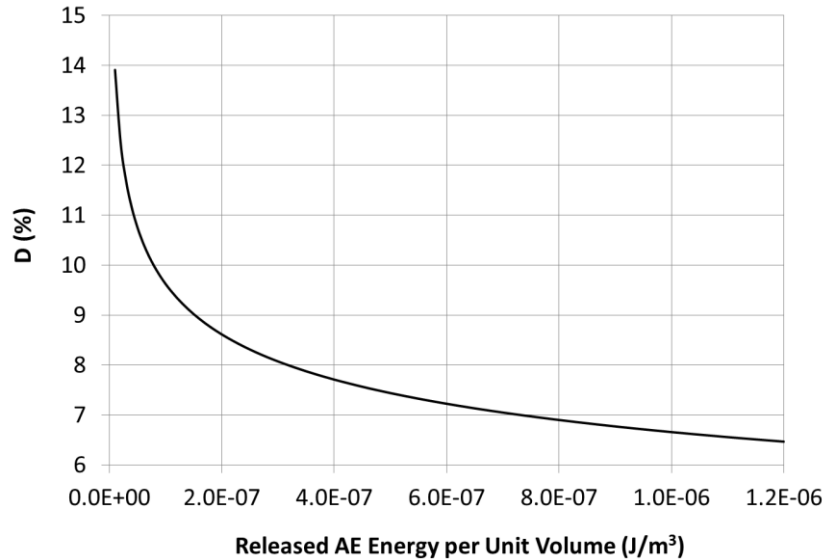


Figure 3.10: Variations of damage parameter versus the released AE energy per volume of rock

### 3.6 A Comparison between Granite and Shale

In this section, Equation (3.11) is used to predict the source radius of a crack-induced microseismic event with a certain magnitude in Lac Du Bonnet granite and typical shale.

Microseismic monitoring of the Lac Du Bonnet granite has been conducted as a part of underground research laboratory (URL) project. The URL is located in Southeast Manitoba about 443 m underground. The UCS and Young's modulus of this granite are about 230 MPa and 70 GPa, respectively. It is known that the Lac Du Bonnet did not have major weak planes. Therefore, the correlations presented in this chapter are applicable to this case. The magnitudes ( $M_w$ ) recorded in the URL range from -2.9 to -4.2. In order to predict the amount of crack surface development, Equation (3.11) is used. Therefore, it is necessary to first have an estimate of the total crack surface area possible in a volume of rock based on its grain size distribution. The grain size for Lac Du Bonnet granite ranges from 3 mm to 7 mm (Martin, 1993). In order to find the total crack surface area possible, using PFC3D, a cubic representative elementary volume (REV) is made with  $0.5 \text{ m} \times 0.5 \text{ m} \times 0.5 \text{ m}$  dimensions ( $0.125 \text{ m}^3$  volume). Selection of the size of REV is a matter of judgment but as will be shown later; it was an appropriate choice for this case. Also, since the same REV will be used to study shale as well, the model is regenerated with different size of particles for any of which the total contact area is obtained from the PFC3D (Figure 3.11).

Using Figure 3.11 and assuming an average 5 mm diameter for grain size of Lac Du Bonnet granite, the total contact area possible for the REV is about 38 m<sup>2</sup>.

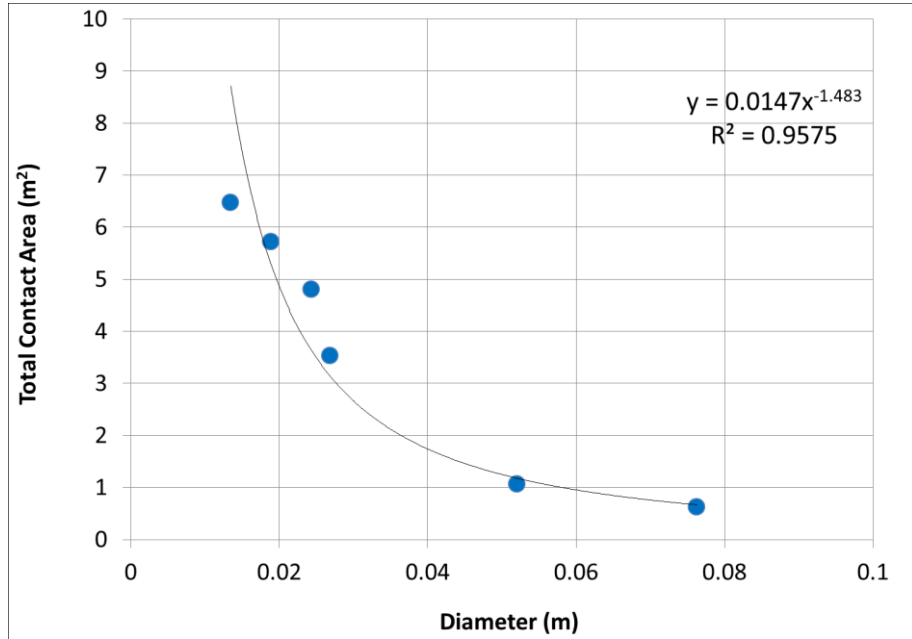


Figure 3.11: Variations of total crack surface area possible versus average diameter of particles in a REV with  $0.5 \times 0.5 \times 0.5$  m dimensions

Considering an average  $M_w$  equal to -3.5, the scalar seismic moment by reversing Equation (2.13) would be 5623.4 J. Therefore, using Equation (2.15), the radiated seismic energy is about 0.09 J and thus the released energy per volume for 0.125 m<sup>3</sup> of REV is 0.72 J/m<sup>3</sup>. Using Equation (3.11), the damage parameter,  $D$ , is equal to 0.77%. Considering the total crack surface area possible equal to 38 m<sup>2</sup>, the observed/anticipated crack surface area is equal to  $\sim 0.3$  m<sup>2</sup>. It means a source radius equal to 0.3 m. This is within the range of source radius from 0.13 m to 0.51 m reported for the URL (Collins & Young, 2000).

In order to test Equation (3.11) for typical shale, it is necessary to have an estimate of the particle size of shales. A general classification based on particle size (not composition) for shale is suggested as a rock composed of mud-sized particles such as clay and silt (Boggs Jr, 2001). According to the Wentworth scale of grain size, the silts have grain size between 0.004-0.031 mm and clays are finer than 0.004 mm (Wentworth, 1922). A REV with the same size as Lac Du Bonnet i.e.  $0.5 \times 0.5 \times 0.5$  m is considered. Using Figure 3.11, and assuming an average grain size (diameter) of 0.004 mm for shales, the possible crack surface area is about  $1.5 \times 10^6$  m<sup>2</sup>. Assuming a

Mw of -3.5 magnitude similar to the previous case, the right hand side of Equation (3.11) as well as the damage parameter would be the same as the previous case.

Therefore, the observed/anticipated crack surface area would be 11445.4 m<sup>2</sup>. For a circular planar source, this is equal to 60.4 m radius. This suggests that for a shale REV with the size considered in this study, a planar source crack is not able to generate a magnitude as large as Mw-3.5. Therefore, a spread damage zone within the sample would have to be the case. Such a spread damage zone should have developed quite fast so that considering the HDT as explained in Chapter 2, one magnitude would have been recorded for the entire damage process.

### 3.7 Discussion

As mentioned before, the tests have been conducted by CANMET using stress-controlled mode that unlike strain-controlled mode, doesn't allow obtaining the post peak stress-strain curve. Therefore, all the analyses on laboratory data are based on stress-strain curves and AE data recorded until peak strength. The controversy of this approach is explained using Figure 3.12 that is compiled from literature. As can be observed in this Figure, there is a general difference between the appearances of AE events with regard to the peak strength in granites (a, b and c) compared to weaker rocks (d, e and f). In the granite rocks, the highest AE activity corresponds to almost pre-peak or peak strength whereas in weaker rocks, the highest AE activity is observed in the post-peak part of the curve. This can be explained considering the greater ductility of weaker rocks that results in larger plastic deformations and higher excess energy in the post peak region.

A comparison between Figure 3.12 and Figure 3.6 suggests that if the post-peak response was recorded in the lab, a larger total AE energy would have been recorded for the weak rocks and the data points belonging to them in Figure 3.6 would have been shifted up. Therefore, in order to study the AE behavior (at least in weak rocks), using the strain-controlled mode seems more appropriate.

Also, the initial non-linear part in stress-strain response of rocks is believed to be due to closure of pre-existing microcracks and thus, the origin of AE events in this part, recorded in laboratory, is due to crack closure too. Therefore, conceptually the damage parameter in Equation (3.11), which is based on crack surface area, needs to be modified to account for this phenomenon. However, as

can be observed in Figure 3.12, the amount of AE activity in this part is very small compared to the rest of emissions and thus this modification is not considered in this work.

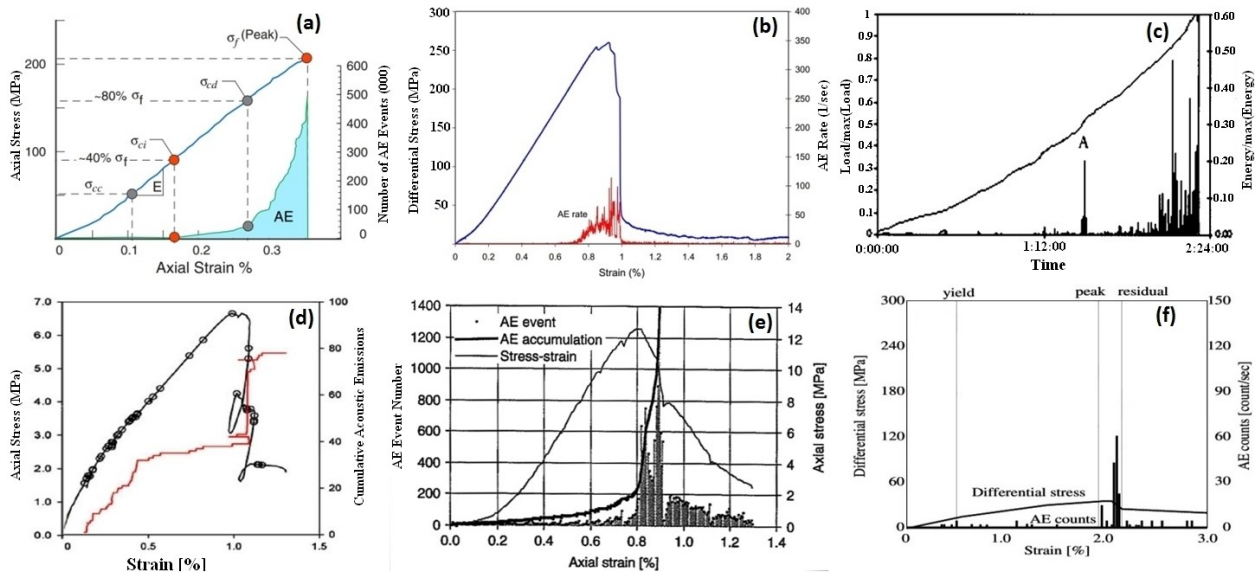


Figure 3.12: A comparison between the MS response of brittle and ductile rocks. (a) Lac Du Bonnet granite modified after [Martin, 1993]. (b) Kannagawa powerhouse granite (Cai et al., 2008). (c) Hong Kong granite (point A was believed to be due cracking within grains) (Liu et al., 2000). (d) Opalinus clay (AE events are shown by circles. The red line shows the cumulative AE events) (Amann et al., 2011) (e) Soft tuff rock called “Tage tuff” (Mori et al., 2007). (f) Soft sedimentary rocks obtained from Horonobe URL (Mito et al., 2007)

In order to get realistic AE magnitudes due to bond breakages (cracking) in PFC3D models, a modified version of Gutenberg-Richter formula was proposed in this research. The reason why magnitudes have been overestimated by the PFC models could be due to contribution of many factors as explained below:

1. In reality, there is breakage of asperities and formation of gouge material at the source causing dissipation of the AE waves and smaller magnitudes while in the PFC3D model, there are no such things and thus the recorded energies are probably too efficient.
2. In PFC3D models, bond breakages and consequently stress drops are instantaneous causing too much energy release while in reality there is a gradual weakening involved between the bonds. It is believed that using a softening contact model in future may solve this problem.
3. Due to practical limitations, not all the AE events are recorded in a lab experiment while PFC records all the events as they occur.

4. PFC3D magnitudes are calculated either by using Equation (3.2) and changes in strain energy or by using  $M_w = (2/3)\log M_0 - 6$  and integrating around the forces surrounding each bond breakage (Hazzard & Young, 2002) as discussed in section 3.1. However, both these formulas have been originally proposed for real earthquake events with shear nature along a fault. Although in PFC, the parallel bonds can break either in tension or shear, it is important to differentiate between the events due to such shear cracks in a compressive stress regime with slip-induced events along pre-existing weak planes. The events along pre-existing weak planes are governed by a “stick-slip” process and will be studied in the next chapter.
5. It is known that calibration of PFC models for uniaxial compressive strength would result in overestimation of the tensile strength of the specimens. An old solution would be to use clumps as suggested by (Cho et al., 2007) or to use flat jointed model as suggested by (Potyondy, 2012). Although the strength of micro parameters in PFC does not linearly correspond to the macro strength, it may be the case that micro tensile strengths are greater than what they should be in reality and thus their breakage yields in release of a higher energy resulting in greater AE magnitudes.

How much any of these factors contribute to larger magnitudes is not clearly known. Also, it is acknowledged that the correlations proposed in the present research are based on curve fittings with low  $R^2$  values indicating a large discrepancy amongst the data point. One reason may be that a realistic level of heterogeneity that is reflected in the shape of particles and definitely varies from rock to rock was not well modeled by using spherical particles for all the numerical specimens studied in present research. However, it is suggested that using Equation (3.8) for calculation of PFC3D magnitudes is a reasonable approach for getting realistic events and therefore in practice, the plots and correlations proposed in the present research are applicable provided the assumption that the recorded events have a crack nature within the intact rock could be justified. In other words, there has to be no weak planes in the space where AE events are located to generate slip-induced events or their contribution in the AE events is negligible. Also, since the energy release per unit volume has been used in this research, in practice, a judgment has to be made on the choice of appropriate “volume” to result in reasonable conclusions.

Also, it was previously mentioned that as the state of stress evolves, the amount of damage is increased until a shear band is formed and the specimen fails. There is generally a correspondence between the state of stress and the amount of released seismic energy as shown in Figure 3.12. However, the damage parameter in Equation (3.11) is inversely proportional to the released seismic energy per volume. This means that upon the use of a larger amount of seismic energy in this formula, a smaller damage is resulted. The reason is that this is a correlation between the entire damage and the entire released seismic energy per volume during the tests conducted on different rock types. Therefore, this equation at its present form cannot be used to predict the evolution of damage during a single test on one rock type. For such application, the released energy per volume term has to be modified. Namely, as the amount of seismic energy released during the test is increasing, the corresponding damage volume has to increase too. However, if the rate of increase in seismic energy is greater than the rate of increase in damaged volume, the damage would still be inversely proportional to the seismic energy per volume. Therefore, a correcting coefficient may be required to result in direct increase of damage parameter as the released seismic energy per volume is increased.

### **3.8 Conclusion**

Acoustic emission response of intact rocks was studied in this research by investigating the recorded AE energies from uniaxial compression tests on 73 specimens of different rock types with UCS values ranging from 3 to 195 MPa reported by CANMET.

The b-values for the lab data were in the range of 0.2 to 1 with a small decrease for stronger rocks. This agrees well with the fact that larger magnitude events are usually expected for harder rocks. Also, studying the maximum energy recorded for each test showed that the largest magnitudes recorded for all the specimens varied between -9 and -10. This is something to consider especially when using uniaxial compressive tests to characterize the AE behavior of rocks in applications where larger magnitude events in the order of, for instance, -1 to -3 have been observed in the field. Also, literature review suggests that in general, the highest level of AE activity appears at pre-peak and post-peak part of stress-strain curve for brittle and ductile rocks, respectively.

According to Figure 3.3, the rocks with smaller UCS are the more ductile ones with smaller Young's moduli and therefore the fact that they are less emissive compared to strong rocks could be easily understood from Figure 3.1. However, using the lab data in Figure 3.6, it was observed that a linear correlation does exist between the total recorded acoustic energies versus total consumed energy by each specimen and therefore Equation (3.5) suggests that the total released acoustic energy is linearly increased with an increase in the total consumed energy by each intact rock.

In order to study the damage process in more details, discrete element models were also used to study the relation between AE energies and consumed energy by synthetic rock samples. The results confirmed that PFC3D magnitudes are significantly greater than the real values recorded in the lab and therefore, a modification of the Gutenberg-Richter formula was suggested for calculating PFC3D magnitudes due to cracking in a compressive stress regime.

A quantitative study of the crack length/surface was not possible in the present research due to lack of data. However, using discrete element models, a damage parameter was proposed based on the observed crack surface area during the failure process and total possible crack area based on the size of particles. Although the correlation between the crack surface data and energies obtained by PFC3D was poor and more investigation would be required, in practice, if real knowledge of aggregate size distribution is available, an estimate of how much crack surface has been developed could be obtained using the recorded AE energies and proposed charts in this paper.

Finally, the analyses presented in this research are based on the assumption that the failure process of all intact rocks studied in the paper involves the same pattern of compression induced cracks growing, coalescing and forming shear bands leading to the rupture. Therefore, the charts and correlations would be useful in cases where there is enough evidence to believe the recorded AE events are due to cracking within the intact rock as opposed to the events with stick-slip nature that are likely along pre-existing weak planes.

# Chapter 4

## Microseismicity along Weak Planes<sup>3</sup>

### 4.1 Abstract

Using Particle Flow Code, a discrete element model is presented in this chapter that allows direct modeling of stick-slip behavior in pre-existing weak planes such as joints, beddings, and faults. The model is used to simulate a biaxial sliding experiment from literature on a saw-cut specimen of Sierra granite with a single fault. The fault is represented by the smooth joint contact model. Also, an algorithm is developed to record the stick-slip induced microseismic events along the fault. Once the results compared well with laboratory data, a parametric study was conducted to investigate the evolution of the model's behavior due to varying factors such as resolution of the model, particle elasticity, fault coefficient of friction, fault stiffness, and normal stress. The results show a decrease in shear strength of the fault in the models with smaller particles, smaller coefficient of friction of the fault, harder fault surroundings, softer faults, and smaller normal stress on the fault. Also, a higher rate of displacement was observed for conditions resulting in smaller shear strength. An increase in b-values was observed by increasing the resolution or decreasing the normal stress on the fault, while b-values were not sensitive to changes in elasticity of the fault or its surrounding region. A larger number of recorded events were observed for the models with finer particles, smaller coefficient of friction of the fault, harder fault surroundings, harder fault, and smaller normal stress on the fault. The results suggest that it is possible for the two ends of a fault to be still while there are patches along the fault undergoing stick-slips. Such local stick-slips seem to provide a softer surrounding for their neighbor patches facilitating their subsequent stick-slips.

---

<sup>3</sup> A version of this chapter was initially published in Pure and Applied Geophysics. It was later selected to be included in the PAGEOPH topical issue "Mathematics and Geosciences: Global and Local Perspectives. Volume II" <http://dx.doi.org/10.1007/s00024-015-1036-7>

## 4.2 Introduction

It is believed that the mechanism of fault instability involves multiple local on-and-off slips of patches referred to as “stick-slip” along the fault (Brace & Byerlee, 1966). Such small stick-slips may be recorded as “foreshocks” leading to “main shocks” and followed by “aftershocks” each releasing different levels of acoustic energy. Various aspects of fault’s instability has been already studied by laboratory experiments (Brune et al., 1993; Byerlee & Brace, 1968; Dieterich, 1981; Julian et al., 1998; Ohnaka, 1973) as well as numerical continuum models (Dalguer & Day, 2006; Day et al., 2005; Galis et al., 2008; Xing et al., 2004) and numerical discontinuum models (Finch et al., 2003; Mora & Place, 1994; Morgan, 2004; Place et al., 2002).

Compared to continuum models, Discrete Element Method (DEM) has the capability of modeling geometrical heterogeneity by size distribution of particles as well as looking into the rupture process of rocks with more details. Using PFC3D v.5.0, a discrete representation of the fault is modeled and release of acoustic energy due to its stick-slip instability is studied. For this purpose, a large scale laboratory experiment conducted on granite with a single fault originally reported by Dieterich (1979) and recently repeated with microseismic recording by McLaskey & Kilgore (2013) has been numerically simulated.

Traditionally, the approach for modeling microseismicity with PFC has been to consider each bond breakage as a single AE event with further possibility of clustering the events to form more realistic magnitudes (Hazzard, 1998). This approach has been successfully used in modeling the intact rock problems where the events are believed to have a compressive induced nature (Hazzard & Young, 2002, 2004; Young et al., 2005, 2001; Zhao & Young, 2011). However, in this chapter, new routines have been developed for recording slip-induced microseismic events. The results have been compared with the experimental data. Then, a parametric study has been conducted to study the effect of various factors on fault’s behavior.

This knowledge could also be useful for problems other than earthquake studies where there is likelihood of two planes sliding on each other such as landslides (Peng & Gombert, 2010), basal gliding of ice glaciers (Helmstetter et al., 2015; Jansen, 2006; Roux et al., 2008) and microseismic monitoring of a sedimentary rock mass in Petroleum projects (Fairhurst, 2013; Kristiansen et al., 2000).

### 4.3 Theory of Slip

The basics of how slip occurs in physics are briefly explained using Figure 4.1a. As the applied driving force to the block,  $F_d$ , is increased, the resistive frictional force (solid red line) also increases until at point a,  $f_f$  reaches the maximum static frictional resistance, the frictional resistance drops to lower values known as kinetic friction (or as simplified by the dotted blue curve), the spring unloads following a line with the slope equal to its stiffness (dashed green line),  $K$ , and the block starts to move.

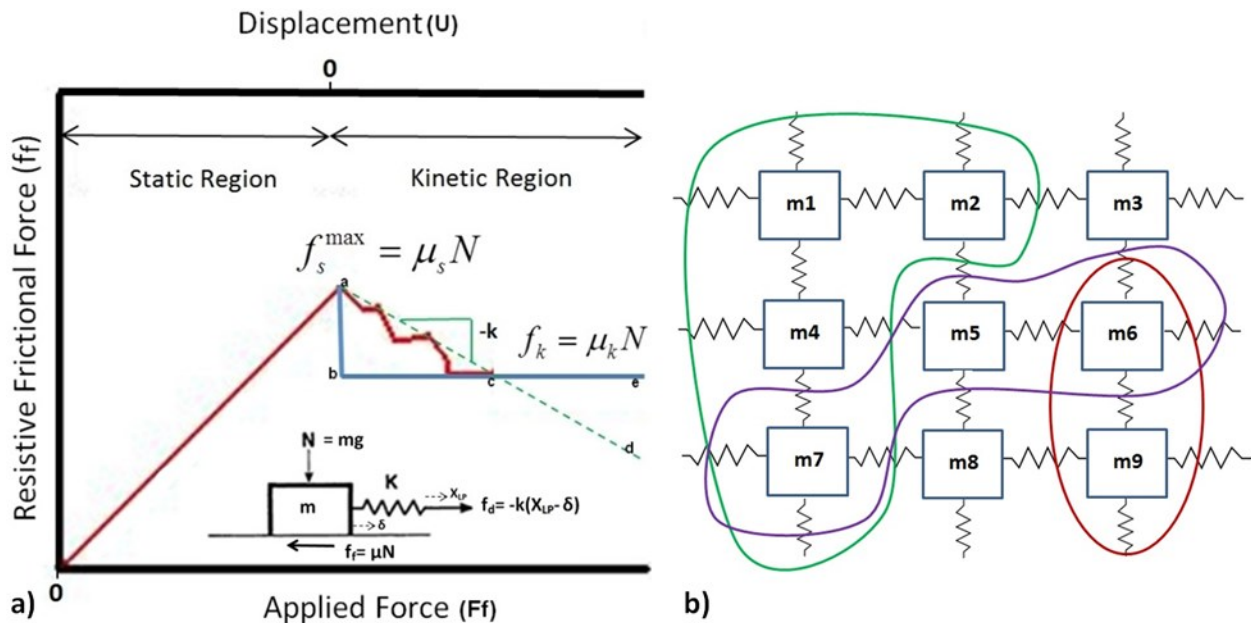


Figure 4.1: a) Solid red line is variations of the resistive frictional force. The simplified change in friction is shown in dotted blue. The dashed green line shows variations of the driving force once the block starts to move until it stops. b) Horizontal section of a more realistic model for the fault. The masses, stiffness of springs and normal stress on each block are not necessarily equal due to heterogeneity. Three arbitrary patches are shown with dotted red, solid purple and dashed green. The red and green patches can slide simultaneously.

The spring's unloading continues even after the applied force equals to kinetic friction at point c, meaning deceleration of the block until the final stop at point e where the excess energy is dissipated ( $\Delta abc$  equals  $\Delta cde$ ) (Scholz, 2002). In reality, once the motion eventually stops (point e), there has to be a “healing” mechanism for friction to regain its static value so that further slips could happen. This process of multiple slips and stops is called “stick-slip” and is believed to be the mechanism of earthquakes (Brace & Byerlee, 1970). Rabinowicz (1951, 1958) first suggested that if two surfaces are in contact in a stationary condition under load for time  $t$ , the coefficient of static friction increases approximately as  $\log(t)$ . He also proposed that a

minimum displacement of  $D_c$ , “critical slip distance”, is required for transition from static friction state to kinetic friction state. With regard to Figure 4.1a, the condition required for the onset of instability can be mathematically expressed by Equation (4.1):

$$\left| \frac{\partial f_f}{\partial u} \right| = \frac{(\mu_s - \mu_k)N}{D_c} > K \quad (4.1)$$

where  $\left| \frac{\partial f_f}{\partial u} \right|$  is variations of resistive frictional force,  $f_f$ , for increments of displacement,  $u$ . The parameters  $\mu_s$  and  $\mu_k$  are static and kinetic coefficients of friction, respectively,  $N$  is the normal stress on the block,  $D_c$  is critical slip distance and  $K$  is the stiffness of spring.

The physical implication of the stiffness of spring in this model,  $K$ , can be thought of as the elastic conditions of the vicinity of a fault in nature or the stiffness of the loading machine in the laboratory. From Equation (4.1), it is obvious that instability depends on the normal stress, elastic properties of the medium surrounding the fault and roughness of the fault. The major microseismic events in the field are believed to be the result of stress drop followed by slip on fractures and consequently release of energy (Damjanac et al., 2010). However, if the stress drop is not large enough to impose excess energy to the system (i.e. after point “a” in Figure 4.1a (left), the drop in resistive frictional force (solid red line) is so that it places above the unloading line (dashed green line), the slip would be aseismic. Therefore, in reality not every slip is the source of instability and considered as seismic.

The assumption behind the model explained by Figure 4.1a is that the block can be regarded as a single mass point. Persson & Tosatti (1999) suggest that for this assumption to be valid the dimension of block,  $L_B$ , has to be smaller than a characteristic “elastic coherence length”,  $\xi$ , otherwise, the block has to be discretized to smaller cells with the size,  $\xi$ , connected to each other by elastic springs. Therefore, it is necessary to take into account heterogeneity and nonuniform geometry of faults (Nielsen et al., 2000, 1995). A more realistic model for the fault is shown in Figure 4.1b. In this model, the mass, stiffness of springs and normal stress on each block is different and thus different patches may form and slide at different times or simultaneously.

#### 4.4 Description of the Experiment

Dieterich (1979) studied the scale dependence of fault instability process through a large-scale biaxial laboratory experiment. A large specimen of Sierra white granite with  $1.5 \times 1.5 \times 0.419$  m dimensions was sawed diagonally at the quarry and roughened in the laboratory by lapping the two surfaces together with 30 grit silicon carbide abrasive to represent the fault with peak-to-trough surface roughness of 0.08 mm (Dieterich, 1981). He concluded that a minimum fault length was required so that confined shear instability could occur along a preexisting fault. Although strain gauges and velocity transducers were mounted on the model, no types of acoustic emission sensors were used during his experiment. The scalar seismic moments were later calculated from the general formula as:

$$M_0 = \mu DA \quad (4.2)$$

where  $\mu$  is the shear modulus,  $D$  is the average local seismic displacement and  $A$  is the area of the fault. A similar experiment on the same specimen was conducted by McLaskey et al. (2014) and McLaskey & Kilgore (2013) at the USGS, California, with 14 piezoelectric sensors recording the microseismic events during the test. This large model would allow the fault to be studied realistically so that some parts of it could slide while the rest was not slipping. This way, individual stick-slips could occur during the loading with the possibility of them triggering other slides. However, since this specimen had been used for 25 years resulting in many stick-slip events and cumulative slips without additional surface preparation, McLaskey et al. (2014) believed that the present surface was smoother than what it was in 1981.

The test setup was a steel frame with four flat jacks between the frame and the specimen as shown in Figure 4.2.

The model was loaded in  $\sigma_2$  direction and unloaded in  $\sigma_1$  direction by increasing and decreasing the pressures slowly along the 1 and 2 directions, respectively, with the same rate of 0.001 MPa/s. This way, the normal pressure on the fault was kept constant while the fault was shearing. They tried to model the earthquake cycle by loading, resetting and holding at four stages. Slip sensors were installed on top of the fault to measure relative slips from one side of the fault to the other. Piezoelectric sensors were also installed on top and bottom of the fault. The

sensors would respond to the vertical component of motion in frequency ranges of  $\sim 100$  Hz to  $\sim 1$  MHz and were installed 200 mm off the fault. The onset of instability was observed at 3.7 MPa of shear stress. At this point, the fault would experience several small falls and rises in the shear stress each accompanied by a small displacement along the fault. These small displacements have been reported to range from 0.08 to 0.15 mm (McLaskey, 2013). The shear modulus and critical slip distance of the Sierra white granite were estimated to be around 20 GPa and 5 micron, respectively (McLaskey, 2013).

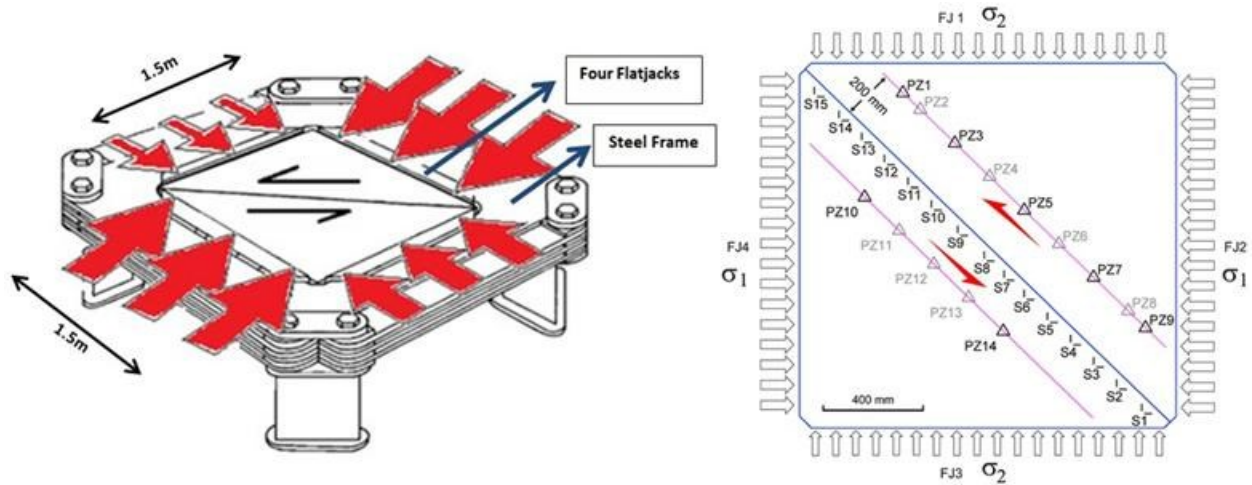


Figure 4.2: (Left) McLaskey’s experimental setup. (Right) Slip sensors and piezoelectric sensors. Piezoelectric sensors are mounted on top and bottom of the sample. Flatjacks are marked with FJ1 to FJ4. Strain gages are shown by S1 to S15. (McLaskey & Kilgore, 2013)

#### 4.5 Algorithm for Recording the Slip-Induced Microseismicity

The numerical representation of the fault is composed of all the contact points where at least one of the particles is located along the fault. Once a slip occurs at any of these contacts, if the normal stress of that contact is greater than 0.1 MPa, an “event” is created and the time at which slip initiated is recorded. The reason for this threshold can be explained using Figure 4.1a. According to Figure 4.1a, if the simple static-dynamic friction law (dotted blue curve) is used instead of the realistic frictional resistance curve (solid red), the rate of decrease in frictional resistance during slip will always be faster than the rate of decrease in driving force and thus every slip will be seismic. It is known that low stiffness, high normal stress and small  $D_C$  facilitate the unstable slip (Dieterich, 1979). Based on Equation (4.1), assuming the frictional properties and the stiffness of surroundings are constant along the fault, normal stress will be the only controlling factor for the

onset of instability and thus a low normal stress results in the fault sliding stably. Therefore, it is necessary to set a minimum normal stress for the slips to be considered seismic. In practice, this threshold has the advantage of reducing the number of recorded events and faster computation time (Hazzard & Pettitt, 2013). However, it will be shown in Section 4.3.2. that the models presented in this study are not sensitive to this threshold.

According to laboratory stick-slip friction data reported by McGarr (1994), the dynamic friction in this study has been assumed equal to 80% of the static friction. Therefore, once a slip passes the normal stress criterion, the friction coefficient of that contact is dropped to 80% of its original value. Once the contact stops sliding, the coefficient of friction is readjusted to its static value. This is implemented to take into account the healing phenomenon (due to processes such as creep in the field or thermal mechanism in the lab causing the micro-asperities to weld together) that is believed to be a necessary component for generation of earthquakes in nature (McLaskey et al., 2012). For each seismic slip, the start and end times as well as displacement of the contact are recorded. Considering each slip as one event, results in all the magnitudes to be almost equal. A good practice is to assume a group of slips close in time and space forming a slip patch and clustering them to form a single event. Therefore, the events have been clustered if they had two conditions: they were within a space window and their duration of slip would overlap for at least one cycle. Another criterion has also been implemented for duration of each slip. Assuming the shear can propagate as slowly as 0.5 times the shear wave velocity of the material (Hazzard & Young, 2000), the minimum duration of a slip to be considered seismic is calculated as:

$$T_{\min} = \text{int} \left( \frac{\text{space\_window}}{0.5 \times \text{ae\_svel}} \right) \quad (4.3)$$

where  $T_{\min}$  is the time required for the shear wave to propagate the space window, *space\_window* is considered to be 0.42 m in this study and *ae\_svel* is the shear wave velocity equal to 2700 m/s for Sierra granite as reported by McLaskey et al. (2014). Equation (4.3) shows that not only the choice of space window affects the size of clusters and therefore distribution of events' magnitudes, but also it affects the minimum lifetime of a slip to be considered seismic.

Therefore, choosing an appropriate space window can be considered as part of the model's calibration. For a similar clustering algorithm but for crack-induced events, Hazzard (1998)

showed that the space window of 5 particle diameters would yield the best results in a 2D model and above this value, the b-values were not dependent on the size of window while for a 3D model a smaller space window would be more reasonable. Later in a study of unstable fault slip in Lac Du Bonnet granite, Hazzard et al. (2002) showed that 3 particle diameters would result in a realistic b-value. In the present model, considering the maximum diameter of the particles is 0.14 m, a space window equal to 0.42 m (3 particle diameters) has been used. Comparison of the results with data reported by McLaskey et al. (2014) and McLaskey & Kilgore (2013) that will be shown in the next sections confirms this has been an appropriate choice.

At the end of the test, all the slips that occurred within the space window and with the durations overlapping at least 1 cycle are clustered together. The area of each clustered event is calculated assuming the event as an ellipse. The largest and smallest radii of the ellipse are calculated based on the farthest and closest particles to the center of the event, respectively.

In order to calculate the centroid of each event, the number of contacts forming that event has been used. However, it has to be emphasized that the number of “contacts” forming an event is not necessarily the same as the number of “slips” forming that event. As an example, the clustering process for three smooth joint contacts, A, B and C, is schematically illustrated in Figure 4.3.

In this Figure, imagine contact A starts slipping from 0.10 s to 0.15 s. At 0.13 s contact B starts slipping within the space window of contact A and therefore; so far these two slips constitute one event. The contact B slips until 0.20. At 0.15 s contact C starts slipping until 0.16 s at which point contact A starts slipping “again” until 0.20 s. No other contacts slipped within the space window of contact A from 0.10 s to 0.20 s. In this example, although there are 4 slips forming one event, there are only three contacts involved and therefore, the location of contact A is used once for calculating the centroid (although it slipped twice). The centroid is simply calculated as the average of the locations of the contacts forming the event. Average displacement is calculated as the sum of all displacements associated to all the slips, 4 slips in this example, forming one event divided by the number of contacts in that event/cluster. Having the area of the event and the average displacement of all the contacts forming the cluster, seismic scalar moment,  $M_0$ , is calculated using Equation (4.2). Eventually, magnitudes are calculated using Equation (4.4):

$$M_w = \frac{2}{3} \log M_0 - 6.0 \quad (4.4).$$

The whole idea of clustering is justified considering the fact that in nature, most seismic events are made up of small ruptures and shearing of asperities (Scholz, 2002).

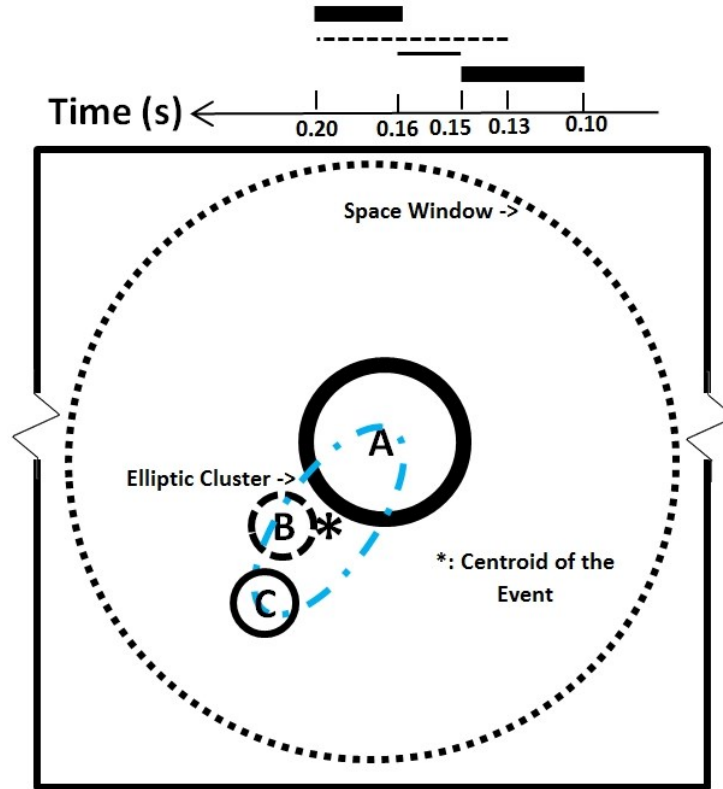


Figure 4.3: A section of the fault illustrating the clustering process for three contacts, A, B and C. It's assumed no other contacts within the space window slipped from 0.10 to 0.20 s. Size of the elliptic event is determined based on the closest and farthest contacts to the center of the event (i.e. B and A, respectively)

## 4.6 Results

A discrete element model of the experiment reported by McLaskey et al. (2014) and McLaskey & Kilgore (2013) is made by PFC3D as shown in Figure 4.4. There are six walls surrounding the model. The wall on the face is not shown in in Figure 4.4 to make the balls visible. The balls are bonded together by parallel bond model. In order to resemble the fault, the smooth joint model has been installed in all the contacts of all the particles located along the diagonal fault extending from top right to the bottom left of the model.

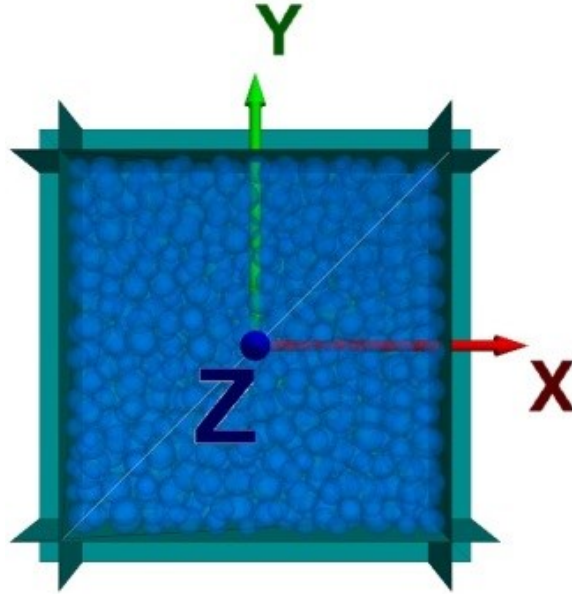


Figure 4.4: The PFC3D model. The fault extends from the top right to the bottom left

There is no direct one to one correspondence between the micro parameters of a discrete element model and macro parameters of the real rock. Therefore, the calibration process involves some trial and error attempt of varying the micro parameters until the desired macro response is observed (Itasca, 1999). However, in the present model, in order to eliminate the effect of possible tensile cracks on the fault's behavior, the strength properties of parallel bonds were set to high values so that they would not control the results and therefore, such calibration for the parallel bond properties was no longer necessary. The fault (smooth joint) parameters were chosen so that the expected stick-slip behavior would be observed at the onset of instability at about 3.7 MPa as reported by McLaskey & Kilgore (2013). In order to keep the normal stress on the fault constant at 5 MPa during the test, the top and bottom walls were moving inwards while the right and left walls were moving outwards all four with the same velocity. The two walls on the back and front were not moving during the test. However, it has to be kept in mind that due to complete symmetry in the fault's location and loading scheme of this test as well as high strength properties of the parallel bonds, there will be practically no damage in any part of the model other than slip along the fault. The PFC3D parameters of the model are summarized in Table 4.1.

Table 4.1: Micro-parameters used in PFC3D model of Sierra granite

Ball Parameters		Smooth Joint Parameters		
Average radius (m)	Young's modulus (GPa)	Normal stiffness (N/m <sup>3</sup> )	Shear stiffness (N/m <sup>3</sup> )	Coefficient of static friction
<b>md_ravg</b>	<b>ba_Ec</b>	<b>sj_kn</b>	<b>sj_ks</b>	<b>sj_fric</b>
0.056	2.1E10	2.1E10	2.1E10	1.05

As the first pass to validate the model, the normal stress along the fault has been obtained during the test. In PFC3D, it is possible to record the stress and strain values in three different ways: wall-based, measurement-sphere based and particle-based. The wall-based stresses are calculated as the sum of out-of-balance forces of all the particles in contact with the wall divided by the wall's area. Measurement-spheres (or "circles" in 2D) are representative volumes in which an average value for the stress or strain is calculated. They can be defined at arbitrary places in the specimen. Particle based measurements represent the value of stress at one particular point.

In order to ensure the normal stress remains constant on the fault, the wall-based stresses (shown in dashed red and purple in Figure 4.5) have been monitored. Considering the whole model as one big element, the normal stress on the fault, however, is calculated using a 2D transformation matrix as shown in Equation (4.5):

$$\sigma_n^{fault} = \frac{\sigma_x + \sigma_y}{2} - \frac{\sigma_x - \sigma_y}{2} \cos 2\theta - \tau_{xy} \sin 2\theta \quad (4.5)$$

where  $\theta$  is  $45^\circ$ ,  $\tau_{xy}$  is assumed to be negligible and  $\sigma_x$  and  $\sigma_y$  are wall-based stresses along the x and y directions, respectively. As another measure of assurance, the normal stress on the fault is also determined by summing up all the normal forces of all the contacts with the smooth joint model assigned to them divided by their area. The wall-based and directly measured normal stresses along the fault as well as the wall-based stresses along the x and y directions are plotted in Figure 4.5. As can be observed in this Figure, if the onset of instability is assumed as the point at which the increase in shear stress stops (i.e. 3.7 MPa), this point corresponds to about 0.22 s past the start of the test. Despite the laboratory experiment, which has practical limitations for how much the fault can slip, in this PFC3D model, there is really no criterion for when the test should stop. Therefore, the test was stopped once 0.1% total displacement of the fault (i.e. 2 mm) was

reached. Total displacement of the fault is calculated mathematically from the wall-based strains in the x and y directions.

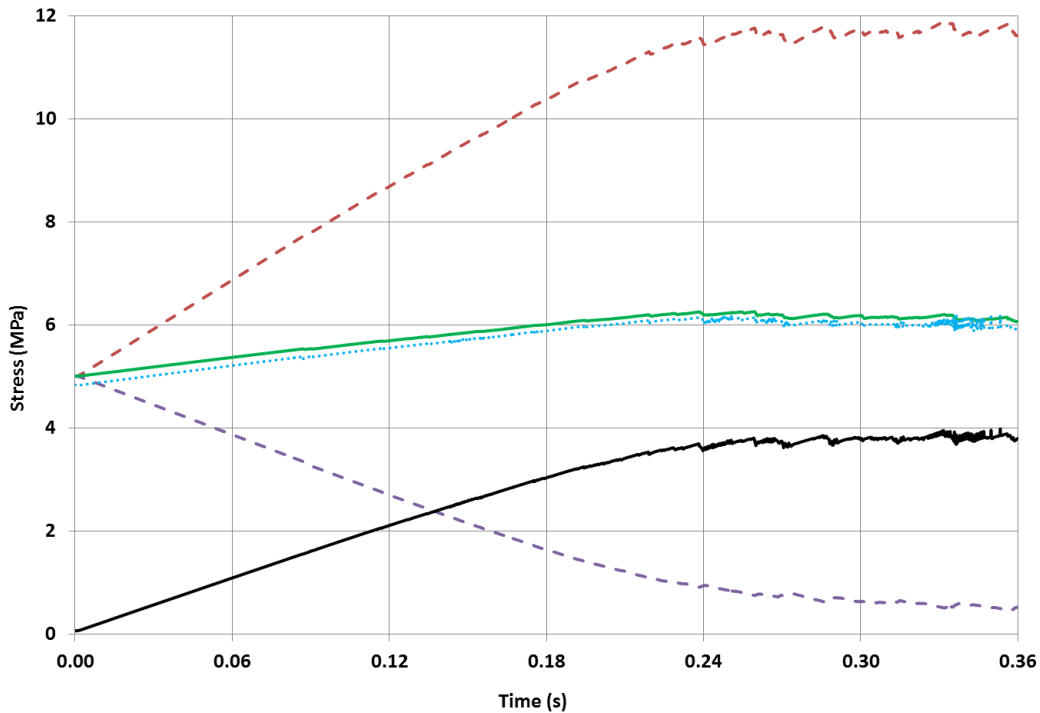


Figure 4.5: Stress measurements during the test. Dotted blue curve starting at 5 MPa is the direct measurement of normal stress from the particles along the fault. The solid green curve at 5 MPa is the normal stress along the fault determined from the wall-based stresses by the transformation matrix. The solid black curve starting at 0 MPa is shear stress along the fault directly measured from the smooth joint contacts. The two dashed symmetrical red and purple curves are the wall-based stresses along the x and y directions, respectively.

As can be observed in Figure 4.5, the normal stress directly measured from the balls is a little bit smaller than the wall-based measurement which is as expected since the fault is modeled as a discontinuum surface. Other than that, the normal stress along the fault has been kept constant during the test. The overall shear stress along the fault versus time as well as a magnified section of the final stick-slip behavior is plotted in Figure 4.6.

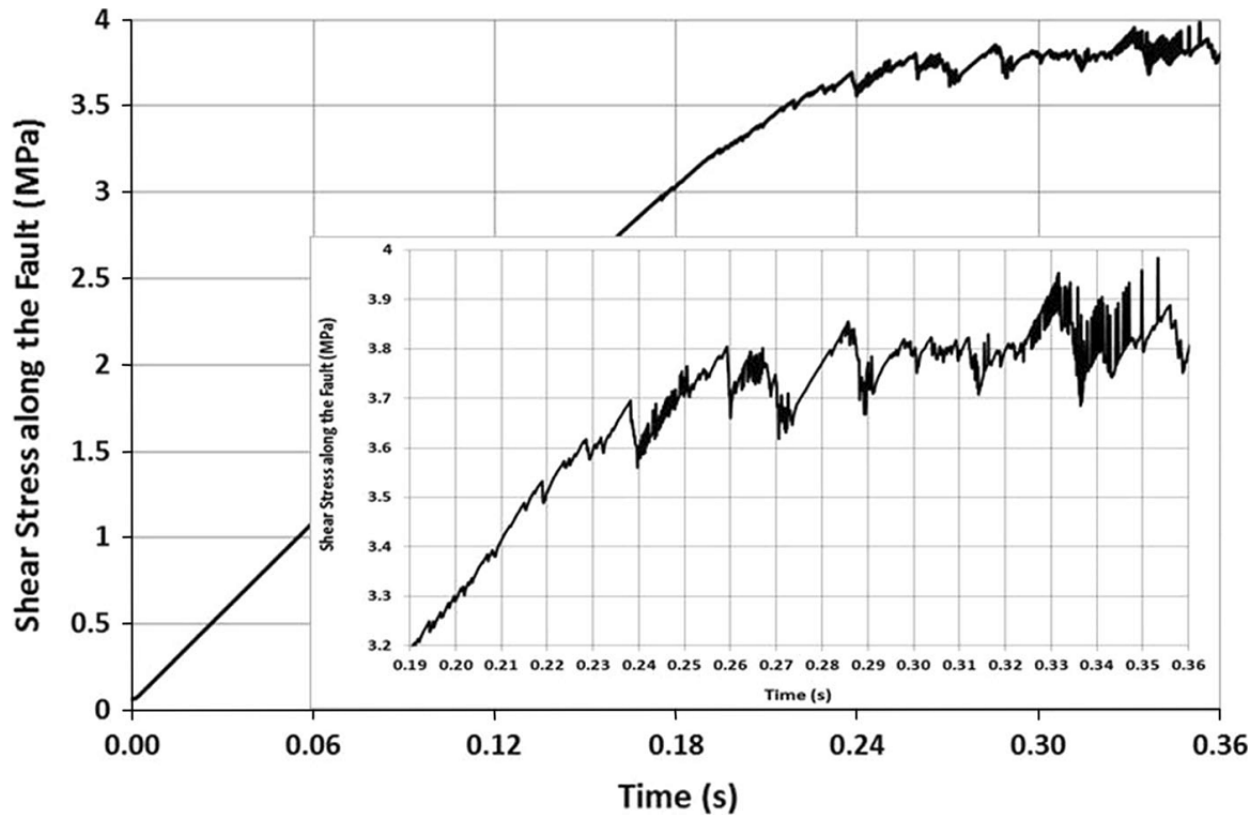


Figure 4.6: The average shear stress along the fault versus time. Shear force is a vector with 3 components. Average shear stress of all the contacts with smooth joint model along the x and y directions are calculated by summing up their respective forces divided by their areas. Then, the average shear stress along the 45° fault has been calculated by the stress transformation matrix.

As can be observed in this Figure, the numerical model has successfully modeled the stick slips. Prior to the onset of instability at 3.7 MPa, McLaskey and Kilgore (2013) observed a linearly increasing shear stress throughout the test. An interesting observation from this Figure is that 3 stages in the slip behavior of the fault can be identified. The first stage is from 0 to about 3.2 MPa where the shear increases linearly with no major stick slips. The second stage starts from 3.2 MPa until about 3.7 MPa with minor stick slips while the shear is still increasing but non-linearly (i.e. the strength is still mobilizing). The final stage starts from 3.7 MPa where the falls and rises of shear stress become more significant and the overall trend of shear stress becomes almost constant while the fault is sliding.

Location of the slips at two sides of the fault recorded in the PFC3D model is shown in Figure 4.7. As can be observed in this Figure, the events are uniformly spread along the fault. This is in agreement with the observation of McLaskey et al. (2014).

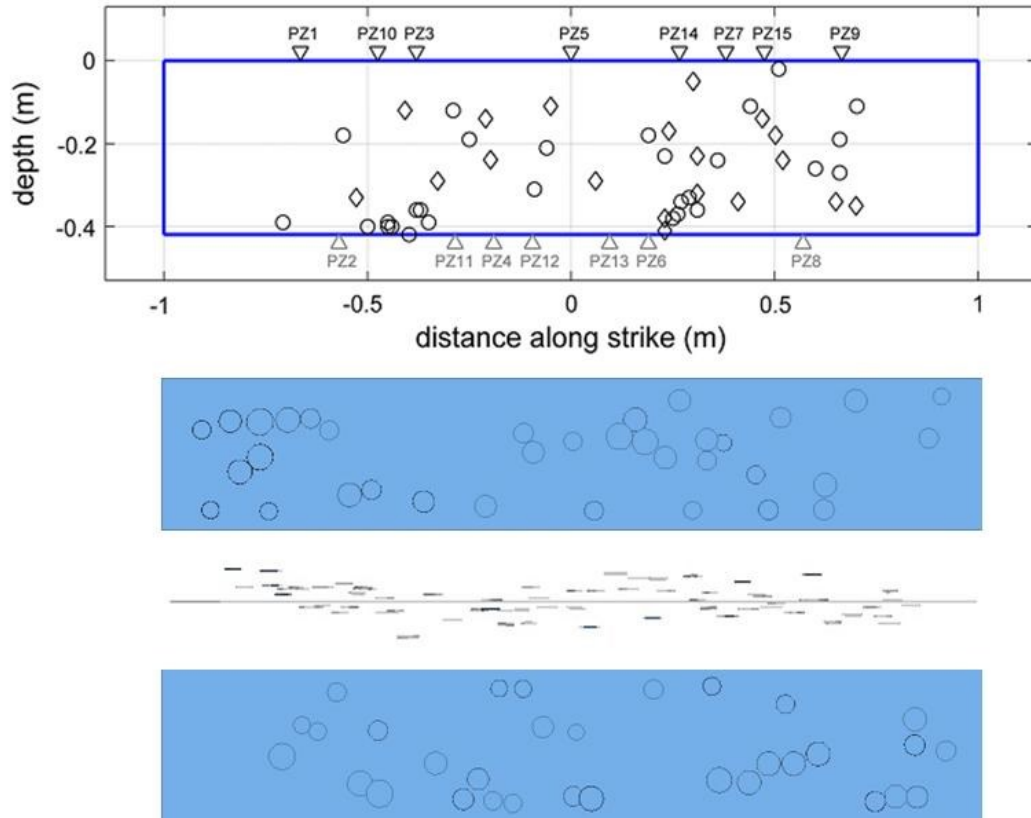


Figure 4.7: The top figure shows the location of events reported by (McLaskey et al., 2014). Foreshocks and aftershocks are shown by circles and diamonds, respectively. They have not reported the events near the fault ends. The two figures at the bottom with blue background are the location of slips in the PFC3D model at both sides of the faults. The figure between these two is a side view of the fault with the location of events around it. No clustering is shown in this figure.

In the PFC3D model, 223 slips have been recorded with the majority of magnitudes around -6 and some -7. As was previously mentioned, a reasonable approach would be to cluster the slips close in time and space to represent more realistic events. After clustering, the number of events is reduced to 131. As can be observed from the clusters shown in Figure 4.8, the largest events have occurred at the central section of the fault which is in agreement with McLaskey & Kilgore (2013). Due to difficulties in plotting ellipses, all the events in Figure 4.8 are illustrated with circles with diameters equal to the major axis of ellipses; otherwise as mentioned before, the area of each event has been calculated assuming it has an elliptic shape in general. It has to be emphasized that the number of events in a PFC model is a function of model's resolution and therefore it is not reasonable to compare the number of PFC events directly with the real number of events recorded in the experiment.

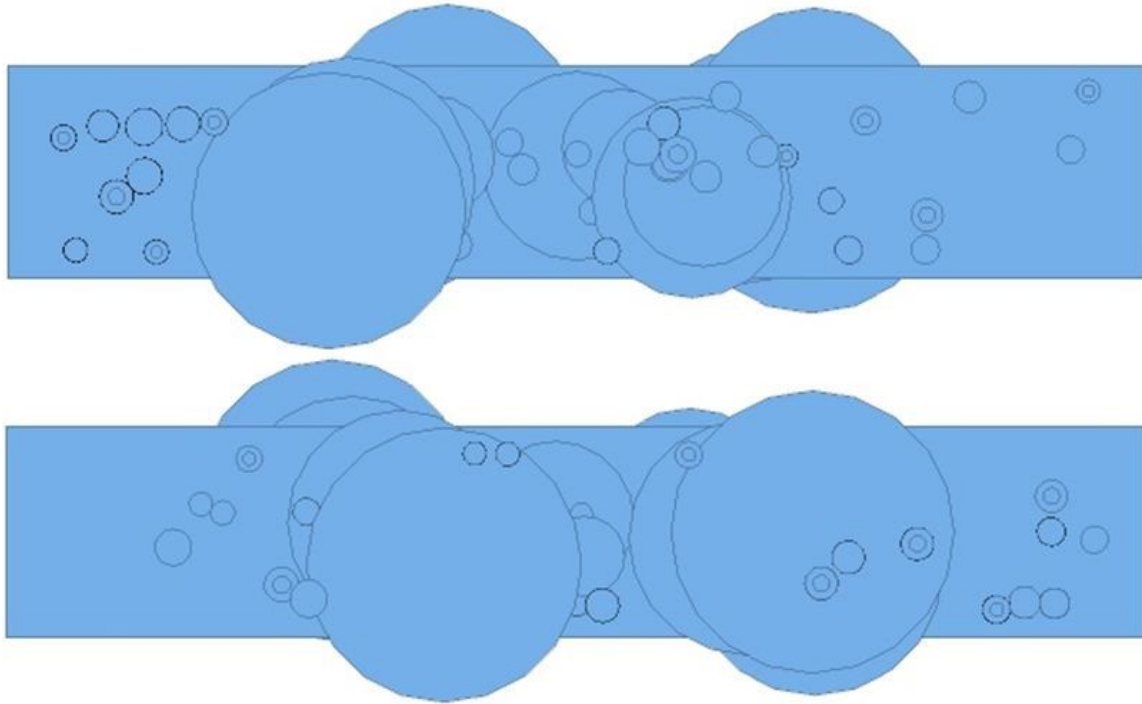


Figure 4.8: The clustered events in PFC3D model. A bigger radius shows a larger patch. Concentric circles represent consecutive slips on the same contact.

In their experiment reported in 2013 (McLaskey & Kilgore, 2013) the normal stress along the fault was kept constant at 5 MPa. However, in their recent 2014 publication, the test has been repeated with 4 and 6 MPa normal stresses along the fault. McLaskey et al. (2014) were able to accurately locate 16 and 32 events for the test with 4 and 5 MPa normal stresses, respectively. In order to determine the mechanism of events, they performed a moment tensor inversion technique and reported that the majority of the events could be modeled by double couple mechanism resulted from frictional slips. The average displacement of each dynamic slip event (DSE) was reported to be about 50-150 microns occurring in about 3-5 ms with the source radii about 3-6 mm. A few larger foreshocks ( $M > -5.0$ ) were not reported due to difficulty in analyzing them. In the PFC3D model, there are 98 smooth joint contacts forming the fault. The stick-slip behavior of a group of them during the test is shown in Figure 4.9.

Although a general trend of increase in the shear stress followed by stick slips is observed for the fault in Figure 4.6, it can be observed from Figure 4.9 that different contacts do not necessarily follow the same stick slip pattern. In other words, for the small patches along the fault, not every drop in shear stress corresponds to a drop in the normal stress. This suggests the likelihood of the

existence of another process responsible for generation of local stick-slips. It is in agreement with McLaskey & Kilgore (2013) that some aseismic slips can possibly trigger repeated earthquakes in their vicinity.

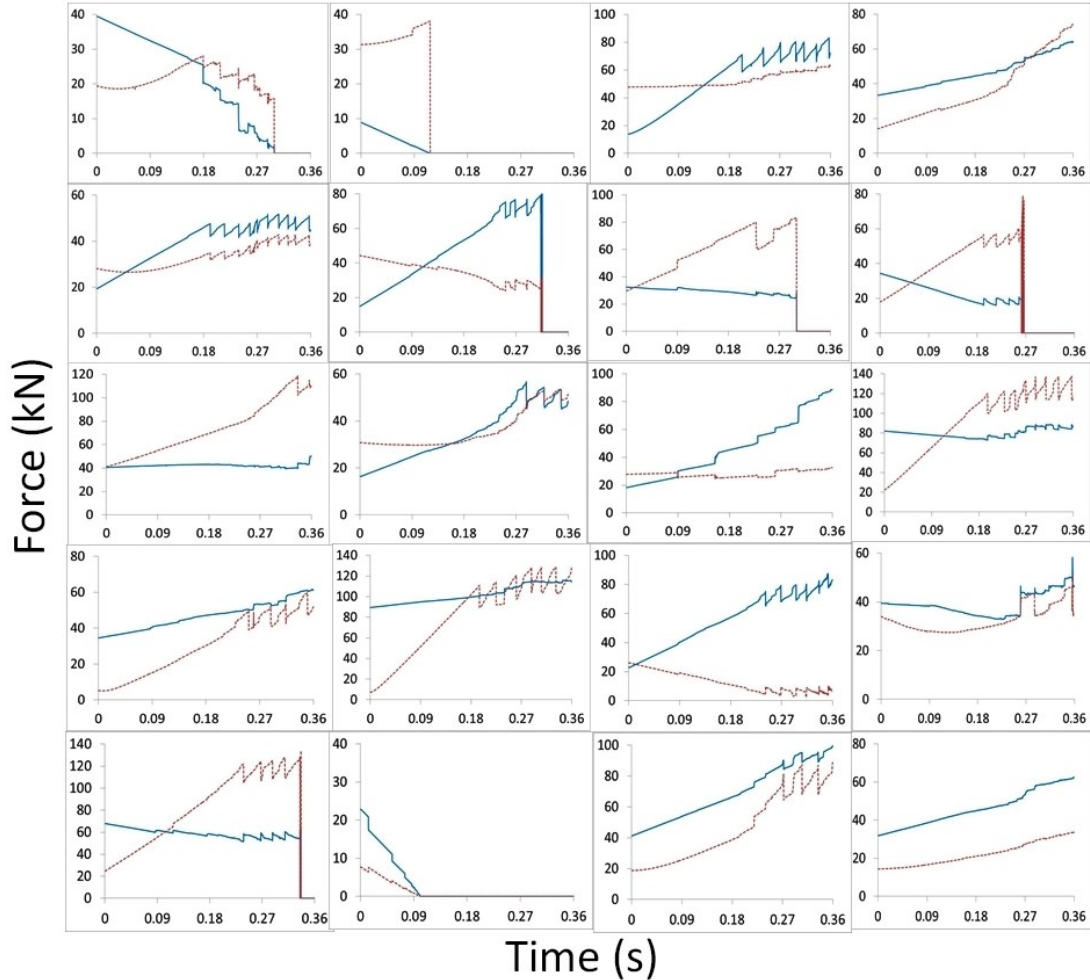


Figure 4.9: Variations of stick-slip behavior in different contacts along the fault. Normal and shear forces are shown with blue and red, respectively.

#### 4.7 Parametric Study

A parametric study is presented in this section to investigate the effect of various parameters on the shear behavior of the fault as well as on generation of microseismic events.

### 4.7.1 Studying the Effect of Space Window's Size

A model with the same properties as mentioned in Table 4.1 is repeated with different space window's sizes of 0.14, 0.28 and 0.42 m (equal to 1, 2 and 3 times the maximum diameter size of the balls, 0.14 m). In order to calculate the magnitudes, the shear modulus of 2 MPa has been used for the slipping patch in all the tests. The b-value plots as well as variations in the number of events for the three tests are shown in Figure 4.10.

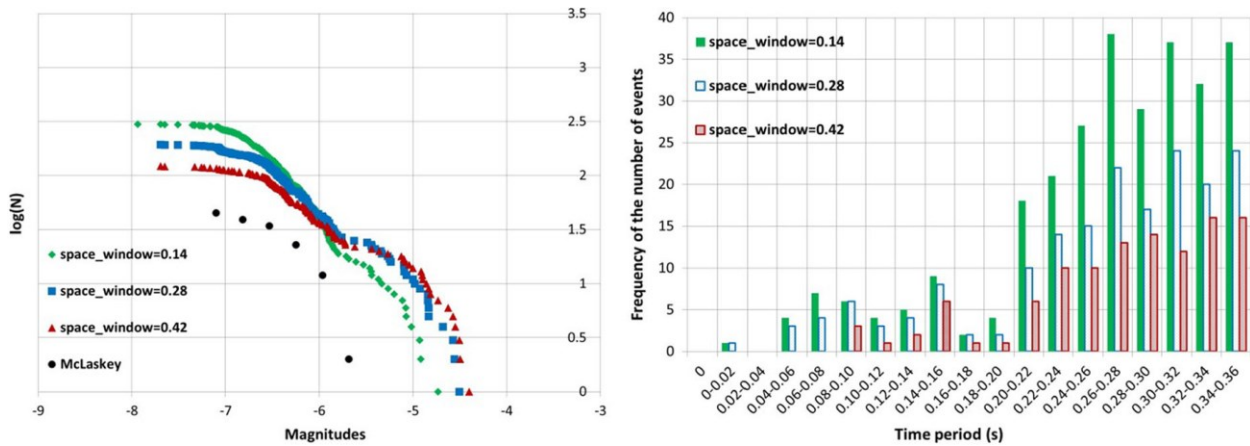


Figure 4.10: b-value plots as well as frequency of the number of events recorded during the tests for three different sizes of space windows

As illustrated in Figure 4.10, an increase in the size of space window causes an increase in the appearance of magnitudes larger than -6 while for the smaller magnitudes, a reverse effect is observed. A comparison between the numerical b-value plots with the experiment is not accurate due to three reasons:

- McLaskey's data belong to the tests with 4 and 6 MPa normal stress (not 5 MPa);
- The loading in this study was continuous while in order to simulate the earthquake cycle their experiments would include loading, resetting and holding at four stages and
- Some magnitudes greater than -5 have not been reported by them.

However, for the sake of comparison and considering the b-values, regardless of a-values, the size of space window equal to 3 times the maximum diameter of the balls, 0.42 m, seems to provide the best match with reality and therefore, it has been used for the other tests presented in

this research. Also, a fewer number of clusters have been observed for greater sizes of space window which is as expected.

#### 4.7.2 Studying the Effect of Normal Stress Threshold for Seismic Events

A model with the same properties as mentioned in Table 4.1 is repeated with three normal stress thresholds of 0.0 MPa (i.e. no threshold), 0.1 MPa and 3 MPa for the slips to be considered seismic (Figure 4.11). As was mentioned in Section 4.1, although for the slips that pass the normal stress threshold the coefficient of friction is decreased to 80% of the static friction and thus it would affect the shear strength as well, no significant difference in shear-displacement and displacement-time plots was observed and therefore they are not included in this chapter. However, as was expected, a lower threshold would result in a greater number of smaller events and also earlier appearance of events in the shear process. The b-values do not seem sensitive to this threshold.

In nature, the overall normal stress on the fault would depend on the in-situ stresses as well as orientation of the fault while for the local patches along the fault, heterogeneity would also play a role. Therefore, this threshold would be more important if faults with different resolutions and or faults in different stress regimes were being compared. However, for the conditions tested in this section, the behavior of model does not seem sensitive to the choice of this threshold and thus 0.1 MPa has been used for the other tests presented in next sections.

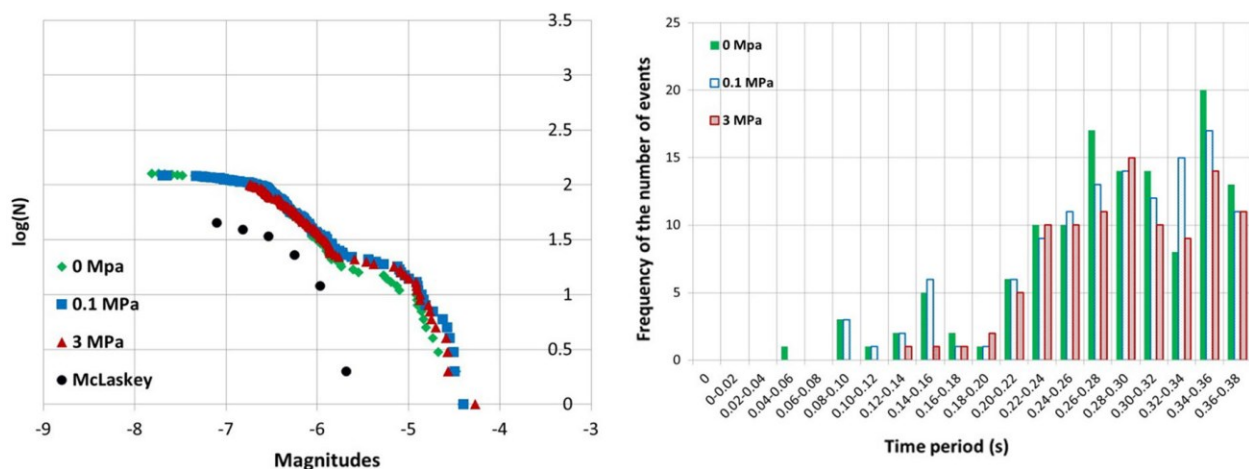


Figure 4.11: b-value plots as well as frequency of the number of events recorded during the simulations illustrating the model's behavior for different normal stress thresholds for the slips to be considered seismic

### **4.7.3 Studying the Effect of Discretization (Size of Particles)**

A model with the same properties as listed in Table 4.1 has been repeated with finer and coarser particles. The average radii of the particles in the three tests were 0.081 m (199 balls), 0.056 m (649 balls) and 0.029 m (5164 balls). As shown in Figure 4.12, coarser balls would result in higher strengths, greater stress drops during stick-slip, slower rate of displacements and smaller b-values. Although the events appear earlier in the finer model and the number of events are higher, the second stage in transitioning from elastic linear increase in shear strength to the final instability where the shear stress becomes constant, from 85% to peak strength, is less obvious in the finer model. This could be observed both in the shear-displacement plots and in frequency of events versus time plots where the slope of getting to the peak number of events is very steep for the finest model.

### **4.7.4 Studying the Effect of Fault's Coefficient of Friction ( $\mu_j$ )**

A model with the same properties as mentioned in Table 4.1 is repeated with different fault's coefficient of friction (1.05, 0.85 and 0.55) which is within the range from 0.6 to 1 as suggested by (Byerlee, 1978). The results shown in Figure 4.13 indicate a decrease in overall shear strength as well as an increase in the rate of displacements for smaller coefficients of friction. The number of magnitudes larger than -5.5 are not much sensitive to the fault's coefficient of friction while an increase in the frequency of events smaller than -5.5 is observed for smaller coefficients which is consistent with the greater number of events observed for these faults.

### **4.7.5 Studying the Effect of Particles Elasticity ( $\mu_{Ec}$ )**

A model with the same properties as mentioned in Table 4.1 is repeated with varying the Young's modulus of the balls ( $2.1 \times 10^9$ ,  $2.1 \times 10^{10}$  and  $2.1 \times 10^{11}$ ). This would represent the stiffness of the medium surrounding the fault. As shown in Figure 4.14, for the softest model ( $\mu_{Ec} = 2.1 \times 10^9$ ), small stick-slip instability was observed as early as 0.1 mm displacements were reached. This behavior continued until about 7 mm displacements (at 3.7 MPa shear stress) that could be considered as the onset of the second stage. The peak shear strength, 4.4 MPa, was reached after 9.6 mm displacements and 1.9 s after the start of the test. This is much longer compared to previous cases

where the maximum shear strength was reached in a fraction of a second. The overall pattern of shear behavior was similar to the model with Young's modulus of balls equal to  $2.1 \times 10^{10}$  but only the portion until 2 mm displacement is shown in Figure 4.14.

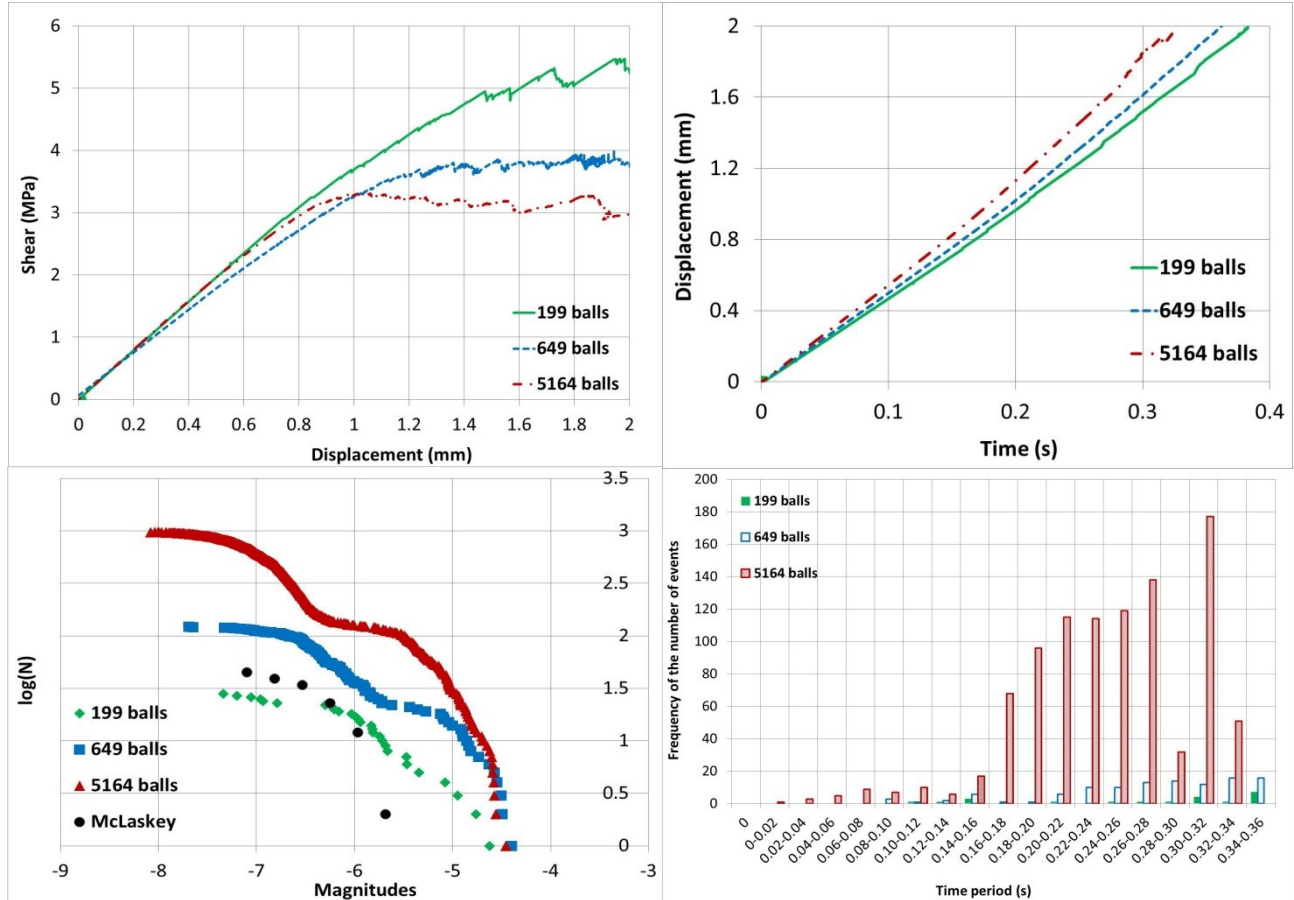


Figure 4.12: Variations of model's behavior for different resolutions

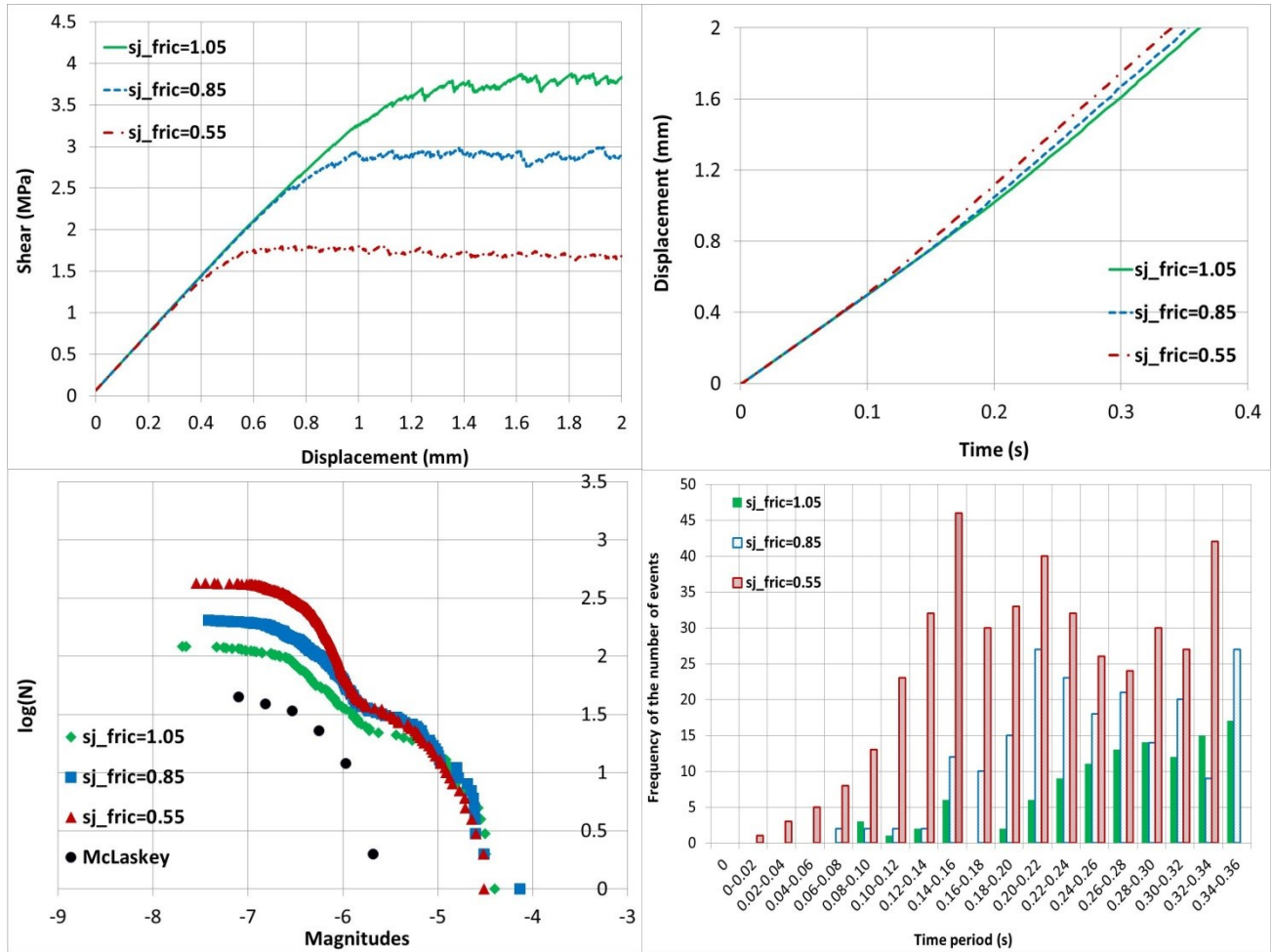


Figure 4.13: Variations of model's behavior for different coefficients of friction

For the model with the surrounding harder than the fault itself a softening behavior is observed with almost no second stage in the shear process. With regard to the number of events, a softer surrounding has not resulted in more emissions for the same amount of displacement and its only contribution has been to delay the process of displacements. An overall shift in the a-values towards larger magnitudes is also observed for the faults with softer surrounding while the b-values are not much sensitive.

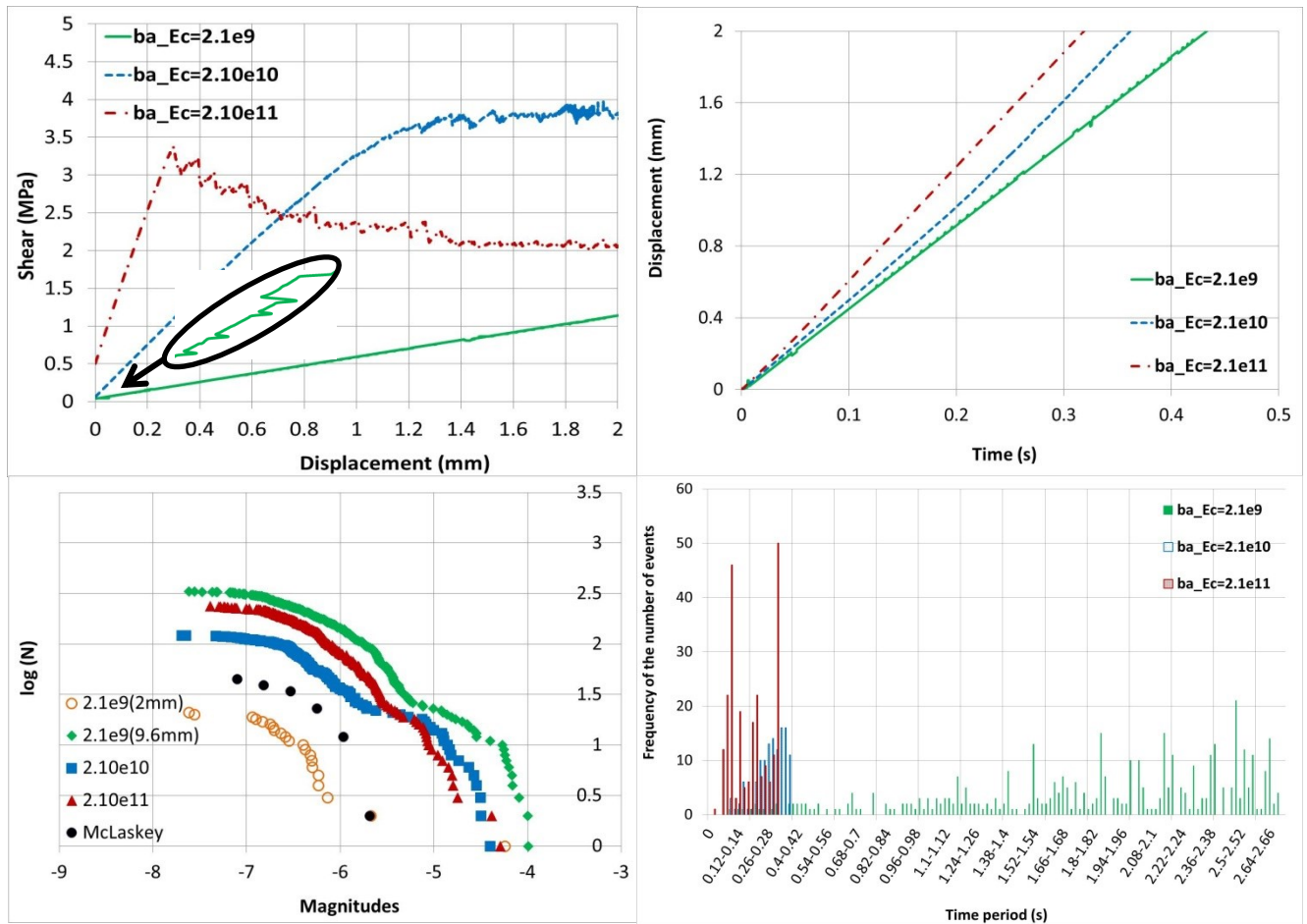


Figure 4.14: Variations of model's behavior for different Young's modulus of the particles. Distribution of magnitudes for the softest model are plotted based on the events recorded until 2 mm and 9.6 mm displacements

#### 4.7.6 Studying the Effect of Fault's Normal Stiffness ( $s_j$ )

A model with the same properties as mentioned in Table 4.1 is repeated with varying the normal stiffness of the smooth joint (2.1e9, 2.1e10 and 2.1e11). According to Figure 2.8, the shear strength is proportional to the normal stiffness of the bond. Therefore, a decrease in normal stiffness results in a smaller strength and thus, a decrease in shear strength and an increase in emissivity of the fault regarding both the number of events and their magnitudes. The effect of normal stiffness on the rate of displacements seems minor however; a smaller normal stiffness has accelerated displacements as well.

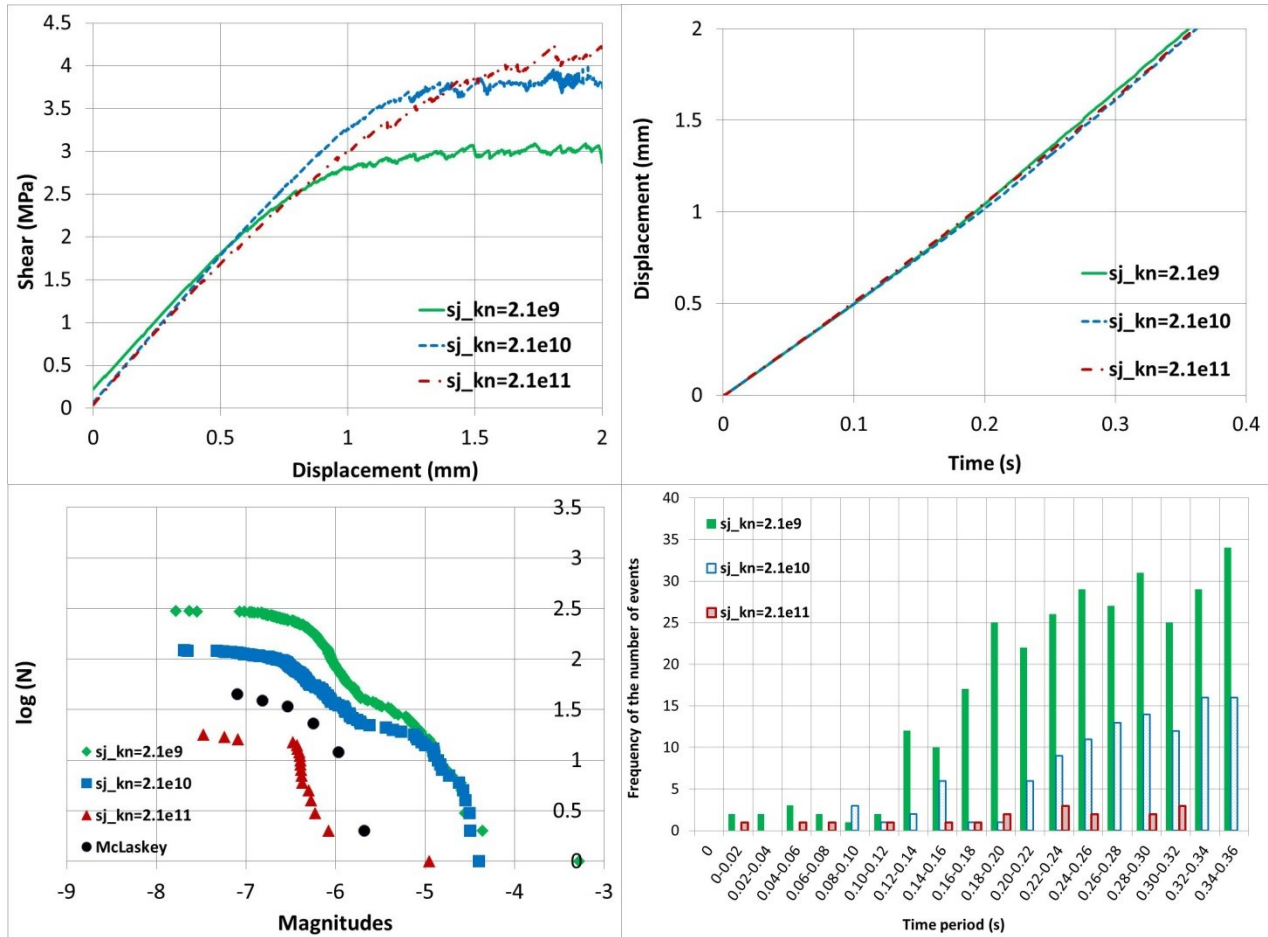


Figure 4.15: Variations of model's behavior for different normal stiffness values of the fault. The shear stiffness of the fault is kept the same in all the models ( $sj\_ks=2.1e10$ )

#### 4.7.7 Studying the Effect of Fault's Shear Stiffness ( $sj\_ks$ )

A model with the same properties as mentioned in Table 4.1 is repeated with varying the shear stiffness of the smooth joint (2.1e9, 2.1e10 and 2.1e11). As shown in Figure 4.16, a greater number of events and larger magnitudes can be observed for the fault with greater shear stiffness. This can be explained considering the fact that a greater shear stiffness results in an increase in the slope of the linear part of the shear-displacement curve and therefore; between two faults that undergo an equal amount of displacements, the one with a greater shear stiffness experiences an overall longer period of third stage in stick-slips that results in a greater number of emissions and possibly greater magnitudes. The effect of shear stiffness on the rate of deformations seems minor however; a reduction in shear stiffness has resulted in a slightly higher rate of deformations.

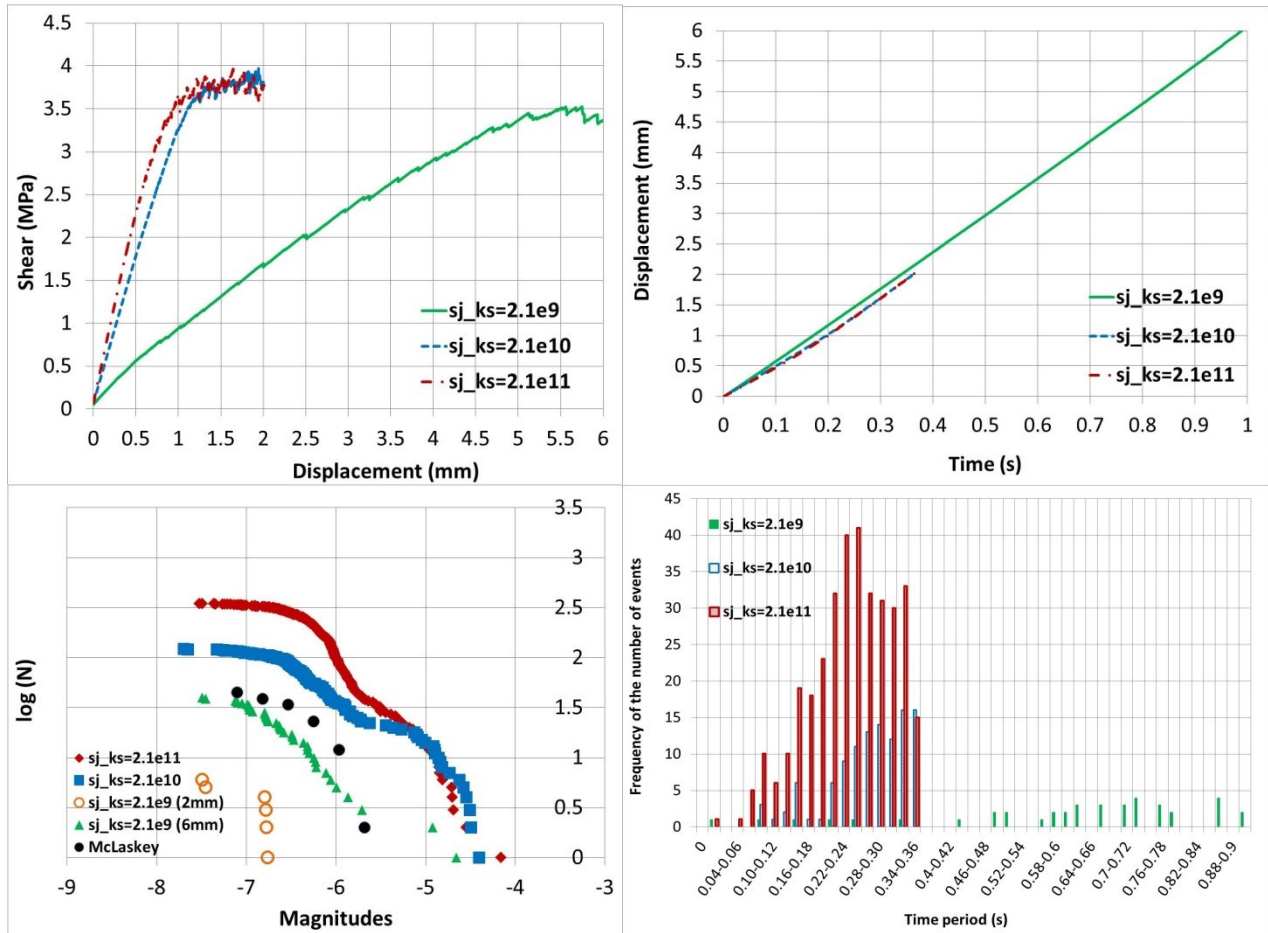


Figure 4.16: Variations of model's behavior for different shear stiffness values of the fault. The normal stiffness of the fault is kept the same in all the models ( $sj\_kn=2.1e10$ )

#### 4.7.8 Studying the Effect of Fault's Elasticity ( $sj\_kn$ & $sj\_ks$ )

A model with the same properties as mentioned in Table 4.1 is repeated with varying both normal and shear stiffness of the smooth joint to the same amount simultaneously. The results can be regarded as a combination of the effects studied in sections 4.7.6 and 4.7.7. Therefore, for two faults that undergo the same amount of displacements, an increase in shear stiffness is in favor of microseismic emissions in terms of the overall duration of stick-slips while an increase in normal stiffness increases the shear strength and thus is against displacements and microseismic emissions. As shown in Figure 4.17, higher shear strength is observed for harder faults. The rate of deformations and b-value plots, however, do not seem to be much affected. A lower number of events is observed for softer faults.

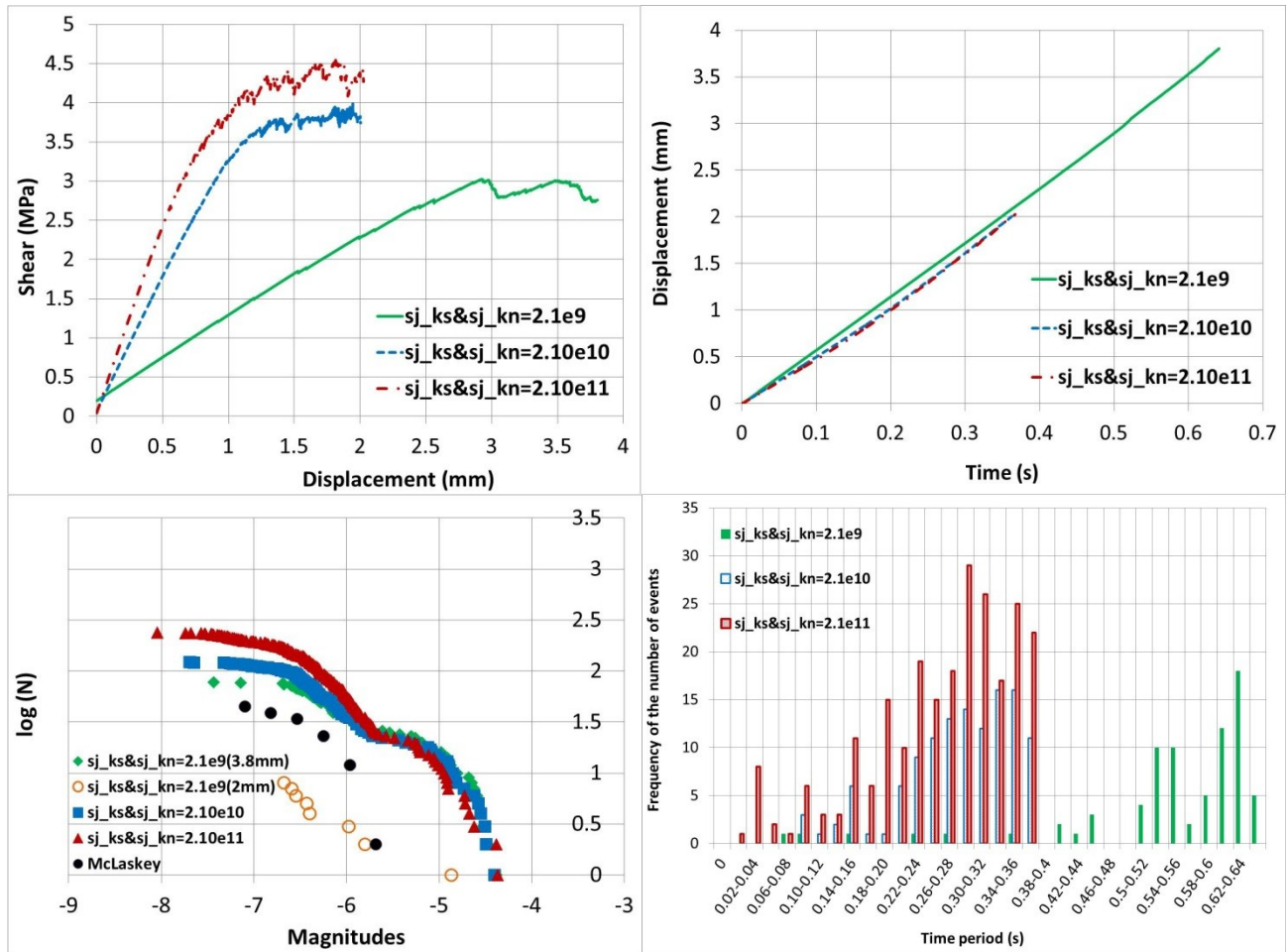


Figure 4.17: Variations of model's behavior for different elastic properties of the fault. Distribution of magnitudes for the model with softest fault properties are plotted based on the events recorded until 2 mm and 3.8 mm displacements

#### 4.7.9 Studying the Effect of Normal Stress

A model with the same properties as mentioned in Table 4.1 is repeated with normal stresses along the fault equal to 3, 5 and 7 MPa. The plots in Figure 4.17 show an increase in the shear strength as well as a decrease in the rate of deformations for higher normal stresses. Also, for the same amount of deformation, higher normal stresses generate fewer emissions. An overall decrease in the  $b$ -value can be observed for higher normal stresses as well.

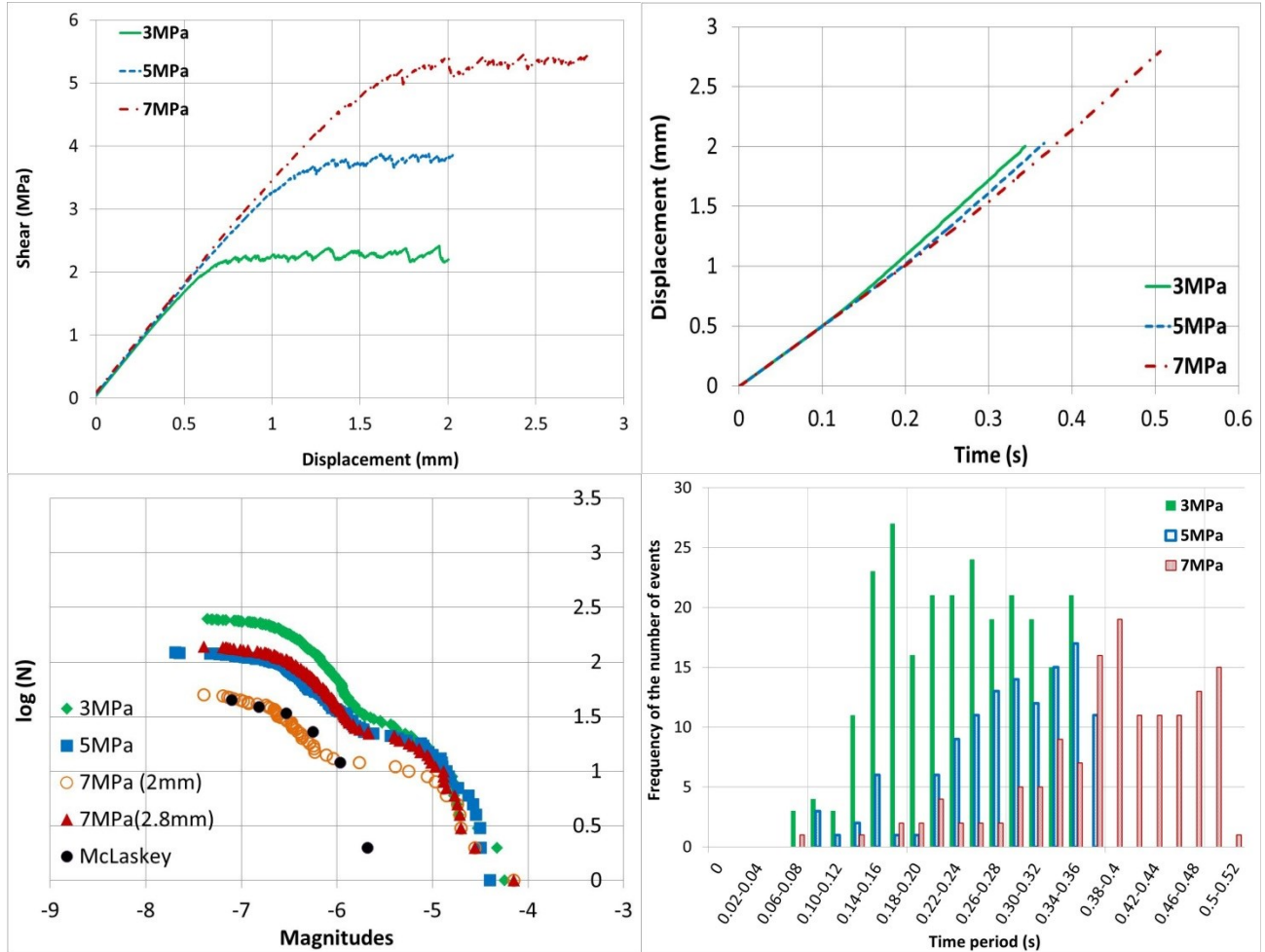


Figure 4.18: Variations of model's behavior for different normal stresses. Distribution of magnitudes for the model with 7 MPa normal stress are plotted based on the events recorded until 2 mm and 2.8 mm displacements

## 4.8 Discussion

As was expected before, the behavior of the numerical model was sensitive to the elastic properties of the medium surrounding the fault as well as fault's properties and the size of particles. It is in agreement with the fundamental mechanism shown in Figure 1. Sensitivity of the numerical model to the frictional parameters is also in agreement with the observation of McLaskey et al. (2014) who believed the recorded events were not due to factors such as grain crushing or fracturing of the fresh rock. The majority of events were believed to have a double-couple mechanism indicating a shear dislocation along the fault. The ones with non-double-couple mechanism were expected not to exceed 20% of all the events (McLaskey et al., 2014).

They observed no specific difference between the focal mechanisms and magnitudes or even stress drop of the foreshocks and aftershocks. Both types of events were broadly distributed along the fault. This is consistent with the results of numerical modeling presented in this study. The results show that largest magnitudes appear mostly in the last stage of unstable stick-slip once the peak shear strength of the fault is already reached.

According to the model shown in Figure 4.1a, whether or not a slip is seismic (or aseismic) would depend on the elasticity of the medium (i.e. stiffness of spring in this model) as well as the amount of stress drop due to unloading the normal stress or frictional properties of the surface. In Figure 4.14, it was shown that stick-slips would occur much earlier in the shear process for the fault with softer surrounding. This is in agreement with the fact that low stiffness facilitates unstable slips (Dieterich, 1979). Also, it has been suggested that local stick-slips could trigger or facilitate other slips in their vicinity (McLaskey & Kilgore, 2013). A possible mechanism for this could be the fact that local slips (or in other words, local unloading normal stress conditions) provide a softened surrounding for their neighbor patches and thus, similar to what was shown in Figure 4.14, facilitating their instability. The amount of how much either of seismic or aseismic slips would contribute to this could be the subject of another study.

## **4.9 Conclusion**

Applicability of the discrete element modeling to successfully reproduce stick-slips in large scale that takes a long time and effort in laboratory to be studied was shown in this chapter. Once the model is calibrated with one set of experiment, it can be used to expand our knowledge to the cases that cannot be easily tested.

In this research, the microseismic release along pre-existing faults during shearing was studied numerically. For this purpose, the experiment reported by McLaskey & Kilgore (2013) was modeled using PFC3D. PFC inherently allows modeling of stick-slips however an algorithm is also developed in this research to record the slip-induced acoustic emissions. Some advantages of the present model are: 1) The three dimensional and discrete nature of model that allows taking into account the geometrical heterogeneity and make the simulations more realistic 2) Focusing on the fault's behavior by use of smooth joint model that allows eliminating the tensile bond breakages

affecting the results. 3) The algorithm developed for recording the stick-slip induced microseismic events.

Once the results compared well with real laboratory data, the model was then expended upon to study the difference in shear and microseismic behavior in faults with different properties. The following provides a summary of the results obtained in this chapter:

1. A decrease in shear strength was observed for the models with smaller particles, smaller coefficient of friction of the fault, harder surrounding of the fault (higher Young's modulus for the particles), softer faults (smaller elasticity moduli of the fault) and smaller normal stress on the fault. Also, a softer behavior (i.e. decrease in the initial slope of shear-displacement curve) was observed for the softer faults as well as faults with softer surrounding.
2. A higher rate of displacements was observed for the faults with finer particles, smaller coefficient of friction, harder surrounding and smaller normal stress. The fault's elastic properties did not seem to have much effect on the rate of displacements; however, a small increase in this rate was observed for the softest fault. A comparison between displacement-time and shear-displacement curves suggests that higher rate of displacements are observed for weaker conditions (i.e. conditions resulting in smaller peak strength) while this conclusion seems less obvious for the softer faults (Figure 4.17).
3. With regard to the magnitudes, a greater size of space window resulted in an increase in the events larger than -6 while a reverse effect was observed for the smaller events. The b-values were not sensitive to the normal stress threshold of slips to be seismic. Increasing the resolution or decreasing the normal stress on the fault both caused an increase in the b-values. Decreasing the coefficient of friction did not have much effect on the magnitudes larger than -5.5 while for the smaller magnitudes, a decrease in this coefficient caused an increase in the number of events. Increasing the particles' elasticity caused a decrease in the a-values but the b-values were not much affected. A decrease in normal stiffness of the fault resulted in emergence of larger magnitudes. Also, an increase in the shear stiffness of the fault resulted in emergence of larger magnitudes that can be explained considering such fault would undergo a longer period of stick-slips. However, b-values were not sensitive to the simultaneous change in normal and shear stiffness of the fault to the same amount.

4. A larger number of recorded events were observed for the models with smaller size of space window, smaller normal stress threshold, finer particles, smaller fault's coefficient of friction, harder fault's surrounding, smaller normal stiffness of the fault, greater shear stiffness of the fault and smaller normal stress on the fault. An obvious observation is that for the same amount of slip, the emissivity would depend on several factors affecting the release of microseismic energy. It was also suggested that there are three stages in the slip behavior of a fault: 1) linear increase in the shear stress until 85% of the peak strength with no or very few stick-slips 2) stable slip from 85% of the peak shear strength until the maximum shear strength is reached 3) unstable continuation of slip until for some reason the fault stops. An exception was observed for the case with fault's surrounding being harder than the fault itself (Figure 4.15) where right after the first elastic stage in the shear process, the third stage started with a post-peak softening pattern. However, among these three stages, the last one, which is unstable, has the greatest number of stick-slips and therefore, a comparison between the number of events versus time and shear versus displacement plots suggests that for the same amount of displacement, the conditions at which the third stage is reached earlier would be the most emissive ones.

Although due to the geometry of the fault and loading scheme used in this research it was not investigated, the results suggest that in reality it is quite possible for the two ends of a fault to be still while there are patches along the fault undergoing stick-slips. Also, local stick-slips seem to provide a softer surrounding for their neighbor patches favoring their subsequent stick-slips.

With regard to the calibration of model for stick-slip behavior, the onset of instability (peak shear strength) as well as b-value seems to be the two most controlling parameters that need to be taken into account.

# Chapter 5

## Weyburn CCS Project: Part 1<sup>4</sup>

### 5.1 Abstract

According to poroelastic theory and also field observations, an increase in reservoir pore pressures can result in a decrease in horizontal stresses in the seal layers. This reduction is in favor of hydrofracture development and reactivation of weak planes and has to be studied in caprock integrity analyses. In this chapter, a field scale reservoir-geomechanical (GEM-FLAC3D) model is developed for the Phase IB area of the Weyburn CCS project that is located in Williston sedimentary basin. The approach for replication of stratigraphy and how the exact pore pressures can be imported to FLAC3D is explained. Using a feature that allows direct importing of the zones' pore pressures to FLAC3D, a one-way coupling has been conducted between the two codes for the period of CO<sub>2</sub> injection in Phase IB area from 2000 to 2010. Therefore, the reservoir pore pressures at selected timesteps are unidirectionally fed to the FLAC3D to study the likelihood of tensile and shear failure in the seal layer on top as a result of stress transfer due to poroelastic effects. The results show that overall; the likelihood of shear failure along preexisting weak planes has been about 27% greater than that of tensile failure in Weyburn. A discussion is also presented on relevance of this study for interpretation of microseismic data recorded in caprock with regard to geomechanics. The importance of taking into account the three dimensional in situ stresses, stratigraphy, and spatial and temporal variations in pore pressures to study the mechanical effects of CO<sub>2</sub> injection on the seal boundaries is emphasized.

### 5.2 Introduction

Injection of CO<sub>2</sub> into underground formations may be practiced as an enhanced oil recovery (EOR) technique and or as part of Carbon Capture and Storage (CCS) chain to avoid greenhouse gas emissions into atmosphere. Some examples are: In Salah (Algeria) (Riddiford et al., 2004;

---

<sup>4</sup> A version of this chapter has been submitted to Geotechnical and Geological Engineering (under review).

Ringrose et al., 2013), Ketzin pilot site (Germany) (Martens et al., 2012; Martens et al., 2013; Schilling et al., 2009), Weyburn (Canada) (Li et al., 2006; Moreno et al., 2005; Wilson & Monea, 2004) and Sleipner (North Sea) (Chadwick & Eiken, 2013; Chadwick et al., 2004; Zweigel & Heill, 2003). The Weyburn CO<sub>2</sub>-EOR project is studied in this chapter.

Discovered in 1954, the Weyburn field is located in South-East of the Saskatchewan province, Canada (Figure 5.1). It is situated in the Northern part of the Williston sedimentary basin at the boundary of strike-slip and normal fault regimes. The production history of Weyburn reservoir can be categorized in four general periods: primary production (1956-1964), water drive (1964-1992), mature water drive (1992-2000) and CO<sub>2</sub>-EOR (2000-2010) (Figure 5.2). The latter is studied in this chapter.

In order to verify the feasibility of storing CO<sub>2</sub> in depleted oil reservoirs, the Weyburn oil field was selected for a research project by Canadian Petroleum Technology Research Center (PTRC) in collaboration with EnCana (now Cenovus) and the International Energy Agency (IEA). Therefore, in 2000, the injection of CO<sub>2</sub> started in the 19 patterns of the Phase IA pilot area and continued until 2003. Following its success, the injection was then continued until 2010 in further patterns of Phase IB, Phase II and adjacent Midale Field with the rate of 74-588 tons per day per well. The CO<sub>2</sub> that was injected into the Weyburn reservoir would come from a coal gasification plan in North Dakota through 323 km pipeline crossing the US-Canada border. In total, about 16 Mt CO<sub>2</sub> has been injected into the reservoir. As a result, there has been an increase in pore pressures after CO<sub>2</sub> injection compared to the initial (and also average) 14 MPa pressure during the 50 years of production (Figure 5.2). The operational pore pressure at Weyburn was about 12-22 MPa (White, 2013). It is estimated that the pressures in Weyburn will reduce to ambient pressures 1000 years after injection has been stopped (Zhou et al., 2004).

A challenge in CO<sub>2</sub> injection is that in order to minimize the injection volume, CO<sub>2</sub> has to be in supercritical state (Chadwick et al., 2008). Therefore, a minimum pressure of ~7.4 MPa as well as ~31°C temperature has to be maintained all the time (Surdam, 2013). The mechanism of CO<sub>2</sub>-EOR can be explained considering the density of supercritical CO<sub>2</sub> which is less than water (0.6 to 0.75 g/cm<sup>3</sup>) (Sminchak & Gupta, 2003). Due to low density and an order of magnitude lower viscosity, CO<sub>2</sub> becomes miscible with oil and there will be a density driven or buoyancy flow. The oil then swells and becomes less viscous resulting in an easier flow and more production

(Whittaker et al., 2011). Once the oil is pumped to the surface, CO<sub>2</sub> is separated from the solution and re-injected into the reservoir.

From a geomechanical perspective, variations in pore pressure and temperature within the reservoir as well as structural geometry may cause a change on in situ stresses (Engelder & Fischer, 1994; Eshiet & Sheng, 2014; Hillis, 2001; Rutqvist et al., 2008; Saeedi, 2012; Segall & Fitzgerald, 1998; Smart et al., 2014). Such changes can lead to reactivation of preexisting weak planes (Orlic & Wassing, 2013; Röhmman et al., 2013) and or if the minimum compressive principal stress is reached, they may cause hydrofracture development (Sibson, 2003). This can happen within the lateral boundaries and or in the seal layers of the reservoir. Therefore, it is important to include geomechanics in caprock-reservoir integrity analyses. Also, in order to monitor the evolution of damage, techniques such as microseismic (MS) monitoring are employed (Maxwell et al., 2004). MS monitoring refers to recording of elastic waveforms emitted as a result of the material undergoing deformations by devices such as geophones that convert deformations to electric signals. The waveforms are then analyzed to provide insight on location and mechanism of damage (Eyre & van der Baan, 2015). Ultimately, the question would be how MS data is related to geomechanics and how much it can contribute to caprock integrity analyses.

In order to study the mutual effect of flow and stresses, coupled reservoir-geomechanical models (two-ways or one-way) can be used (Klimkowski et al., 2015; Longuemare et al., 2002; Magri et al., 2013; Settari & Walters, 2001; Vidal-Gilbert et al., 2009; Zhang et al., 2015). In a two-way coupling, flow variables (pore pressures and maybe temperature) and geomechanical variables (stresses and strains) may be solved together (i.e. full coupling) or they may be calculated separately by the reservoir simulator and geomechanical simulator, respectively, and then sequentially iterated between the two codes (i.e. partial coupling) (Dean et al., 2006). The two-way coupling improves flow calculations. On the other hand, in a one-way coupling, the changes in flow variables are used by the geomechanical simulator to update stresses and strains but no information is passed back to the reservoir simulator. Therefore, the effect of mechanical changes on flow parameters is not taken into account but it is a useful technique for geomechanical analyses (Minkoff et al., 2013).

For Weyburn, there have been two previous coupled numerical studies. Using FLAC3D, (Gomez, 2006) used a one-way reservoir-geomechanical (ECLIPSE-FLAC3D) model to study

the caprock integrity in Phase IA area for the entire history of reservoir using recorded pressures as well as for the period of CO<sub>2</sub> injection. However, since CO<sub>2</sub>-EOR operations were not completed by that time, he artificially increased the reservoir pressures after 2001 in the same model to study the effect of CO<sub>2</sub> injection on caprock integrity. It was concluded that 64% increase in pore pressures would cause hydrofracturing. As can be observed in Figure 5.2, the average reservoir pressure in 2001 was ~14.2 MPa. A 64% increase means ~23.3 MPa which is lower than 29.5 MPa maximum allowed pressure recommended by (Wilson & Monea, 2004). In 2009, the pressures became very close to 23.3 MPa. This indicates the possibility of hydrofracturing. In his study, the temperature drop due to cold injection was not taken into account. Also, due to the large aspect ratio of the reservoir model and limitations of FLAC3D in terms of aspect ratio, although the stratigraphy in his model was honored as much as possible, no one-to-one match between the reservoir zones and those in the geomechanical model could be obtained. Therefore, the reservoir and geomechanical grids were non-identical and thus, a simple arithmetic averaging was used to calculate the reservoir zone pressures for FLAC3D “grids”.

Using a two-way coupled model, (Verdon et al., 2012) studied the CO<sub>2</sub> injection in Phase IB area. They coupled the flow simulator, TEMPEST, with the geomechanical simulator, ELFEN. The model was a flat box in both codes (No stratigraphic features were modeled) and temperature drop was not considered. They tried to explain the observed microseismic events in the caprock by using a fracture potential parameter defined as the current state of stress divided by the state of stress at failure. Upon using the known reservoir properties, they did not observe a high fracture potential in the caprock. Then, repeating the model with a softer reservoir that resulted in an increase in the fracture potential in the caprock, they concluded that a softer reservoir may have been the case. It was also concluded that the microseismic events recorded in the caprock of Weyburn did not represent fluid migration through the caprock.

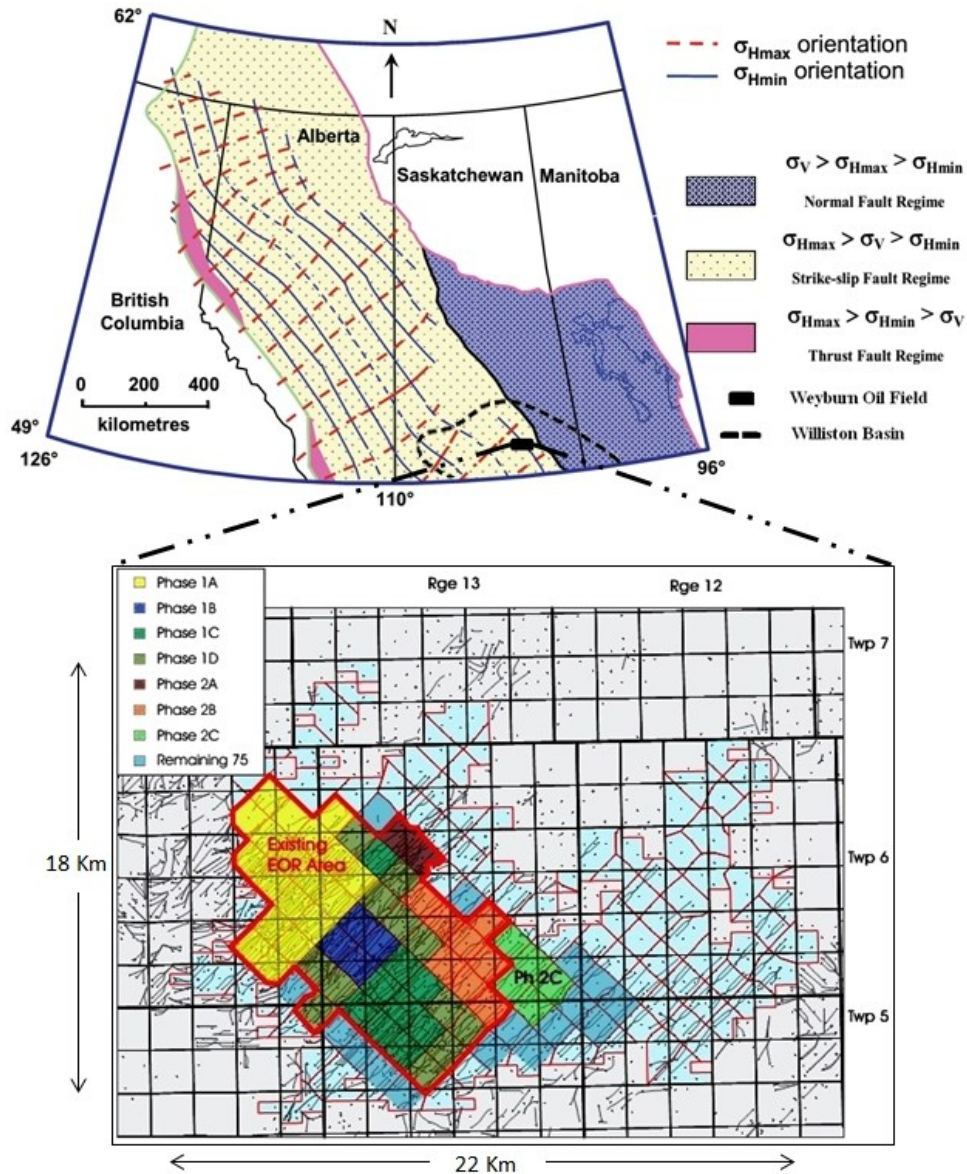


Figure 5.1: Location of the Weyburn field and Phases as well as stress orientations (modified after (Bell & Babcock, 1986; Bell et al., 1994; Soltanzadeh, 2009; Whittaker, 2010a)). The Phase map is courtesy of Cenovus Energy. The dots in the map represent wells.

In this chapter, a one-way reservoir-geomechanical model has been made with as much details as possible to investigate the likelihood of tensile and shear failure due to changes in pore pressures in the Phase IB area of the Weyburn CCS project. Therefore, the flow simulator output (i.e. pore pressures) is fed to the geomechanical simulator to investigate the stress/strain variations in the seal layer. Finally, a discussion is presented on the relevance of this study for interpretation of microseismic events recorded in the Phase IB area.

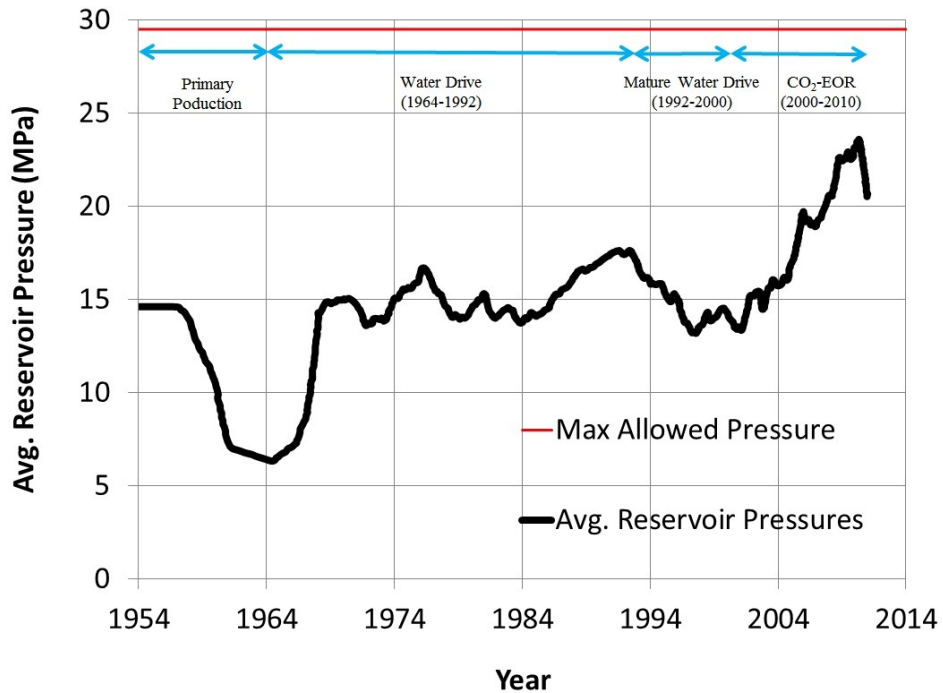


Figure 5.2: Average reservoir pressure after history matching (modified after (Jafari et al., 2011)). The red line shows the maximum recommend pressure, 29.5 MPa (Wilson & Monea, 2004)

### 5.3 Geology of Weyburn Field

Located within the Williston sedimentary basin (Figure 5.1), the geological units of the Weyburn reservoir are shown in Figure 5.3. The Mississippian Madison group has been subdivided into stratigraphic units called “Beds”. Hydrocarbon is produced from the Midale Beds within the Charles formation of the Madison group along the Mississippian strata at depths of 1310 m to 1500 m under the ground surface (Zhao & Tian, 2003).

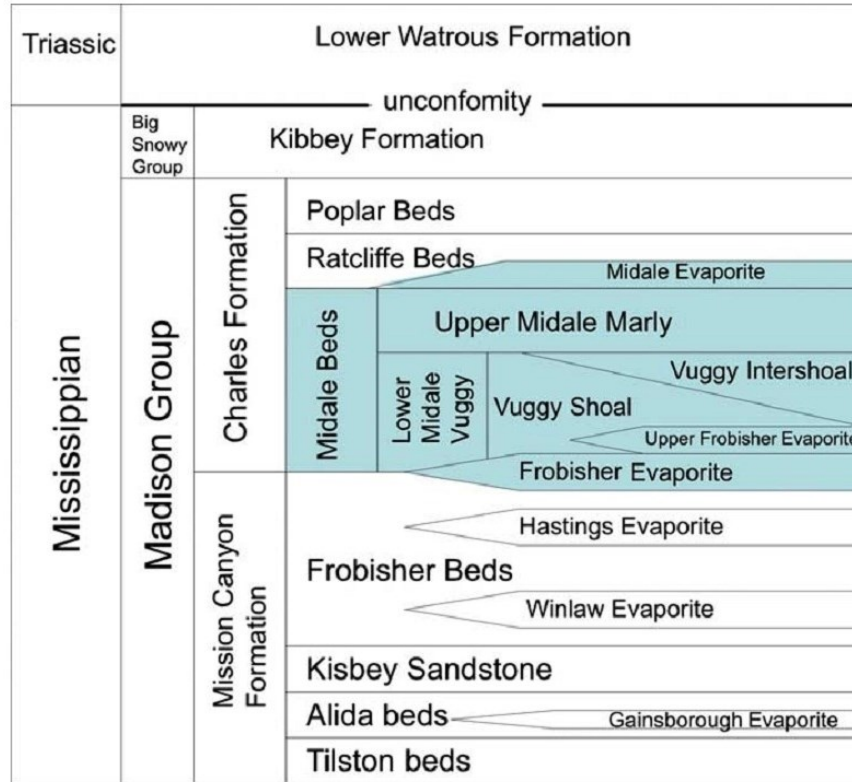


Figure 5.3: Geological units of the Mississippian strata (Baharvand Ahmadi et al., 2011)

The reservoir is usually divided in two groups: upper Marly and lower Vuggy. Figure 5.4 shows the six lithological units identified in the Vuggy zone that yield in general division of this zone into lower and upper units (Wegelin, 1984). The Vuggy unit can be generally divided into shoal and inter-shoal members (Brown, 2002). The upper Vuggy unit is overlain by Marly dolostones. However, a widespread marker bed (M2) within the Marly bed divides it into two layers of M1 and M3 (Burrowes & Gilboy, 2000). The lithological properties of the reservoir layers are summarized in Table 5.1. Vuggy unit is more permeable than the Marly unit.

The upper Marly layer is covered by a non-reservoir transitional unit with 1-3 m thickness often referred to as “Three Fingers” (so called due to its characteristic gamma response) (Burrowes & Gilboy, 2000). The Three Fingers layer is capped by the Midale Evaporite unit consisted of low permeability anhydrite with the thickness ranging from 2 to 10 m that covers most of the Saskatchewan (Whittaker et al., 2011; Wilson & Monea, 2004).

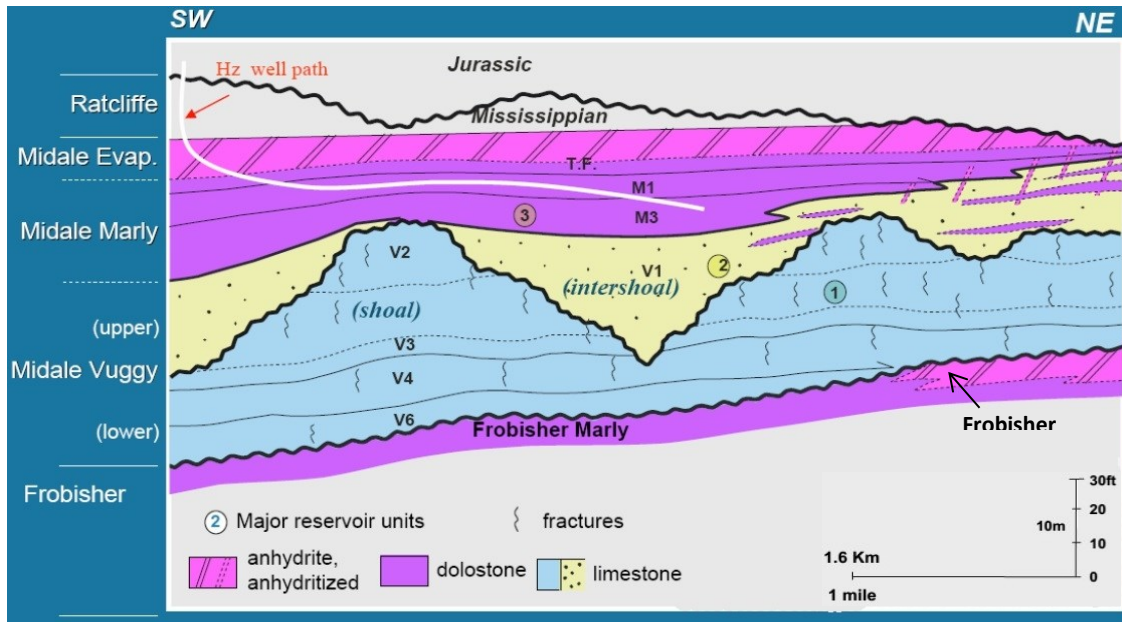


Figure 5.4: Schematic generalized SW-NE cross-section of the Weyburn reservoir. Subdivisions of Vuggy are shown with V1, V2 etc. and subdivisions of Marly are shown with M1 and M3 (modified after (Burrowes & Gilboy, 2000; Steve Whittaker, 2010b))

Table 5.1: Lithological properties of the Weyburn reservoir (Burrowes & Gilboy, 2000)

Reservoir Zone	Lithology & Textures	Porosity (avg., Type)	Matrix Permeability (avg.)	Heterogeneity	Fracture Density
Marly (M1, M3)	Dolostone mudstone, wachestone	20-37 % (26 %) intercrystalline moldic	<0.1 - 100 md (10 md)	Low bioturbation dolomitization	Low - Moderate (2-4m spacing) >25% $\phi$ ~unfract.
Upper Vuggy (V1)	Limestone packstone, wachestone	2-15 % (10 %) interparticle interparticle	<0.01-20 md (1 md)	Medium thick bedded, bioturbation	High (<1m spacing)
Lower Vuggy (V2-V6)	Limestone mudstone to grainstone	5-20 % (15 %) fenestral vuggy	<1-500 md (50 md)	High well bedded, high order cyclicality, complex diagenesis	Moderate- High (<1-2m spacing) microfractured

The Vuggy unit overlies dolostones of Frobisher Marly except for the Northern parts where a margin of Frobisher Anhydrite is present (Figure 5.4). The Frobisher Marly under the reservoir is

characterized as non-reservoir argillaceous, silty and anhydritic dolostones and marls (Burrowes & Gilboy, 2000). Therefore, the low permeability dolostones and anhydrites of the Frobisher layers at the bottom and the Midale Evaporite on top act as the primary seals for the reservoir.

In addition to these primary seals, on top of the Midale Evaporite, there are Ratcliffe Beds a sequence composed of Dolostone and Evaporite overlain by the Watrous Formation (White, 2013). The Watrous Formation can be divided into lower and upper members. The Lower member is impermeable Watrous shale with ~65 m thickness. The upper Watrous Member is mainly a stacked succession of massive anhydrite, dolomitic limestone and shale sequences (White, 2013). The main seal usually referred to as the caprock is the Lower Watrous Formation. The thickness of both lower and upper Watrous Members ranges from 110 m along the border with North Dakota to zero at the erosional edge (WEBLEX Canada, 2016).

#### **5.4 Stress Regime in Weyburn**

As mentioned before, the Weyburn reservoir is situated in sedimentary Williston basin. In sedimentary basins with relatively flat stratigraphic layers, given that the shear stress in vertical direction is negligible, it is reasonable to assume that the vertical stress is only due to the weight of overburden and is a principal stress component. Since principal stresses are orthogonal, the other two should be located in the horizontal plane. Using the density logs, (Gomez, 2006) suggested the rate of increase in vertical in situ stress equal to 24 kPa/m. As illustrated in Figure 5.1, the Weyburn field is almost located at the boundary of strike-slip and normal fault regimes. Therefore, the vertical in situ stress is the intermediate principal component.

Considering the fact that fractures open perpendicular to the direction of minimum compressive principal stress and propagate in direction of maximum compressive principal stress (Hubbert & Willis, 1954), the magnitude and orientation of horizontal in situ stresses can be determined using fractures and borehole breakout observations as well as direct measurements by hydraulic fracturing. (Stauffer & Gendzwill, 1987) studied the natural fractures at different depths in Williston basin and observed two sets of vertical fracture with average azimuth of 49 and 139. (Churcher & Edmunds, 1994) investigated the cores recovered from the Weyburn field and observed a dominant vertical to sub-vertical fractures pattern along the NE-SW. This observation is in agreement with the study of (Bunge, 2001) on the fractures of the Midale beds. Using the

breakouts data as well as the results of an anelastic strain recovery test in Midale Field, (Gomez, 2006) suggested that the orientation of maximum and minimum horizontal stresses are along NE-SW and NW-SE, respectively. Based on hydraulic fracturing measurements from Regina (McLennan et al., 1986) and acid stimulation treatment data from the Midale field (McLellan et al., 1992) both in southeastern Saskatchewan, (Gomez, 2006) suggested the rate of minimum horizontal stress as 18 kPa/m (Figure 5.5).

The maximum horizontal stress gradient was estimated assuming the coefficient of friction of faults equal to 0.6 and using the state of stress formula in strike-slip regimes as suggested by (Townend & Zoback, 2000). A summary of the data collected for the maximum horizontal stress in Western Canadian Basin is shown in Figure 5.6. (Gomez, 2006) suggests that the maximum horizontal stress in Williston Basin and the Western Canadian Basin are likely to be equal. Therefore, in order to be conservative, he suggested the use of 28 kPa/m as the upper limit for the maximum horizontal stress gradient.

Therefore, the stress regime in Weyburn can be estimated as following (Gomez, 2006):

$$\begin{aligned}\sigma_H &= 28h \\ \sigma_V &= 24h \\ \sigma_h &= 18h\end{aligned}\tag{5.1}$$

where  $h$  is the depth from the ground surface in meters,  $\sigma_h$  and  $\sigma_H$  are the minimum and maximum horizontal stresses, respectively, and  $\sigma_V$  is the intermediate (vertical) principal stress all in  $kPa$ .

For the models presented in this chapter, the directions of maximum and minimum horizontal stresses are considered to be along NE-SW and NW-SE directions, respectively (both making an angle of  $45^\circ$  with the North direction).

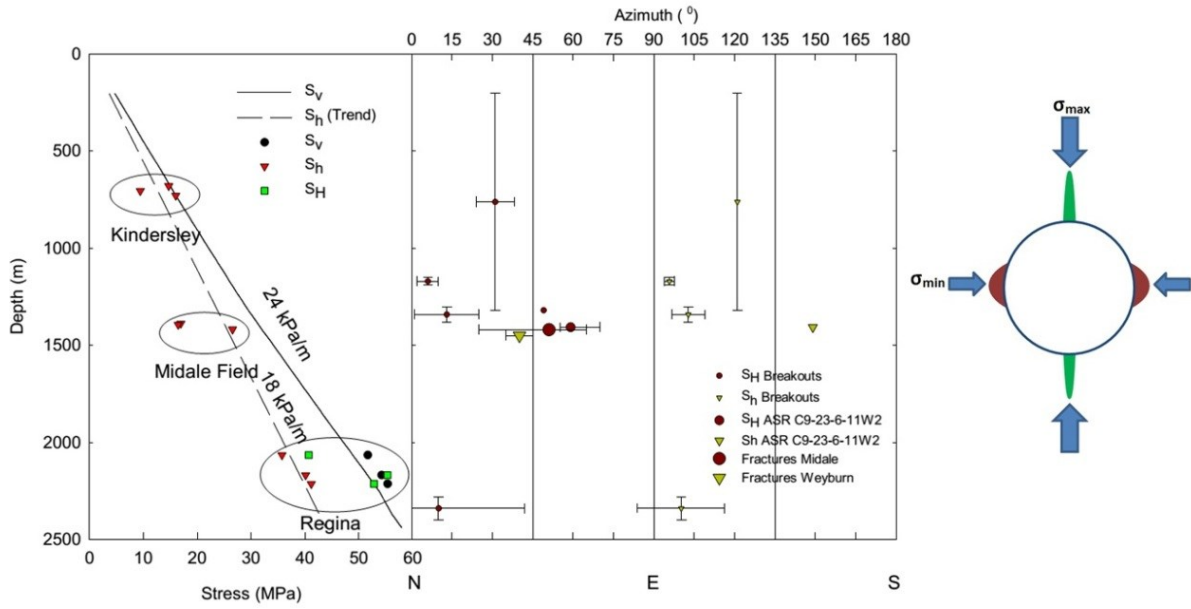


Figure 5.5: (Left) In situ stresses at Weyburn (Jimenez, 2007) and (Right) schematic illustration of the principal stresses with regard to the borehole breakout (red) and direction of fracture propagation (green) (modified after Gomez, 2006))

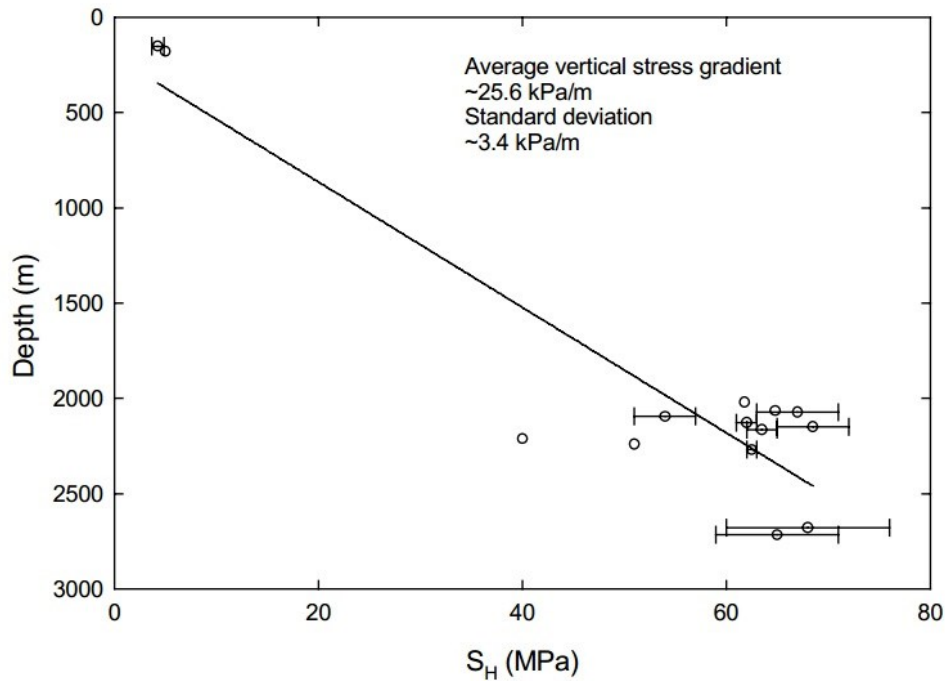


Figure 5.6: Summary of the maximum horizontal stress in Western Canadian Sedimentary Basin (data plotted by Gomez, 2006) after (Bell et al., 1994))

## 5.5 Microseismic Monitoring in Weyburn

In 2000, carbon capture and storage (CCS) component was added to the enhanced oil recovery (EOR) operations in Weyburn. In order to verify the applicability of MS monitoring for CCS projects, MS recording was conducted by ESG Solutions, a seismic monitoring contractor, in the Eastern pattern of Phase IB area (Figure 5.7). This location is the only place where microseismic monitoring has been conducted in Weyburn.

In August 2003, an array of 8 triaxial geophones was installed in a disused vertical production well. In the literature, the terms “observation well”, “monitoring well”, “101/06-08-006-13W2/00” and the abbreviated form “101/06-08” are used interchangeably referring to this well. The geophones were installed from ~1180 m to ~1355 m depth with ~25 m intervals (Verdon, 2010). The lowcut filter was 3 Hz. The high cut filter was  $\frac{3}{4}$  linear phase. The preamplifier gain was 36 dB. From August 2003 until October 2004, the microseismic events were monitored with the purpose of system health checks except for a short period of lock down. The monitoring was halted from November 2004 until September 2005 (Verdon, 2010). In October 2005, a new recording system was connected to the already existing geophones and monitoring was continued for Phase II period (but in the same eastern pattern of Phase IB area) until December 2010.

The injection well<sup>5</sup> was located 50 m east of the monitoring well (Figure 5.7). The injection well was completed in November 2003. The injection of water in this well started in December 15<sup>th</sup> 2003 and continued until September 2010. In January 22, 2004 the injection of CO<sub>2</sub> started in the same well (121/06-08) with a rate between 50-250 MSCM/day (100-500 tonnes/day).

The volume of injected water and CO<sub>2</sub> in this well as well as the number of recorded microseismic events at each month are illustrated in Figure 5.8. Although Figure 5.2 shows an “overall” increase in average reservoir pore pressures for the CO<sub>2</sub>-EOR period and also there has been periods of not recording microseismic data in Weyburn, as can be observed in Figure 5.8, the general correspondce between the amount of injected fluid and the number of microseismic events is poor. This suggest the need for a more detailed study of the local pressures in that area.

---

<sup>5</sup> 121/06-08-006-13W2/00

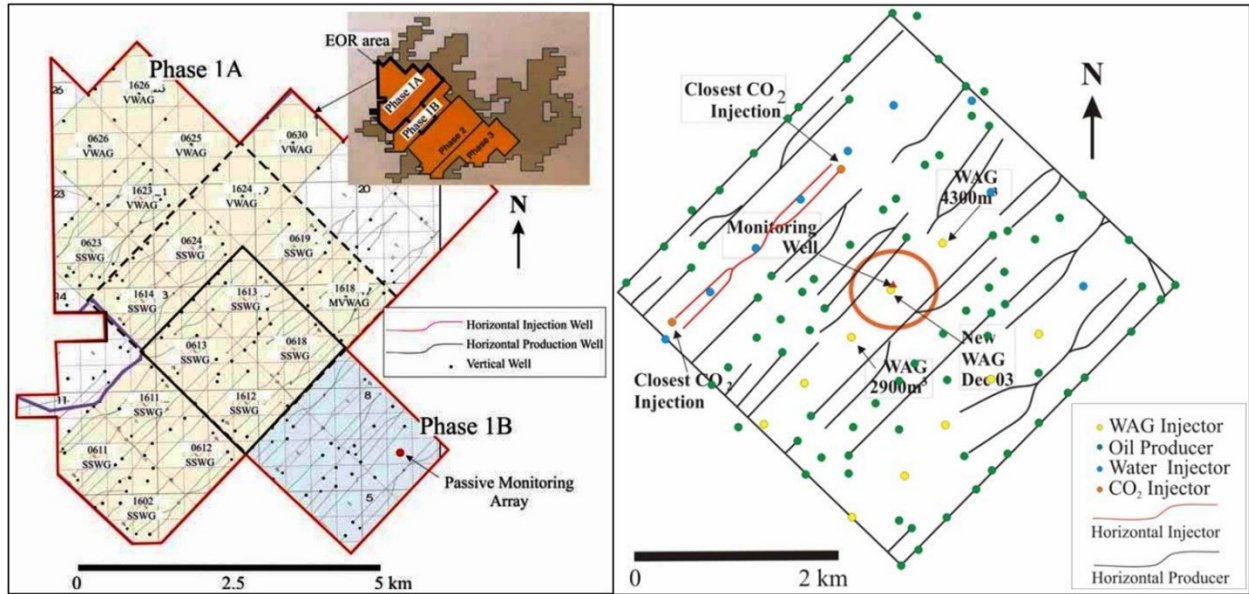


Figure 5.7: (Left) Location map of phases IA and IB. The location of the monitoring well for microseismic study is the red dot in the east pattern of Phase IB – (Right) map of wells in vicinity of the microseismic monitoring well in the Eastern pattern of Phase IB. The microseismic array was installed in August 2003 (Wilson and Monea, 2004).

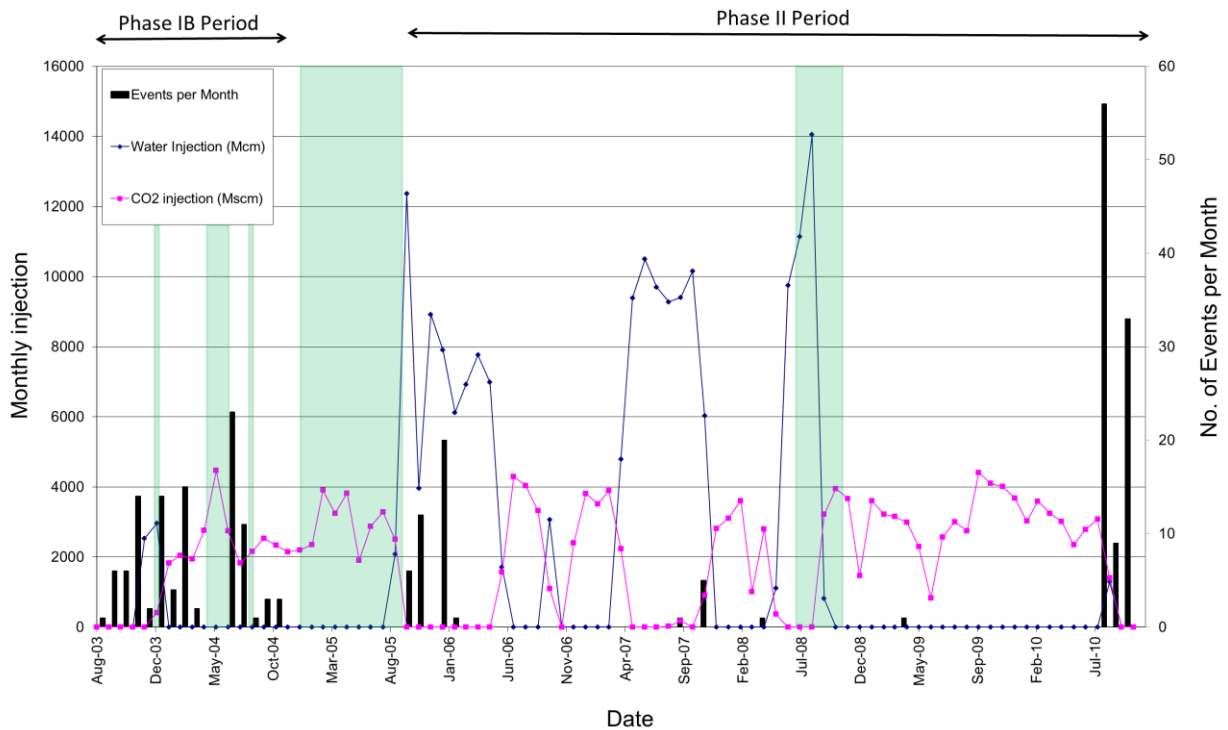


Figure 5.8: The injection rates in well 121/06-08. Periods of not recording MS events are shown with green (Verdon, 2012). The black bars show the number of reliably locate microseismic events (“ESG Weyburn Microseismic Progress Report,” 2011)

The location of the events was calculated by ESG's automated picking algorithm using a 1D velocity model computed from the dipole sonic velocity log of an adjacent well. The locations were calculated using the P-wave arrival azimuth and P and S-wave ray tracing through the velocity model for event depth and radial distance.

Microseismic events have been located 420 m radially around the observation well. This cross section is referred to as "Microseismic/MS Area" in this thesis. Figure 5.9 shows the microseismic area with the events color coded based on the year of occurrence. The total number of events is 250 three of which (two events in 2004 and one event in 2007) are not shown since they were far away from this area.

The frequency of geophones determines how far they can record the waves. In mining operations, high frequency geophones are used that can record waves arriving from up to few meters. In CCS applications, low frequency geophones are used that can record waves arriving from hundreds of meters. For Weyburn, the dominant frequency of events ranged from 15 to 80 Hz. Due to the low frequency and poor signal-to-noise ratio, the error in source location has been as large as 100 m in some cases (Verdon, 2010). Since only one array of geophones was used, no moment tensor inversion was conducted and only magnitudes and source locations have been reported (Verdon, 2010). The magnitudes were determined using the frequency spectra of arriving phases (Verdon, 2016) and ranged from  $\sim -0.56$  to  $\sim -3.62$ .

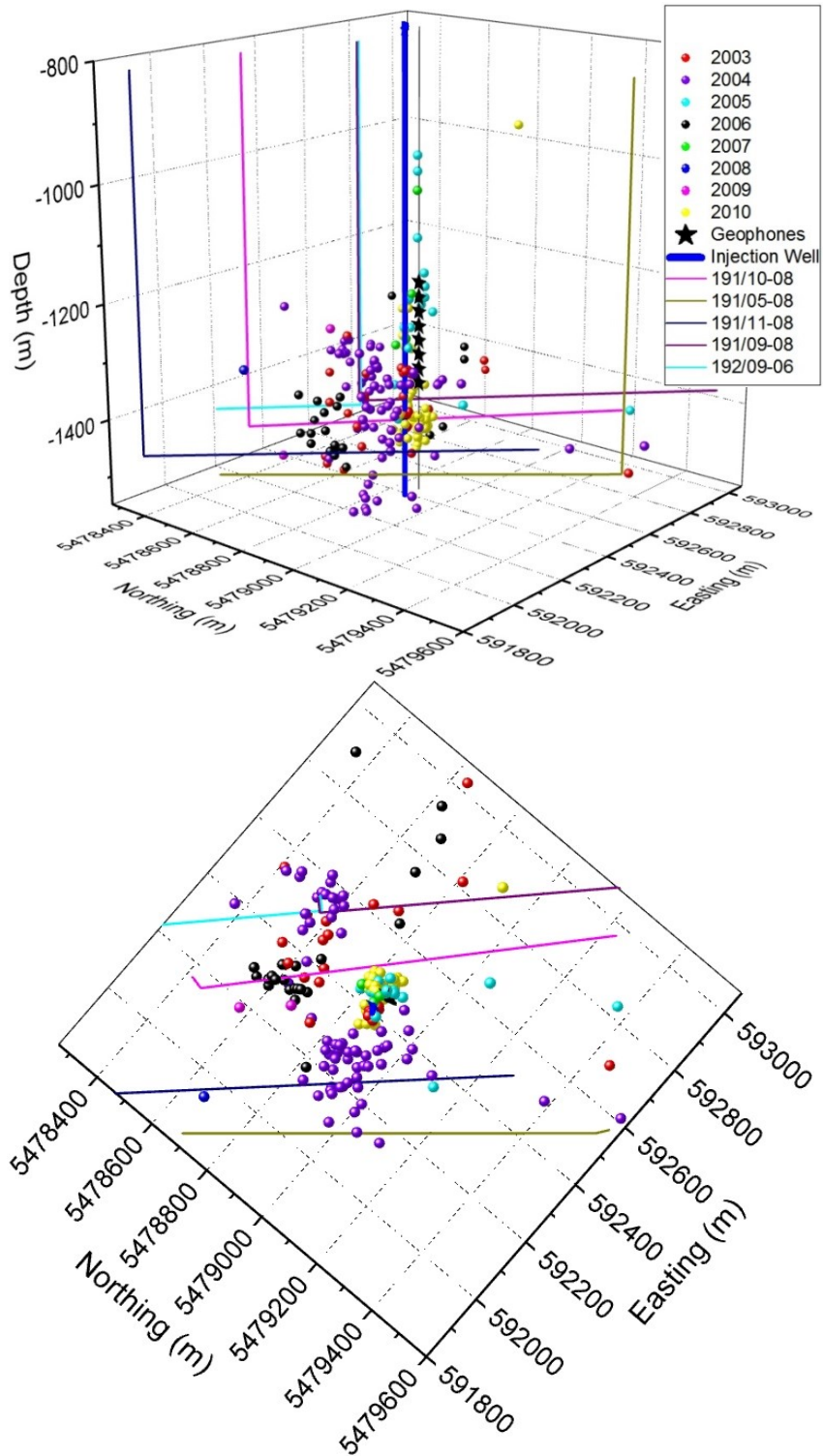


Figure 5.9: Microseismic events located in Weyburn during 7 years of monitoring. The color coding is based on the time of occurrence (data plotted after (“ESG Weyburn Microseismic Progress Report,” 2011)). Two events on February 27<sup>th</sup> of 2004 and one event in September 24<sup>th</sup> of 2007 are not shown since they were far away from this area.

## 5.6 Numerical Modeling

In order to investigate the evolution of stress field due to changes in reservoir pore pressures and its implication on tensile and shear failure, a one-way coupling between the reservoir simulator, GEM (CMG, 2006) and geomechanical simulator, FLAC3D (Itasca, 2010) is conducted in this chapter. Therefore, first a summary of the theory of poroelasticity and stress transfer in a caprock-reservoir system is presented. Then, the reservoir model is introduced followed by the construction of the geomechanical model. Finally, the methodology for coupling is explained and the results are discussed.

### 5.6.1 Caprock-Reservoir Stress Transfer in a CO<sub>2</sub> Injection Scenario

It has been observed that a change in pore pressures within the reservoir can actually cause a local change in in situ stress field due to poroelastic effects (Hillis, 2001; Teufel et al., 1991). In this chapter, the in situ stresses prior to a change in pore pressures (i.e. prior to injection) are referred to as “initial stresses”.

In general, injection of CO<sub>2</sub> into the reservoir can be regarded as putting excess energy into the caprock-reservoir system, which is already in the state of equilibrium. Therefore, in order to dissipate this excess energy, as injection begins and pore fluid pressures increase within the reservoir, the reservoir tends to expand (Figure 5.10). This reduces the effective stresses within the reservoir but also results in an increase in total stresses around the reservoir.

Theoretically, since the vertical direction is bound by the ground surface, which is free to move, there will be no change in the vertical stress field (i.e.  $\Delta\sigma_v=0$ ). However, in practice, there may be some increase in the vertical stress due to stress arching above the reservoir that may lead to reactivation of normal faults. In case that the width to height ratio of the reservoir is large and or the overburden is relatively compliant, the amount of this increase can be very small (Kaldi et al., 2011).

With regard to horizontal stresses, since the lateral expansion of the reservoir is constrained, there has to be a counterbalancing increase in total horizontal stresses within the lateral boundaries of the reservoir (Figure 5.10) that results in stabilizing the faults in this region.

However, in order for the whole system of caprock-reservoir to regain equilibrium, this increase has to be counterbalanced above and below the reservoir by a reduction in horizontal stresses (Figure 5.10). This reduction is in favor of fracturing and reactivation of faults in the seal layers and has to be studied in caprock integrity analyses. The change in horizontal stress can be estimated using the theory of poroelasticity as shown in Equation (5.2) (Engelder & Fischer, 1994):

$$\Delta\sigma_h = \frac{\nu_s}{1-\nu_s} \Delta\sigma_v + \left(1 - \frac{\nu_s}{1-\nu_s}\right) \alpha_s \Delta P \quad (5.2)$$

The ratio of  $\Delta\sigma_h/\Delta P$  for an increase in pore pressure is reported to be about 0.7 in field data (Engelder & Fischer, 1994; Teufel et al., 1991).

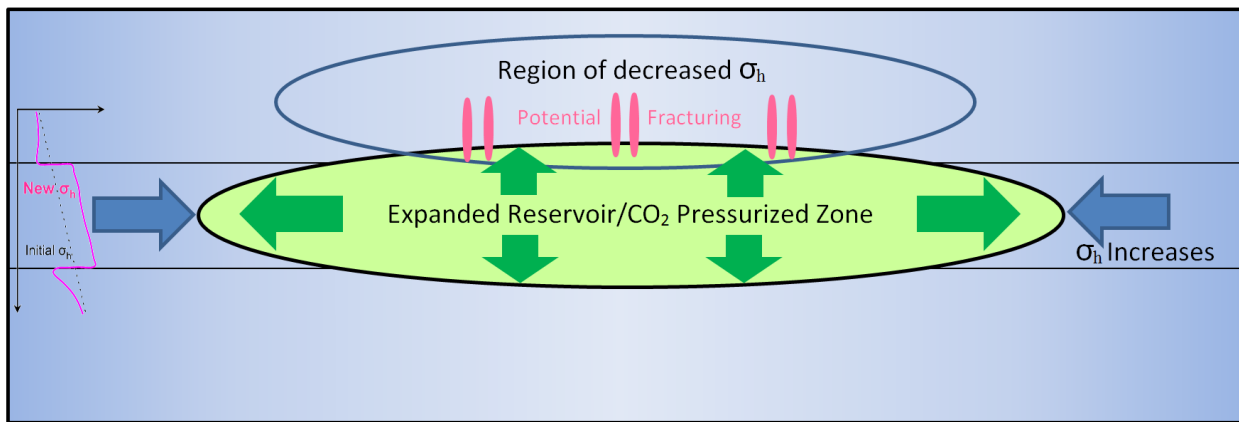


Figure 5.10: Schematic representation of stress transfer in a caprock-reservoir system. The regions of decreased minimum stress are shown with light blue (modified from (Kaldi et al., 2011) after (Marsden, 2007))

## 5.6.2 Reservoir Model (GEM)

Using the reservoir compositional simulator, GEM, (Jafari et al., 2011) modeled the Phase IB of the Weyburn project. The model includes all the four patterns of Phase IB (roughly 4 km sides) as well as small portions of Phase IA, IC and ID (Figure 5.11). The average thickness of the reservoir in the GEM model is 26 m. In their model, the horizontal resolution (i.e.  $77 \times 78$  zones) of the geological model was kept the same but the 113 layers were upscaled to eight layers based on the flow units of the pool. These eight layers include four units in the Vuggy zone (i.e. V1, V2, V3 and V6) and two units in the Marly zone (i.e. M1 and M3). The other two layers on top

and bottom include a combination of M0 and Three Fingers units (referred to as M03F in this research) and a combination of Frobisher Evaporite and Upper Frobisher Marly units (referred to as FEUFM in this research), respectively. These two layers act as primary seals for the reservoir and have no-flow boundary conditions in the GEM model. Since relative permeability tables and hydrocarbon PVT (pressure, volume, temperature) data were not available for the Phase IB, they used these data from adjacent patterns in Phase IA and did the history matching from 1956 until 2010. Also, GEM is an isothermal simulator and thus, the reservoir temperature was set constant to 63°C.

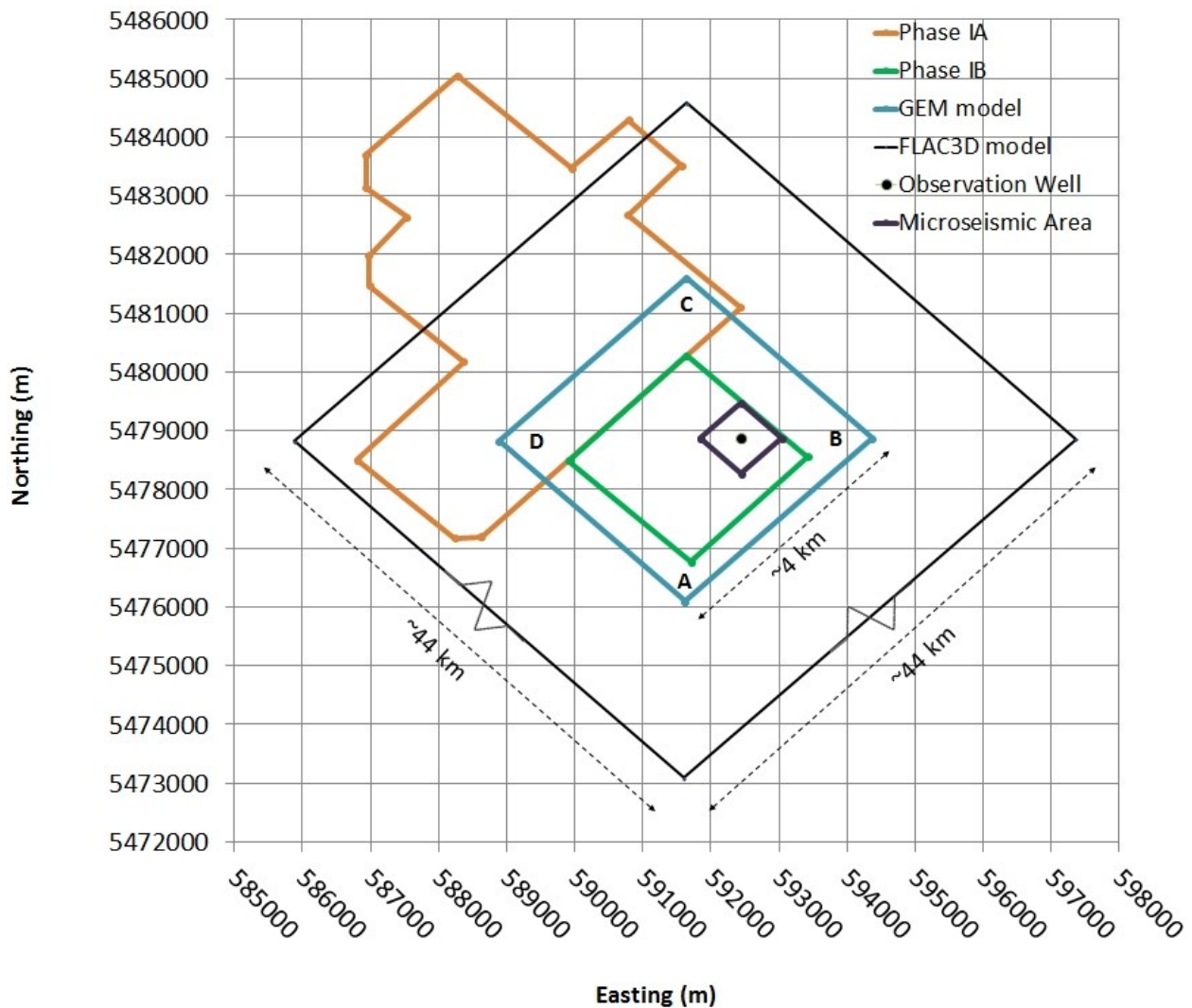


Figure 5.11: Phases IA and IB as well as the area modeled by GEM ( $\Delta ABCD$ ). The area modeled by FLAC3D includes the reservoir section similar to the GEM model plus 20 km sideburden at each side. The boundaries of the FLAC3D model are not to scale in this figure.

In order to validate the history matching results, they compared some of the history-matched well pressures with measured in-situ values. Figure 5.12 shows the GEM model as well as the location of wells where this comparison has been performed.

As was illustrated in Figure 5.9, since the MS events have been located about 420 m radially around the observation well and the only well in this vicinity is the horizontal well, 194090600613W2, only the comparison between the history-matched pressures and measured in-situ pressure for this well is shown here (Figure 5.13). The results showed an overall agreement between the results of numerical modeling and the values measured in-situ before 2001. After 2001, the pressures were over-estimated by the model. However, since in order to maintain the miscibility of injected CO<sub>2</sub>, an operational pressure of 18 MPa would have been required, the reported in situ measurement may not be accurate (Jafari et al., 2011).

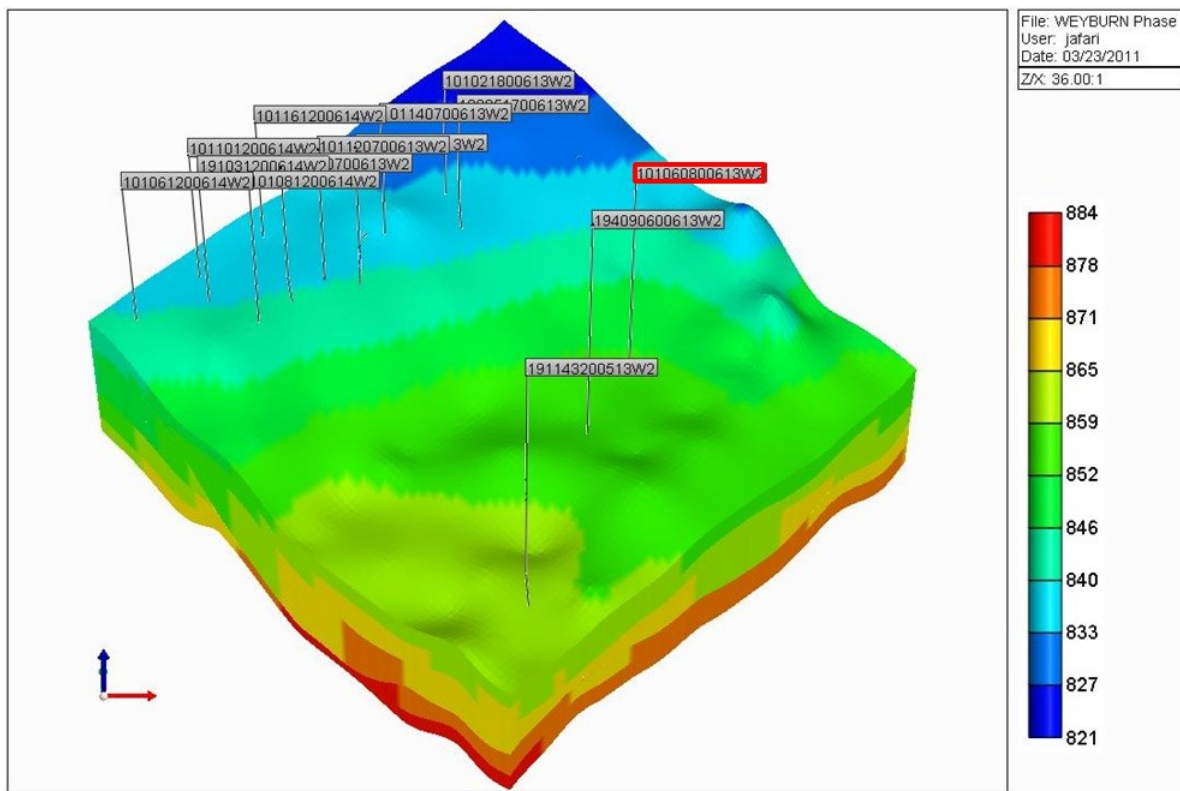


Figure 5.12: Location of the wells for which the in-situ pressure has been measured (the microseismic observation well is marked by red). The color coding is based on the “Grid Top” elevation below mean sea level (Jafari et al., 2011)

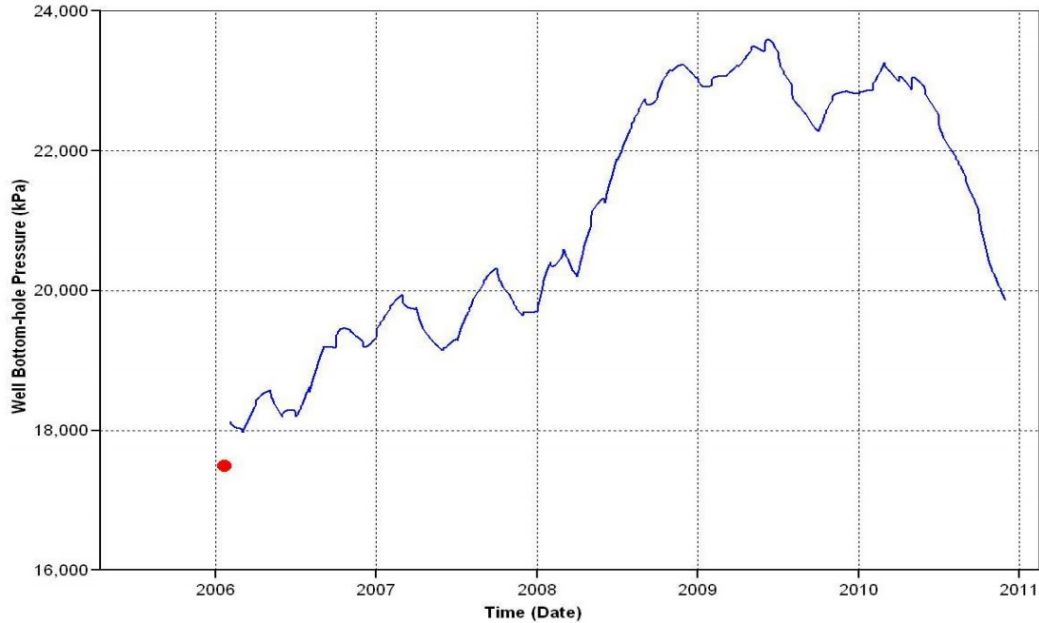


Figure 5.13: Comparison between the measured (red dot) and simulated pressures (blue line) for the well 194090600613W2 (Jafari et al., 2011)

### 5.6.3 Geomechanical Model (FLAC3D)

In this research, FLAC3D (Fast Lagrangian Analysis of Continua) is used to build the geomechanical model from the reservoir model. FLAC3D is an explicit finite difference code developed by Itasca Inc. In this code, the material is meshed into polyhedral zones of different shapes (ex., brick, wedge, pyramid and tetrahedral-shaped zones). Various constitutive models such as Mohr-Coulomb, Cam Clay etc. could be prescribed to the zones based on which their mechanical response to applied stresses is calculated.

As the first step, a FLAC3D model with the same horizontal resolution as the GEM model (i.e.  $77 \times 78$  zones approximately  $50 \text{ m} \times 50 \text{ m}$  each) is built. The model is then extended from -2300 m to +560 m to account for underburden and overburden layers. Also, the model is extended  $\sim 20$  km at each side to account for the laterally infinite boundary conditions (Figure 5.11 and Figure 5.14).

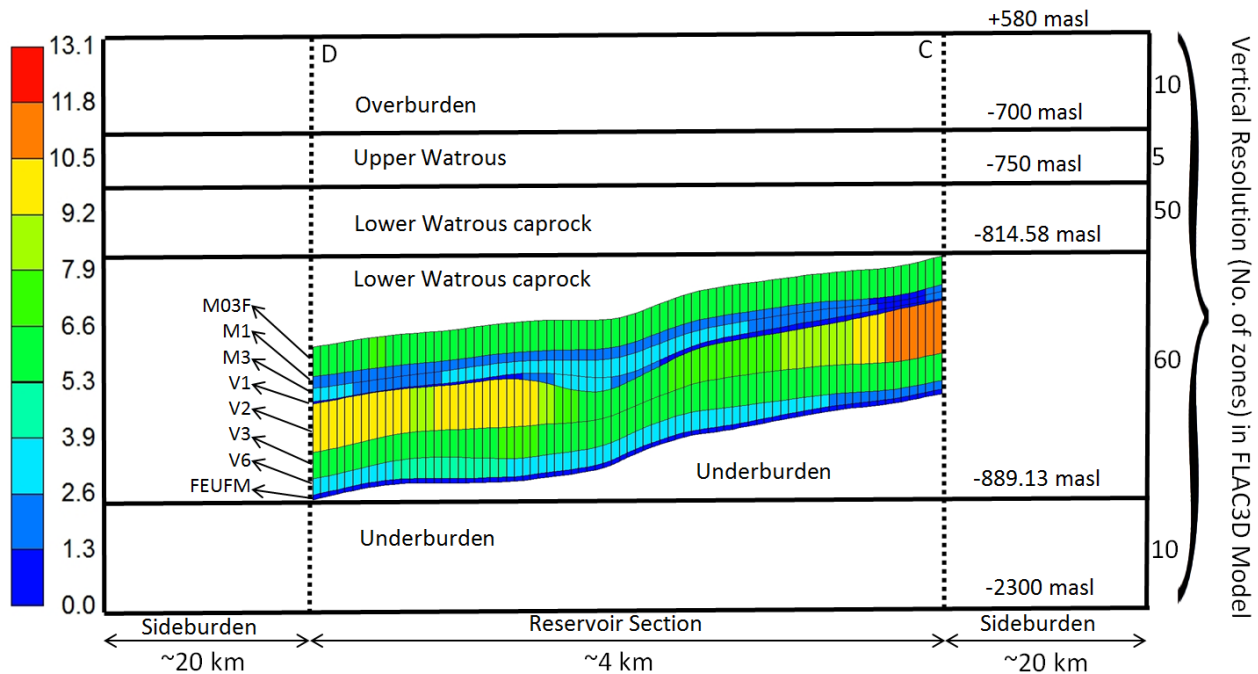


Figure 5.14: A 2D vertical cross section of the GEM model (CD side in Figure 5.11) as well as elevations of the layers added to the FLAC3D model. The reservoir and primary seal layers are color coded based on their thickness in meters (figure is not to scale).

In order to do a proper reservoir-geomechanical coupling, it is necessary to replicate the stratigraphy of the reservoir layers in FLAC3D. For this purpose, first the grid coordinates of the GEM model are exported with “Eclipse COORD format” (Schlumberger, 2010). Then, the exported file containing nine horizons (eight layers) is imported to Petrel as a “model” with “ECLIPSE keywords”. The horizon nodes are then converted to “points” in Petrel and exported as nine separate files with “Irap classic points” format (This format provides x, y and z coordinates for all the zones making a layer). An algorithm is developed to read these horizon files, one by one, into FLAC3D. Having the zones’ coordinates read, the zones of each reservoir layer are distinguished by being assigned the same “group name” in FLAC3D model. As schematically shown in Figure 5.15, a higher vertical resolution results in better replication of stratigraphy. Therefore, the reservoir section has to be fine enough otherwise some pinch-outs or even layers will be lost. Therefore, a finer resolution is considered for elevations containing the reservoir zones (Figure 5.14).

Once the overall geometry is built and the stratigraphy of reservoir layers is replicated (Figure 5.16), the bottom of the model and its four sides are fixed in normal directions as boundary conditions. The top of the model is free to move. In order to apply the in-situ stresses,

based on Figure 5.1, the maximum and minimum horizontal stresses are considered to be along NE-SW and NW-SE, respectively. Therefore, the elastic constitutive model is assigned to all the zones, in-situ stress gradients are applied based on Equation (5.1) and the model is solved to mechanical equilibrium (Figure 5.17). The stresses at this stage are referred to as “initial stresses” in this chapter.

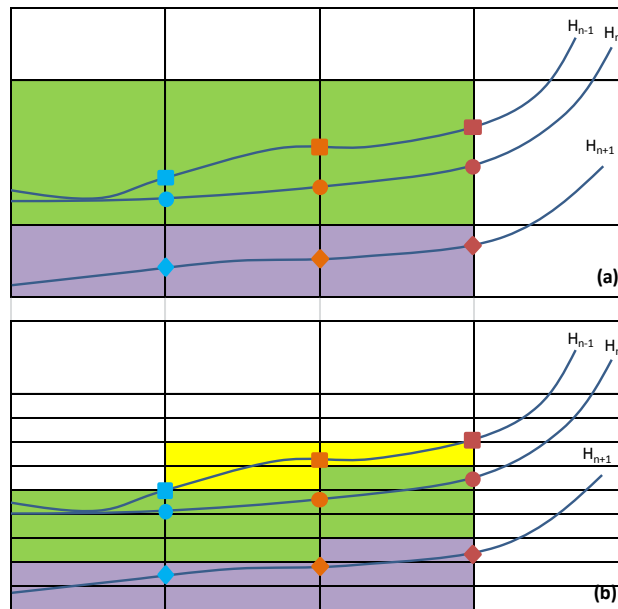


Figure 5.15: A schematic illustration of how refining the zones contributes to better replication of stratigraphy. Three reservoir layers (purple, green and yellow) separated by three horizons ( $H_{n-1}$ ,  $H_n$  and  $H_{n+1}$ ) are shown. The zones with centers bound between two horizons are assigned the same “group name”. However, in figure 8(a), the layer bound between  $H_{n-1}$  and  $H_n$  cannot be identified due to low resolution.

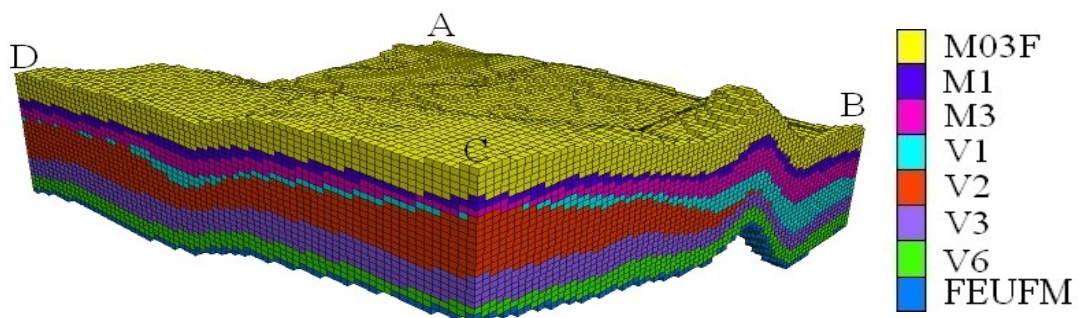


Figure 5.16: Zoomed reservoir section in FLAC3D.

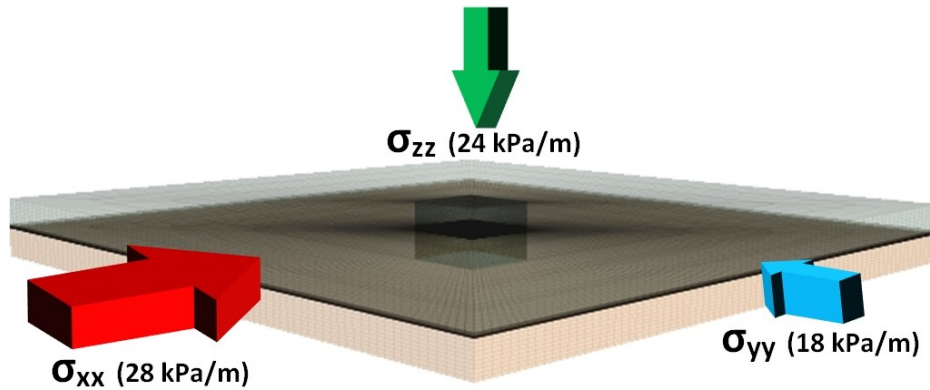


Figure 5.17: The entire FLAC3D model as well as the orientation and in-situ stress gradients as reported by (Gomez, 2006)

Finally, displacements and velocities are set to zero and Mohr-Coulomb model with properties listed in Table 5.2 and Table 5.3 is assigned to all the zones. At this stage the model is ready for the coupling.

Table 5.2: Properties used in the geomechanical model (Gomez, 2006; Verdon, 2010)

Name	Average Thickness (m)	E (GPa)	$\nu$	$\rho$ (kg/m <sup>3</sup> )	$\phi$ (°)	$c'$ (MPa)	Tensile Strength (MPa)
Overburden	1280	5	0.25	2500	44	18.15	1
Watrous	114	14	0.23	2000	44	18.15	1
M03F	40	24	0.34	2700	44.4	18.15	5
M1		14.5	0.31	2200	40	3.5	3
M3		14.5	0.31	2200	40	3.5	3
V1		14.5	0.31	2200	46.8	3.5	3
V2		14.5	0.31	2200	46.8	3.5	3
V3		14.5	0.31	2200	46.8	3.5	3
V6		14.5	0.31	2200	46.8	3.5	3
FEUFM		24	0.34	2700	44.4	18.15	5
Underburden	1410	20	0.25	2500	45	18	1

Table 5.3: Sideburden properties in the geomechanical model. The properties are chosen equal to the zones with the same elevation in the reservoir section

Elevation (masl)	E (GPa)	$\nu$	$\rho$ (kg/m <sup>3</sup> )	$\phi$ (°)	$c'$ (MPa)	Tensile Strength (MPa)
From -700 to +580	5	0.25	2500	44	18.15	1
From -814.58 to -700	14	0.23	2000	44	18.15	1
From -889.13 to -814.58	14.5	0.31	2200	40	3.5	3
From -2300 to -889.13	20	0.25	2500	45	18	1

#### 5.6.4 One-way Reservoir Geomechanical Coupling

The purpose of coupling applied in this research is to study the change in initial stresses as a result of a change in reservoir pore pressures. Therefore, only a one-way coupling between the GEM reservoir simulator and FLAC3D geomechanical simulator has been conducted.

For this purpose, the keyword, “zonebasedpp”, has been used that allows direct importing of zone based values to FLAC3D. This feature only takes into account the mechanical changes in the model due to “changes” in pore pressure in a zone(s). In order to extract the reservoir pressures in a format readable by FLAC3D, the RESCUE (REServoir Characterization Using Epicentre) (CMG, 2006) version of GEM model is imported into Petrel. Using Petrel (Schlumberger, 2010), the zone pressures as well as their cell index (I, J and K) and center coordinates (X, Y and Z) are exported with GSLib format (Deutsch & Journel, 1998) at 56 GEM timesteps listed in Table 5.4. According to Figure 5.2, except for a ten year period from 1960 to 1970, the pressures in Weyburn prior to injection of CO<sub>2</sub> were almost always close to the hydrostatic values (i.e. ~14 MPa). Therefore, the modeling in this chapter is started from the year 2000. The exported pressures are then read into FLAC3D by an algorithm and each zone pore pressure is assigned to its corresponding zone in the geomechanical model. As an example, Figure 5.18, Figure 5.19 and Figure 5.20 show the pressures at one timestep (Jan 1<sup>st</sup>, 2003) for reservoir layers in FLAC3D and GEM models. The little discrepancy in pressures in these figures is because of the minor difference in color scale divisions. Also, the small discrepancy in the stratigraphy is because of the resolution in FLAC3D model for identifying the layers as explained before. Also, since the vertical resolution of reservoir zones in FLAC3D model is greater than that of the GEM model (Figure 5.14), using an algorithm, a uniform gradient is applied to the pore pressures of FLAC3D zones of each reservoir layer along the height of the model (ex. Figure 5.21).

Therefore, after the pore pressures for the first FLAC3D timestep (i.e. Jan 1<sup>st</sup>, 2000 and then Feb 1<sup>st</sup>, 2000) are applied, the model is cycled to equilibrium. Then, the pressures for the second timestep (May 1<sup>st</sup>, 2000) are applied and the model is cycled to equilibrium again and so on. The new stresses are calculated by FLAC3D based on Equation (5.3):

$$\sigma_{ii} = \sigma_{ii} - \alpha_s \times \Delta P - \beta \times \Delta T \quad (5.3)$$

where  $\alpha_s$  is the Biot coefficient,  $\Delta P$  and  $\Delta T$  are changes in zone pore pressure and temperature, respectively, and  $\beta$  is equal to three times the coefficient of linear thermal expansion times the bulk modulus of the zone. In this study, no temperature drop is taken into account (i.e.  $\Delta T = 0$ ). Also, the Biot coefficient is taken equal to one which seems to be a reasonable assumption for most reservoir rocks (Lorenz et al., 1991; Moghadam & Chalaturnyk, 2015).

Table 5.4: GEM and FLAC3D timesteps. Each timestep in FLAC3D includes cycling the model to equilibrium after pressures of two consecutive GEM timesteps are applied to the model. The average pore pressures (PP) are calculated based on pore pressures of all the 33316 reservoir zones in the GEM model.

No.	GEM Timestep	Avg. PP (MPa)	No.	GEM Timestep	Avg. PP (MPa)
0	1-Jan-00	14.30	28	1-Feb-06	19.23
1	1-Feb-00	14.07	29	1-May-06	19.36
2	1-May-00	13.81	30	1-Jul-06	19.04
3	1-Jul-00	13.53	31	1-Sep-06	19.14
4	1-Oct-00	13.32	32	1-Nov-06	18.89
5	1-Jan-01	13.33	33	1-Jan-07	19.23
6	1-Mar-01	13.46	34	1-Apr-07	19.30
7	1-Apr-01	13.75	35	3-Jul-07	19.93
8	1-Oct-01	15.32	36	1-Aug-07	19.98
9	1-Jan-02	15.22	37	1-Dec-07	20.75
10	1-Feb-02	15.24	38	1-Feb-08	20.57
11	1-Jun-02	15.54	39	1-Jun-08	21.61
12	1-Oct-02	14.31	40	1-Aug-08	22.41
13	19-Nov-02	14.70	41	1-Oct-08	22.77
14	1-Jan-03	15.15	42	1-Jan-09	22.45
15	1-Apr-03	15.68	43	1-Mar-09	22.49
16	1-Jul-03	16.12	44	1-May-09	22.99
17	1-Nov-03	15.72	45	1-Jul-09	22.62
18	1-Jan-04	15.71	46	1-Sep-09	22.64
19	1-Jun-04	16.22	47	1-Nov-09	23.17
20	1-Sep-04	16.04	48	1-Feb-10	23.42
21	1-Dec-04	16.87	49	1-Apr-10	23.74
22	22-Jan-05	17.04	50	2-Sep-10	21.78
23	1-Feb-05	17.07	51	13-Sep-10	21.63
24	29-May-05	18.08	52	26-Sep-10	21.45
25	1-Jun-05	18.10	53	30-Sep-10	21.39
26	1-Sep-05	18.98	54	1-Oct-10	21.38
27	3-Nov-05	19.84	55	1-Dec-10	20.58

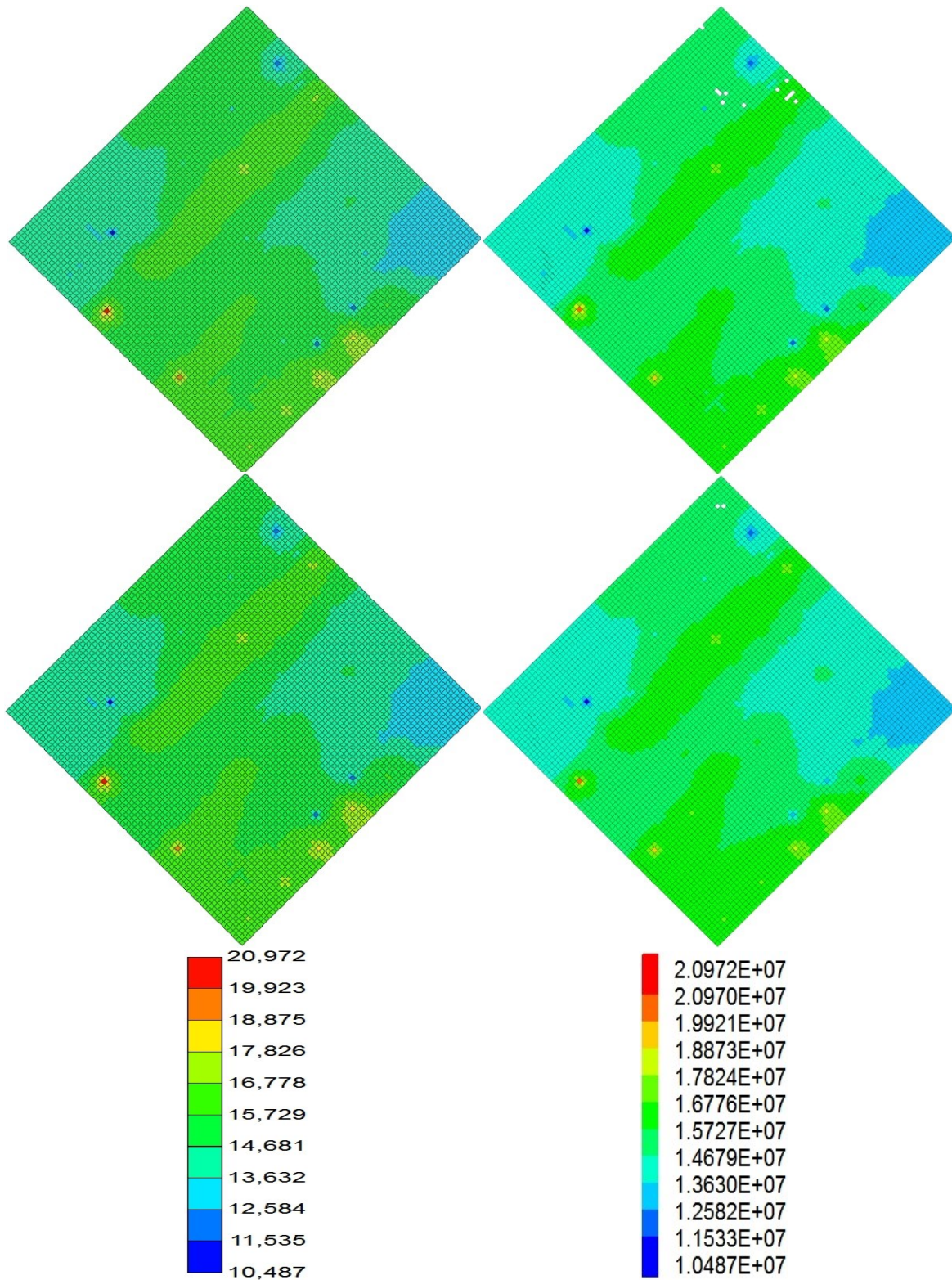


Figure 5.18: Reservoir pressures of the M1 layer (Top) and M3 layer (Bottom) in July 1<sup>st</sup>, 2003 imported from GEM (Left) to FLAC3D (Right). This cross section corresponds to ( $\Delta$ ABCD) in Figure 5.11. The GEM and FLAC3D pore pressures in the legend are in kPa and Pa, respectively.

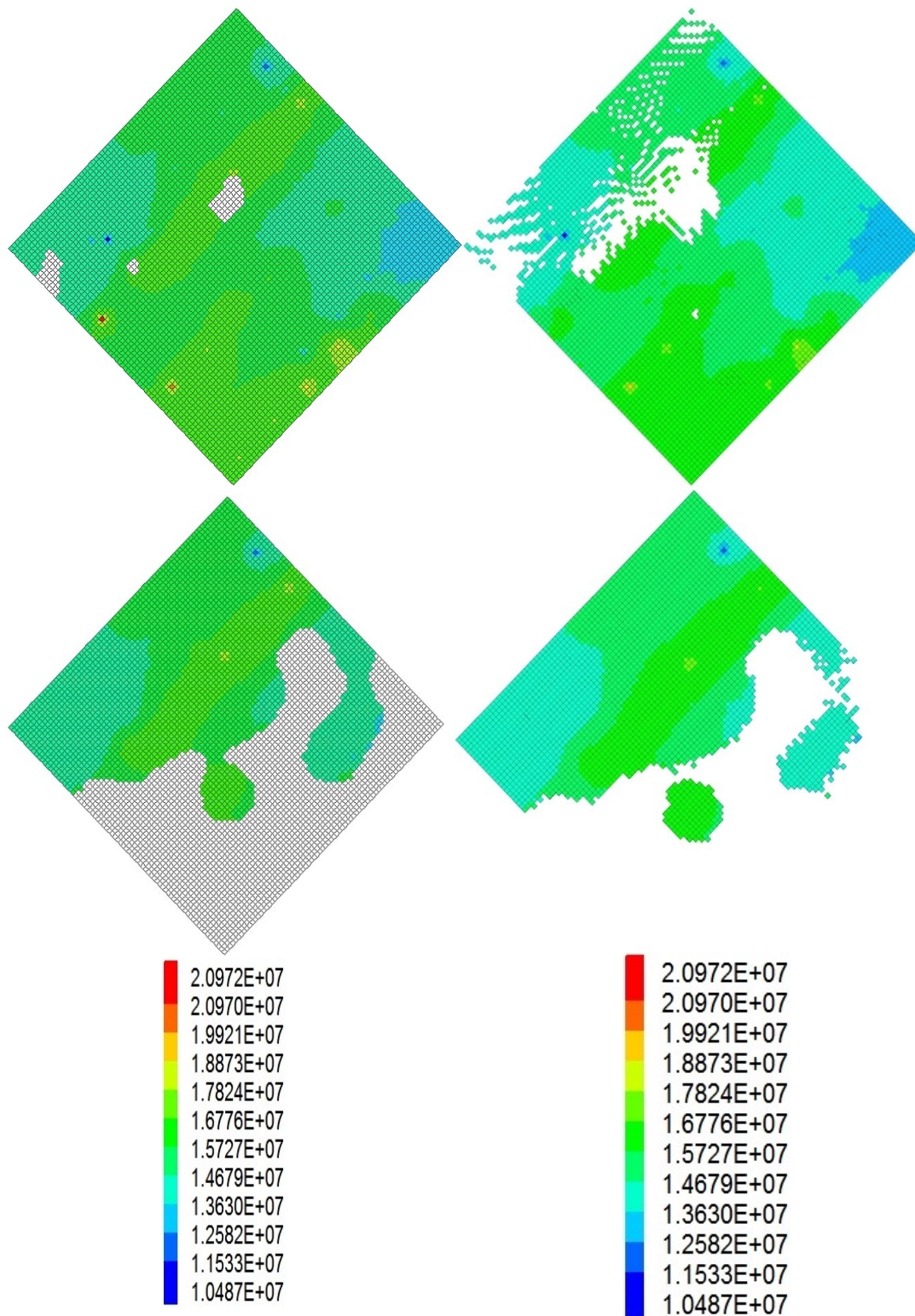


Figure 5.19: Reservoir pressures of the V1 layer (Top) and V2 layer (Bottom) in July 1<sup>st</sup>, 2003 imported from GEM (Left) to FLAC3D (Right). This cross section corresponds to ( $\Delta ABCD$ ) in Figure 5.11. The blank zones in the GEM layers are due to stratigraphy and pinch-outs. The GEM and FLAC3D pore pressures in the legend are in kPa and Pa, respectively.

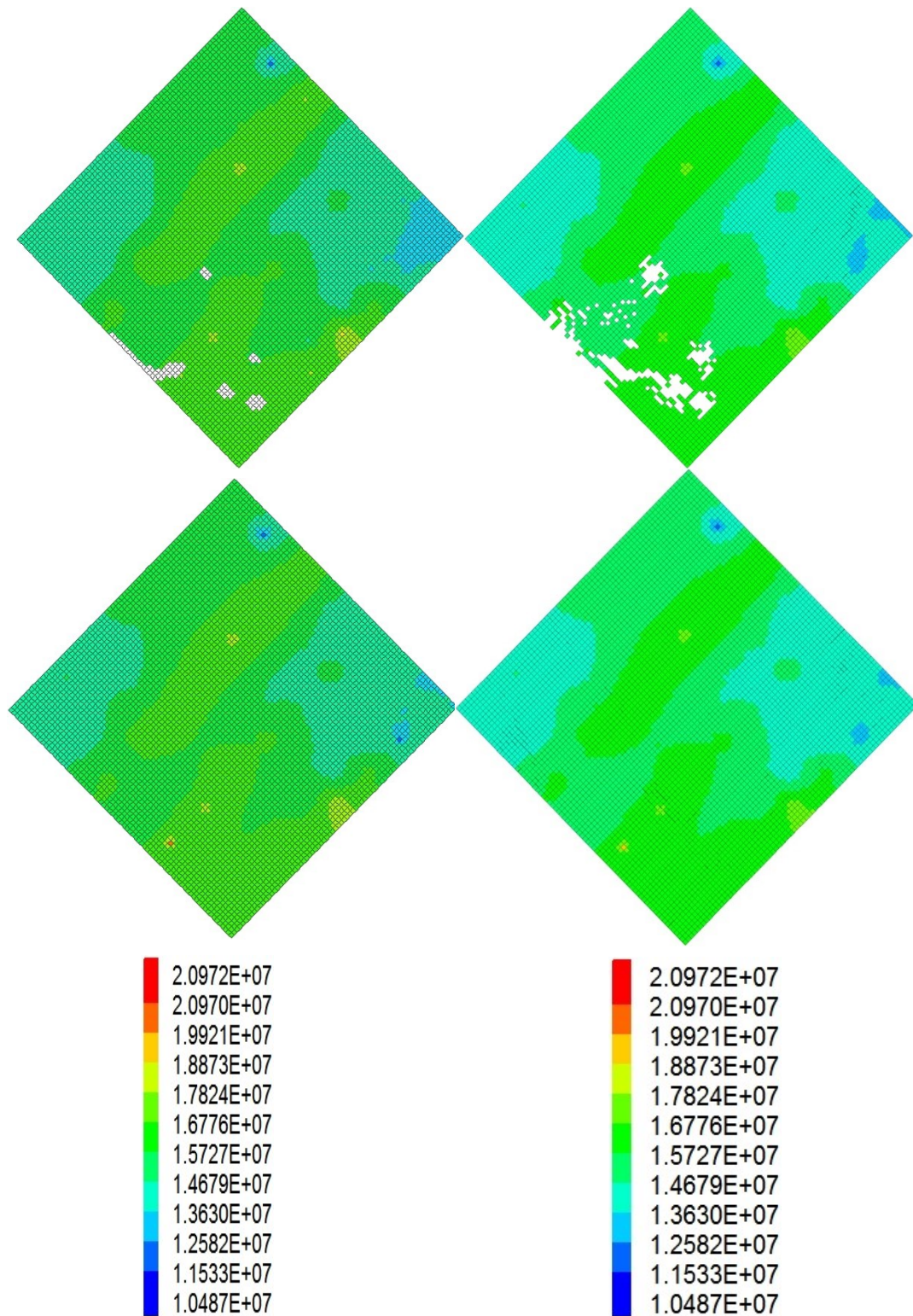


Figure 5.20: Reservoir pressures of the V3 layer (Top) and V6 layer (Bottom) in July 1<sup>st</sup>, 2003 imported from GEM (Left) to FLAC3D (Right). This cross section corresponds to ( $\Delta ABCD$ ) in Figure 5.11. The blank zones in the GEM layers are due to stratigraphy and pinch-outs. The GEM and FLAC3D pore pressures in the legend are in kPa and Pa, respectively.

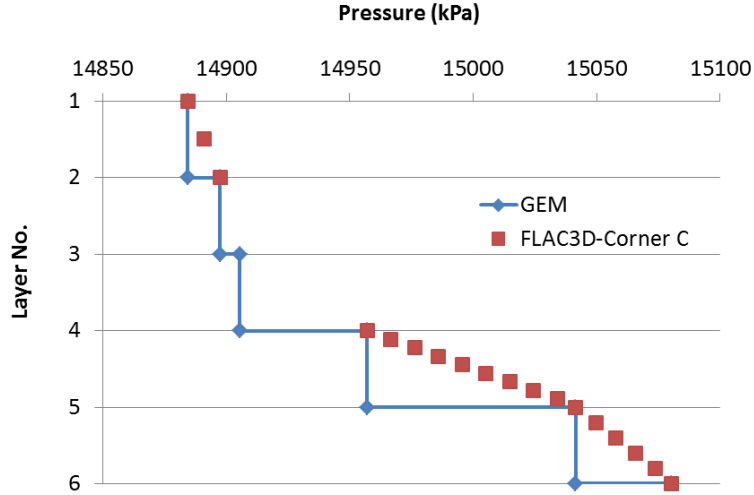


Figure 5.21: An example of pressure distribution along the height of the reservoir layers at corner C shown in Figure 5.16. The layers 1, 2, 3, 4, 5 and 6 represent M1, M3, V1, V2, V3 and V6, respectively.

### 5.6.5 Results

As previously explained, the numerical feature used in this research only takes into account the mechanical effect of a change in pore pressure on the zone(s). In other words, it is implicitly assumed that the caprock is fully sealed. However, the real reservoir pore pressures are available for all the reservoir zones including those in the top layer of reservoir, M1. Therefore, the pore pressures of M1 zones are used as the base of comparison to see whether or not they have been large enough to cause tensile or shear failure in the seal zones of M03F layer right above them.

For this purpose, two conservative criteria for the onset of tensile and shear failure are considered in present study. For tensile failure, it is assumed that if the pore pressure of a M1 zone reaches its critical value, which is equal to the minimum principal stress of the zone above it in the M03F layer, tensile failure may occur as shown in Equation (5.4):

$$p_{fc} = \sigma_3 \quad (5.4)$$

where  $\sigma_3$  is the minimum principal stress in the seal layer, M03F, and  $p_{fc}$  is the critical pore pressure for the onset of fracturing in the top layer of reservoir, M1. This assumption is similar to the one used by (Rutqvist et al., 2008) and includes studying both the likelihood of tensile opening of new fractures as well as tensile reactivation of preexisting ones.

In order to study the likelihood of shear failure along preexisting weak planes, the Mohr-Coulomb criterion is used as following:

$$|\tau_{m2}| = (\sigma_{m2} - p_{sc}) \sin \phi + c \cos \phi \quad (5.5)$$

where  $c$ ,  $\phi$  and  $p_{sc}$  are the cohesion, internal friction angle and critical pore pressure for the onset of shear failure, respectively. Also,  $\tau_{m2}$  and  $\sigma_{m2}$  are the maximum shear stress and mean principal stress, respectively, calculated as:

$$\begin{aligned} \tau_{m2} &= \frac{1}{2}(\sigma_1 - \sigma_3) \\ \sigma_{m2} &= \frac{1}{2}(\sigma_1 + \sigma_3) \end{aligned} \quad (5.6)$$

where  $\sigma_3$  and  $\sigma_1$  are the minimum and maximum principal stresses, respectively. Using this criterion implies the conservative assumption that a weak plane can exist anywhere with an arbitrary orientation (Rutqvist et al., 2008). Assuming zero cohesion for the weak plane as the worst case scenario,  $p_{sc}$  can be written as:

$$p_{sc} = \sigma_{m2} - \frac{\tau_{m2}}{\tan \phi} \quad (5.7)$$

Also, considering the typical range of 25-35° for friction angle (Goodman, 1989), an average  $\phi=30^\circ$  is assumed in this study. In order to illustrate the results, two pressure margin ratios for fracturing,  $p_{fmr}$ , and shearing,  $p_{smr}$ , will be used as defined by Equation (5.8):

$$\begin{aligned} p_{fmr} &= p / p_{fc} \\ p_{smr} &= p / p_{sc} \end{aligned} \quad (5.8)$$

where  $p$  is pore pressure of each zone in M1 layer and  $p_{fc}$  and  $p_{sc}$  are calculated based on the new stresses in the seal zones, M03F, after injection. These ratios should be smaller than one to prevent failure. Using these ratios allows comparing the likelihood of tensile and shear failure in different regions across the caprock as shown in Figure 5.22. Since there have been many timesteps in the model, only the results for three timesteps are presented to demonstrate the applicability of the model. As can be observed in this figure, as the pressures have been

increased, the margin ratios are increased too which is as expected. Also, it can be observed that variations are really local depending on pore pressure distributions in that region.

Finally, in order to investigate the overall likelihood of tensile and shear failure, maximum failure margin ratio observed at each timestep is shown in Figure 5.23. The first timestep at which  $P_{fmr}$  exceeds one is the 38<sup>th</sup> Timestep. This corresponds to the average pore pressure of 20.57 MPa according to Table 5.4 which is slightly smaller than 23.3 MPa predicted by (Gomez, 2006) for the onset of hydrofracturing. It may not be clearly observable in Figure 5.22 due to color scale, but only a few zones have experienced a greater than one  $p_{fmr}$  at this timestep. This suggests the importance of using high resolution models for geomechanical analyses to identify the critical zones locally. According to Figure 5.15, in general, it seems that for the CO<sub>2</sub>-EOR period in Weyburn, the likelihood of shear failure along preexisting weak planes has been about 27% greater than the likelihood of tensile failure.

## 5.7 Discussion

From 2003 to 2010, microseismic monitoring was conducted in Weyburn with the purpose of testing its applicability for CCS projects (Verdon et al., 2011; Verdon, 2010). The challenge in microseismic data is to link them to geomechanics. There are two general mechanisms for microseismic events (i.e. crack-induced emissions within intact rocks and slip-induced emissions along weak planes). Weak planes can be preexisting or they may form as a result of propagation and coalescence of cracks. Either of these two (shearing or cracking/fracturing) would have a different implication in terms of hydraulic integrity. Cracks represent an enhancement in permeability due to crack surface development within intact rocks. Slips along weak planes represent an enhancement in permeability due to possible normal dilation of the two surfaces of the weak plane after shearing. Therefore, in order to comment on the hydraulic integrity of caprock by looking at microseismic observations, the first question would be what type of mechanism generated the events.

In Weyburn, since only one array of geophones was used, no source mechanism has been reported and the magnitudes were determined using the frequency spectra of arriving phases (Verdon, 2016). Therefore, in order to investigate the likelihood of tensile and shear failure

mechanisms that resulted in emission of microseismic energies, variations of  $p_{fmr}$  and  $p_{smr}$  in the M03F layer but only within the MS area along with the number of microseismic events are shown in Figure 5.24. According to Figure 5.14, -1430 m is taken as the average depth of M03F layer. Therefore, since margin ratios in Figure 5.24 are presented for this layer, only the number events recorded above -1430 m is shown in the Figure. Also, considering the temporal distribution of the events in Figure 5.24, the b-value plots are shown for four periods in Figure 5.25.

In Figure 5.24, it can be observed that from 2003 to 2004, both failure margin ratios were below one but there have been recorded microseismic events. It is noteworthy that there is uncertainty around the cause and reliability of the events in this period. Considering the operations, (Verdon, 2010) reports that some of these events are the result of calibration shots, drilling noise, and perforation shots. In a most recent paper, he refers to 68 events from 2003 to 2004 and a total of 207 events from 2003 to 2010 (Verdon, 2016). Regardless of the actual number of events, the trend in emergence of microseismic events in Weyburn as shown in Figure 5.8 is similar in our study and Verdon's research.

However, emergence of even a few MS events while both failure margin ratios are below one can be explained considering another study by (Khazaei et al., 2016). In that paper, a cubic discrete element model with a weak plane at its center was used to study the microseismic events recorded in Weyburn between September and November of 2010. It was shown that a weak plane could be emissive due to a small amount of loading even long before the failure of its surrounding was reached. It was also reported that for the conditions studied in that paper, slip-induced magnitudes ranged from -1 to -6 while crack-induced magnitudes ranged from -7 to -11. Therefore, considering the capability of geophones and the range of recorded magnitudes in Weyburn ( $-3.62 < M < -0.56$ ), it was suggested that the events recorded in Weyburn were more likely to be generated by stick-slips along weak planes. According to Figure 5.24, the first time that  $p_{smr}$  exceeds one is between September and November of 2005 when also the largest magnitudes (Figure 5.25) are observed. Considering the magnitudes, these events are presumably released due to some slip along a weak plane(s) that becomes relatively quiet afterward although the  $p_{smr}$  keeps going up. This can be explained considering the possibility of gradual "slow slip/aseismic deformations" along the weak plane due to continuous upward pressure applied to caprock as a result of injection

into the reservoir. One possible scenario for slow-slip deformations can be explained considering Figure 4.1 that shows the theory of slip. It was mentioned in Section 4.3 that there are healing mechanisms in nature that weld the two surfaces of a fault so that the friction drop due to slip will be restored in time. However, in Figure 4.1, once the excess energy is dissipated due to slip and the state of displacement is at point e, hypothetically, as a continuous upward pressure is applied to the caprock due to CO<sub>2</sub> injection, if there is not enough time for the two surfaces of the weak plane to be healed, and also further stress drops are not large enough to impose excess energy, there will be no seismic energy release while gradual displacements are still happening. More information on the importance and cause of slow slips can be found in (Rutqvist et al., 2015; Zoback et al., 2012).

The most emissive period in Weyburn is between September and November of 2010. The events in this final period are believed to be due to a pressure pulse as a result of recent shut down of a nearby injection well (Jafari et al., 2011).

With regard to preexisting weak planes, no major faults have been reported in the seal layers of Weyburn reservoir. However, studying the core samples and gamma ray logs of the Midale beds obtained from horizontal wells, (Bunge, 2001) reported the existence of small scale faults with less than 5 m throw in both NE-SW and NW-SE directions, parallel to maximum and minimum horizontal stresses. (Wilson & Monea, 2004) also report that no significant fractures have been observed in the lower Watrous unit except for microfractures (1-2 mm offset) that exist in muddier layers. In a later study, using seismic AVOA (amplitude variation with offset and azimuth) techniques, (Duxbury et al., 2012) observed anisotropy in the primary seal layers as well as Watrous formation parallel and normal to the direction of maximum horizontal stress. This observation was in agreement with previous research of (Bunge, 2001) and suggests the existence of discontinuities along these directions. According to Figure 5.24, although there is a period between 2008 and 2009 that  $p_{fmr}$  becomes slightly greater than one; it seems more likely for the recorded microseismic events to be generated by reactivation of such discontinuities as a result of stress transfer due to increase in reservoir pore pressures.

The importance of using continuum models such as the one presented in this study along with discrete element models that allow capturing the MS magnitudes and mechanisms as shown by (Khazaei et al., 2016) for interpretation of microseismic data in general, is whether or not lack of

microseismicity is a conclusive evidence for lack of deformation and or hydrofracture initiation in the caprock. In other words, we suggest that although the events recorded in a caprock may be more likely to be generated due to shearing along weak planes, lack of “recorded” microseismic data does not rule out the possibility of hydrofracture initiation and thus a change in the hydraulic integrity of caprock. The reason is that magnitudes of fracture induced events may be too small to be captured by geophones. Therefore, the likelihood of hydrofracture initiation/development in the caprock will still have to be investigated using other techniques such as numerical modeling. Obviously, lack of microseismic activity does not rule out the possibility of slow slip deformations either.

With regard to considering temperature in caprock integrity analyses, (Perkins & Gonzalez, 1985) suggest that temperature drop due to cold injection of CO<sub>2</sub> can result in a decrease in initial stresses. This decrease can be a problem if the subsequent increase in pore pressures reaches the minimum principal stress gradient. The research of (Gor et al., 2013) also shows that in the long term, thermal induced stresses may lead to tensile or shear failure of caprock. Therefore, injection of CO<sub>2</sub> at a temperature close to the ambient value can reduce the risk of fracturing. On the other hand, some other studies indicate that cold injection should not be feared (Vilarrasa & Laloui, 2016; Vilarrasa et al., 2014).

In order to realistically take into account the thermal effects in present study, it would have been necessary to have the temperature profile of the reservoir at each timestep so that a reasonable  $\Delta T$  could be used in Equation (5.3). Such data was not available since GEM is an isothermal simulator. However, in general, the reduction in in situ stresses including the minimum principal stress,  $\sigma_3$ , as a result of cold injection will cause a smaller critical fracture pressure and critical shear pressure, according to Equations (5.4) and (5.7), respectively. This, in turn, will result in greater failure margin ratios considering Equation (5.8). However, the failure would still depend on the actual amount of pore pressure change that varies from zone to zone across the reservoir and therefore, it needs to be studied in a high resolution model.

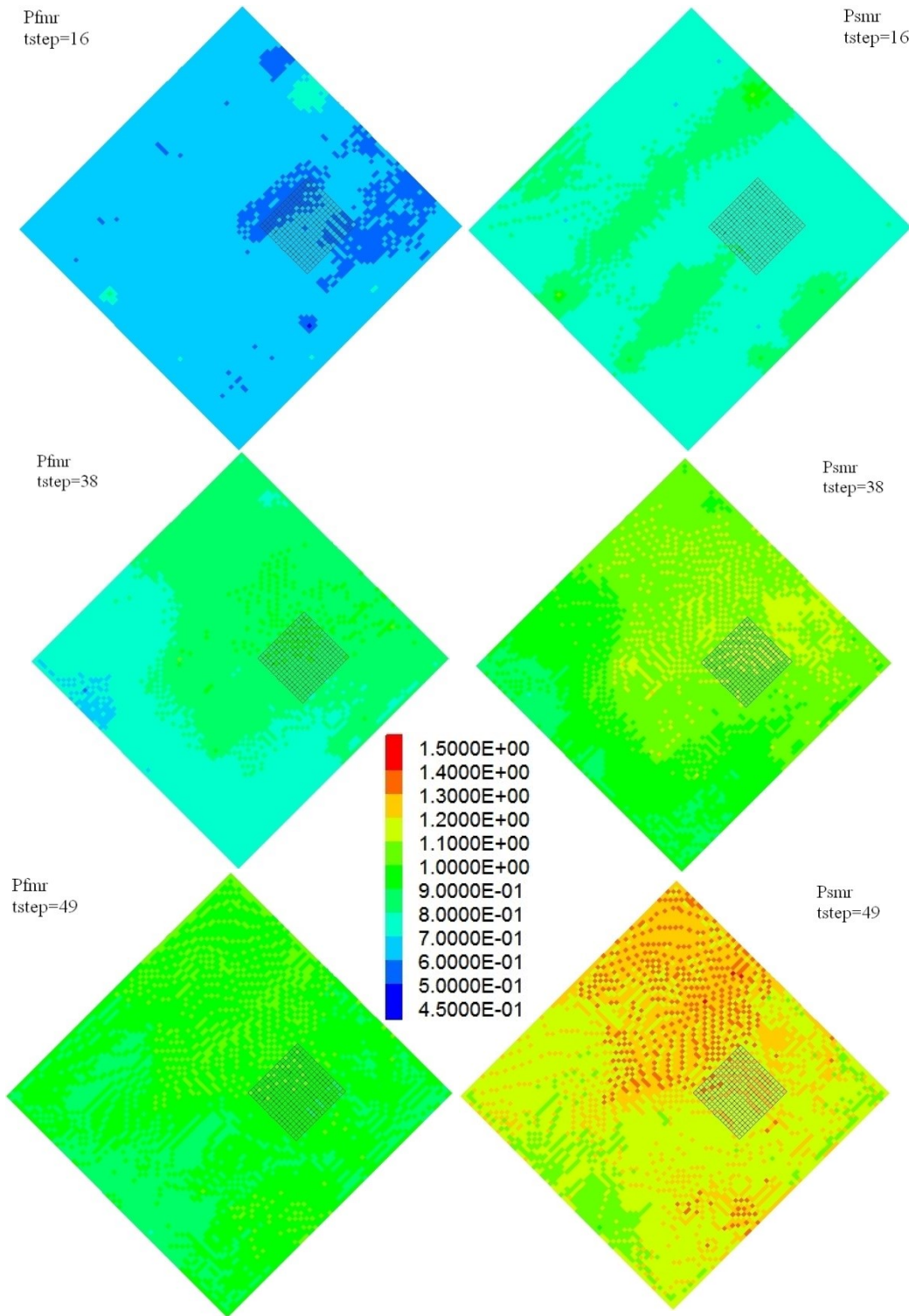


Figure 5.22: Contours of fracture margin ratio,  $P_{fmr}$ , and shear margin ratio,  $P_{smr}$ , for the M03F layer at nine timesteps. The MS area is shown with grid. The areas with values greater than one are prone to failure.

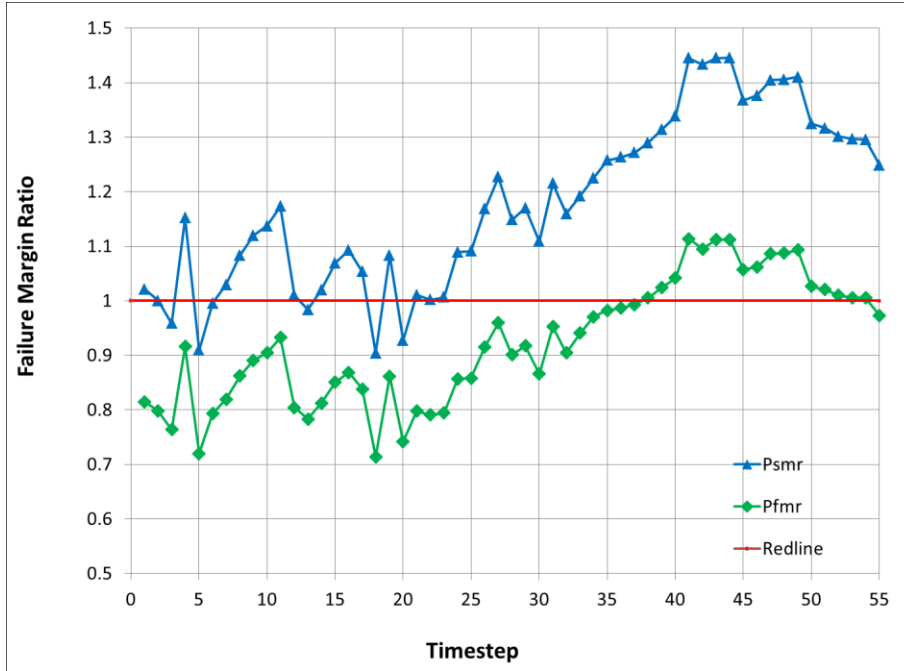


Figure 5.23: Maximum failure margin ratios (tensile and shear) observed in the entire M03F layer for the timesteps modeled in present study

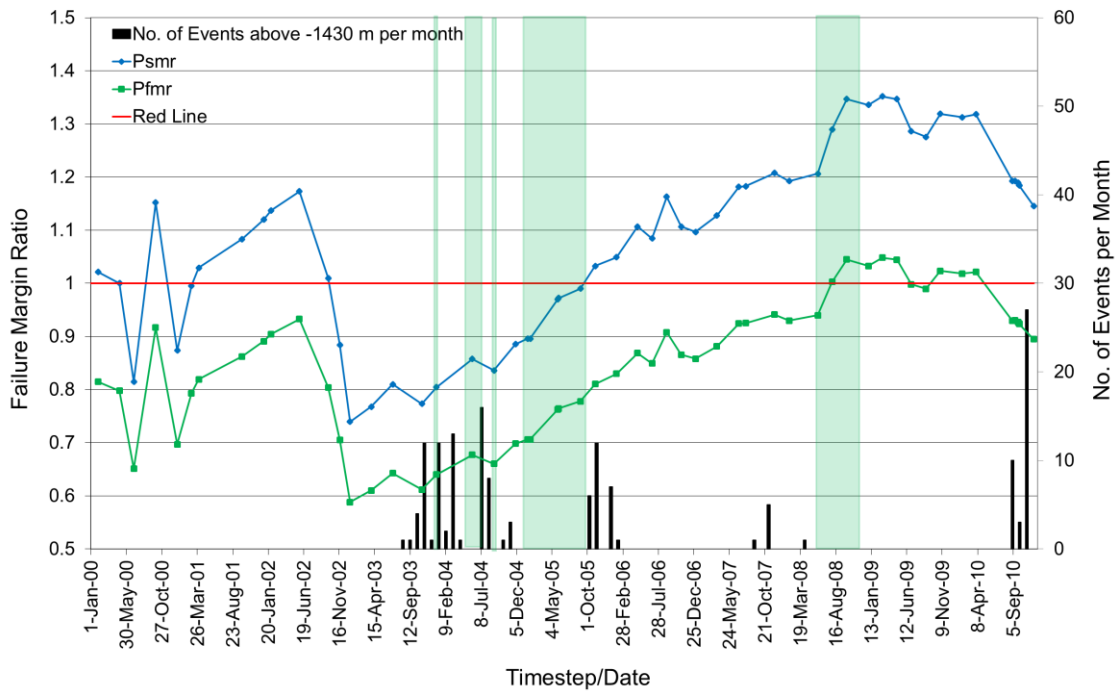


Figure 5.24: Maximum failure margin ratios (tensile and shear) observed only in the MS area within the M03F layer for the timesteps modeled in present study along with the number of microseismic events located above -1430 m. Periods of not recording are shown with green.

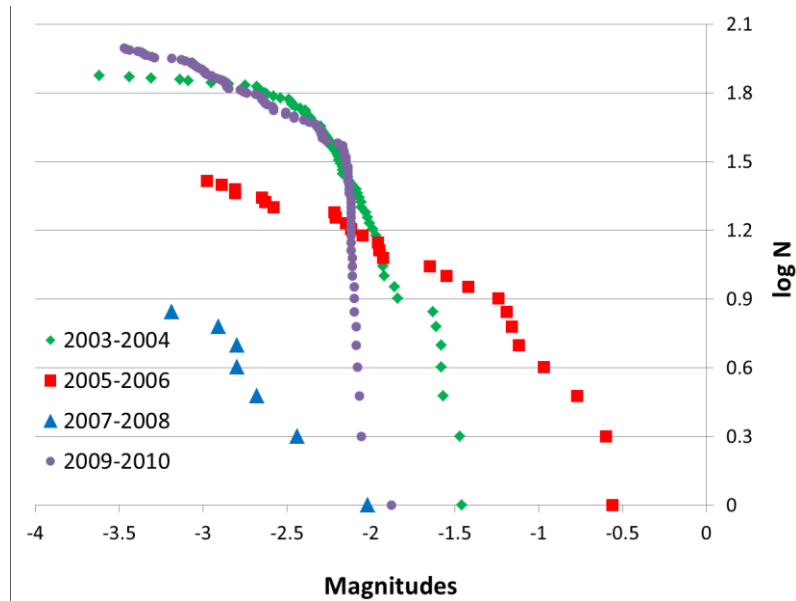


Figure 5.25: b-value plots at four periods in Weyburn. Each plot belongs to the events only recorded in that period above -1430 m. Data plotted after (“ESG Weyburn Microseismic Progress Report,” 2011)

## 5.8 Conclusion

In this paper, a one-way coupling between reservoir simulator, GEM, and geomechanical simulator, FLAC3D, was presented to study the effect of variations in pore pressures within the Weyburn reservoir on far field in situ stresses during the period of CO<sub>2</sub> injection from 2000 to 2010. A feature that allows direct importing of the reservoir zone pore pressures to FLAC3D was employed. This feature only takes into account the mechanical effect of a change in zone(s) pore pressure on the model. Therefore, it was assumed that the caprock is fully sealed and thus no initial leakage through the caprock was considered. The numerical details on how to build the geomechanical model by honoring stratigraphy and importing the real zone pressures rather than average pressures was also presented. In order to cover the entire period of CO<sub>2</sub> injection in Weyburn, 55 timesteps were considered. Using two conservative failure criteria, the likelihood of shear failure along preexisting weak planes as well as tensile failure was investigated in the primary seal layer on top. For tensile failure, it was assumed that if pore pressures of the top layer of reservoir, M1, reached the minimum principal stress in the seal layer, hydrofracturing would occur. For shear failure along pre-existing weak planes, the Mohr-Coulomb criterion was employed assuming a weak plane could exist anywhere with an arbitrary orientation. The results showed that in general, shear failure along preexisting weak planes was more likely to occur in

Weyburn. Also, it was suggested that the majority of events recorded in Weyburn were more likely to have a slip origin along weak planes than having a tensile mechanism. Moreover, with regard to general application of microseismic monitoring in caprock, it was discussed that lack of recorded microseismic events is not conclusive evidence for lack of hydrofracture initiation in the caprock due to small magnitude of such events. Therefore, possibility of slow slip deformations and hydrofracture initiation still needs to be investigated. Also, there can be slow slip deformations along the weak planes that are not large enough to generate seismicity.

# Chapter 6

## Weyburn CCS Project: Part 2<sup>6</sup>

### 6.1 Abstract

The microseismic response of intact rock as well as weak planes was studied in Chapters 3 and 4, respectively. In Chapter 5, a one way coupled model was presented to study the likelihood of shear and tensile failure in the caprock of Weyburn reservoir. It was shown that in general, the likelihood of shear failure has been greater than that of tensile failure. In this chapter, the knowledge gained in previous chapters is incorporated to study the actual microseismic events recorded in caprock. For this purpose, a discrete element model is presented to study slip-induced microseismic events along weak planes and crack-induced microseismic events within the intact rock for a representative elementary volume, REV, in the caprock of Weyburn reservoir. Also, the effect of varying factors such as orientation, coefficient of friction and elasticity of the weak plane on release of microseismic energies is studied.

According to the results, for the conditions studied in this chapter, the magnitudes of slip-induced events range from  $\sim -1$  to  $-6$  while crack-induced events range from  $\sim -7$  to  $-11$ . Considering the capability of geophones, this suggests that events “recorded” in the caprock are more likely to have slip origins along weak planes than having crack origins within the intact rock.

In order to show the applicability of the model in practice, the events recorded in Weyburn during September and November of 2010 are analyzed. Also, a simple model is presented that correlates the amount of consumed energy per volume of the REV with the seismic energy released due to stick-slips along a weak plane. The model provides a tool for estimating the state of stress based on MS events recorded in the caprock. The results show that weak planes can be emissive even long before the failure of their surrounding is reached and therefore, there can be a level of tolerance for the observed MS events in the caprock.

---

<sup>6</sup> A version of this chapter has been accepted for publication in Acta Geotechnica <http://dx.doi.org/10.1007/s11440-016-0489-x>

## 6.2 Introduction

Petroleum operations may result in pressure and temperature changes within the reservoir that can lead to reactivation of preexisting weak planes and or development and propagation of new cracks in the caprock. Such damage (both cracks and slips) may provide a leakage path for the contaminant (i.e. CO<sub>2</sub>, brine, hydrocarbon etc.). Leakage of contaminants must be prevented first because its presence in the biosphere and the human environment can be deleterious and secondly because hydrocarbons are a valuable resource and poses challenges with resource conservation. As a result, caprock integrity has become one of the main concerns in Western Canada and around the world (Harrison & Falcone, 2014; Shukla et al., 2010; Xie et al., 2014). Therefore, once the operations begin, techniques such as microseismic (MS) monitoring are employed to ensure the safety requirements are met (Maxwell et al., 2010; Maxwell & Urbancic, 2001). Microseismic monitoring refers to recording of elastic waves generated as a result of the material undergoing deformations. Successful applications of this technique for tracking the evolution of damage have been reported in laboratory experiments (Ingraham et al., 2013; Lockner, 1993) as well as field operations (Cai et al., 2001; Gale et al., 2001). Analyzing the recorded waveforms by geophysics provides information such as the location and mechanism of damage (Eyre & van der Baan, 2015). However, the question of how this data could inform caprock integrity analyses remains a challenge.

Therefore, there have been attempts to link the microseismic (MS) data to geomechanical observations for caprock integrity assessments using a coupled reservoir (MORE) - geomechanical (ELFEN) model (Angus et al., 2010; Verdon et al., 2011) as well as studies on fault reactivation and permeability using a continuum TOUGH-FLAC model (Cappa & Rutqvist, 2011), combination of a pore network model with discontinuum PFC3D model (Raziperchikolaee et al., 2014) and analyzing real data from a geophysical perspective (Goertz-Allmann et al., 2014).

However, there are aspects that also need to be considered such as:

- a) Caprock is a rock mass composed of intact parts and weak planes. The MS release of energy through weak planes is governed by a stick-slip process (Brace & Byerlee, 1966) whereas

within the intact rock, it is governed by development of cracks (Martin & Chandler, 1994; Scholz, 1968a);

- b) Even though there may be no mature active faults, a sedimentary rock mass may contain weak planes in various scales and
- c) Numerical modeling, both continuum and discontinuum, can help relate the MS data to geomechanical response of the formation. Compared to discontinuum models, continuum models are fast and allow a more detailed simulation of real conditions. However, they are not capable of directly modeling the damage mechanism and thus the MS events and magnitudes may not be easily simulated.

In order to address these issues, this chapter is focused on the caprock of Weyburn reservoir that is located in a shale sedimentary basin. Therefore, using a discrete element model (DEM) as well as two algorithms for recording MS response of a weak plane (Khazaei et al., 2015b) and MS response of intact rock (Hazzard & Damjanac, 2013; Khazaei et al., 2015a), a representative elementary volume (REV) with a weak plane at its center is modeled in different conditions to identify the most likely mechanism behind “recorded” events in the caprock of Weyburn reservoir. The model is then used to study the events recorded in the caprock of Weyburn from September to November of 2010. This is the most emissive period in 7 years of MS monitoring in Weyburn. Eventually, a simple model is presented that allows estimating the state of stress from microseismic observations in the caprock.

### **6.3 A Representative Elementary Volume (REV) Model for the Caprock of Weyburn**

Geology of the Weyburn field as well as history of microseismic monitoring in Weyburn was previously introduced in sections 5.3 and 5.5 of this thesis, respectively. The logic behind the models presented in this chapter is schematically illustrated in Figure 6.1. Figure 6.1 (bottom) shows a reservoir model along with a chart showing history matched average pore pressures reported by (Jafari et al., 2011). Figure 6.1 (top) is the REV within the caprock considered as the basis for the modeling studies in this chapter. As the average pore pressures within the reservoir are increased due to injection of CO<sub>2</sub>, an upward compressive pressure is applied to the caprock in undrained condition that can cause reactivation of preexisting weak planes or development of new cracks within intact parts. The weak planes can have various orientations and properties. Due to

any of these possibilities, various levels of acoustic energy may be released as a result of crack development within intact parts or slip along weak planes. In the parametric study that will be presented later, the emission of both crack-induced and slip-induced magnitudes in any of these conditions will be investigated.

The REV is a cubic PFC3D model with  $2\text{ m} \times 2\text{ m} \times 2\text{ m}$  dimensions surrounded by six walls with a square weak plane with  $1\text{ m}^2$  surface area at its center. All the particles are bonded by parallel bond model except for those forming the weak plane that is bonded by the smooth joint model. The weak plane is modeled as a single planer fault representing a highly localized slip surface where slip occurs along a network of individual particles. The reason why overall dimensions of the model are larger than the weak plane is to minimize the end effects that force the slip behavior and also allowing the stick slips to develop independently from the ends.

The parallel bond properties of the REV need to be calibrated to represent the intact strength of Watrous formation in Weyburn. The Young's modulus, cohesion and internal friction angle of Watrous shale are estimated to be 14 GPa, 10 MPa and  $30^\circ$ , respectively (Gomez, 2006). Therefore, using the Mohr-Coulomb relations, the unconfined compressive strength is estimated as 35 MPa. The micro-properties of the REV are calibrated based on Young's modulus and UCS values using a cylindrical specimen with 2 m height and 1 m diameter (Table 6.1).

Considering the elevation of the reservoir and thickness of caprock as shown in Figure 5.14 as well as the depth of the microseismic events in Figure 5.9, a depth of 1340 m has been considered as a point at the middle of caprock where modeling is conducted. Therefore, once the model was built, using Equation (5.1), the stresses at this depth have been applied to the REV as initial stresses (i.e. isotropic stresses of 37.5, 32.2 and 24.1 MPa along the x, y and z directions, respectively). Then, the model was loaded by moving the bottom wall along Y direction inwards. A servo-mechanism has also been implemented during the loading to keep the horizontal stresses, along x and z directions, constant to resemble the real underground conditions. During the loading, there will be slips along the weak plane as well as crack development within the intact parts; any of which mechanisms release microseismic energies that have to be recorded. Although fluid pressure can facilitate the slip by reducing the shear strength of the weak plane, no fluid-mechanical coupling has been conducted.

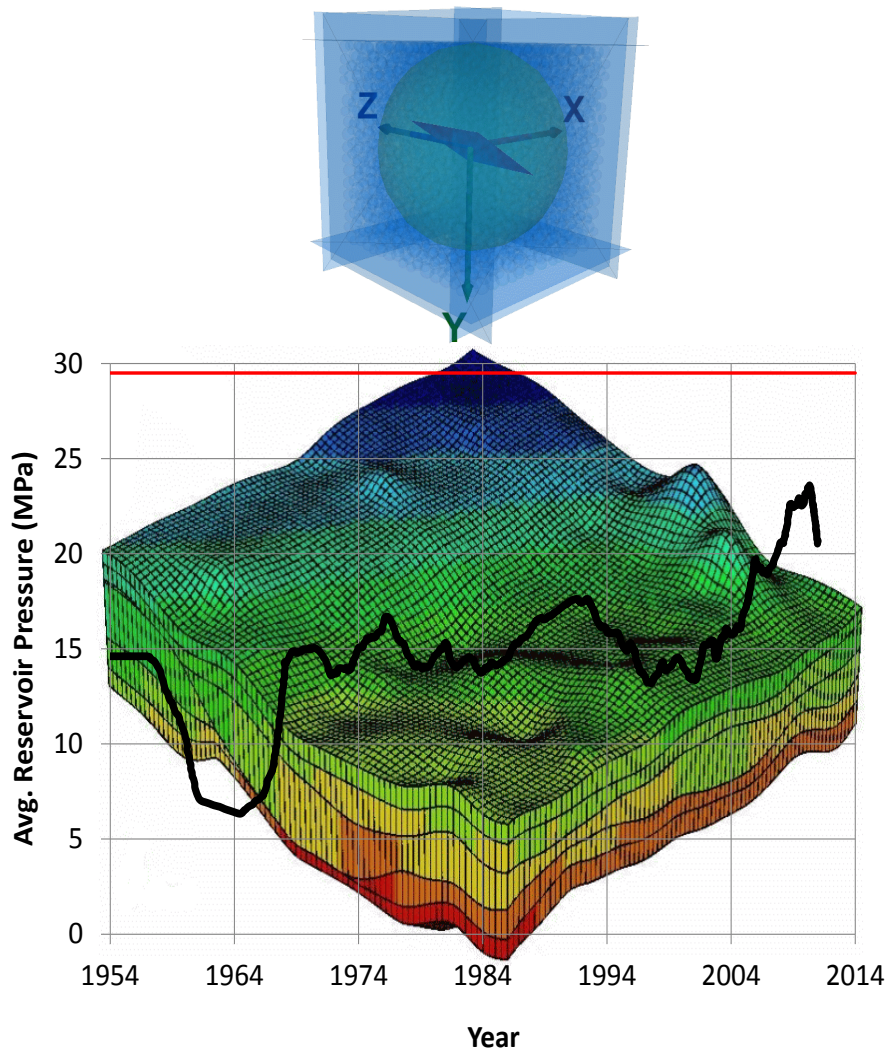


Figure 6.1: (Top) The PFC3D model (REV) in the caprock above the reservoir. A weak plane with  $1\text{m}^2$  area is implemented at the center of it and the load is applied along the y direction by moving the bottom platen upwards to resemble the loading scheme applied to the caprock as a result of stress transfer due to increase in reservoir pressures. The measurement sphere is shown with green. (Bottom) A reservoir model along with the chart shows history matched average reservoir pressures (Jafari et al., 2011). Red line is the maximum allowed pressure, 29.5 MPa (Wilson & Monea, 2004). This figure is schematic to illustrate the logic behind the model and is not to scale.

Table 6.1: Calibration parameters for parallel bond properties in REV

Macro Properties			Ball Parameters			Parallel Bond Parameters	
UCS (MPa)	Young's Modulus (GPa)	Poisson's Ratio	Avg. Particle Radius (m)	Young's Modulus $ba\_Ec$ (GPa)	Young's Modulus $pb\_Ec$ (GPa)	Mean Normal Strength $pb\_sn\_mean$ (MPa)	Standard Deviation of the Strength $pb\_sn\_sdev$ (MPa)
37	14.3	0.25	0.0057	16.5	16.5	30	8.1

## 6.4 Calibration of Microseismic Recording Algorithms for Weyburn

The two algorithms introduced in Chapters 3 and 4 for recording the crack-induced MS events and slip-induced MS events, respectively, are used in this chapter. The idea behind the crack-induced MS recording algorithm is that the strain energy change,  $\Delta E_s$ , of the entire system can be approximated by the  $\Delta E_s$  of a small volume around each crack monitored for a short period of time (Hazzard & Damjanac, 2013). Theoretically, to get accurate results, this volume should be large enough and the monitoring period should be long enough. However, in order to be computationally efficient, the smallest volume and shortest period that provide a good estimation of  $\Delta E_s$  of the entire system had to be found. Therefore, (Hazzard & Damjanac, 2013) monitored  $\Delta E_s$  around 30 isolated cracks over areas of 2 and 5 average particle diameters. For both cases, the peak  $\Delta E_s$  was reached within the number of steps about 10-15 times the monitored radius in average particle diameters. Also, in both cases, a linear correlation, but with slightly different coefficients of linearity, was observed between  $\Delta E_s$  of that small volume and  $\Delta E_s$  of the entire system. It was suggested that this coefficient would presumably depend on the size of the specimen, type of the test and dimensionality (2D or 3D). However, due to the logarithmic scale of the magnitude, it was suggested that a very accurate coefficient would be probably not necessary. Since they observed a good correlation (with  $R^2=0.98$ ) for a volume even as small as 2 particle diameters (and thus duration of 40 steps), similar values have been used in present study.

For the slip-induced MS recording algorithm, the calibration is conducted using the model presented in Chapter 4 (Figure 4.4). In this model, a 1.5 m  $\times$  1.5 m  $\times$  0.4 m specimen is loaded biaxially by moving the walls along the Y and X axes inwards and outwards, respectively, all with the same velocity. The fault is installed diagonally by smooth joint contact model and the rest of particles are bonded together by parallel bond model. In order to prevent unnecessary bond breakages affecting the shear process, the parallel bond strengths are set to extremely high values.

It was shown in Chapter 4 that resolution of the model, elasticity of the fault's surrounding medium, normal stress on the fault, fault's coefficient of friction, fault's elasticity, minimum normal stress criterion for slips to be considered seismic, and size of space window for clustering the events are all effective on seismic response of the fault. Choice of these parameters for calibration of the model for Weyburn is discussed below:

- a) Although an increase in resolution causes an increase in b-values (Khazaei et al., 2015b), it is also a critical parameter that increases the computation time so a reasonable choice has to be made first. Therefore, the model used for calibration is built with an average 0.056 m radius of particles. Similar resolution will be used for the rest of models presented in next sections.
- b) Stiffness of the medium surrounding a weak plane could vary depending on the fractures around it as well as possible heterogeneity. However, stiffness of the surrounding medium is assumed equal to the reported Young's modulus for Watrous formation, 14 GPa (Gomez, 2006b). Therefore, the Young's modulus of balls and parallel bonds are set almost equal to 14 GPa ( $ba_{Ec}=pb_{Ec}= 16.5$  GPa). The small difference is because the relation between micro and macro properties of PFC3D models are not linear and thus the choice of 16.5 GPa would result in a macro Young's modulus closer to 14 GPa, as shown in Table 6.2.
- c) In a real problem, the value of normal stress on the fault would be a function of in-situ stresses and orientation of the fault. In this research, we are not modeling a specific fault. Therefore, although it was shown that an increase in normal stress would cause a decrease in b-value (Khazaei et al., 2015b), it is not possible to calibrate the algorithm for every single weak plane with different properties and thus, the algorithm is calibrated for an average condition in the caprock of Weyburn. As mentioned before, the average depth of 1340 m is taken as a point at the middle of caprock for modeling. Therefore, using 24 kPa/m for the rate of intermediate stress in the strike-slip regime as shown in Equation (5.1), the average/intermediate stress at the average depth of 1340 m has been used as the normal stress on the fault shown in Figure 4.4 (i.e.  $1340 \times 24 = 32.16$  MPa).
- d) The coefficient of friction of most faults in nature is known to vary between 0.6 and 1 (Byerlee, 1978). An average value of 0.8 has been used for calibration of the algorithm ( $sj\_fric=0.8$ ).
- e) Shear wave velocity is required in Equation (4.3) to determine the minimum duration of each slip to be considered seismic. The shear wave velocity for lower Watrous is considered equal to 2260 m/s (Gomez, 2006).
- f) Khazaei et al. (2015b) used 0.1 MPa for the minimum normal stress threshold for the events to be seismic and showed that the results were not much sensitive to the choice of this parameter. Therefore, similar value is used in this study.

The parameters of the calibration model are summarized in Table 6.2.

Figure 6.2 shows the calibration results for two different sizes of space window. As can be observed in this figure, the largest magnitudes from PFC3D models are almost equal to M-1.4, which is smaller than the largest magnitude observed in the field (M-1.1). Using the Least Square method, b-values are also computed. The dip at the middle of the numerical plots (between M-2 and M-3) seems to be due to the shape of the fault and presumably size distribution of particles. In other words, for a square fault with surroundings that undergoes a larger amount of displacement (see b-value plots in next sections), the dip becomes less pronounced and the shape of b-value plots become more uniform. With regard to the number of events, a larger space window results in fewer smaller events making the end of the numerical plot closer to the real data. Therefore, a space window equal to three times the maximum particle diameter similar to previous study by (Khazaei et al., 2015b) along with shear modulus equal to 14 GPa in Equation (4.2) have been used for this study.

Table 6.2: Micro-parameters used in PFC3D model for calibration of slip-induced microseismic recording routines

Ball Parameters		Smooth Joint Parameters		
Average radius (m)	Young's modulus (GPa)	Normal stiffness (N/m <sup>3</sup> )	Shear stiffness (N/m <sup>3</sup> )	Coefficient of static friction
<b>md_ravg</b>	<b>ba_Ec</b>	<b>sj_kn</b>	<b>sj_ks</b>	<b>sj_fric</b>
0.056	1.65E10	1.65E10	1.65E10	0.8

The difference between largest numerical and real magnitudes in Figure 6.2 may be due to possibility of larger patches or displacements involved in real caprock. This may be resolved by using bigger models as will be shown in the next section. Also, it is worth mentioning that the real b-value plot based on Verdon's reported magnitudes belongs to events distributed in the microseismic area that were not necessarily released from one single fault. However, for the sake of comparison, this data is used in calibration.

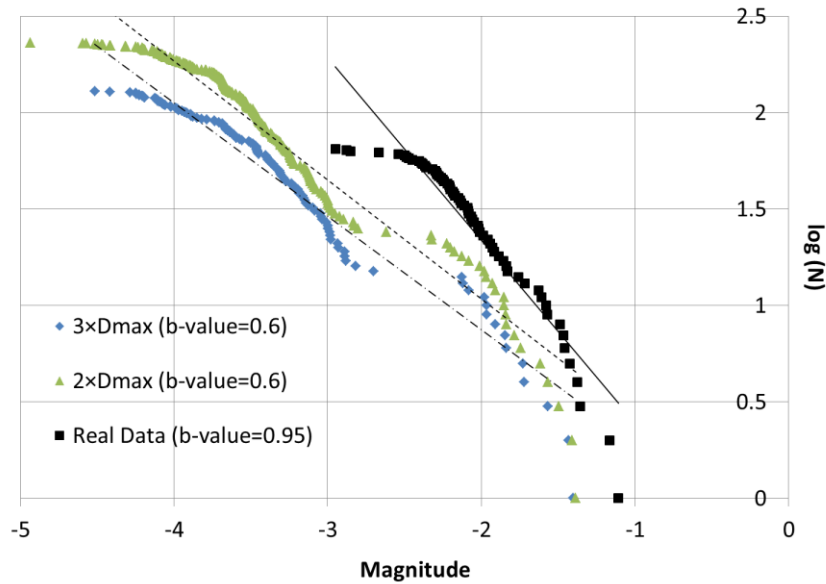


Figure 6.2: b-value plots for real data and numerical models with two different sizes of space window (Real data plotted after (Verdon, 2010))

According to what was mentioned, the varying factors in this problem are orientation of weak plane as well as coefficient of friction and elasticity of the weak plane. These factors will be explored in the next section in the parametric study.

## 6.5 Parametric Study

For the model shown in Figure 6.1 (top), a parametric study has been conducted on orientation of the weak plane, coefficient of friction of the weak plane and elasticity of the weak plane.

### 6.5.1 Studying the effect of weak plane's orientation

A model with the same smooth joint properties as listed in Table 6.2 and parallel bond properties as listed in Table 6.1 has been repeated for nine weak planes with different orientations as shown in Figure 6.3. The weak planes have been generated by rotating a square weak plane symmetrically placed at the center of the model around each axis. Due to symmetry of the weak plane and model, similar cases are shown once in this Figure.

Then the bottom wall in Figure 6.1 has been accelerated upwards. Various quantities were monitored within the model during the loading process such as overall stress and strain along the Y

direction as shown in Figure 6.3. As can be observed in this Figure, first the 32.2 MPa stress equal to the vertical in-situ stress is reached. Then, the overall deviator stress starts to increase. MS energies have also been recorded during the loading. However, since faults would undergo different amounts of displacement and stress, a criterion was required for stopping all the tests and thus, they were stopped once 0.4% overall strain along the Y axis was reached. Figure 6.3 shows that this would almost correspond to the peak strength of all the REV's. The strength of all models ranged from 59.2 MPa (case 4) to 64.3 MPa (case with no weak plane).

Since we would like to investigate the most likely mechanism of recorded events in the caprock of Weyburn, b-value plots for both slip-induced events along the weak plane and crack-induced events are obtained as shown in Figure 6.4. Regarding the slip-induced events, the least amount of emissions is observed for case 4 where the weak plane is normal to the loading direction. The most emissive case is case 7, which is normal to the direction of minimum in situ stress (Z axis) and is along the direction of maximum in situ stress (X axis). Since everything has been kept the same in all the models except orientation that would result in different states of stress on the weak plane, this should be the only reason behind different slip-induced behaviors observed.

Considering the range of magnitudes for slip-induced and crack-induced emissions and considering the capability of geophones, it seems that "recorded" emissions in the caprock of Weyburn are more likely to have slip origin along weak planes than having crack origins within intact parts.

Since the orientation of weak plane in case 9 is very close to the case history of Weyburn that will be explored in Section 6.6 and also the b-value plot for stick-slip events in this case is close to the real data, this case is chosen for the rest of parametric studies.

With regard to the location of slip-induced events (Figure 6.5), the largest magnitudes are located at the middle parts of the faults. This indicates that shear displacements are maximum at the center and minimum at the tips which is as expected.

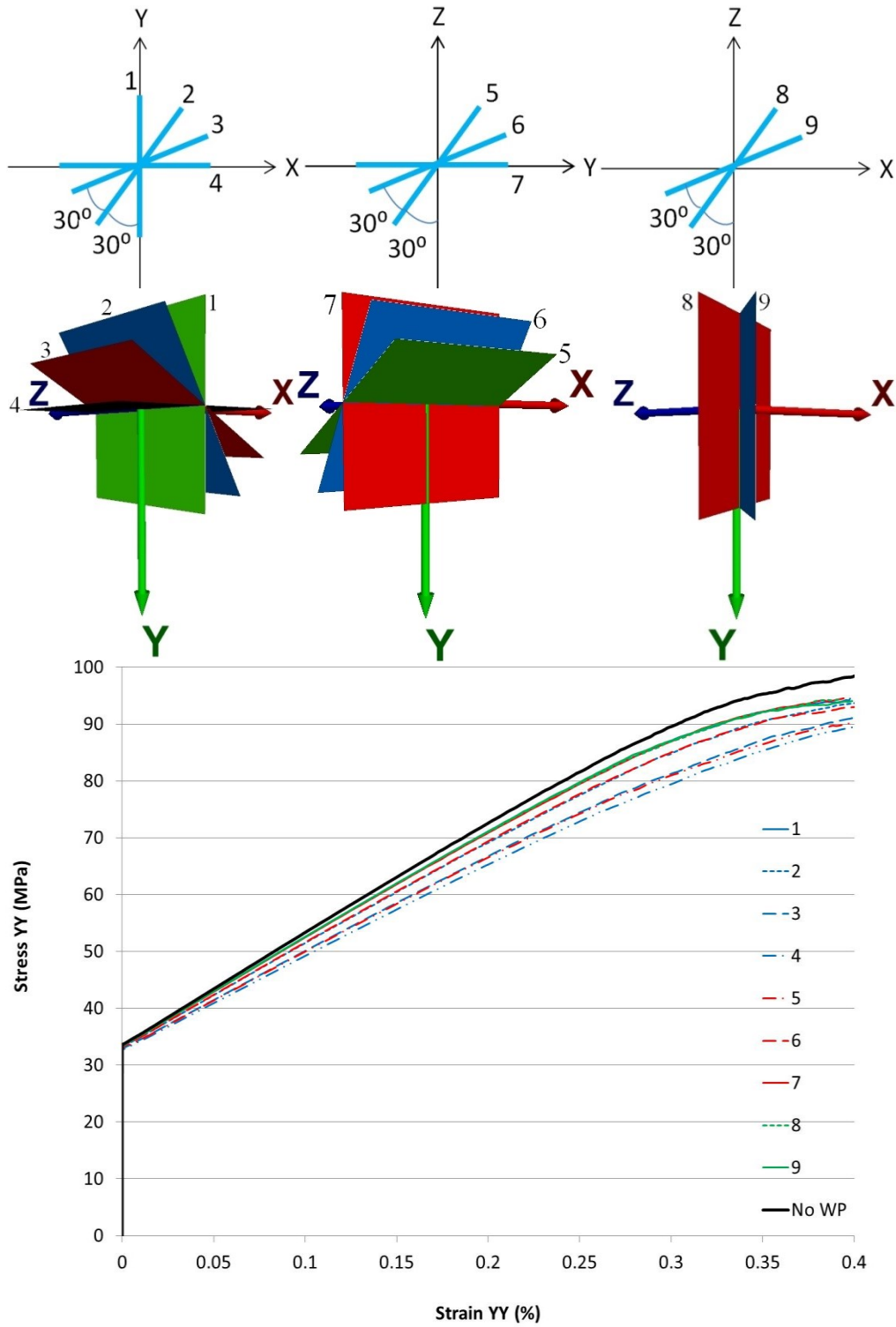


Figure 6.3: The top two plots show nine orientations of weak plane considered in parametric study. The bottom plot is the overall stress-strain curve obtained from measurement sphere shown in Figure 6.1

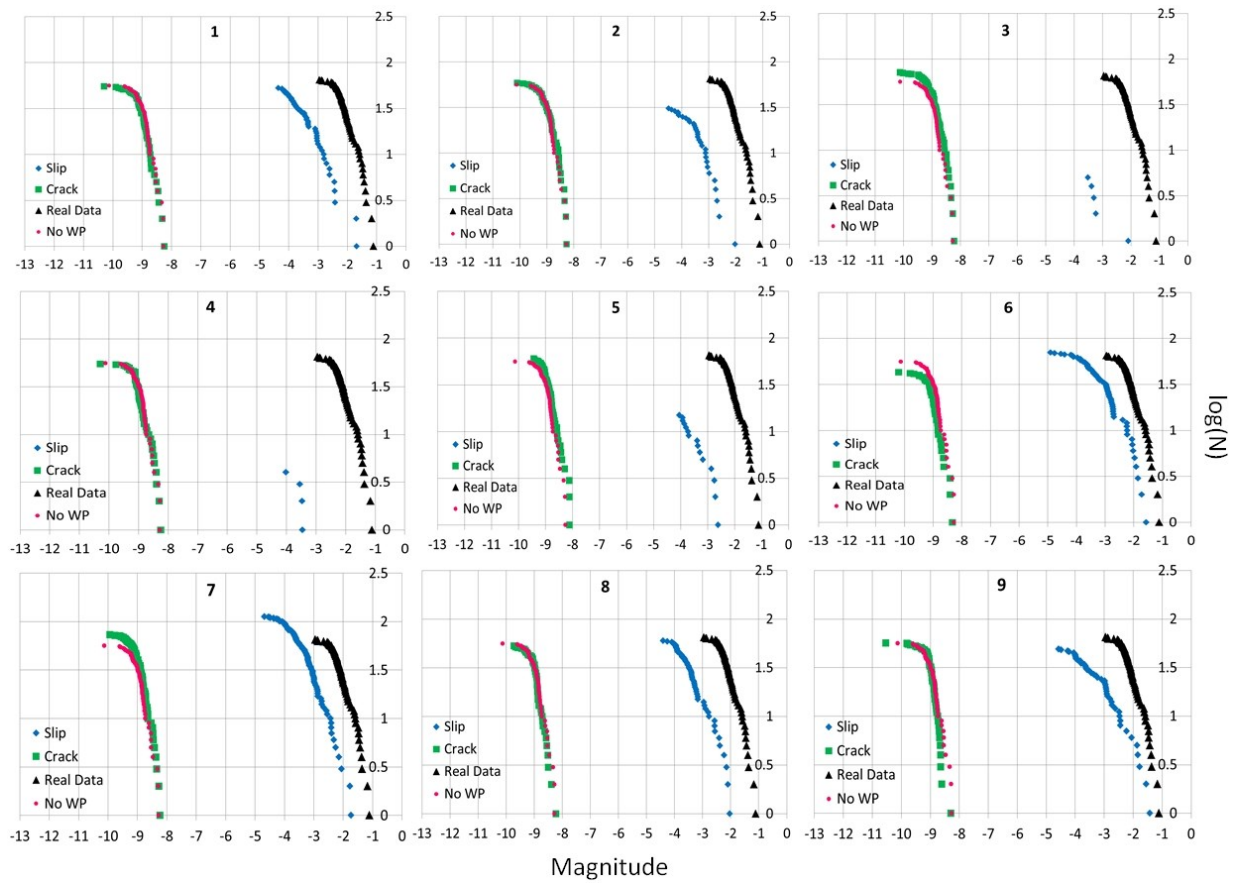


Figure 6.4: b-value plots for the nine orientations of weak plane shown in Figure 6.3. Real b-value plots are obtained using data after (Verdon, 2010)

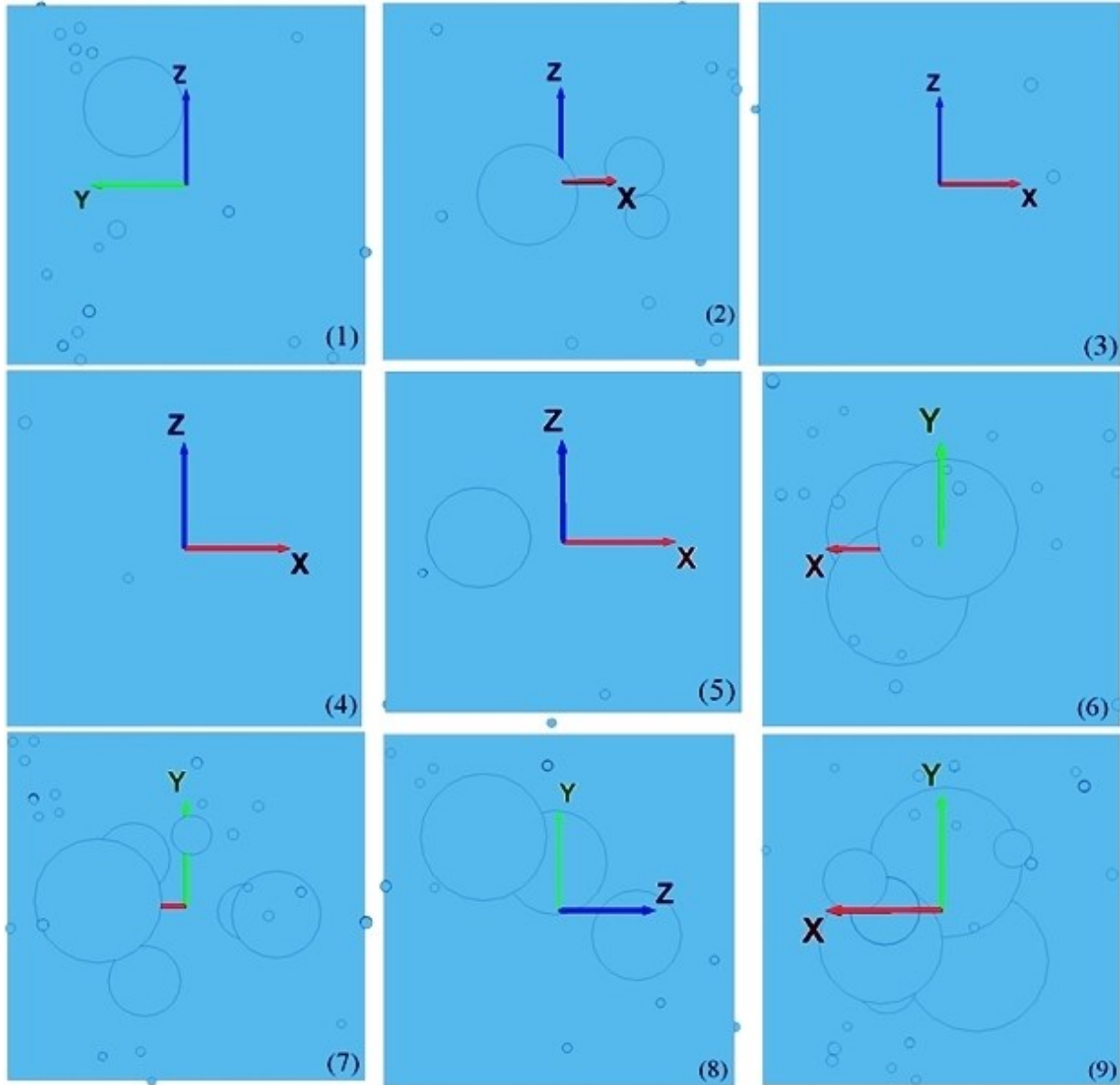


Figure 6.5: Location of slip-induced events along the faults. Although the events are spread at both sides of each fault, only one side is shown in this figure. The area of each slip patch for calculation of scalar seismic moment is calculated as an ellipse (Khazaei et al., 2015b). However, due to plotting difficulties, the events are shown with circles. The faults in this figure have been rotated, if necessary, to increase the visibility of the events

### 6.5.2 Studying the effect of coefficient of friction

A model with the same smooth joint properties as listed in Table 6.2, parallel bond properties as listed in Table 6.1 and orientation of weak plane the same as case 9, has been repeated for three

values of coefficient of friction (i.e. 0.6, 0.8 and 1) as shown in Figure 6.6. This is a well-known range for most faults in nature (Byerlee, 1978).

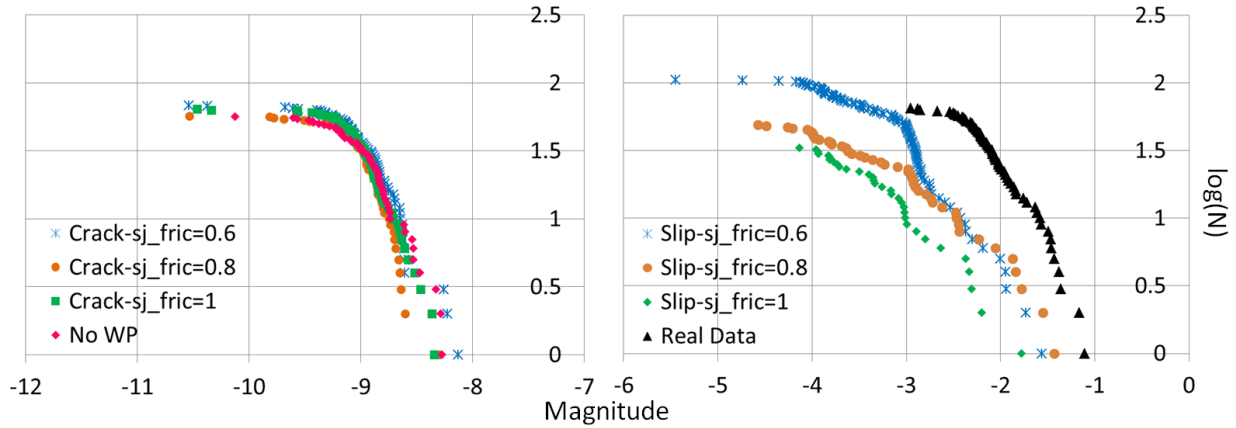


Figure 6.6: b-value plots for models with different coefficients of friction of the fault

For the slip-induced events, this figure shows that generally a decrease in the coefficient of friction results in more emissions. Also, a smaller coefficient of friction results in larger shear displacements of the smooth joints and thus greater magnitudes would be expected.

With regard to crack-induced events, the small variations shown in Figure 6.6 make it difficult to draw conclusions on these events. However, as discussed in the next section, in general, the excess energy put into the system by external loading has to dissipate by causing slip along the weak plane and or by developing cracks within the intact parts. Therefore, since everything else is kept the same in all the models, the conditions that cause more stick-slips along the fault and greater slip-induced magnitudes result in generation of fewer and smaller crack-induced magnitudes.

### 6.5.3 Studying the effect of weak plane's elasticity

A model with the same smooth joint properties as listed in Table 6.2, parallel bond properties as listed in Table 6.1 and orientation of weak plane the same as case 9, has been repeated for different values of normal and shear stiffness of the weak plane. In order to make the presentation of results easier, two ratios of  $r_n$  and  $r_s$  are defined as the ratios of normal and shear stiffness of the weak plane to the Young's modulus of the surrounding rock mass, respectively (i.e.  $r_n = \text{sj\_kn} / \text{ba\_Ec}$  and  $r_s = \text{sj\_ks} / \text{ba\_Ec}$ ).

The variations of b-value plots in Figure 6.7 could be explained considering that the onset of slip for a contact is determined by comparing the shear force with the shear resistance as shown in Equation (6.1) (Potyondy & Cundall, 2004):

$$F^s \leq \mu F^n \Rightarrow -k_s \Delta U^s \leq \mu k_n U^n \quad (6.1)$$

where the shear force,  $F^s$ , is updated incrementally multiplying the shear stiffness of the contact,  $k^s$ , by the shear displacement increment,  $\Delta U^s$ . The shear resistance is calculated using the coefficient of friction,  $\mu$ , the normal stiffness of the contact,  $k^n$ , and the overlap of two contacts,  $U^n$ .

Considering Equation (6.1), a decrease in normal stiffness of the weak plane reduces the shear resistance resulting in greater number of slip-induced emissions and larger MS magnitudes (Figure 6.7a). With regard to shear stiffness, Khazaei et al. (2015b) observed three stages in the shear stress versus displacement behavior of a fault:

1. a linear increase in shear with no or very few stick-slips;
2. a non-linear increase in shear with minor stick-slips and
3. a final stage where the shear strength of the fault is reached and the overall shear stress becomes constant or drops (depending on the stiffness of fault and its surrounding) while the fault is still undergoing displacements.

The majority of stick-slip events were observed in this final stage. On the other hand, an increase in the shear stiffness of the fault causes an increase in the slope of the linear part of the shear-displacement curve and thus the shear strength is reached at smaller displacement levels. Therefore, between two faults that undergo the same amount of total displacements, the one with greater shear stiffness will experience a longer period of stick-slips (i.e. a longer third stage). This results in an increase in the b-value and possibly larger magnitudes (Figure 6.7b).

However, if the fault is softened by reducing its stiffness values to the same amount simultaneously (Figure 6.7c), the reduction in normal stiffness would be in favor of stick-slips, on one hand, while on the other hand, the reduction in shear stiffness would result in a shorter third stage and thus a shorter period of stick-slips (for the same amount of total

displacement). Therefore, both effects need to be considered at the same time for interpretation of the results. However, from Figure 6.7c, it seems that the effect of simultaneous change in stiffness properties is less significant compared to the two previous cases that there is a contrast between normal and shear stiffness of the weak plane.

With regard to crack-induced emissions, greater slip-induced magnitudes along the weak plane correspond to fewer and smaller crack-induced magnitudes. This could be explained considering that the loading (the excess energy put into the system) is the same for all the tests. Therefore, if the dissipation of excess energy along the weak plane is limited by a greater normal stiffness or smaller shear stiffness, the excess energy will have to dissipate by developing more cracks resulting in larger crack-induced emissions.

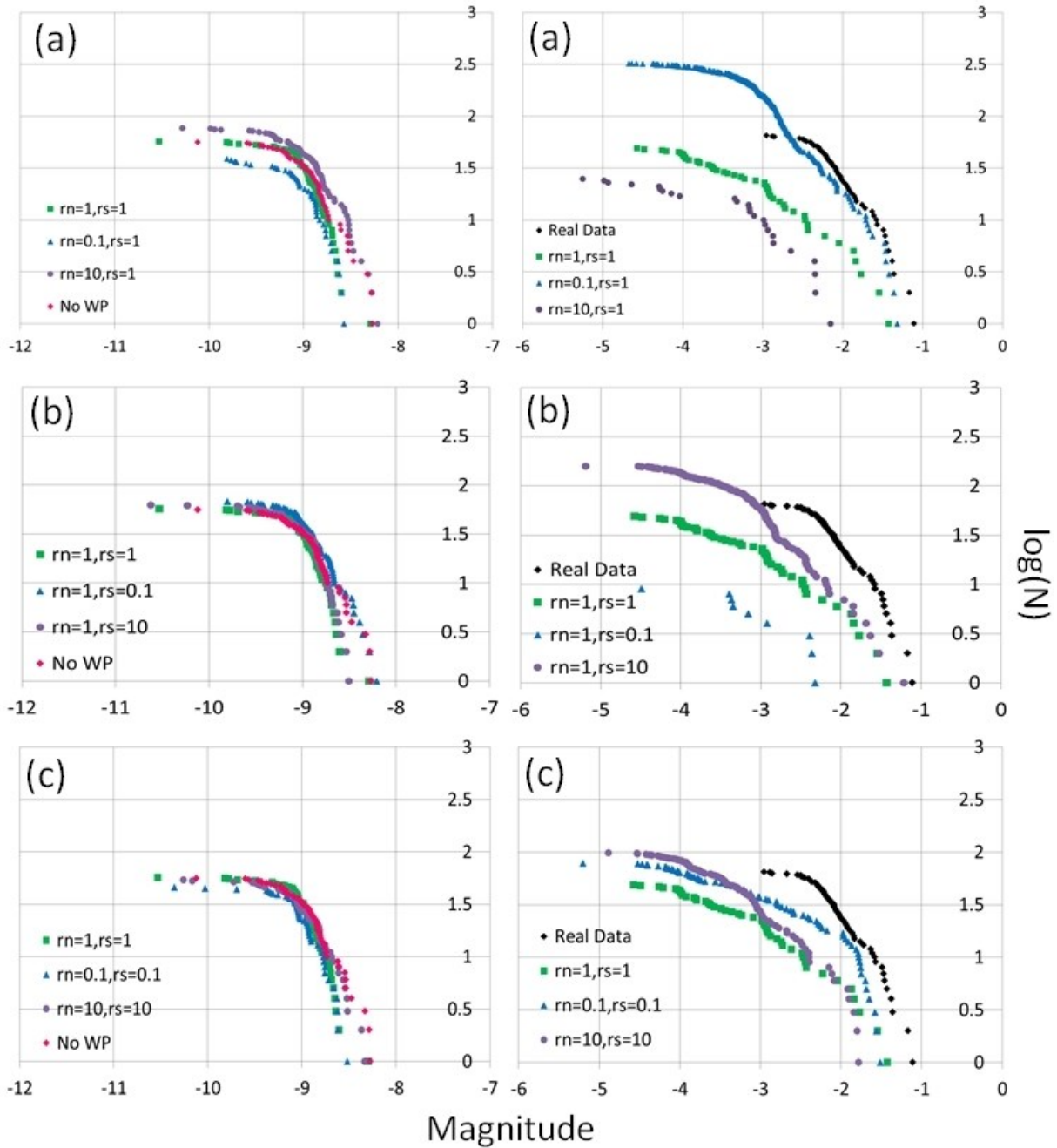


Figure 6.7: Effect of stiffness properties of weak plane on MS energies

## 6.6 Post-observation analysis of microseismic events

In this section, the events recorded from September to November of 2010 at Weyburn are analyzed using a discrete element model similar to previous sections. The events recorded in September were believed to be triggered by an increase in pressure due to recent abandonment of

a single vertical injection well nearby the monitoring well. However, the events continued to appear in October and November as well. More details could be found in (Jafari et al., 2011; Verdon et al., 2012).

The magnitudes ranged from -2.06 to -3.47. Figure 6.8 shows the location of wells and MS events recorded in this period in the microseismic area. The single event circled red is far from the MS cloud and has been excluded from the analyses. Also, since only the caprock is studied in this research, the events below 1400 m depth have been excluded from analyses.

The approach for analyzing the events with regard to geomechanics is presented in steps as following:

- a) In the light of what was presented in this chapter and considering the range of magnitudes, the events are more likely to have slip origin along a weak plane. Same calibration properties as explained in section 6.4 for the MS recording algorithms are used here. Also, it is assumed that all the events were generated from a single weak plane.
- b) Having the location of events, orientation of the parent weak plane with regard to in-situ stresses needs to be identified. Figure 6.8 shows a general equation for a possible plane,  $f(x,z)$ , along the Y axis on which the events with general  $(x,z)$  coordinates are located. As explained before, for the models presented in this chapter, the maximum and minimum horizontal stresses in Weyburn are considered along NE-SW and NW-SE directions, respectively (Figure 5.1). The distance between each event and the plane is  $d$ . Assuming the best plane is the one with minimum sum of distances (i.e.  $\Sigma d$ ),  $\alpha$  is obtained equal to  $49.88^\circ$ . However, for simplicity, we build the model with a weak plane  $45^\circ$  to the direction of max and min horizontal stresses (i.e. N-S direction).
- c) The coefficient of friction and weak plane's elastic properties are chosen similar to case 9.
- d) Having a calibrated MS recording algorithm, orientation of the weak plane and in-situ stresses, a REV model similar to the one presented in Section 6.3 needs to be built. However, a judgment has to be made on dimensions of appropriate REV. Regardless of the single event far from the cloud in Figure 6.8 that is located at a depth of 945.5 m, the MS cloud extends from  $\sim 1209$  m to  $\sim 1476$  m depth. Since the focus of this study is on caprock only, the events below 1400 m depth have been excluded from analyses. The width of a plane to include all the events located between 1209 m and 1400 m depth would be about

80 m. However, building a model with this size is not practical. Therefore, a model with  $5\text{ m} \times 5\text{ m} \times 5\text{ m}$  is built (89,946 balls) with a weak plane  $2.5\text{ m} \times 2.5\text{ m}$  at its center (Figure 6.9).

- e) As shown in Figure 6.1, the average reservoir pressure was 14.6 MPa in 1954. Thus, once the pressures reached to  $\sim 24$  MPa in 2010, the excess upward pressure to the caprock would be only 9.4 MPa. Therefore, the bottom wall in Figure 6.1 was accelerated upward until 41.6 MPa (i.e.  $32.2+9.4$  MPa) was reached within the REV. Also, in order to study the worst-case scenario, the loading of REV was then continued until 0.4% strain similar to previous cases. Both crack-induced and slip-induced events were monitored during the loading and b-value plots were obtained (Figure 6.10).

For the REV loaded to 9.4 MPa deviator stress, no crack-induced emissions were observed (Figure 6.10). With regard to slip-induced events, although the overall range of numerical magnitudes agrees with the real data, the slope of the PFC3D plots (b-values) is underestimated. According to the parametric study in section 6.5 as well as the previous study of Khazaei et al. (2015b), several factors could result in an increase in the numerical b-values such as a model with finer particles, a lower coefficient of friction, a lower normal stiffness and a higher shear stiffness. However, no further attempts have been made to match the numerical plots with the real data in present chapter.

Comparing the b-value plot for slip-induced events from PFC3D model with those for real data recorded in September as well as September to November suggests the likelihood of a local increase in pressures from September to November that has resulted in more emissions causing the evolution of b-value plot. However, the stress-strain curve in Figure 6.10 shows that although several events were recorded during this short period of time in Weyburn, the overall state of stress in that vicinity is still far from the peak strength of the REV.

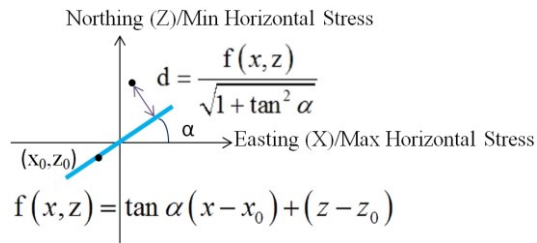
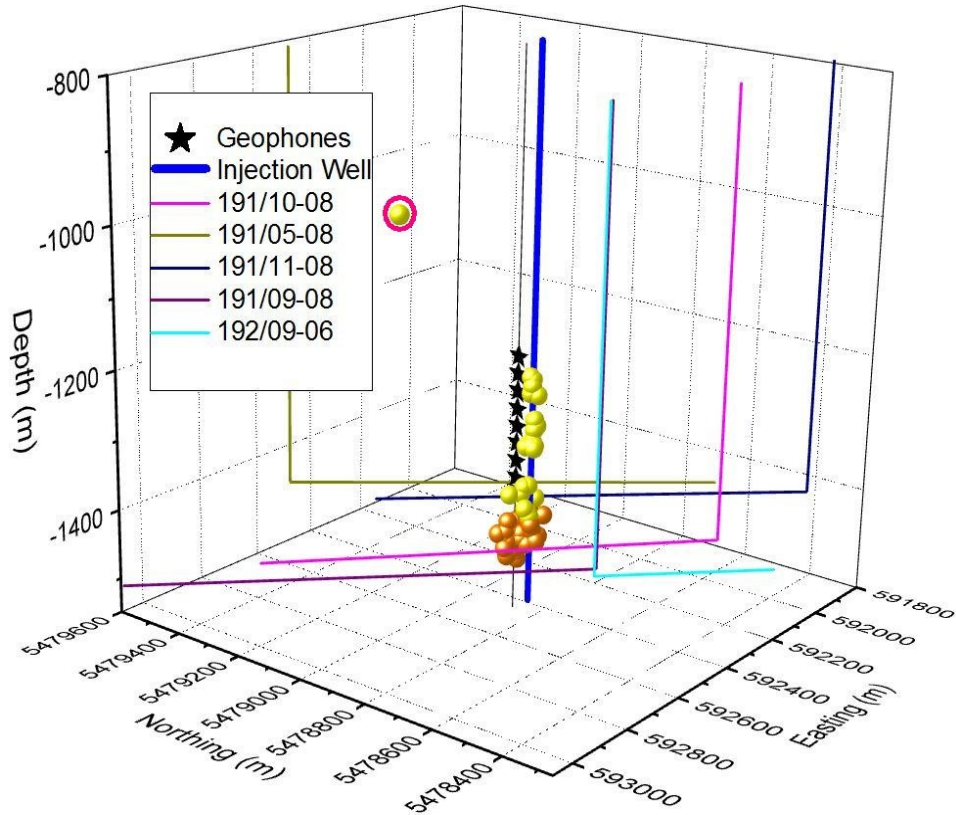


Figure 6.8: Events recorded in Weyburn between Sep and Oct of 2010. The events above -1400 m are marked with yellow and have been used for analyses. The orange events are located below -1400 m. The single event circled with red is excluded from the analyses. The axes  $x$  and  $z$  are along the maximum and minimum horizontal stresses, respectively. The plane makes the angle  $\alpha$  with  $x$  direction and passes through  $(x_0, z_0)$  that is an arbitrary point on the plane taken as (591800, 5479600). The distance of each event with this plane is  $d$ .

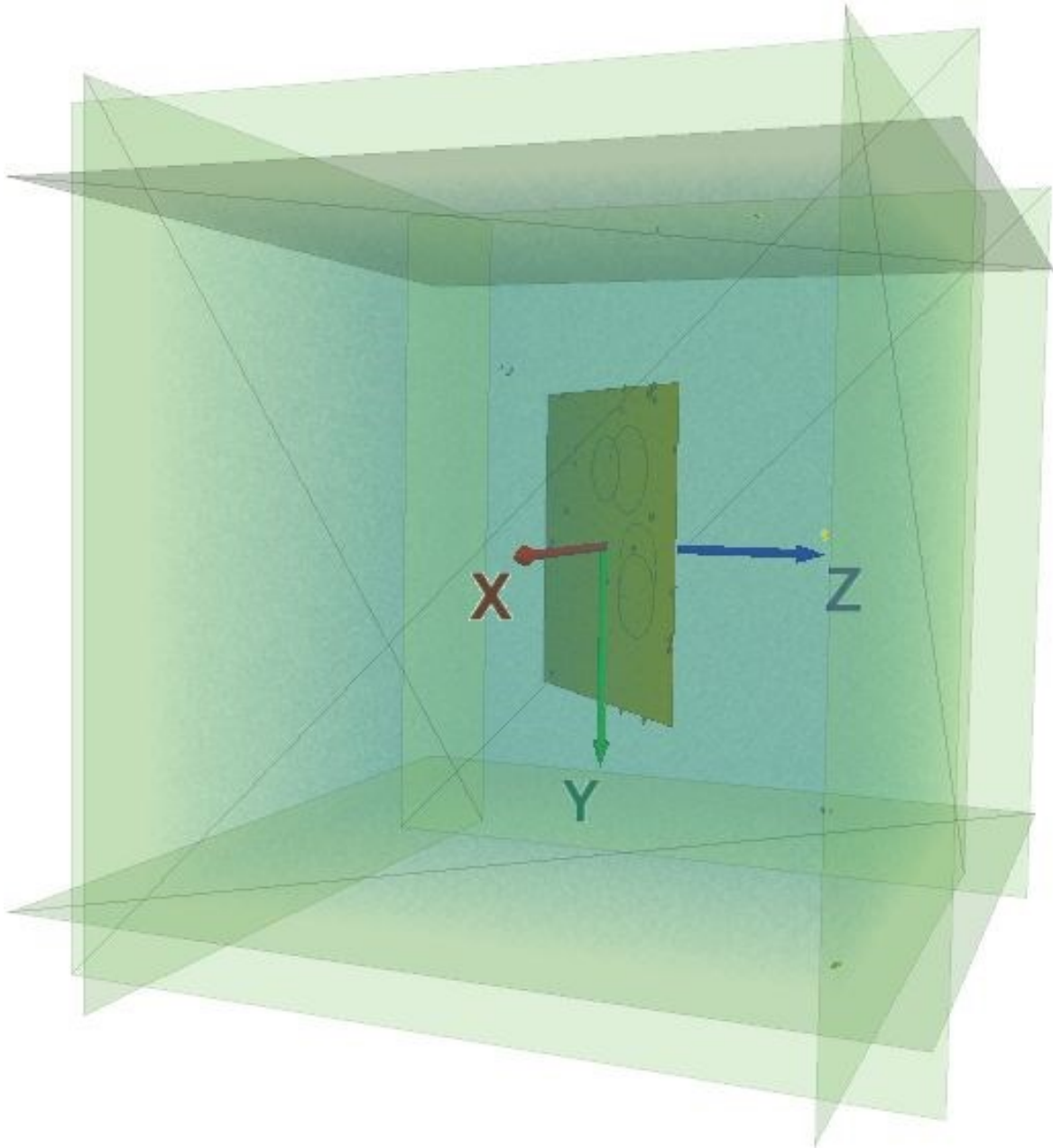


Figure 6.9: The REV with  $5\text{ m} \times 5\text{ m} \times 5\text{ m}$  dimensions made for studying the events in the caprock of Weyburn from September to November of 2010. The weak plane makes an angle of  $45^\circ$  with x and z directions.

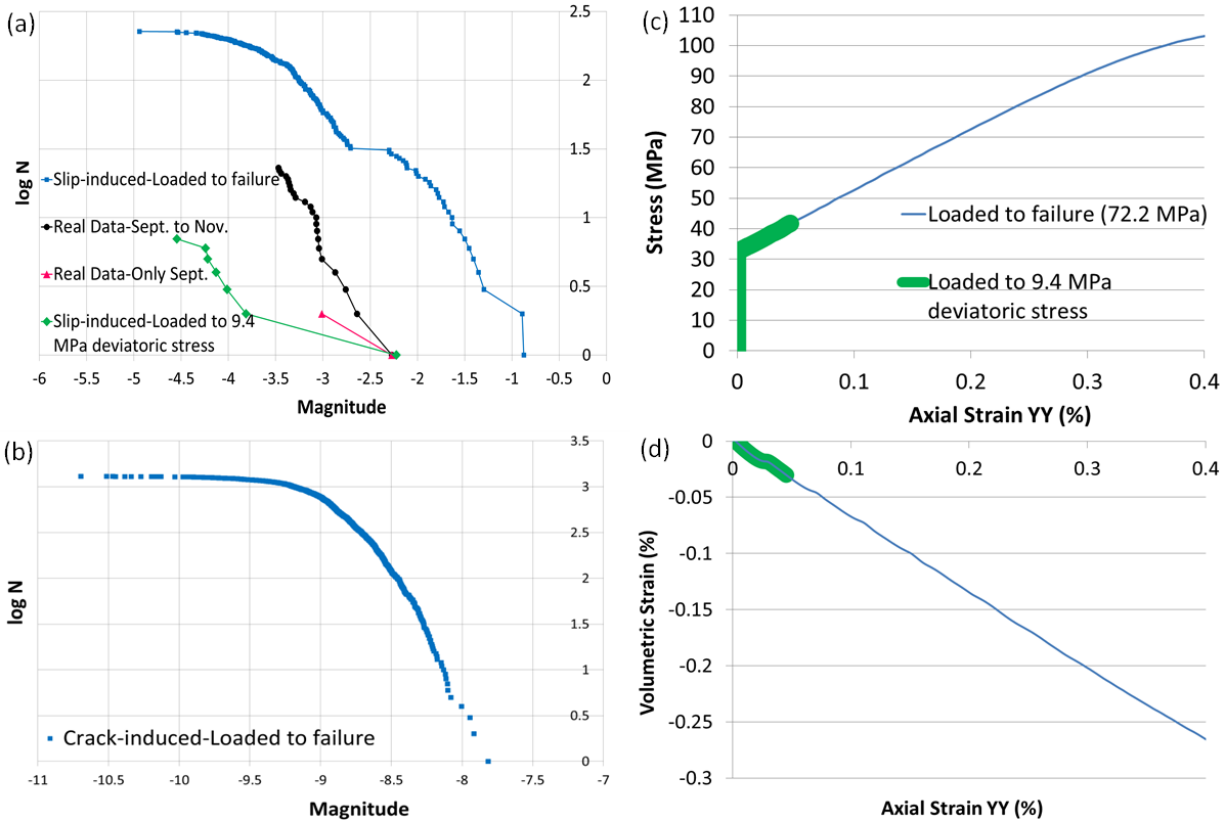


Figure 6.10: a) The b-value plot for events located above -1400 m in September of 2010 (red) and the b-value plot for all the events above -1400 m recorded from September to November of 2010 in Weyburn (black) (Real data plotted after (“ESG Weyburn Microseismic Progress Report,” 2011)). The b-value plots obtained from PFC3D are also shown for two states of loading. b) b-value plot for crack-induced events recorded by PFC3D for the REV loaded to failure. No crack-induced events were observed for the REV loaded to 9.4 MPa deviatoric stress c,d) The Stress-strain and volumetric strain-axial strain curves for the REV loaded to 9.4 M (green) and loaded to failure (blue)

## 6.7 A general model for estimating the state of stress from MS energies recorded in the caprock

Comparing the stress-strain curves with numerical b-value plots shown in Figure 6.10 reveals that as the state of stress evolves within the REV, the weak plane also undergoes larger displacements and becomes more emissive. At the same time, more cracks develop within the REV that results in evolution of crack-induced emissions too. Therefore, the b-value plots shift toward larger magnitudes for both slip-induced and crack-induced events. This observation as schematically illustrated in Figure 6.11 is the idea behind the model presented in this section.

In this Figure, different b-value plots are shown for different states of stress until failure at point C. The area under stress-strain curve represents the consumed energy per volume by the REV,  $W_{\text{cons/vol}}$ . According to this figure, there is a correspondence between  $W_{\text{cons/vol}}$  and the amount of released seismic energy due to stick-slips so that as  $W_{\text{cons/vol}}$  is increased, the emissions evolve too both in terms of number and magnitude.

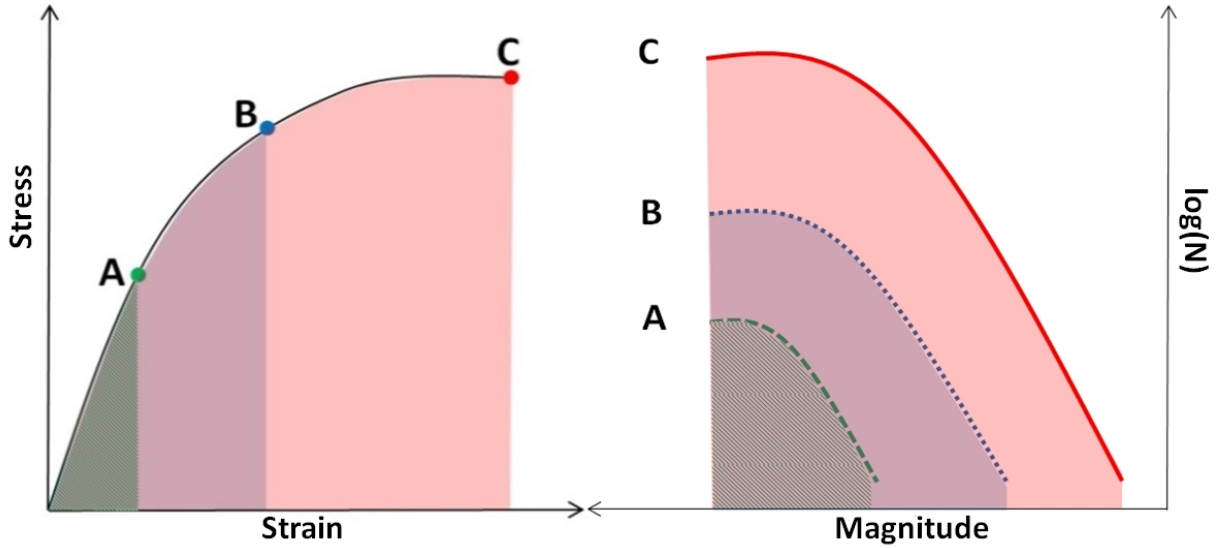


Figure 6.11: Schematic illustration of how evolution of b-value plots for microseismic events can be related to the state of stress in the surrounding rock. Each b-value plot corresponds to a state of stress within the REV

The number of events in a PFC3D model is a function of the resolution and thus a direct comparison between this number and real number of events recorded in caprock is not reasonable. However, the released seismic energy for each event,  $E_s$ , can be roughly calculated from the scalar moment magnitude,  $M_0$ , using Equation (6.2) (Bormann & Di Giacomo, 2011):

$$E_s \approx (1.6 \times 10^{-5}) M_0 \quad (6.2)$$

Therefore, it is suggested that a measure of total released seismic energy, hereafter referred to as  $E_T$ , can be roughly obtained by summing up all the  $E_s$  values for slip-induced events in the PFC3D at each state of loading. In order to find the relation between  $W_{\text{cons/vol}}$  and  $E_T$ , the same REV as shown in Figure 6.9 was loaded five times to different states of stress. Each time, the MS data were extracted and the b-value plot was obtained (Figure 6.12).

For all the five states of stress, the consumed energy by the REV,  $W_{\text{cons/vol}}$ , is simply calculated as the area under the stress-strain curve. Also, the total seismic energy released due to stick-slips,  $E_T$ , is calculated as the sum of all the seismic energies of the PFC3D events using Equation (6.2).

Variations of  $W_{\text{cons./vol}}$  versus  $E_T$  (Figure 6.13) suggest a bilinear correlation between the energy consumed per volume of the REV,  $W_{\text{cons./vol}}$ , and total released seismic energies due to stick-slips,  $E_T$ . However, for simplicity, a linear correlation is used here as shown in Equation (6.3):

$$W_{\text{cons./vol}} \approx 62.5E_T \quad (6.3)$$

Since  $E_T$  is in Joules, the 62.5 coefficient has the unit of ( $1/\text{m}^3$ ). It has to be noted that the models studied in this research are on a small scale compared to the large scale of MS monitoring in the caprock. Presumably, the number of events would increase as the volume of rock modeled increased. However, it is not feasible to generate a high-resolution model on the same scale as the field due to computational limits. Therefore, correlating  $E_T$  with the consumed energy per volume of the rock seems to overcome (at least to some extent) this limitation of the numerical modeling.

As suggested before, since crack-induced energies are too small, the events actually recorded by geophones in the caprock are more likely to have slip origins along weak planes. Therefore, in practice, using the numerical modeling approach presented in this chapter, charts similar to Figure 6.12(a) and correlations similar to Equation (6.3) can be obtained for different orientations of weak planes with different properties. Upon observation of MS events in the caprock and assuming the events have a slip origin; orientation of the possible parent weak plane can be roughly calculated. Then, using the appropriate chart or correlation, the state of stress in that vicinity can be estimated.

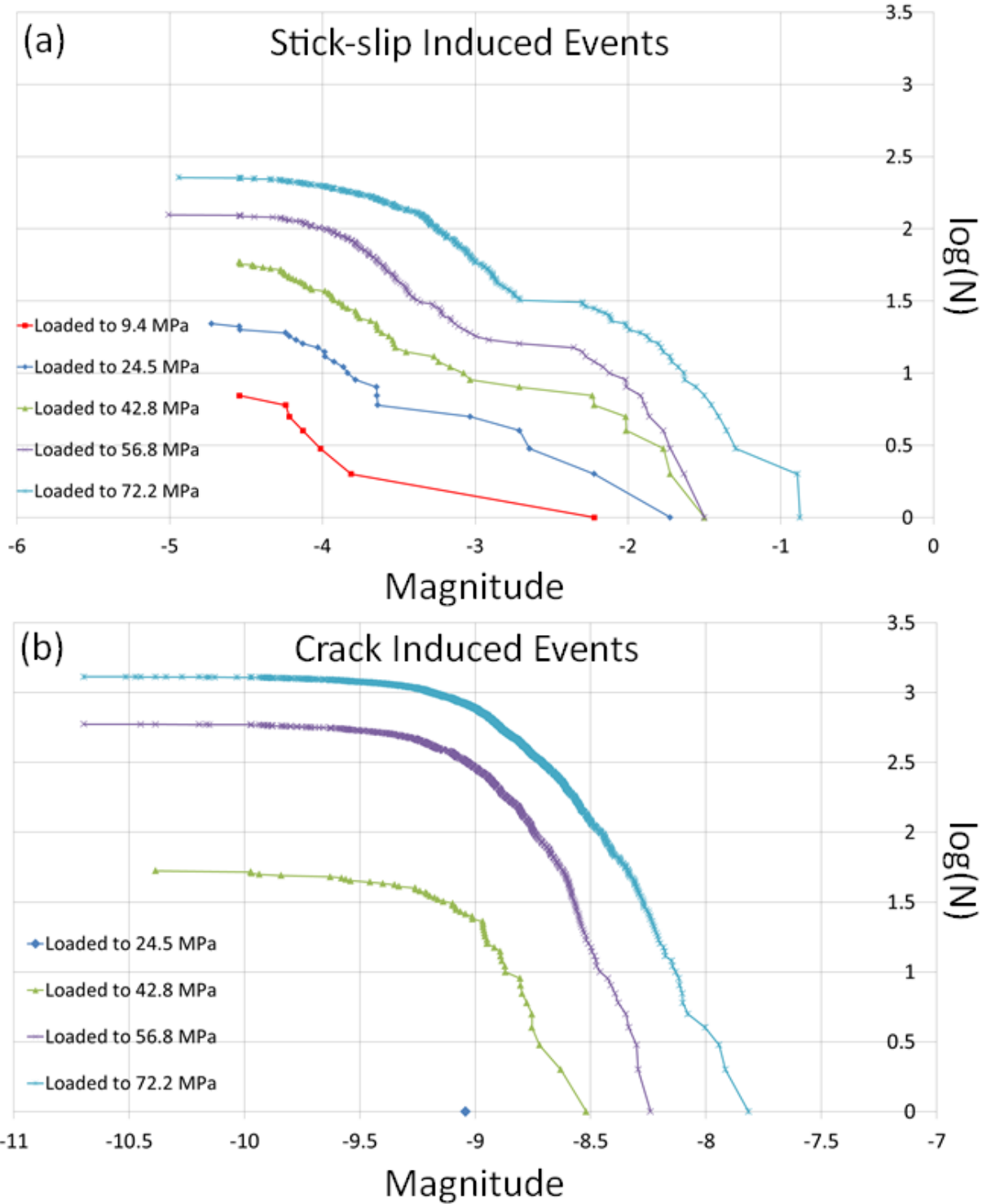


Figure 6.12: (a) The b-value plots for slip-induced events obtained from PFC3D at five states of loading. (b) b-value plot for crack-induced events recorded by PFC3D for the REV at five states of loading. No crack-induced events were observed for the REV loaded to 9.4 MPa deviator stress.

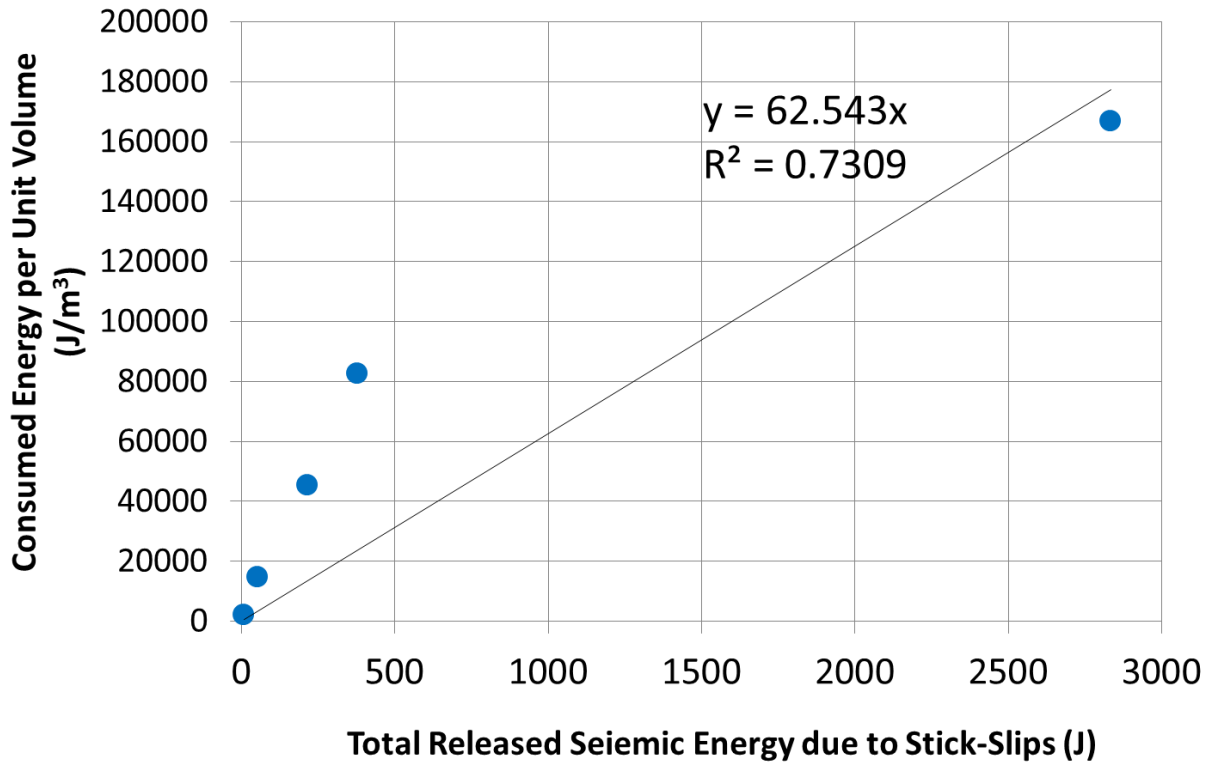


Figure 6.13: Consumed energy per volume of REV,  $W_{\text{cons./vol}}$ , versus total released seismic energy due to stick-slips,  $E_T$

## 6.8 Conclusions

In this chapter, a simple discrete element model with a single fracture fault was presented to study the release of MS energies under conditions similar to the caprock of Weyburn reservoir. Using two separate algorithms, the computed MS magnitudes were distinguished between those originating from the breakage of particle bonds (i.e. intact rock failure) and those originating from slips along a pre-existing weak plane. Also, a parametric study was conducted to investigate the effect of orientation of weak plane, coefficient of friction and elasticity of the weak plane on release of microseismic energies.

For the conditions studied in this research, it was shown that variations of magnitudes are in the range of  $\sim -1$  to  $-6$  for slip-induced events and  $\sim -7$  to  $-11$  for crack-induced events. This indicates that the events that are likely to be recorded in the caprock have a slip origin along weak planes while crack-induced events are too small to be recorded by geophones.

From the parametric study, it was shown that a decrease in the coefficient of friction, a decrease in the normal stiffness and also an increase in the shear stiffness of the weak plane all result in a greater number of stick-slips and larger slip-induced magnitudes. On the other hand, since the excess energy due to loading has to dissipate either by causing stick-slips along the weak plane and or by developing cracks within the intact parts, such conditions result in fewer numbers of crack-induced emissions and smaller crack-induced magnitudes.

Finally, a practical approach for post-analysis of MS events recorded in the caprock was proposed and a model was presented to link the consumed energy per volume of the REV to the released seismic energy due to stick-slips along a weak plane. The approach was tested with real data recorded between September and November of 2010 in the caprock of Weyburn. The results suggest that even if pressures are kept below the recommended pressure, weak planes can be emissive even long before the failure of REV is reached and thus, there can be a level of tolerance for the MS energies recorded in the caprock.

# Chapter 7

## Summary and Conclusions

In this research, using PFC3D, the microseismic response of rock masses was studied as the microseismic response of intact parts as well as that of weak planes. No laboratory experiments have been conducted.

In order to study how microseismic response differs for different type of intact rocks, a dataset of 73 uniaxial compression tests were used. The tests have been conducted by CANMET as a part of nuclear waste repository design on a wide range of rocks with different strength and stiffness properties. The relation between the total consumed energy by each type of rock with the total released seismic energy was studied. Using PFC3D, numerical tests were also conducted on specimens within the same range of strength and stiffness. A routine for recording microseismic events based on the strain energy of each bond breakage was used during the tests. The results can be summarized as following:

- a) A correlation was suggested between the total consumed energy per volume of each rock with the total released microseismic energy due to crack development. Therefore, the effect of stiffness and strength properties on microseismic release of energy would be to vary the total energy consumption by each rock type. Also, the b-values for the weak rocks were slightly greater than b-values of strong rocks. This suggests that in terms of the number of events, generally, weak/soft rocks are more emissive than strong/hard rocks. However, in terms of magnitudes, it was observed that larger magnitudes should be expected from strong/hard rocks compared to weak/soft rocks.
- b) Comparing the energies recorded for the lab tests with those obtained from PFC3D models, a modification of Gutenberg-Richter formula was suggested to get more realistic magnitudes from PFC3D models.
- c) A damage parameter was defined as the total crack surface area observed during the test divided by the total crack surface area possible based on the size of particles. A correlation was

suggested to predict the amount of crack surface development by microseismic energy observations.

In order to study the microseismic response of weak planes, a large scale biaxial shear test on a specimen of granite with a diagonal fault was modeled with PFC3D. A new algorithm was also developed to record stick-slip microseismic emissions. The results were compared with real data. A parametric study was conducted to study the effect of various parameters on MS emissions as a result of fault's instability.

In order to investigate the applicability of numerical modeling for caprock integrity analysis using microseismic data, Weyburn CCS project was studied. For this purpose, a field scale one-way reservoir-geomechanical model was developed. A one-way coupling was conducted between the reservoir simulator GEM, and geomechanical simulator, FLAC3D. A feature that allows direct importing of zone pore pressures to FLAC3D was employed. Geometrical stratigraphy and real zone pore pressures were honored as much as possible. No temperature drop due to cold injection was taken into account. It was shown that in the microseismic area of the Weyburn CCS project, the likelihood of shear failure along weak planes was about 27% greater than that of tensile failure. Therefore, the events recorded in the caprock were more likely to be generated as a result of shearing along weak planes.

In order to investigate the magnitudes of crack-induced and slip-induced emissions and the likelihood of each one's being recorded by geophones, using PFC3D, a representative elementary volume (REV) model with a weak plane at its center was made for the caprock of Weyburn reservoir. The REV was loaded to the conditions similar to those in the caprock of Weyburn. Two algorithms for recording crack-induced emissions and slip-induced emissions were used simultaneously during the loading. The results showed that for the conditions studied in this research, magnitudes of slip-induced events ranged from  $\sim -1$  to  $-6$  while crack-induced magnitudes ranged from  $\sim -7$  to  $-11$ .

With regard to the first hypothesis of this research presented in section 1.2, it is important to note that the mechanism of damage plays a crucial role in quantifying the extent of damage based on MS observation in caprock integrity analyses as opposed to small scale hard rock problems. For instance, it was discussed in section 3.6 that the MS magnitudes recorded in Lac Du Bonnet

granite in the URL project ranged from -2.9 to -4.2. This is almost within the range of MS magnitudes recorded in the shale caprock of Weyburn (i.e.  $-3.62 < M < -0.56$ ). However, assuming a traditional shear mechanism for the events recorded in the URL, (Cai et al., 2001) calculated the source dimensions and observed that considering the excavation size, source dimensions were overestimated. Then repeating the calculations assuming a tensile mechanism, the source dimensions were more reasonable. Therefore, a tensile fracturing mechanism for MS emissions in brittle rocks in the scale of that problem was shown to provide better results.

With regard to caprock, the implication of shear-induced or tensile-induced events would be significantly different in terms of hydraulic integrity analysis. In this research, considering the discussion presented in Section 3.6 on the difference of crack-induced magnitudes in shale and granite, as well as the range of crack-induced magnitudes observed in Chapter 6, it was suggested that slip-induced MS events larger than certain magnitudes are likely to be recorded by geophones while crack-induced events, if any, are too small to be recordable in the caprock. On the other hand, the extent of shear damage would obviously depend on the magnitude of recorded events. Also, it was shown that weak planes can be emissive due to small amount of loading and thus, there can be a level of tolerance for the observed MS events in the caprock.

With regard to the second hypothesis of this research presented in section 1.2, it was shown that processes such as crack development, slow-slips and hydrofracture initiation may not be recordable by geophones in the caprock. However, emergence of MS events in the caprock suggests the existence of a weak plane(s) that is likely to undergo larger displacements in future and emit larger magnitudes. Therefore, MS observations can serve as an early warning detection system for possible shear displacements in future. However, absence of MS events cannot, in isolation, be used as definite proof that no rock mass damage and hence permeability changes are occurring.

With regard to numerical analysis of caprock integrity, a combination of both continuum and discontinuum modeling seems to be the best approach. Detailed continuum models such as what was presented in Chapter 5 allow taking into account geological heterogeneity and complexity of pore pressure distribution (and temperature profile if available) all over the reservoir and its seal layers. Such models are relatively fast and allow identifying the critical areas in terms of tensile or shear failure. However, the downside is that the damage mechanism (either tensile or stick-

slip shear) cannot be easily modeled using continuum models. Therefore, making conclusions about the microseismic magnitudes and quantity of damage would be a challenge.

On the other hand, discrete element technique is capable of directly modeling the damage process. Therefore, microseismic magnitudes can be obtained and the damage process can be observed during the loading. Also, because of the size distribution of particles, some level of geometrical heterogeneity is inherently taken into account. However, DEM models are slow and thus there are limitations in terms of the scale of the models.

Therefore, it is suggested to first identify the critical zones using continuum models. Then, DEM models can be used to study in details the damage process and relate the microseismic data to geomechanics as was shown in Chapter 6.

## References

- Aki, K. (1966). Generation and Propagation of G Waves from the Niigata Earthquake of June 16, 1964: Part 1. A statistical analysis.
- Aki, K., & Richards, P. G. (2002). *Quantitative seismology*. University Science Books.
- Amann, F., Button, E. A., Evans, K. F., Gischig, V. S., & Blümel, M. (2011). Experimental study of the brittle behavior of clay shale in rapid unconfined compression. *Rock Mechanics and Rock Engineering*, 44(4), 415–430.
- Angus, D. A., Kendall, J., Fisher, Q. J., Segura, J. M., Skachkov, S., Crook, A. J. L., & Dutko, M. (2010). Modelling microseismicity of a producing reservoir from coupled fluid- flow and geomechanical simulation. *Geophysical Prospecting*, 58(5), 901–914.
- ASTM. (2005). ASTM D5878 - Standard Guides for Using Rock-Mass Classification Systems for Engineering Purposes. In *Annual Book of ASTM Standards Vol. 04.08*.
- ASTM. (2007). Standard Test Method for Compressive Strength and Elastic Moduli of Intact Rock Core Specimens under Varying States of Stress and Temperatures. In *Annual Book of ASTM Standards*.
- Baharvand Ahmadi, A., Gao, L., Ma, J., & Morozov, I. (2011). CO<sub>2</sub> Saturation vs. Pressure Effects from time-lapse 3-D P-S surface and VSP seismic data. *Final Report as Part of IEA GHG Weyburn-Midale CO<sub>2</sub> Monitoring and Storage Project*, 102.
- Baker, C., & Young, R. P. (1997). Evidence for extensile crack initiation in point source time-dependent moment tensor solutions. *Bulletin of the Seismological Society of America*, 87(6), 1442–1453.
- Barzilai, A. (2014). Geophone Research. Retrieved March 6, 2014, from <http://micromachine.stanford.edu/projects/geophones/GeophoneResearch.html>
- Bell, J. S., & Babcock, E. A. (1986). The stress regime of the Western Canadian Basin and implications for hydrocarbon production. *Bulletin of Canadian Petroleum Geology*, 34(3), 364–378. Retrieved from <http://bcpg.geoscienceworld.org/content/34/3/364.citation>
- Bell, J. S., Price, P. R., & McLellan, P. J. (1994). In-situ stress in the western Canada Sedimentary Basin. *Geological Atlas of the Western Canada Sedimentary Basin*, 439–446.
- Boggs Jr, S. (2001). Sedimentary structures. *Principles of Sedimentology and Stratigraphy, 3rd Edition: Upper Saddle River (New Jersey), Prentice-Hall*, 88–130.

- Bonnin, J., Cara, M., Cisternas, A., & Fantechi, R. (1988). *Seismic Hazard in Mediterranean Regions* (Vol. 7). Springer Science & Business Media.
- Bormann, P., & Di Giacomo, D. (2011). The moment magnitude  $M_w$  and the energy magnitude  $M_e$ : common roots and differences. *Journal of Seismology*, *15*(2), 411–427.
- Brace, W. F., & Byerlee, J. (1966). Stick-slip as a mechanism for earthquakes. *Science*, *153*(3739), 990–992.
- Brace, W. F., & Byerlee, J. (1970). California earthquakes: why only shallow focus? *Science (New York, N.Y.)*, *168*(3939), 1573–5. doi:10.1126/science.168.3939.1573
- Brown, E. T. (1981). ISRM suggested methods. Rock characterization testing and monitoring. Pergamon Press, Oxford.
- Brown, L. T. (2002). Integration of rock physics and reservoir simulation for the interpretation of time-lapse seismic data at Weyburn Field, Saskatchewan. Colorado School of Mines.
- Brune, J. N., Brown, S., & Johnson, P. A. (1993). Rupture mechanism and interface separation in foam rubber models of earthquakes: a possible solution to the heat flow paradox and the paradox of large overthrusts. *Tectonophysics*, *218*(1-3), 59–67. doi:10.1016/0040-1951(93)90259-M
- Bunge, R. J. (2001). Weyburn reservoir fracture characterization using integrated well and seismic data, Weyburn field, Saskatchewan. *M.Sc Thesis*. doi:10.1306/61EED79C-173E-11D7-8645000102C1865D
- Burrowes, G., & Gilboy, C. (2000). Investigating Sequestration Potential of Carbonate Rocks during Tertiary Recovery from a Billion Barrel Oil Field, Weyburn, Saskatchewan: the Geoscience Framework (IEA Weyburn CO<sub>2</sub> Monitoring and Storage Project).
- Byerlee, J. (1978). Friction of rocks. *Pure and Applied Geophysics PAGEOPH*, *116*(4-5), 615–626. doi:10.1007/BF00876528
- Byerlee, J., & Brace, W. F. (1968). Stick slip, stable sliding, and earthquakes—effect of rock type, pressure, strain rate, and stiffness. *Journal of Geophysical Research*, *73*(18), 6031–6037.
- Cai, M. (2010). Practical estimates of tensile strength and Hoek–Brown strength parameter  $m_i$  of brittle rocks. *Rock Mechanics and Rock Engineering*, *43*(2), 167–184.
- Cai, M., Kaiser, P. K., & Martin, C. D. (2001). Quantification of rock mass damage in underground excavations from microseismic event monitoring. *International Journal of Rock Mechanics and Mining Sciences*, *38*(8), 1135–1145.

- Cai, M., Kaiser, P. K., Morioka, H., Minami, M., Maejima, T., Tasaka, Y., & Kurose, H. (2007). FLAC/PFC coupled numerical simulation of AE in large-scale underground excavations. *International Journal of Rock Mechanics and Mining Sciences*, 44(4), 550–564.
- Cai, M., Kaiser, P. K., Tasaka, Y., Kurose, H., Minami, M., & Maejima, T. (2008). Numerical Simulation of Acoustic Emission in Large-scale Underground Excavations. In *The 42nd US Rock Mechanics Symposium (USRMS)*. American Rock Mechanics Association.
- Cai, M., Morioka, H., Kaiser, P. K., Tasaka, Y., Kurose, H., Minami, M., & Maejima, T. (2007). Back-analysis of rock mass strength parameters using AE monitoring data. *International Journal of Rock Mechanics and Mining Sciences*, 44(4), 538–549.
- Cappa, F., & Rutqvist, J. (2011). Modeling of coupled deformation and permeability evolution during fault reactivation induced by deep underground injection of CO<sub>2</sub>. *International Journal of Greenhouse Gas Control*, 5(2), 336–346. doi:10.1016/j.ijggc.2010.08.005
- Chadwick, A., Arts, R., Bernstone, C., May, F., Thibeau, S., & Zweigel, P. (2008). Best practice for the storage of CO<sub>2</sub> in saline aquifers. *Observations and Guidelines from the SACS and CO<sub>2</sub>STORE Projects*.
- Chadwick, A., & Eiken, O. (2013). Offshore CO<sub>2</sub> storage: Sleipner natural gas field beneath the North Sea. *Geological Storage of Carbon Dioxide (CO<sub>2</sub>): Geoscience, Technologies, Environmental Aspects and Legal Frameworks*, 227.
- Chadwick, A., Zweigel, P., Gregersen, U., Kirby, G. A., Holloway, S., & Johannessen, P. N. (2004). Geological reservoir characterization of a CO<sub>2</sub> storage site: The Utsira Sand, Sleipner, northern North Sea. *Energy*, 29(9), 1371–1381.
- Cho, N., Martin, C. D., & Segoo, D. C. (2007). A clumped particle model for rock. *International Journal of Rock Mechanics and Mining Sciences*, 44(7), 997–1010. doi:10.1016/j.ijrmms.2007.02.002
- Choy, G. L., & Boatwright, J. L. (1995). Global patterns of radiated seismic energy and apparent stress. *Journal of Geophysical Research: Solid Earth (1978–2012)*, 100(B9), 18205–18228.
- Churcher, P. L., & Edmunds, A. C. (1994). Reservoir characterization and the geological study of Weyburn unit: PanCanadian internal report.
- CMG. (2006). GEM Manual. *Calgary CA*.
- Collins, D. S., & Young, R. P. (2000). Lithological controls on seismicity in granitic rocks. *Bulletin of the Seismological Society of America*, 90(3), 709–723.
- Cox, S. J. D., & Meredith, P. G. (1993). Microcrack formation and material softening in rock measured by monitoring acoustic emissions. In *International journal of rock mechanics and mining sciences & geomechanics abstracts* (Vol. 30, pp. 11–24). Elsevier.

- Dalguer, L. A., & Day, S. M. (2006). Comparison of fault representation methods in finite difference simulations of dynamic rupture. *Bulletin of the Seismological Society of America*, 96(5), 1764–1778.
- Damjanac, B. (2010). *Energy release due to fracturing in BPM*. Minneapolis, MN, USA.
- Damjanac, B., Gil, I., Pierce, M., Sanchez, M., Van As, A., & McLennan, J. (2010). A New Approach to Hydraulic Fracturing Modeling In Naturally Fractured Reservoirs. *44th U.S. Rock Mechanics Symposium and 5th U.S.-Canada Rock Mechanics Symposium*. Retrieved from <https://www.onepetro.org/conference-paper/ARMA-10-400>
- Day, S. M., Dalguer, L. A., Lapusta, N., & Liu, Y. (2005). Comparison of finite difference and boundary integral solutions to three- dimensional spontaneous rupture. *Journal of Geophysical Research: Solid Earth (1978–2012)*, 110(B12).
- Dean, R. H., Gai, X., Stone, C. M., & Minkoff, S. E. (2006). A comparison of techniques for coupling porous flow and geomechanics. *Spe Journal*, 11(01), 132–140.
- Deutsch, C. V., & Journel, A. G. (1998). GSLib. *Geostatistical Software Library and User's Guide*, 369.
- Dieterich, J. H. (1979). Modeling of rock friction: 1. Experimental results and constitutive equations. *Journal of Geophysical Research*, 84(B5), 2161. doi:10.1029/JB084iB05p02161
- Dieterich, J. H. (1981). Potential for geophysical experiments in large scale tests. *Geophysical Research Letters*, 8(7), 653–656. doi:10.1029/GL008i007p00653
- Duxbury, A., White, D., Samson, C., Hall, S. A., Wookey, J., & Kendall, J.-M. (2012). Fracture mapping using seismic amplitude variation with offset and azimuth analysis at the Weyburn CO 2 storage site. *Geophysics*, 77(6), B295–B306.
- Eaton, D. W., & Forouhideh, F. (2011). Solid angles and the impact of receiver-array geometry on microseismic moment-tensor inversion. *GEOPHYSICS*, 76(6), WC77–WC85. doi:10.1190/geo2011-0077.1
- Eberhardt, E., Stead, D., & Stimpson, B. (1999). Quantifying progressive pre-peak brittle fracture damage in rock during uniaxial compression. *International Journal of Rock Mechanics and Mining Sciences*, 36(3), 361–380. doi:10.1016/S0148-9062(99)00019-4
- Elaqra, H., Godin, N., Peix, G., R'Mili, M., & Fantozzi, G. (2007). Damage evolution analysis in mortar, during compressive loading using acoustic emission and X-ray tomography: Effects of the sand/cement ratio. *Cement and Concrete Research*, 37(5), 703–713. doi:10.1016/j.cemconres.2007.02.008

- Engelder, T., & Fischer, M. P. (1994). Influence of poroelastic behavior on the magnitude of minimum horizontal stress,  $S_h$  in overpressured parts of sedimentary basins. *Geology*, 22(10), 949–952.
- ESG Weyburn Microseismic Progress Report. (2011).
- Eshiet, K. I., & Sheng, Y. (2014). Carbon dioxide injection and associated hydraulic fracturing of reservoir formations. *Environmental Earth Sciences*, 72(4), 1011–1024.
- Eyre, T. S., & van der Baan, M. (2015). Overview of moment-tensor inversion of microseismic events. *The Leading Edge*, 34(8), 882–888.
- Fairhurst, C. (2013). Fractures and Fracturing: Hydraulic Fracturing in Jointed Rock. *ISRM International Conference for Effective and Sustainable Hydraulic Fracturing*. Retrieved from <https://www.onepetro.org/conference-paper/ISRM-ICHF-2013-012>
- Finch, E., Hardy, S., & Gawthorpe, R. (2003). Discrete element modelling of contractional fault-propagation folding above rigid basement fault blocks. *Journal of Structural Geology*, 25(4), 515–528. doi:10.1016/S0191-8141(02)00053-6
- Forouhideh, F. (2011). *Microseismic moment tensor inversion*. University of Calgary.
- Fujii, H., Saito, Y., Tanaka, M., Machijima, Y., & Mori, T. (2009). The AE Characteristic in Hard rock and Soft Rock Specimens of Compression Failure Using Optical Type AE Sensor (FOD). *NATIONAL CONFERENCE ON ACOUSTICAL EMISSION*, (17), 99–102. Retrieved from <https://getinfo.de/app/VI-4-The-AE-Characteristic-in-Hard-rock-and-Soft/id/BLCP%3ACN076722467>
- Gale, W. J., Heasley, K. A., Iannacchione, A. T., Swanson, P. L., Hatherly, P., & King, A. (2001). Rock damage characterisation from microseismic monitoring. In *DC Rocks 2001, The 38th US Symposium on Rock Mechanics (USRMS)*. American Rock Mechanics Association.
- Galis, M., Moczo, P., & Kristek, J. (2008). A 3-D hybrid finite-difference—finite-element viscoelastic modelling of seismic wave motion. *Geophysical Journal International*, 175(1), 153–184.
- Ganne, P., Vervoort, A., & Wevers, M. (2007). Quantification of pre-peak brittle damage: Correlation between acoustic emission and observed micro-fracturing. *International Journal of Rock Mechanics and Mining Sciences*, 44(5), 720–729. doi:10.1016/j.ijrmms.2006.11.003
- Goertz-Allmann, B. P., Kuhn, D., Oye, V., Bohloli, B., & Aker, E. (2014). Combining microseismic and geomechanical observations to interpret storage integrity at the In Salah CCS site. *Geophysical Journal International*, 198(1), 447–461. doi:10.1093/gji/ggu010

- Gomez, J. A. J. (2006). Geomechanical performance assessment of CO<sub>2</sub>—EOR geological storage projects. *PhD Thesis (University of Alberta, Edmonton, AB, Canada)*.
- Goodman, R. E. (1989). *Introduction to rock mechanics* (Vol. 2). Wiley New York.
- Gor, G. Y., Elliot, T. R., & Prévost, J. H. (2013). Effects of thermal stresses on caprock integrity during CO<sub>2</sub> storage. *International Journal of Greenhouse Gas Control*, 12, 300–309. doi:10.1016/j.ijggc.2012.11.020
- Gorski, B., Anderson, T., & Conlon, T. (2009a). *Labratory Geomechanical Strength Testing of DGR-1 & DGR-2 Core*. Retrieved from DGR Site Characterization Document, Intra Engineering Project 06-219
- Gorski, B., Anderson, T., & Conlon, T. (2009b). *Labratory Geomechanical Strength Testing of DGR-3 & DGR-4 Core*.
- Griffith, A. A. (1921). The phenomena of rupture and flow in solids. *Philosophical Transactions of the Royal Society of London. Series A, Containing Papers of a Mathematical or Physical Character*, 221, 163–198.
- Griffith, A. A., Biezeno, C. B., & Burgers, J. M. (1997). The theory of rupture. *SPIE MILESTONE SERIES MS*, 137, 96–104.
- Guest, A., & Settari, T. (2010). Numerical model of microseismicity in hydrofracturing : our prediction for seismic moment tensors. *GeoCanada - Working with the Earth*.
- Gutenberg, B. u., & Richter, C. F. (1954). *Seismicity of the earth and related phenomena. Princeton (NJ)*.
- Hall, S. A., De Sanctis, F., & Viggiani, G. (2006). Monitoring fracture propagation in a soft rock (Neapolitan Tuff) using acoustic emissions and digital images. *Pure and Applied Geophysics*, 163(10), 2171–2204.
- Hanks, T. C., & Kanamori, H. (1979). A moment magnitude scale. *Journal of Geophysical Research: Solid Earth*, 84(B5), 2348–2350. doi:10.1029/JB084iB05p02348
- Hardy Jr, H. R. (1981). Applications of acoustic emission techniques to rock and rock structures: a state-of-the-art review. *Acoustic Emission in Geotechnical Engineering Practice, ASTM STP750, American Society for Testing and Materials*, 4–92.
- Harrison, B., & Falcone, G. (2014). Carbon capture and sequestration versus carbon capture utilisation and storage for enhanced oil recovery. *Acta Geotechnica*, 9(1), 29–38.
- Harrison, J. P., & Hudson, J. A. (2000). *Engineering rock mechanics-an introduction to the principles*. Elsevier.

- Hazzard, J. (1998). *Numerical modelling of acoustic emissions and dynamic rock behaviour. [electronic resource]*. University of Keele.
- Hazzard, J., Collins, D. S., Pettitt, W. S., & Young, R. P. (2002). Simulation of unstable fault slip in granite using a bonded-particle model. In *The Mechanism of Induced Seismicity* (pp. 221–245). Springer.
- Hazzard, J., & Damjanac, B. (2013). Further investigations of microseismicity in bonded particle models.
- Hazzard, J., & Pettitt, W. S. (2013). Advances in Numerical Modeling of Microseismicity. In *47th US Rock Mechanics/Geomechanics Symposium*. American Rock Mechanics Association.
- Hazzard, J., & Young, R. P. (2000). Simulating acoustic emissions in bonded-particle models of rock. *International Journal of Rock Mechanics and Mining Sciences*, 37(5), 867–872. Retrieved from <http://cat.inist.fr/?aModele=afficheN&cpsidt=1419981>
- Hazzard, J., & Young, R. P. (2002). Moment tensors and micromechanical models. *Tectonophysics*, 356(1), 181–197.
- Hazzard, J., & Young, R. P. (2004). Dynamic modelling of induced seismicity. *International Journal of Rock Mechanics and Mining Sciences*, 41(8), 1365–1376.
- Helmstetter, A., Nicolas, B., Comon, P., & Gay, M. (2015). Basal icequakes recorded beneath an Alpine glacier (Glacier d'Argentière, Mont Blanc, France): Evidence for stick-slip motion? *Journal of Geophysical Research: Earth Surface*, 120(3), 379–401. doi:10.1002/2014JF003288
- Hill, R., Dixon, N., & Kavanagh, J. (1998). Monitoring deformation of soil slopes using AE : Case histories. *Series on Rock and Soil Mechanics*, 21, 381–400.
- Hillis, R. R. (2001). Coupled changes in pore pressure and stress in oil fields and sedimentary basins. *Petroleum Geoscience*, 7(4), 419–425. doi:10.1144/petgeo.7.4.419
- Hubbert, M. K., & Willis, D. G. (1954). Mechanics of Hydraulic Fracturing.
- Ingraham, M. D., Issen, K. A., & Holcomb, D. J. (2013). Use of acoustic emissions to investigate localization in high-porosity sandstone subjected to true triaxial stresses. *Acta Geotechnica*, 8(6), 645–663.
- Itasca, C. G. (1999). PFC 3D-User manual. *Itasca Consulting Group, Minneapolis*.
- Itasca, C. G. (2010). *FLAC3D manual*.
- Itasca, C. G. (2015). PFC3D v5.0-User manual. *Itasca Consulting Group, Minneapolis*.

- Jafari, A., Talman, S., & Perkins, E. (2011). *Numerical Simulation of Four-Pattern CO<sub>2</sub>-Flood EOR in the Weyburn Phase 1B Area*. Edmonton.
- Jansen, F. (2006). Numerical Simulation of Stick-slip Processes with Application to Seismology and Rock Glacier Dynamics.
- Jost, M. L. u, & Herrmann, R. B. (1989). A student's guide to and review of moment tensors. *Seismological Research Letters*, 60(2), 37–57.
- Julian, B. R., Miller, A. D., & Foulger, G. R. (1998). Non-double-couple earthquakes 1. Theory. *Reviews of Geophysics*, 36(4), 525. doi:10.1029/98RG00716
- Kaldi, J., Daniel, R., Tenthorey, E., Michael, K., Schacht, U., Nicol, A., Underschultz, J., Backe, G. (2011). *Caprock Systems for CO<sub>2</sub> Geological Storage*.
- Khazaei, C., & Chalaturnyk, R. (2016). A large scale one-way reservoir-geomechanical model to study the likelihood of tensile failure in the caprock of Weyburn reservoir. *Geotechnical and Geological Engineering*.
- Khazaei, C., Hazzard, J., & Chalaturnyk, R. J. (2015a). Damage Quantification of Intact Rocks Using Acoustic Emission Energies Recorded During Uniaxial Compression Test and Discrete Element Modeling. *Computers and Geotechnics*. doi:10.1016/j.compgeo.2015.02.012
- Khazaei, C., Hazzard, J., & Chalaturnyk, R. J. (2015b). Discrete element modeling of stick-slip instability and induced microseismicity. *Pure and Applied Geophysics*. doi:10.1007/s00024-015-1036-7
- Khazaei, C., Hazzard, J., & Chalaturnyk, R. J. (2016). A Discrete Element Model to Link the Microseismic Energies Recorded in Caprock to Geomechanics. *Acta Geotechnica (Under Review)*.
- Kishi, T., Ohtsu, M., & Yuyama, S. (2000). *Acoustic emission-beyond the millennium*. Elsevier.
- Klimkowski, Ł., Nagy, S., Papiernik, B., Orlic, B., & Kempka, T. (2015). Numerical Simulations of Enhanced Gas Recovery at the Załęcze Gas Field in Poland Confirm High CO<sub>2</sub> Storage Capacity and Mechanical Integrity. *Oil & Gas Science and Technology–Revue d'IFP Energies Nouvelles*, 70(4), 655–680.
- Koerner, R. M., & Lord, A. E. (1984). *Spill alert device for earth dam failure warning*. Cincinnati, OH: U.S. Environmental Protection Agency, Municipal Environmental Research Laboratory : Center for Environmental Research Information [distributor].
- Koerner, R. M., McCabe, W. M., & Lord, A. E. (1977). Acoustic emission behavior of cohesive soils. *Journal of the Geotechnical Engineering Division*, 103(8), 837–850.

- Koerner, R. M., McCabe, W. M., & Lord Jr, A. E. (1981). Acoustic emission behavior and monitoring of soils. In *Acoustic emissions in geotechnical engineering practice: a symposium* (p. 93). ASTM International.
- Kristiansen, T. G., Barkved, O., & Pattillo, P. D. (2000). Use of passive seismic monitoring in well and casing design in the compacting and subsiding Valhall field, North Sea. In *EUROPEC: European petroleum conference* (pp. 231–241).
- Lam, T., Martin, D., & McCreath, D. (2007). Characterising the geomechanics properties of the sedimentary rocks for the DGR excavations. In *Canadian Geotechnical Conference, Ottawa*.
- Lavrov, A., Vervoort, A., Filimonov, Y., Wevers, M., & Mertens, J. (2002). Acoustic emission in host-rock material for radioactive waste disposal: comparison between clay and rock salt. *Bulletin of Engineering Geology and the Environment*, 61(4), 379–387.  
doi:10.1007/s10064-002-0160-7
- Li, H., Wang, R., & Cao, S. (2015). Microseismic forward modeling based on different focal mechanisms used by the seismic moment tensor and elastic wave equation. *Journal of Geophysics and Engineering*, 12(2), 155.
- Li, Z., Dong, M., Li, S., & Huang, S. (2006). CO<sub>2</sub> sequestration in depleted oil and gas reservoirs—caprock characterization and storage capacity. *Energy Conversion and Management*, 47(11), 1372–1382.
- Liu, H., Lee, P., Tusi, Y., & Tham, L. (2000). Acoustic emission behavior of brittle rocks under uniaxial compression. In *SEM IX International Congress*. Florida.
- Lockner, D. A. (1993). The role of acoustic emission in the study of rock fracture. *International Journal of Rock Mechanics and Mining Sciences & Geomechanics Abstracts*, 30(7), 883–899. doi:10.1016/0148-9062(93)90041-B
- Lockner, D. A., Byerlee, J., Kuksenko, V., Ponomarev, A., & Sidorin, A. (1991). Quasi-static fault growth and shear fracture energy in granite. *Nature*, 350(6313), 39–42.
- Longuemare, P., Mainguy, M., Lemonnier, P., Onaisi, A., Gérard, C., & Koutsabeloulis, N. (2002). Geomechanics in reservoir simulation: overview of coupling methods and field case study. *Oil & Gas Science and Technology*, 57(5), 471–483.
- Lorenz, J. C., Teufel, L. W., & Warpinski, N. R. (1991). Regional Fractures I: A Mechanism for the Formation of Regional Fractures at Depth in Flat-Lying Reservoirs (1). *AAPG Bulletin*, 75(11), 1714–1737.
- Lozev, M. G. (1997). *Acoustic emission monitoring of steel bridge members*.

- Magri, F., Tillner, E., Wang, W., Watanabe, N., Zimmermann, G., & Kempka, T. (2013). 3D hydro-mechanical scenario analysis to evaluate changes of the recent stress field as a result of geological CO<sub>2</sub> storage. *Energy Procedia*, 40, 375–383.
- Manthei, G., Eisenbltter, J., & Spies, T. (2000). *Acoustic Emission in Rock Mechanics Studies in Acoustic Emission-Beyond the Millennium*. Elsevier, London.
- Marsden, R. (2007). Geomechanics for reservoir management. In *Algeria Well Evaluation Conference* (p. 398).
- Martens, S. ... Group, K. (2013). CO<sub>2</sub> Storage at the Ketzin Pilot Site, Germany: Fourth Year of Injection, Monitoring, Modelling and Verification. *Energy Procedia*, 37, 6434–6443. doi:10.1016/j.egypro.2013.06.573
- Martens, S. ... Kühn, M. (2012). Europe's longest-operating on-shore CO<sub>2</sub> storage site at Ketzin, Germany: a progress report after three years of injection. *Environmental Earth Sciences*, 67(2), 323–334.
- Martin, C. D. (1993). *The strength of massive Lac du Bonnet granite around underground openings*. Retrieved from <http://mspace.lib.umanitoba.ca/jspui/handle/1993/9785>
- Martin, C. D., & Chandler, N. A. (1994). The progressive fracture of Lac du Bonnet granite. In *International Journal of Rock Mechanics and Mining Sciences & Geomechanics Abstracts* (Vol. 31, pp. 643–659). Elsevier.
- Mas Ivars, D. (2008). Bonded-Particle Model for the Deformation, Yield and Failure of Jointed Rock Masses. In *PhD Thesis*. Stockholm, Sweden.
- Mas Ivars, D., Potyondy, D. O., Pierce, M., & Cundall, P. A. (2008). The smooth-joint contact model. *Proceedings of WCCM8-ECCOMAS*.
- Maxwell, S. C., Rutledge, J., Jones, R., & Fehler, M. (2010). Petroleum reservoir characterization using downhole microseismic monitoring. *Geophysics*, 75(5), 75A129–75A137.
- Maxwell, S. C., & Urbancic, T. I. (2001). The role of passive microseismic monitoring in the instrumented oil field. *The Leading Edge*, 20(6), 636–639.
- Maxwell, S. C., White, D. J., & Fabriol, H. C. (2004). Passive seismic imaging of CO<sub>2</sub> sequestration at Weyburn. In *2004 SEG Annual Meeting*.
- McCalpin, J. P. (2009). Earthquake Magnitude Scales in Paleoseismology. *International Geophysics Series, McCalpin, JP (éditeur), 2nd Edition, London: Elsevier*.
- McGarr, A. (1994). Some comparisons between mining-induced and laboratory earthquakes. *Pure and Applied Geophysics PAGEOPH*, 142(3-4), 467–489. doi:10.1007/BF00876051

- McLaskey, G. C. (2013). Personal communication.
- McLaskey, G. C., & Kilgore, B. D. (2013). Foreshocks during the nucleation of stick-slip instability. *Journal of Geophysical Research: Solid Earth*, 118(6), 2982–2997. doi:10.1002/jgrb.50232
- McLaskey, G. C., Kilgore, B. D., Lockner, D. A., & Beeler, N. M. (2014). Laboratory Generated M -6 Earthquakes. *Pure and Applied Geophysics*. doi:10.1007/s00024-013-0772-9
- McLaskey, G. C., Thomas, A. M., Glaser, S. D., & Nadeau, R. M. (2012). Fault healing promotes high-frequency earthquakes in laboratory experiments and on natural faults. *Nature*, 491(7422), 101–104. Retrieved from <http://dx.doi.org/10.1038/nature11512>
- McLellan, P. J., Lawrence, K. H., & Cormier, K. W. (1992). A Multiple-Zone Acid Stimulation Treatment Of A Horizontal Well, Midale, Saskatchewan. *Journal of Canadian Petroleum Technology*, 31(04).
- McLennan, J. D., Hasegawa, H. S., Roegiers, J.-C., & Jessop, A. M. (1986). Hydraulic fracturing experiment at the University of Regina Campus. *Canadian Geotechnical Journal*, 23(4), 548–555.
- Mercerat, E., Souley, M., Driad, L., & Bernard, P. (2005). Induced seismicity in a salt mine environment evaluated by a coupled continuum-discrete modelling. In *AGU Fall Meeting Abstracts* (Vol. 1, p. 141).
- Metz, B., Davidson, O., De Coninck, H., Loos, M., & Meyer, L. (2005). *Carbon dioxide capture and storage*. UK: IPCC Geneva, Switzerland.
- Minkoff, S. E., Stone, C. M., Arguello, J. G., Bryant, S., Eaton, J., Peszynska, M., & Wheeler, M. (2013). Staggered In Time Coupling of Reservoir Flow Simulation and Geomechanical Deformation: Step 1 - One-Way Coupling. In *SPE Reservoir Simulation Symposium*. Society of Petroleum Engineers. doi:10.2118/51920-MS
- Mito, Y., Chang, C. S., Aoki, K., Matsui, H., Niunoya, S., & Minami, M. (2007). Evaluation of Fracturing Process of Soft Rocks At Great Depth By AE Measurement And DEM Simulation. In *11th ISRM Congress*. International Society for Rock Mechanics.
- Moghadam, A. A., & Chalaturnyk, R. (2015). Laboratory Investigation of Shale Permeability. In *SPE/CSUR Unconventional Resources Conference*. Society of Petroleum Engineers. doi:10.2118/175919-MS
- Mora, P., & Place, D. (1994). Simulation of the frictional stick-slip instability. *Pure and Applied Geophysics*, 143(1-3), 61–87.

- Moreno, F. J., Chalaturnyk, R., & Jimenez, J. (2005). Methodology for assessing integrity of bounding seals (Wells and Caprock) for geological storage of CO<sub>2</sub>. In *Proceedings of the 7. international conference on greenhouse gas control technologies*.
- Morgan, J. K. (2004). Particle Dynamics Simulations of Rate- and State-dependent Frictional Sliding of Granular Fault Gouge. *Pure and Applied Geophysics*, 161(9-10). doi:10.1007/s00024-004-2537-y
- Mori, T., Nakajima, M., Iwano, K., Tanaka, M., Kikuyama, S., & Machijima, Y. (2007). Application of the fiber optical oscillation sensor to AE measurement at the rock compression test. In *11th Congress of the International Society for Rock Mechanics* (pp. 1101–1104).
- Niandou, H., Shao, J. F., Henry, J. P., & Fourmaintraux, D. (1997). Laboratory investigation of the mechanical behaviour of Tournemire shale. *International Journal of Rock Mechanics and Mining Sciences*, 34(1), 3–16. doi:10.1016/S1365-1609(97)80029-9
- Nielsen, S., Carlson, J. M., & Olsen, K. B. (2000). Influence of friction and fault geometry on earthquake rupture. *Journal of Geophysical Research*, 105(B3), 6069. doi:10.1029/1999JB900350
- Nielsen, S., Knopoff, L., & Tarantola, A. (1995). Model of earthquake recurrence: role of elastic wave radiation, relaxation of friction, and inhomogeneity. *Journal of Geophysical Research: Solid Earth (1978–2012)*, 100(B7), 12423–12430.
- Nivesrangsan, P., Steel, J. A., & Reuben, R. L. (2007). Source location of acoustic emission in diesel engines. *Mechanical Systems and Signal Processing*, 21(2), 1103–1114.
- Ohnaka, M. (1973). Experimental studies of stick-slip and their application to the earthquake source mechanism. *Journal of Physics of the Earth*, 21(3), 285–303.
- Ohnaka, M., & Mogi, K. (1982). Frequency characteristics of acoustic emission in rocks under uniaxial compression and its relation to the fracturing process to failure. *Journal of Geophysical Research*, 87(B5), 3873. doi:10.1029/JB087iB05p03873
- Orlic, B., & Wassing, B. B. T. (2013). A study of stress change and fault slip in producing gas reservoirs overlain by elastic and viscoelastic caprocks. *Rock Mechanics and Rock Engineering*, 46(3), 421–435.
- Pacheco, J. F., Scholz, C. H., & Sykes, L. R. (1992). Changes in frequency–size relationship from small to large earthquakes. *Nature*, 355(6355), 71–73.
- Peng, Z., & Gomberg, J. (2010). An integrated perspective of the continuum between earthquakes and slow-slip phenomena. *Nature Geoscience*, 3(9), 599–607. doi:10.1038/ngeo940

- Perkins, T. K., & Gonzalez, J. A. (1985). The effect of thermoelastic stresses on injection well fracturing. *Society of Petroleum Engineers Journal*, 25(01), 78–88.
- Persson, B. N. J., & Tosatti, E. (1999). Theory of friction: elastic coherence length and earthquake dynamics. *Solid State Communications*, 109(12), 739–744.
- Pirayeshgar, A., & Dusseault, M. B. (2015). NUMERICAL INVESTIGATION OF SEISMIC EVENTS ASSOCIATED WITH HYDRAULIC FRACTURING.
- Place, D., Lombard, F., Mora, P., & Abe, S. (2002). Simulation of the micro-physics of rocks using LSMearth. In *Earthquake Processes: Physical Modelling, Numerical Simulation and Data Analysis Part I* (pp. 1911–1932). Springer.
- Pollock, A. A. (2013). AE signal features: energy, signal strength, absolute energy and RMS (Rev. 1.2). *Mistras Group INC - Technical Note 103-22-9/11*, 3.
- Potyondy, D. O. (2012). A Flat-Jointed Bonded-Particle Material For Hard Rock. *46th U.S. Rock Mechanics/Geomechanics Symposium*. Retrieved from <https://www.onepetro.org/conference-paper/ARMA-2012-501>
- Potyondy, D. O. (2015). The bonded-particle model as a tool for rock mechanics research and application: current trends and future directions. *Geosystem Engineering*, 18(1), 1–28.
- Potyondy, D. O., & Cundall, P. A. (2004). A bonded-particle model for rock. *International Journal of Rock Mechanics and Mining Sciences*, 41(8), 1329–1364. doi:10.1016/j.ijrmms.2004.09.011
- Přikryl, R., Lokajíček, T., Li, C., & Rudajev, V. (2003). Acoustic emission characteristics and failure of uniaxially stressed granitic rocks: the effect of rock fabric. *Rock Mechanics and Rock Engineering*, 36(4), 255–270.
- Rabinowicz, E. (1951). The Nature of the Static and Kinetic Coefficients of Friction. *Journal of Applied Physics*, 22(11), 1373. doi:10.1063/1.1699869
- Rabinowicz, E. (1958). The Intrinsic Variables affecting the Stick-Slip Process. *Proceedings of the Physical Society*, 71(4), 668–675. doi:10.1088/0370-1328/71/4/316
- Raziperchikolae, S., Alvarado, V., & Yin, S. (2014). Microscale modeling of fluid flow-geomechanics-seismicity: Relationship between permeability and seismic source response in deformed rock joints. *Journal of Geophysical Research: Solid Earth*, 119(9), 6958–6975. doi:10.1002/2013JB010758
- Reches, Z., & Lockner, D. A. (1994). Nucleation and growth of faults in brittle rocks. *Journal of Geophysical Research: Solid Earth (1978–2012)*, 99(B9), 18159–18173.

- Riddiford, F., Wright, I., Bishop, C., Espie, T., & Tourqui, A. (2004). Monitoring geological storage: the In Salah gas CO<sub>2</sub> storage project. In *Proceedings of the 7th International Conference on Greenhouse Gas Control Technologies* (Vol. 2, pp. 1353–1359).
- Ringrose, P. S., Mathieson, A. S., Wright, I. W., Selama, F., Hansen, O., Bissell, R., Saoula, N., & Midgley, J. (2013). The In Salah CO<sub>2</sub> Storage Project: Lessons Learned and Knowledge Transfer. *Energy Procedia*, 37, 6226–6236. doi:10.1016/j.egypro.2013.06.551
- Rodriguez, I. V., Gu, Y. J., & Sacchi, M. D. (2011). Resolution of seismic-moment tensor inversions from a single array of receivers. *Bulletin of the Seismological Society of America*, 101(6), 2634–2642.
- Röhmann, L., Tillner, E., Magri, F., Kühn, M., & Kempka, T. (2013). Fault reactivation and ground surface uplift assessment at a prospective German CO<sub>2</sub> storage site. *Energy Procedia*, 40, 437–446.
- Roux, P.-F., Marsan, D., Métaxian, J.-P., O'Brien, G., & Moreau, L. (2008). Microseismic activity within a serac zone in an alpine glacier (Glacier d'Argentiere, Mont Blanc, France). *Journal of Glaciology*, 54(184), 157–168. doi:10.3189/002214308784409053
- Rutqvist, J., Birkholzer, J. T., & Tsang, C.-F. (2008). Coupled reservoir–geomechanical analysis of the potential for tensile and shear failure associated with CO<sub>2</sub> injection in multilayered reservoir–caprock systems. *International Journal of Rock Mechanics and Mining Sciences*, 45(2), 132–143.
- Rutqvist, J., Rinaldi, A. P., Cappa, F., & Moridis, G. J. (2015). Modeling of fault activation and seismicity by injection directly into a fault zone associated with Hydraulic fracturing of shale-gas Reservoirs. *Journal of Petroleum Science and Engineering*.
- Saeedi, A. (2012). *Experimental Study of Multiphase Flow in Porous Media during CO<sub>2</sub> Geo-Sequestration Processes*. Springer Science & Business Media.
- Schilling, F., Borm, G., Würdemann, H., Möller, F., Kühn, M., & Group, C. S. (2009). Status report on the first European on-shore CO<sub>2</sub> storage site at Ketzin (Germany). *Energy Procedia*, 1(1), 2029–2035.
- Schlumberger. (2010). *Petrel help manual*.
- Scholz, C. H. (1968a). Microfracturing and the inelastic deformation of rock in compression. *Journal of Geophysical Research*, 73(4), 1417–1432. doi:10.1029/JB073i004p01417
- Scholz, C. H. (1968b). The frequency-magnitude relation of microfracturing in rock and its relation to earthquakes. *Bulletin of the Seismological Society of America*, 58(1), 399–415.
- Scholz, C. H. (2002). *The mechanics of earthquakes and faulting*. Cambridge university press.

- Segall, P., & Fitzgerald, S. D. (1998). A note on induced stress changes in hydrocarbon and geothermal reservoirs. *Tectonophysics*, 289(1-3), 117–128. doi:10.1016/S0040-1951(97)00311-9
- Sellers, E. J., Kataka, M. O., & Linzer, L. M. (2003). Source parameters of acoustic emission events and scaling with mining- induced seismicity. *Journal of Geophysical Research: Solid Earth (1978–2012)*, 108(B9).
- Seto, M., Utagawa, M., & Katsuyama, K. (2002). Some fundamental studies on the AE method and its application to in-situ stress measurements in Japan. In *Proc. 5th Int. Workshop on the Application of Geophysics in Rock Engineering, Toronto, Canada, (2002.)* (Vol. 67, p. 71).
- Settari, A., & Walters, D. A. (2001). Advances in coupled geomechanical and reservoir modeling with applications to reservoir compaction. *Spe Journal*, 6(03), 334–342.
- Shukla, R., Ranjith, P., Haque, A., & Choi, X. (2010). A review of studies on CO<sub>2</sub> sequestration and caprock integrity. *Fuel*, 89(10), 2651–2664.
- Sibson, R. H. (2003). Brittle-failure controls on maximum sustainable overpressure in different tectonic regimes. *AAPG Bulletin*, 87(6), 901–908.
- Silver, P. G., & Jordan, T. H. (1982). Optimal estimation of scalar seismic moment. *Geophysical Journal of the Royal Astronomical Society*, 70(3), 755–787. doi:10.1111/j.1365-246X.1982.tb05982.x
- Slemmons, D. B. (1990). Estimation of earthquake size for seismic hazards. *Reviews in Engineering Geology*, 8, 1–28.
- Smart, K. J., Ofoegbu, G. I., Morris, A. P., McGinnis, R. N., & Ferrill, D. A. (2014). Geomechanical modeling of hydraulic fracturing: Why mechanical stratigraphy, stress state, and pre-existing structure matter. *AAPG Bulletin*, 98(11), 2237–2261.
- Sminchak, J., & Gupta, N. (2003). Aspects of induced seismic activity and deep-well sequestration of carbon dioxide. *Environmental Geosciences*, 10(2), 81–89.
- Soltanzadeh, H. (2009). Geomechanical analysis of caprock integrity.
- Sondergeld, C. H., & Estey, L. H. (1981). Acoustic emission study of microfracturing during the cyclic loading of Westerly granite. *Journal of Geophysical Research: Solid Earth (1978–2012)*, 86(B4), 2915–2924.
- Stauffer, M. R., & Gendzwill, D. J. (1987). Fractures in the northern plains, stream patterns, and the midcontinent stress field. *Canadian Journal of Earth Sciences*, 24(6), 1086–1097. doi:10.1139/e87-106

- Stein, S., & Wysession, M. (2009). *An introduction to seismology, earthquakes, and earth structure*. John Wiley & Sons.
- Surdam, R. C. (2013). *Geological CO<sub>2</sub> storage characterization: The key to deploying clean fossil energy technology*. Springer Science & Business Media.
- Suzuki, T., Ogata, H., Takada, R., Aoki, M., & Ohtsu, M. (2010). Use of acoustic emission and X-ray computed tomography for damage evaluation of freeze-thawed concrete. *Construction and Building Materials*, 24(12), 2347–2352. doi:10.1016/j.conbuildmat.2010.05.005
- Teufel, L. W., Rhett, D. W., & Farrell, H. E. (1991). Effect of reservoir depletion and pore pressure drawdown on in situ stress and deformation in the Ekofisk field, North Sea. In *The 32nd US Symposium on Rock Mechanics (USRMS)*. American Rock Mechanics Association.
- Thoeny, R., Amann, F., & Button, E. (2010). Ground conditions and the relationship to ground behavior—a new mine-by project in Opalinus clay at Mont Terri Rock Laboratory. *Rock Mechanics and Environmental Engineering*, (Zhao J, Labiouse V, Dudt J-P, Mathier J-F (eds)), 775–778.
- Townend, J., & Zoback, M. D. (2000). How faulting keeps the crust strong. *Geology*, 28(5), 399–402.
- U.S. (EIA). (2014). Country Analysis Briefs: Canada. Retrieved March 6, 2014, from <http://www.eia.gov/countries/cab.cfm?fips=CA>
- Utsu, T. (1958). Aftershocks and Earthquake Statistics (1): Some Parameters. *Geophysics*, 3(3), 129–195.
- Utsu, T. (1961). A statistical study on the occurrence of aftershocks. *Geophysical Magazine*, 30(4).
- Valès, F., Nguyen Minh, D., Gharbi, H., & Rejeb, A. (2004). Experimental study of the influence of the degree of saturation on physical and mechanical properties in Tournemire shale (France). *Applied Clay Science*, 26(1-4), 197–207. doi:10.1016/j.clay.2003.12.032
- Vavryčuk, V. (2001). Inversion for parameters of tensile earthquakes. *Journal of Geophysical Research: Solid Earth (1978–2012)*, 106(B8), 16339–16355.
- Verdon, J. P. (2010). *Microseismic monitoring and geomechanical modelling of CO<sub>2</sub> storage in subsurface reservoirs*. University of Bristol.
- Verdon, J. P. (2012). *Microseismic Monitoring and Geomechanical Modelling of CO<sub>2</sub> Storage in Subsurface Reservoirs*. doi:10.1007/978-3-642-25388-1

- Verdon, J. P. (2016). Using microseismic data recorded at the Weyburn CCS-EOR site to assess the likelihood of induced seismic activity. *International Journal of Greenhouse Gas Control*.
- Verdon, J. P., Jones, B., & Kendall, J. (2012). *Microseismic monitoring and geomechanical deformation during co2 injection at weyburn*.
- Verdon, J. P., Kendall, J.-M., Stork, A. L., Chadwick, R. A., White, D. J., & Bissell, R. C. (2013). Comparison of geomechanical deformation induced by megatonne-scale CO<sub>2</sub> storage at Sleipner, Weyburn, and In Salah. *Proceedings of the National Academy of Sciences of the United States of America*, 110(30), E2762–71. doi:10.1073/pnas.1302156110
- Verdon, J. P., Kendall, J.-M., White, D. J., & Angus, D. A. (2011). Linking microseismic event observations with geomechanical models to minimise the risks of storing CO<sub>2</sub> in geological formations. *Earth and Planetary Science Letters*, 305(1), 143–152.
- Vidal-Gilbert, S., Nauroy, J.-F., & Brosse, E. (2009). 3D geomechanical modelling for CO<sub>2</sub> geologic storage in the Dogger carbonates of the Paris Basin. *International Journal of Greenhouse Gas Control*, 3(3), 288–299. doi:10.1016/j.ijggc.2008.10.004
- Vilarrasa, V., & Laloui, L. (2016). Impacts of Thermally Induced Stresses on Fracture Stability During Geological Storage of CO<sub>2</sub>. *Energy Procedia*, 86, 411–419.
- Vilarrasa, V., Olivella, S., Carrera, J., & Rutqvist, J. (2014). Long term impacts of cold CO<sub>2</sub> injection on the caprock integrity. *International Journal of Greenhouse Gas Control*, 24, 1–13. doi:10.1016/j.ijggc.2014.02.016
- Watanabe, K., Niwa, J., Iwanami, M., & Yokota, H. (2004). Localized failure of concrete in compression identified by AE method. *3rd Kumamoto International Workshop on Fracture, Acoustic Emission and NDE in Concrete (KIFA-3)*, 18(3), 189–196. doi:10.1016/j.conbuildmat.2003.10.008
- WEBLEX Canada. Natural Resources Canada, Ottawa, ON. Government of Canada. (2016). Retrieved April 4, 2016, from <http://weblex.nrcan.gc.ca/html/016000/GSCC00053016133.html>
- Wegelin, A. (1984). GEOLOGY AND RESERVOIR PROPERTIES OF THE WEYBURN FIELD, SOUTHEASTERN SASKATCHEWAN, 71–82. Retrieved from <http://archives.datapages.com/data/sgs/1984/071/071.htm>
- Wentworth, C. K. (1922). A scale of grade and class terms for clastic sediments. *The Journal of Geology*, 377–392.

- White, D. (2013). Seismic characterization and time-lapse imaging during seven years of CO<sub>2</sub> flood in the Weyburn field, Saskatchewan, Canada. *International Journal of Greenhouse Gas Control*, 16, S78–S94. doi:10.1016/j.ijggc.2013.02.006
- Whittaker, S. (2010a). An update on the Saskatchewan CO<sub>2</sub> floods (Weyburn+Midale) and storage monitoring activities. In *16th annual CO<sub>2</sub> flooding conference*. Midland, Texas.
- Whittaker, S. (2010b). IEA GHG Weyburn-Midale CO<sub>2</sub> Storage & Monitoring Project. *Regional Carbon Sequestration Partnerships Annual Review*.
- Whittaker, S., Rostron, B., Hawkes, C., Gardner, C., White, D., Johnson, J., Chalaturnyk, R., & Seeburger, D. (2011). A decade of CO<sub>2</sub> injection into depleting oil fields: monitoring and research activities of the IEA GHG Weyburn-Midale CO<sub>2</sub> Monitoring and Storage Project. *Energy Procedia*, 4, 6069–6076.
- Wilson, M., & Monea, M. (Eds.). (2004). *IEA GHG WEYBURN CO<sub>2</sub> MONITORING & STORAGE PROJECT SUMMARY REPORT 2000-2004*.
- Xie, H. ... Hou, Z. (2014). Carbon geological utilization and storage in China: current status and perspectives. *Acta Geotechnica*, 9(1), 7–27.
- Xing, H. L., Mora, P., & Makinouchi, A. (2004). Finite element analysis of fault bend influence on stick-slip instability along an intra-plate fault. In *Computational Earthquake Science Part I* (pp. 2091–2102). Springer.
- Young, R. P., Collins, D. S., Hazzard, J., Pettitt, W., & Baker, C. (2001). *Use of acoustic emission and velocity methods for validation of micromechanical models at the URL*. Toronto, Ont.: Ontario Power Generation, Nuclear Waste Management Division.
- Young, R. P. ... Dedecker, F. (2005). Seismic Validation of 3-D Thermo-Mechanical Models for the Prediction of the Rock Damage around Radioactive Waste Packages in Geological Repositories-SAFETI. *Final Report, European Commission Nuclear Science and Technology*.
- Yukalov, V. I., Moura, A., & Nechad, H. (2004). Self-similar law of energy release before materials fracture. *Journal of the Mechanics and Physics of Solids*, 52(2), 453–465. doi:10.1016/S0022-5096(03)00088-7
- Zang, A., Wagner, F. C., Stanchits, S., Janssen, C., & Dresen, G. (2000). Fracture process zone in granite. *Journal of Geophysical Research: Solid Earth (1978–2012)*, 105(B10), 23651–23661.
- Zhang, Y., Langhi, L., Schaub, P. M., Piane, C. D., Dewhurst, D. N., Stalker, L., & Michael, K. (2015). Geomechanical stability of CO<sub>2</sub> containment at the South West Hub Western Australia: A coupled geomechanical–fluid flow modelling approach. *International Journal of Greenhouse Gas Control*, 37, 12–23. doi:10.1016/j.ijggc.2015.03.003

- Zhao, G., & Tian, S. (2003). CO<sub>2</sub> flooding performance monitoring and forecasting in the Weyburn oil field. *Report Submitted to Petroleum Research Technology Center (PTRC) Research.*
- Zhao, X., & Young, R. P. (2011). Numerical modeling of seismicity induced by fluid injection in naturally fractured reservoirs. *Geophysics*, 76(6), WC167–WC180.
- Zhou, W., Stenhouse, M. J., Arthur, R., Whittaker, S., Law, D. H. S., Chalaturnyk, R., & Jazrawi, W. (2004). The IEA Weyburn CO<sub>2</sub> monitoring and storage project—Modeling of the long-term migration of CO<sub>2</sub> from Weyburn. In *Proceedings of the 7th international conference on greenhouse gas control technologies (GHGT-7)* (pp. 721–730).
- Zoback, M. D., Kohli, A., Das, I., & McClure, M. W. (2012). The importance of slow slip on faults during hydraulic fracturing stimulation of shale gas reservoirs. In *SPE Americas Unconventional Resources Conference*. Society of Petroleum Engineers.
- Zweigel, P., & Heill, L. K. (2003). Studies on the likelihood for caprock fracturing in the Sleipner CO<sub>2</sub> injection case. *Saline Aquifer CO<sub>2</sub> Storage Project.*